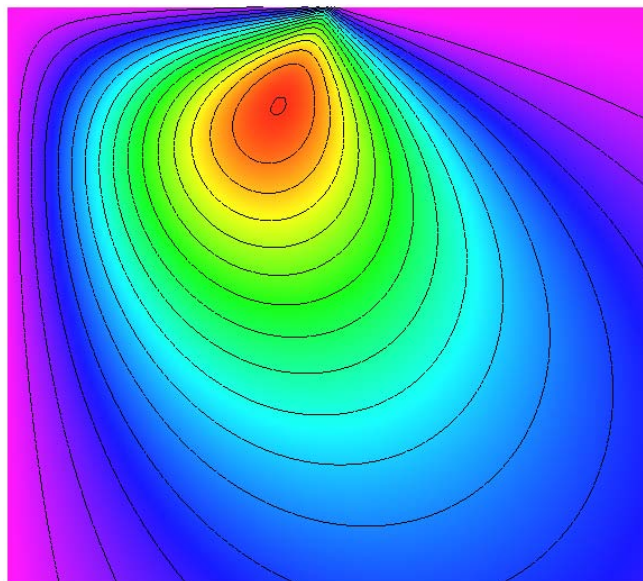

Hydrogen embrittlement,
revisited by in situ electrochemical
nanoindentation

Dissertation

Zur Erlangung des Grades des
Doktors der Ingenieurwissenschaften (Dr.-Ing.)
der Naturwissenschaftlich-Technischen Fakultät III
Chemie, Pharmazie, Bio- und Werkstoffwissenschaften
der Universität des Saarlandes



Von

Dipl.-Ing. Afrooz Barnoush

Saarbrücken, 2007

Eingereicht am: 16.10.2007
Tag der Kolloquiums: 14.03.2008
Dekan: Prof. Dr. Uli Müller
Vorsitzender: Prof. Dr. Hempelmann
Berichterstatter: Prof. Dr. H. Vehoff
Prof. Dr. W. Arnold
Prof. Dr. R. Johnsen
Akad. Mitarbeiter: Dr. Isabella Gallino

CONTENTS

LIST OF FIGURES	vi
LIST OF TABLES	xvi
ACKNOWLEDGMENT	xvii
ABSTRACT	xix
ZUSAMMENFASSUNG	xx
ACRONYMS	xxiii
SYMBOLS	xxv
1. Introduction	1
2. Hydrogen Embrittlement	5
2.1 Phenomenology of hydrogen embrittlement	5
2.2 Entry of hydrogen into metals	8
2.2.1 Gas phase	8
2.2.2 Liquid phase	9
2.2.2.1 Mechanism of the cathodic evolution of hydrogen from aqueous electrolytes	10
2.2.2.2 Entry of electrolytic hydrogen into metals	13
2.2.2.3 Promoter of hydrogen entry into metals	14
2.3 Hydrogen interaction with defects in metal	14
2.3.1 Point defects	15
2.3.2 Solutes and solute-defect complexes	16
2.3.3 Dislocations	17
2.3.4 Internal boundaries	19
2.4 Experimental methodologies of HE study	20
2.4.1 Conventional Methods	22
2.4.2 Environmental transmission electron microscopy	25

2.5	HE mechanisms	28
2.5.1	Hydride-induced embrittlement	28
2.5.2	Hydrogen enhanced decohesion	28
2.5.3	Hydrogen enhanced localized plasticity	31
2.6	A new approach to HE study	32
3.	NI-AFM	35
3.1	Nanoindentation	35
3.2	Contact Mechanics	36
3.3	Depth sensing nanoindentation	48
3.4	Instrumentation	55
3.4.1	Hysitron Triboscope	55
3.4.2	Nanoindentation tips	59
3.5	NI-AFM in liquid	63
3.5.1	Complexities of NI in liquid	64
3.5.1.1	Meniscus force	65
3.5.1.2	Buoyant force	66
3.5.2	Controlling the forces acting on the tip	67
3.6	Indentation phenomena	68
3.6.1	Geometry-based phenomena	69
3.6.1.1	Surface roughness	69
3.6.1.2	Inhomogeneities	71
3.6.1.3	The indentation size effect	72
3.6.2	Material-based phenomena	74
3.6.2.1	Pile-up and Sink-in	74
3.6.2.2	Phase transformation	77
3.6.2.3	Pop-in	77
3.6.2.4	Creep	84
3.6.2.5	Fracture	85
4.	Experimental	87
4.1	General aspects of sample preparation	87
4.1.1	Electropolishing procedure	90
4.2	Mechanical property measurements	92
4.2.1	Microindentation	92
4.2.2	Nanoindentation	93
4.3	In situ electrochemical NI-AFM	93

5. Results	99
5.1 Why not ex situ tests?	100
5.1.1 Ex situ electrochemical hydrogen charging	100
5.1.1.1 Nanoindentation measurements on ex situ charged nickel	100
5.1.1.2 Microhardness measurements on ex situ charged nickel	103
5.1.2 Ex situ hydrogen hydrogen charging in autoclave	106
5.2 In situ ECNI-AFM tests on copper	107
5.3 In situ ECNI-AFM tests on aluminum	111
5.3.1 ECNI-AFM of aluminum in pH 6, sulfate solution	118
5.3.2 ECNI-AFM of aluminum in pH 8.9, borate buffer	118
5.3.3 pH effect on pop-in load in aluminum	122
5.4 In situ ECNI-AFM tests on Fe-3wt.%Si	126
5.5 In situ ECNI-AFM tests on a FeAl intermetallic alloy	133
5.6 In situ ECNI-AFM tests on Nickel	140
5.6.1 Time delay experiments	145
5.7 In situ ECNI-AFM tests on stainless steels	151
5.7.1 Austenitic Stainless steel	151
5.7.2 Super Duplex Stainless steel	160
5.7.3 Hydrogen effect on stainless steels	173
6. Discussion	183
6.1 Indentation induced homogeneous dislocation nucleation	183
6.2 Hydrogen effect on dislocation nucleation	193
6.2.1 Shear modulus	204
6.2.2 Stacking fault energy	206
6.2.3 Dislocation core radius	208
6.3 Time delay experiments	210
7. Conclusion and outlooks	213
7.1 Conclusion	213
7.2 Outlooks	214
7.2.1 Micro compression tests	215
7.2.2 Low temperature ECNI-AFM	215

APPENDIX

A. Pop-in finder program	218
B. In situ ECNI-AFM operation	220
B.1 Overview	220
B.2 Procedure	221
B.2.1 Starting the software	221
B.2.2 Install the sample in the electrochemical cell	221
B.2.3 Install the electrochemical cell on the microscope stage	222
B.2.4 Install the nanoindentation head	223
B.2.5 Align the nanoindentation head on the microscope	224
B.2.6 Put the microscope inside the chamber	225
B.2.7 Engage the tip in air	225
B.2.8 Engage the tip in electrolyte	226
PUBLICATIONS	227
Peer-reviewed publications	227
Conference papers	228
REFERENCES	229
INDEX	256

LIST OF FIGURES

1.1	Global description of HE interaction aspects	2
2.1	Damage parameter for different single-crystalline and polycrystalline super-alloys	6
2.2	Schematic of critical variables affecting the threshold values (K_{TH}) and the crack growth rate da/dt	7
2.3	Schematic diagram of the metal/electrolyte interface, showing fully and partially solvated ions.	11
2.4	Schematic presentation of defects in metal and accumulation of hydrogen atoms in the low-concentration range.	15
2.5	Embrittlement index from 465 tests on 34 different steel grades as a function of yield stress.	22
2.6	The effect of hydrogen charging condition and temperature on $\sigma_{UTS(Hydrogen)}$ versus $\sigma_{UTS(Air)}$	23
2.7	The effect of in situ hydrogen charging on the flow stress of high purity iron at various temperatures	24
2.8	The effect of hydrogen on the mobility of dislocations in α -Ti	26
2.9	Reduction of the separation distance between dislocations in a pileup in 310s stainless steel due to solute hydrogen	27
2.10	The dependence of in situ measured crack tip opening angle, α , on hydrogen pressure for Fe-3wt%Si	29
2.11	Crack tip opening angles obtained in Fe-3wt%Si single crystals after straining.	30
3.1	Schematic of the interaction between a rigid spherical indenter and a flat surface	37
3.2	Graphical representation of the σ_r in Huber stress tensor	41

3.3	Graphical representation of the σ_θ in Huber stress tensor	42
3.4	Graphical representation of the σ_z in Huber stress tensor	43
3.5	Graphical representation of the τ_{rz} in Huber stress tensor	44
3.6	Graphical representation of the σ_1 principle stress	45
3.7	Graphical representation of the σ_3 principle stress.	46
3.8	Graphical representation of the τ_{13} principle shear stress	47
3.9	Loading profile and the resulted load displacement curve	49
3.10	Representative load-displacement data demonstrating differences in elasticity	50
3.11	Schematic of an indenter at maximum load P_{max} with an associated total depth of h_{max}	53
3.12	Schematic of the NI-AFM system	56
3.13	Schematic circuit diagram of the Hysitron TriboScope transducer assembly.	57
3.14	Schematic of a three plate capacitor force-displacement transducer of the Hysitron Triboscope.	57
3.15	Graph of $1/S$ versus $1/\sqrt{P_{max}}$ for a series of indents performed in fused quartz	59
3.16	Schematic of nanoindentation probe tips	60
3.17	Schematics of a Berkovich indenter	61
3.18	Indentation tests on fused silica	62
3.19	Area function curve determined from load displacement curves given in figure 3.18b.	63
3.20	Special fluid cell tip for nanoindentation inside liquid	65
3.21	Meniscus force acting on the nanoindenter shaft during nanoindentation inside the liquid	65
3.22	Representation of wetting angle and its dependence on interfacial energies	66
3.23	Change in the meniscus force with contact angle, calculated for the case of pure water and shaft radius of 700 μm	67

3.24	Dependence of the buoyant force on the density of the solution (a) and the immersion depth of the tip (b)	68
3.25	Different cases of ratio of lateral dimension of tip to the lateral dimension of surface roughness.	70
3.26	Schematic of the non-uniform contact between an indentation tip and a rough surface.	70
3.27	Geometrically necessary dislocations created by a rigid conical indentation	72
3.28	Schematic representation of pile-up and sink-in.	75
3.29	Graphical representation of the hydrostatic pressure calculated from Huber stress tensor	78
3.30	Effect of phase transformation on load displacement curves observed during nanoindentation of silicon	79
3.31	The time-series TEM images of an Al grain during an in-situ nanoindentation experiment	82
3.32	Homogeneous defect nucleation in $\langle 111 \rangle$ spherical indentation of Al	83
3.33	Schematic of the theoretical shear stress, the force required to slide one row of atoms over another, to a location of perfect registry.	84
4.1	EBSD pattern showing the orientation of a FeAl single crystal	88
4.2	EBSD pattern showing the orientation of a nickel single crystal	89
4.3	Dependence of pop-in load on surface preparation.	89
4.4	Typical curves for determining conditions for electropolishing	91
4.5	Potentiodynamic polarization curves for nickel in different concentration of sulphuric acid in methanol (scan rate 20mV/s).	92
4.6	Localized corrosion process happening on the surface of nickel single crystal.	94
4.7	Experimental setup for in situ electrochemical nanoindentation. Protective atmosphere chamber and vibration control.	95
4.8	Drawing of the special cell designed for performing in situ electrochemical nanoindentation experiments.	96
4.9	Schematic representation of the experimental setup for in situ ECNI-AFM experiments.	97

4.10	Artifact in load displacement curve resulted from impurities inside the electrolyte	97
4.11	Impurities in solution start to deposit on the surface and influence the imaging and nanoindentation measurements	98
5.1	Light microscope micrograph of nickel surface in freshly electropolished condition	100
5.2	Load displacement curves of nickel (a) before hydrogen charging, (b) after ex situ hydrogen charging	101
5.3	Comparison of nanohardness measurement on ex situ hydrogen charged and uncharged nickel sample.	102
5.4	Distribution of the pop-in load for hydrogen free and ex situ hydrogen charged situations in nickel.	102
5.5	Comparison between the microhardness of the hydrogen free and the ex situ hydrogen charged single crystal nickel.	103
5.6	Schematic of hydrogen outgassing model used for analysis of hydrogen outgassing from the sample	104
5.7	Schematic of a Vickers indenter utilized for microhardness measurement	104
5.8	Increase in nickel microhardness as a result of hydrogen charging	105
5.9	Surface damage in nickel as a result of ex situ hydrogen charging in an autoclave at 300 °C and 200 bar.	106
5.10	Potentiodynamic polarization curve of copper (1 1 1) single crystal in Borate buffer	107
5.11	Surface topography of electropolished copper (1 1 1) single crystal.	109
5.12	Load displacement curves of in situ ECNI-AFM on copper (1 1 1) single crystal under cathodic polarization.	110
5.13	Load displacement curves of in situ ECNI-AFM on copper (1 1 1) single crystal under anodic polarization.	110
5.14	OIM and optical microscope images of annealed pure aluminum	113
5.15	Surface topography of electropolished pure aluminum sample.	114
5.16	SEM image of the freshly electropolished pure aluminum sample.	115
5.17	Typical load displacement curves of aluminum in air	115

5.18	SEM image of the freshly electropolished pure aluminum sample, which was cyclic deformed during fatigue test.	116
5.19	Surface topography image taken from electropolished cyclic deformed pure aluminum sample during nanoindentation tests.	116
5.20	ECCI from electropolished pure aluminum sample cyclic deformed during a fatigue test.	117
5.21	Load displacement curves of electropolished pure aluminum sample cyclic deformed during a fatigue test.	118
5.22	Typical load displacement curves of aluminum in pH 6, 0.05 M Na ₂ SO ₄ solution.	119
5.23	Surface topography of the aluminum sample in pH 6, 0.05 M Na ₂ SO ₄ solution.	120
5.24	Typical load displacement curves of aluminum in pH 8.9 Borate buffer solution.	121
5.25	Typical surface topography images of aluminum in pH 8.9 Borate buffer solution.	123
5.26	Optical microscope images of Fe-3wt.%Si alloy after heat treatment	126
5.27	Complete orientation map of the Fe-3wt.%Si sample after heat treatment	127
5.28	Pourbaix diagram of iron	127
5.29	Polarization curve of Fe-3wt.%Si sample measured inside ECNI-AFM setup.	128
5.30	Cyclic voltammetry curves of Fe-3wt.%Si sample measured inside ECNI-AFM setup.	129
5.31	Chronoamperometry curve measured during anodic polarization of the Fe-3wt.%Si sample	130
5.32	Topography image of the Fe-3wt.%Si sample after a short time of anodic polarization in side borate buffer solution.	130
5.33	Load displacement curves of in situ ECNI-AFM on Fe-3wt.%Si sample in air	131
5.34	Load displacement curves of in situ ECNI-AFM on Fe-3wt.%Si under cathodic polarization of -1000 mV (hydrogen charged).	131

5.35	Surface topography of the Fe-3wt.%Si sample under cathodic polarization of -1000 mV (hydrogen charged).	132
5.36	Fe-Al equilibrium phase diagram	133
5.37	B2 crystal structure of ordered FeAl alloy	134
5.38	Load displacement curves of in situ ECNI-AFM on FeAl (100) single crystal under anodic polarization.	135
5.39	Load displacement curves of in situ ECNI-AFM on FeAl (100) single crystal under -900 mV cathodic polarization.	136
5.40	Load displacement curves of in situ ECNI-AFM on FeAl (100) single crystal under -1100 mV cathodic polarization.	136
5.41	Load displacement curves of in situ ECNI-AFM on FeAl (100) single crystal after switching back the potential to 100 mV	137
5.42	The mean value of the pop-in loads observed during in situ nanoindentation of FeAl (100) single crystal	137
5.43	The surface topography of the FeAl sample in air (a), under anodic potential (b), and cathodic potential (c)	139
5.44	Cyclic polarization curve nickel single crystal in pH 6, 0.05 M Na ₂ SO ₄ solution.	141
5.45	Chronoamperometry curves for reduction of two different NiO oxide layers.	142
5.46	Load displacement curves of in situ ECNI-AFM on nickel (111) single crystal under cathodic polarization (hydrogen charged).	142
5.47	Load displacement curves of in situ ECNI-AFM on nickel (111) single crystal under anodic polarization (hydrogen free).	143
5.48	Comparison between two load displacement curves of in situ ECNI-AFM on nickel (111) single crystal.	143
5.49	Mean values of the pop-in loads in nickel under cyclically changed electrochemical polarization	144
5.50	Surface topography during in situ ECNI-AFM on the nickel (111) surface under different electrochemical polarization.	145
5.51	Typical time delay experiment under anodic potential.	146
5.52	Typical time delay experiment with switching to cathodic potential during hold.	148

5.53	Typical time delay experiment with switching to cathodic potential during hold. Effect of hold load on time to pop-in	149
5.54	Reproducibility of the load-displacement curves for the time delay experiments under anodic potential.	150
5.55	Complete orientation map of the solution annealed austenitic stainless steel sample	153
5.56	Orientation map of solution annealed SS analyzed for twin boundaries	153
5.57	Load displacement curves of solution annealed austenitic stainless steel sample in air.	154
5.58	Electrochemical potential applied to the solution annealed austenitic stainless steel.	154
5.59	Effect of the electrochemical potential on load displacement curves of the solution annealed austenitic stainless steel sample.	156
5.60	Effect of switching back to anodic polarization on load displacement curves of solution annealed austenitic stainless steel sample	158
5.61	Mean values of the hardness under different electrochemical polarization of austenitic stainless steel.	158
5.62	The surface topography of austenitic stainless steel sample in air (a), under anodic potential (b), and cathodic potential (c)	159
5.63	OIM and SEM images of SDSS sample used for in situ ECNI-AFM tests. OIM image of ferrite phase (a), austenite (b), SEM image (c) .	161
5.64	Contact mode AFM surface topography of electropolished SDSS. Austenite phase with convex grain boundaries is electropolished deeper. . .	162
5.65	Load displacement curves of as received SDSS sample in pH 8.9 borate buffer solution.	163
5.66	Gradient images taken during in situ ECNI-AFM on as received SDSS sample.	165
5.67	Frequency of pop-in events under anodic and cathodic potential in ferrite and austenite phases of SDSS.	166
5.68	Pop-in load distribution in austenite and ferrite phases of the as received SDSS sample	167
5.69	Pop-in load distribution in austenite and ferrite phases of the aged SDSS for hydrogen charged and without hydrogen conditions.	169

5.70	The load functions with constant loading rate of 100 $\mu\text{N/s}$	170
5.71	The load functions with constant loading time of 2.5 s	170
5.72	The effect of loading rate and hydrogen charging on hardness of ferrite phase in as received SDSS	171
5.73	The effect of loading rate and hydrogen charging on hardness of austenite phase in as received SDSS	172
5.74	Electron micrograph of a precipitate free ferritic region belonging to a continuous ferritic grain cluster.	174
5.75	Electron micrograph of an austenitic region belonging to a continuous austenitic grain cluster.	175
5.76	Micrograph of a typical SDSS sample microstructure.	175
5.77	Electron micrograph of an austenitic region aged in 500 °C.	176
5.78	Effect of aging heat treatment on pop-in event frequency observed in SDSS	177
5.79	Effect of aging heat treatment on hardness of different phases in SDSS	177
5.80	Schematic representation of existing dislocations in austenite phase of as received SDSS.	178
5.81	Schematic representation of plastic zone interaction with Cr_2N particles in the lattice	179
5.82	The effect of loading rate on hardness of austenite in as received SDSS. The data is fitted with Gao-Nix model	181
5.83	Difference in pinned dislocation density for different loading rates as function of time.	182
6.1	Effect of loading time on pop-in and elastic events frequency during nanoindentation on a (111) nickel single crystal.	184
6.2	Relationship between the load of the first pop-in and the resulting displacement of the burst (pop-in width) for different materials.	186
6.3	Relationship between the load of the first pop-in and the resulting displacement of the burst.	186
6.4	Schematic load displacement curve for a material which shows an unstable elastic to plastic transition	187

6.5	Time activated pop-in observed during nanoindentation of FeAl (100) single crystal.	188
6.6	Position of the maximum shear stress responsible for the homogeneous dislocation nucleation.	188
6.7	Change in free energy of homogeneous dislocation nucleation for nickel.	189
6.8	Change in free energy of homogeneous dislocation nucleation for copper.	194
6.9	Change in free energy of homogeneous dislocation nucleation for nickel.	195
6.10	Possible changes in shear modulus, dislocation core radius and SFE due to hydrogen.	197
6.11	Change in free energy of homogeneous dislocation nucleation (partial dislocation) for aluminum.	198
6.12	Change in free energy of homogeneous dislocation nucleation (perfect dislocation) for aluminum.	199
6.13	Possible changes in shear modulus and dislocation core radius due to hydrogen for aluminum.	200
6.14	Change in free energy of homogeneous dislocation nucleation for Fe-3wt.%Si	201
6.15	Change in free energy of homogeneous dislocation nucleation for FeAl202	
6.16	Possible changes in shear modulus and dislocation core radius due to hydrogen for Fe-3wt.%Si	203
6.17	Possible changes in shear modulus and dislocation core radius due to hydrogen for FeAl	203
6.18	Bulk energies of various metals scaled using equation	205
6.19	Schematic representation of the indentation geometry and hydrogen diffusion path in the experiments	210
6.20	Change in observed time to pop-in with hydrogen diffusion path for the time delay experiments under cathodic potentials	211
6.21	Graphical representation of the τ_{13} principle shear stress on the vicinity of the surface and edge of the tip	212

7.1	Schematic representation of in situ electrochemical micro-compression tests on micro pillars and micro spheres	215
7.2	Micropillar test in air on single slip oriented single crystal nickel sample	216
7.3	Micropillar test in air on double slip oriented single crystal nickel sample	216
7.4	Trapping of hydrogen in FPZ as function of partial hydrogen pressure and temperature	217
A.1	GUI of the pop-in finder program developed for automatic pop-in analysis of nanoindentation data	219
B.1	Nanoscope screen with the appropriate values before engaging the tip	221
B.2	Electrochemical cell and a typical sample to be fitted into it	221
B.3	Retaining springs	222
B.4	Fixing the electrochemical cell on the microscope stage	222
B.5	Installation of the nanoindentation head on the microscope stage	223
B.6	Tip up switch	223
B.7	Coarse adjustment screws	224
B.8	Securing the retaining springs	224
B.9	Positioning Vibration isolation table	225
B.10	The TriboScope [®] control unit	225

LIST OF TABLES

2.1	Some experimental methodologies, techniques and theoretical investment into HE	21
4.1	Etching solutions and parameters used for achieving proper laser reflection patterns in single crystal samples.	88
4.2	Electropolishing solutions and parameters used for different materials.	92
5.1	Effect of hydrogen charging on mean values of pop-in load for the aluminum sample under different conditions.	121
5.2	Composition of Fe-3wt.%Si alloy used in this study	126
5.3	Effect of hydrogen charging on mean values of pop-in load for the Fe-3wt.%Si sample	132
5.4	Thickness and cationic fraction of aluminum in the oxide films formed on FeAl	135
5.5	Effect of hydrogen charging on mean values of pop-in load for the FeAl sample.	138
5.6	Effect of hydrogen charging on mean values of pop-in load for the nickel sample.	144
5.7	Composition of austenitic stainless steel used in this study	152
5.8	Composition of SDSS used in this study provided by the supplier	160
5.9	Composition of SDSS used in this study measured by EDX	160
5.10	Hardness of austenite at the same depth for different loading rate	181
6.1	Physical constants used to reproduce the free energy plots of dislocation nucleation	192
6.2	Hydrogen effect on shear modulus, dislocation core radius and SFE.	200

ACKNOWLEDGMENT

First and foremost, I would like to thank Prof. Dr. rer. nat. Horst Vehoff, who supervised my work with continuous encouragement and support. Our scientific, as well as non-scientific discussions, invariably gave me thinking material for a few days of mental digestion, resulting in an extremely stimulating guidance. He patiently allowed for all the time and freedom I seemed to need and I am greatly indebted for his trust.

Furthermore, I want to thank Prof. Arnold of Saarland University and Prof. Johnsen of the Norwegian University of Science and Technology for being part of the Reading Committee and their inspiring comments about this thesis.

Special thanks to Marit Øverland, my Norwegian master student, who carried out the nanoindentation tests on the Duplex stainless steel and Christian Bies my diploma student who carried out the nanoindentation tests on the FeAl and Fe-3wt.%Si presented in this thesis. We spent many long but unforgettable hours together during the tests in our institute. Thank you both for not giving up.

I also especially want to thank Frau Ohm, whose help and advice in paper entanglements was very precious. She was remarkably efficient in assuring that none of the administrative problems ever disturbed scientific work.

Dr. Michael Marx is a great multi tasking friend who can; solve any problem with SEM, cook the most delicious Thai food, direct films, and swim in ice water. I would like to recognize and thank my fellow graduate colleagues. Bo Yang for teaching me how to work with our Hysitron and sharing all his knowledge about AFM with me. Mark Henning for his fruitful scientific discussions and juristic instructions. Wolfgang Schäf for being so nice to everyone and for his joyful music. Markus Welsch, it was very nice discussing the Formula 1 results with you every Monday and I thank you for teaching me \LaTeX . Kerstin Schüler thank you for the joy you brought to the group and of course for introducing Dirk to me. Monsieur Camille Perrin Je vous en remercie beaucoup. I thank other diploma and master students of the group Nousha Kheradmand, Dephine Lemaire, Simone Schug, Jürgen Braun, Thomas Waschkies, Andreas Noll, Jens

Weggler, Tao Quian, Jules Dake and Pierrick Simonet.

A very special thank to the *masters* of our *Leonardo da Vinci's workshop* (i.e. Prototyping lab), Herr Horst Vogel-Knels, Peter Limbach and Stefan Schmitz who are able to realize any sketch. Frau Maron, Andreas Kirsch and Rolf Kiefer, thank you for your always available spontaneous cooperativeness. Thanks to Frau Galli and her assistants Melanie and Jutta for being such nice ladies and organizing our library incredibly well.

I would like to thank my parents, for their constant guidance and support. As a young child they provided a home that was ever vigilant to the wonders of science and nature around us. As an adult, they have been an incredible technical and philosophical resource. Thanks to my sister for her charm, I miss the sound of your piano.

To my precious wife Noosha I really have to say: Thank you so much for your patience and encouragement during my work on this thesis. I still didn't understand why whenever you walked into the lab I've got good results, Thank you!

ABSTRACT

The fine scale mechanical probing capability of NI-AFM was used to examine hydrogen interaction with plasticity. To realize this, an electrochemical three electrode setup was incorporated into the NI-AFM. The developed ECNI-AFM is capable of performing nanoindentation as well as imaging surfaces inside electrolytes.

The developed ECNI-AFM setup was used to examine the effect of cathodically charged hydrogen on dislocation nucleation in pure metals and alloys. It was shown that hydrogen reduces the pop-in load in all of the tested materials except Cu. The reduced pop-in load can be interpreted as the HELP mechanism. Classical dislocation theory was used to model the homogeneous dislocation nucleation and it was shown that H reduces the activation energy for dislocation nucleation in H sensitive metals which are not undergoing a phase transformation. The activation energy for dislocation nucleation is related to the material specific parameters; shear modulus μ , dislocation core radius ρ and in the case of partial dislocation nucleation, stacking fault energy γ . These material properties can be influenced by H resulting in a reduced activation energy for dislocation nucleation.

The universality of cohesion in bulk metals relates the reduction of the shear modulus to the reduction of the cohesion, meaning HEDE mechanism. The increase in the core radius of a dislocation due to H is a direct evidence of decrease in dislocation line energy and H segregation on the dislocation line. In the case of partial dislocations, the H can segregate on to the stacking fault ribbon and decrease γ . This inhibits the cross slip process and enhances the slip planarity.

Thus, HELP and HEDE are the two sides of a coin resulting in H embrittlement. However depending on the experimental approach utilized to probe the H effect, either HELP or HEDE can be observed. In this study, however, by utilizing a proper experimental approach, it was possible to resolve the interconnected nature of the HE.

ZUSAMMENFASSUNG

Die Motivation dieser Arbeit war es, die feinscaligen Möglichkeiten des NI-AFM zur Untersuchung des Einflusses von H auf die Plastizität einzusetzen. Es wurde mit der Integration einer elektrochemischen Dreielektrodenzelle in die Anlage die Möglichkeit der Ni-AFM Technik genutzt, in einer Flüssigkeit einsetzbar zu sein.

Der hier entwickelte ECNI-AFM Versuchsaufbau wurde eingesetzt um den H-Effekt unter kathodischer Beladung auf die Versetzungsnukleation in reinen Metallen und Legierungen zu untersuchen. Es konnte für alle untersuchten Werkstoffe außer für Cu gezeigt werden, dass H die pop-in-Load reduziert. Die reduzierte pop-in-Load kann als HELP interpretiert werden. Die klassische Versetzungstheorie wurde angewendet um die homogene Versetzungsnukleation im Metall zu modellieren. Es konnte gezeigt werden, dass H in "H-sensibelen" Metallen, die keine Phasentransformation durchlaufen, die Aktivierungsenergie für die Nukleation von Versetzungen senkt. Die klassische Versetzungstheorie verbindet die Aktivierungsenergie für Versetzungsnukleation mit werkstoffspezifischen Parametern, die möglicherweise durch H beeinflusst werden können. Diese Parameter sind Schubmodul, Radius des Versetzungskerns und im Falle der Nukleation von Partialversetzungen die Stapelfehlerenergie. Als Konsequenz aus Universalität der Kohäsion in metallischen Festkörpern ist es möglich die Reduzierung des Schubmoduls mit der Reduktion der Kohäsion (HEDE) in Beziehung zu setzen.

Die durch H hervorgerufene Vergrößerung des Kernradius ist ein direkter Beweis für die Verringerung der Versetzungslinienenergie und die H-Segregation entlang der Versetzungslinie. H kann im Falle von Partialversetzungen innerhalb des Stapelfehlers segregieren und dessen Oberflächenenergie herabsetzen. Dadurch wird der Quergleitprozess unterdrückt (slip planarity).

Zusammengefasst kann geschlossen werden, dass HELP und HEDE die beiden Seiten einer Medaille sind, die zu H-Versprödung führen. Je nach dem, welcher Ansatz gewählt wird, um den Einfluss von H zu untersuchen, kann entweder HELP oder HEDE beobachtet werden. Innerhalb der vorliegenden

Arbeit war es durch die Verwendung eines geeigneten experimentellen Ansatzes möglich, die komplizierte Natur der H-Versprödung ein Stück weiter zu entschlüsseln.

ACRONYMS

AFM	Atomic force microscope
BE	Backscatter electron
DBT	Ductile to brittle transition
EBSD	Electron backscatter diffraction
EC-AFM	Electrochemical atomic force microscope
EC-STM	Electrochemical scanning tunneling microscope
ECCI	Electron channeling contrast imaging
ECNI-AFM	Electrochemical nanoindentation atomic force microscopy
EDM	Electrical discharge machining
EDX	Energy dispersive x-ray analysis
ETEM	Environmental transmission electron microscope
FPZ	Fracture process zone
FTIR	Fourier transform infrared spectroscopy
GND	Geometrically necessary dislocations
HAR	Hydrogen absorption reaction
HEAC	Internal hydrogen assisted cracking
HEDE	Hydrogen enhanced decohesion
HELP	Hydrogen enhanced localized plasticity
HER	Hydrogen evolution reaction

IEP	Isoelectric point
IHAC	Hydrogen environment assisted cracking
ISE	Indentation size effect
MMIC	Monolithic microwave integrated circuits
NI-AFM	Nanoindentation atomic force microscope
OCP	Open circuit potential
OGM	Orientation gradient mapping
OIM	Orientation Imaging Microscopy
RDS	Rate-determining step
SDSS	Super duplex stainless steel
SE	Secondary electron
SEM	Scanning electron microscope
SFE	Stacking fault energy
SPM	Scanning probe microscope
SS	Austenitic stainless steel
STM	Scanning tunneling microscopy
TEM	Transmission electron microscope
XPS	X-ray photoelectron spectroscopy
XRD	X-ray diffraction

SYMBOLS

α	Empirical constant depending on the tip shape
β	Inclination angle of a partial dislocation
ΔG	Free energy of dislocation loop formation
ΔG_c	Activation energy for formation of a dislocation loop
Δv	Atomic volume change
ℓ	Dislocation length
ϵ_f	Fracture strain
η	Electrochemical over potential
Γ	Excess of solute per unit area of the surface
γ	Stacking fault energy
Γ^D	Excess of solute per unit length of the dislocation
γ_H	Stacking fault energy for hydrogen charged condition
λ	Total line length of dislocation loops
a	Surface area
d	Interplanar spacing
R	Ideal gas constant
r	Distance from the dislocation core
\mathcal{R}	Integration limit in line energy calculation of a single dislocation
\mathcal{C}	Length of the radial cracks

\mathcal{D}	Damage parameter
\mathcal{E}	Interaction energy between hydrogen and defects
μ	Shear modulus
μ_H	Shear modulus for hydrogen charged condition
ν	Poisson's ratio
ψ	Saturation hydrogen concentration in the neighborhood of a dislocation
ρ	Dislocation core radius
ρ_H	Dislocation core radius for hydrogen charged condition
σ_i	Principle stresses ($i = 1, 2, 3$)
σ_{UTS}	Ultimate tensile stress
σ_{ys}	Yield stress
θ	Angle between a conical indenter surface and sample
θ_c	Contact angle angle
γ	Surface energy
γ_D	Helmholtz free energy per unit length of dislocation
γ_{LG}	Liquid-gas interfacial energy
γ_{SG}	Solid-gas interfacial energy
γ_{SL}	Solid-liquid interfacial energy
μ	Chemical potential
ϱ	Dislocation density
ϱ_G	Density of the geometrically necessary dislocations
ϱ_L	Density of the liquid
ϱ_s	Density of the statistically stored dislocations
ϑ	Angle between the glide plane and the position vector \mathbf{r}

a	contact radius
B	Bulk modulus
b	Burgers vector
$C(x, t)$	Concentration of hydrogen in position x and time t
C_0	Internal hydrogen concentration
C_H	Local hydrogen concentration
C_S	Surface concentration of hydrogen
D	Hydrogen diffusion coefficient
d	Interatomic separation distance
E	Young's modulus
E_r	Reduced elastic modulus
f	Correction factor for Nix and Gao's model
F_b	Buoyant force
F_m	Meniscus force
g	The gravity acceleration constant
H	Hardness
h_t	Total depth of indentation
$h_{Vickers}$	Indentation depth in Vickers hardness
k	Boltzman's constant
k_i	Rate constant of i^{th} step in a reaction
$K_{\mathcal{C}}$	Fracture toughness (in indentation tests)
K_{IC}	Critical stress intensity factor
K_I	Stress intensity factor in mode I crack
K_{TH}	Threshold of stress intensity factor in hydrogen

L	Unit length of dislocation
l	Scaling length in universal function of binding energy
$n_{(d_m)}$	Electron density at the equilibrium position of the atom
P	Indentation load
p	Pressure during indentation
$P_{H_2}^0$	H ₂ pressure in the reference state
P_{H_2}	External hydrogen pressure
q_D^{eff}	Effective activation energy for diffusion
R	Indenter tip radius
r	Dislocation loop radius
r_s	Minimum thermodynamically stable dislocation loop radius
r_c	Critical dislocation loop radius
r_{ws}	Wigner-Seitz radius
RA	Fracture area in a tensile test
s_p	Spacing between individual slip steps on the indentation surface
U_c	The crystal energy
$U_c(d)$	Total energy as a function of the interatomic separation distance d
V_0	Molar volume at zero pressure
V_H	Partial molar volume of hydrogen
W	Dislocation line energy
w	Width of stacking fault ribbon between partial dislocations
w_e	Equilibrium separation of partials
x	Shear translation of crystal planes from equilibrium position

CHAPTER 1

Introduction

*Warum sieht der Mensch die Dinge nicht?
Er steht selber im Wege: er verdeckt die Dinge.*

Morgenröte. Gedanken über die moralischen
FRIEDRICH NIETZSCHE

HYDROGEN assisted mechanical degradation of structural materials is a serious problem that has received increasing attention over the last sixty years. The vast number of hydrogen sources (corrosion in aqueous solutions, absorption into pipelines carrying humid and/or contaminated hydrocarbons, contaminants in the melting and welding processes, hydrogen uptake during electroplating or cathodic protection) contributes to the severity of the problem. The degradation is manifested in diverse ways, such as the catastrophic fracture of high-strength steels, the contribution to stress corrosion cracking of ferritic stainless steels, the failure in nuclear reactors of zircalloy tubing by hydride formation [1], and the degradation of GaAs monolithic microwave integrated circuits (MMIC) in satellites [2].

The deleterious effect of hydrogen on mechanical properties was reported for the first time in 1875 by W. H. Johnson [3]. In his publication titled as “*some remarkable changes produced in iron by the action of hydrogen and acids*” he defined the phenomena as:

“This change is at once made evident to any one by the extraordinary decrease in toughness and breaking strain of the iron so treated, and is all the more remarkable as it is not permanent, but only temporary in character, for with lapse of time the metal slowly regains its original toughness and strength” [3].

Since that time, materials scientists have had many successes in developing metals with outstanding combinations of high tensile strength and high fracture

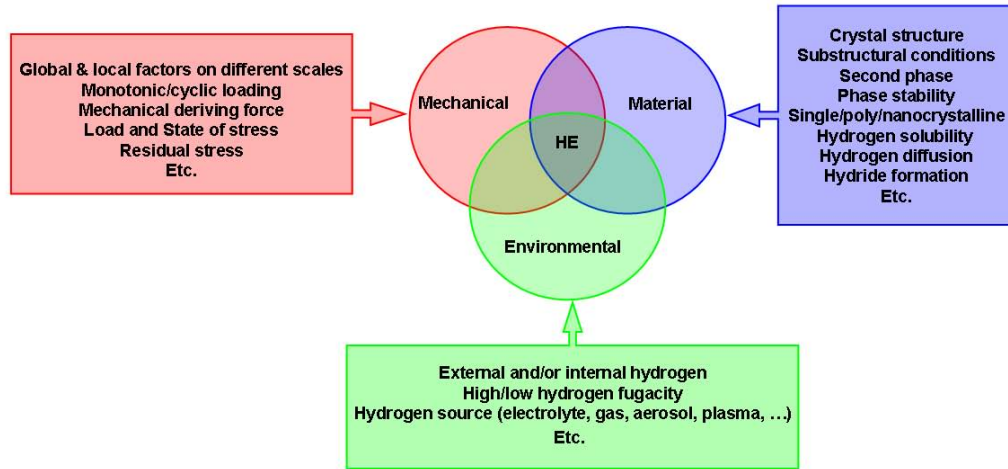


Figure 1.1: Global description of hydrogen embrittlement (HE) interaction aspects

toughness. In spite of this, hydrogen embrittlement still has a wide spread effect that severely degrades the fracture resistance of these alloys. Various strong views on micromechanisms of hydrogen embrittlement have been vigorously discussed and thoroughly reviewed in the literature [4, 5, 6, 7, 8, 9, 10]. Despite the remarkable research investment involving coupled theory and physical findings, “critical experiments” still remain the key issue for further progress in the understanding of hydrogen embrittlement. Hydrogen embrittlement have many facets with broad implications as shown in figure 1.1. Numerous systems and circumstances in terms of environmental aspects or even purely mechanical aspects are only one side of the issue. The additional aspect addresses the wide range of intrinsic and extrinsic variables within the material itself. The complicated interaction between the different aspects of hydrogen embrittlement (figure 1.1) have resulted in an enormous number of sometimes controversial findings. Moreover, most of the research was focused on solving urgent technical problems. The goal of these investigations was the development or selection of appropriate materials with acceptable properties for the chosen application and environment. This ad hoc approach raises the obvious question of how each isolated case or interpretation really reflects on any general concepts. As such, it seems apparent that the voluminous activity gathered so far cannot be attributed to a single dominant mechanism.

A more realistic approach to be invoked in this study is that hydrogen embrittlement may be governed by multiple dominant mechanisms. Hydrogen enhanced fracture introduces a wide range of complexities beyond the normal frac-

ture process. Even in the absence of hydrogen, plasticity plays a key role in the fracture process. In this sense the evaluation of microplasticity findings leading to the conclusion that brittle processes are actually “ductile” has provided some confusion. The fact that plasticity enhances brittle fracture in semibrittle materials highlights the interwoven nature of the fracture process even in the absence of hydrogen. This is amplified by the addition of hydrogen. The complexity may be further increased by substructural changes or local damage introduced by the different hydrogenation methods. For example, some trap binding sites such as grain boundaries and precipitate interfaces may compete differently for hydrogen depending on the relative coherency of each boundary. Superimpose upon this the relative strength of each interface in the presence and absence of hydrogen and the prediction of initiation sites becomes problematic. Finally, since initiation may favor grain boundary failure in one instance and precipitate shearing in another, either boundary decohesion or shear decohesion as enhanced by localized plasticity may result ¹. Either outcome can be favored by just changing the external state of stress, yield strength level or thermal history. This makes the general separation between stress criteria and strain criteria for hydrogen-enhanced fracture very difficult. It also becomes apparent here, that depending on the experimental approach, one might conclude that a given material is failing due to enhanced cleavage, enhanced grain boundary fracture, enhanced shear, enhanced localized microvoid formation or all of the above.

At this point we must admit that much of the hydrogen embrittlement research has been conducted on commercial microstructures or “*model materials*” which were nearly impossible to fully characterize in the sense of impurity, defect density, etc. As such, these experiments have most often addressed a myriad of competing phenomena without addressing the basic building blocks i.e. crystal structure and dislocation process. We propose that the time is ripe for these basic building blocks to be examined on two fronts in more fundamental ways. First, there are now techniques that can probe small volumes, i.e. the building blocks themselves. Second, there are computational models that can simulate hydrogen embrittlement on this scale. The combination of the experimental and modeling results leads to better understanding of the hydrogen embrittlement process.

The research described in this thesis focuses on small volumes and is confined to nanoscale probing and fine feature observations. The potential of such new avenues for analyzing highly localized flow and dislocation events will be shown.

¹In section 2.5 details of hydrogen embrittlement mechanisms will be given

In recognizing the role of interactive effects (Fig. 1.1) on structural integrity, the incorporation of nanometric resolution appears beneficial. In our attempt to perform the so called “*critical experiments*” we focused on the use of scanning probe microscopy (SPM): The nanoindentation atomic force microscope (NI-AFM) with in-situ electrochemical hydrogen charging was used to probe hydrogen effects on the micromechanical response of metals, alloys and intermetallics.

In chapter 2 a brief overview on hydrogen embrittlement will be given. In section 2.1 hydrogen embrittlement will be discussed from the phenomenological point of view. Whereby its effect on crack growth and the complicated effect of intrinsic and extrinsic parameters are included. The entry of hydrogen into metals will be discussed in section 2.2. The interaction of hydrogen with defects in metal is the subject of section 2.3. Section 2.4 will review the experimental methodology applied to hydrogen embrittlement. In section 2.5 the proposed atomistic models of hydrogen embrittlement will be discussed. The supporting theoretical and experimental evidence and the shortcomings in the description of the effects will be reviewed. At the end, in section 2.6, NI-AFM will be introduced as a new experimental approach for hydrogen embrittlement research.

Chapter 3 begins with a discussion of nanoindentation, the theory behind it, the properties derived from it and the instrumentation used to perform the tests, presented in section 3.1. Section 3.2 is an introduction to contact mechanics, starting with elastic deformation and some basic plasticity. Mechanical property values such as Young’s modulus and hardness are calculated from idealized elastic contact theory and load-displacement data. Section 3.3 presents the specifics of depth sensing nanoindentation, how a test is performed and the calculations necessary to determine property values. Section 3.4 describes the instrumentation we used to perform these tests, along with details about indentation probes and calibration methods. How to perform NI-AFM tests in fluids and the complexities that come along with it are dealt with in section 3.5. The different phenomena observed during nanoindentation are summarized in section 3.6.

The development and design of the experimental setup and sample preparation procedure are presented in Chapter 4. Results are provided in the chapter 5. Starting with preliminary ex situ tests presented in section 5.1, showing the necessity of in situ tests. Following sections will present the results of in situ electrochemical nanoindentation on different materials. Chapter 6 describes the model proposed for hydrogen effect on dislocation nucleation. Further on the results are analyzed with the model to explain the hydrogen embrittlement mechanism in the examined materials. Conclusive remarks and outlooks for future works are presented in chapter 7.

CHAPTER 2

Hydrogen Embrittlement

This is Miching Malicho, that meanes Mischeefe

Hamlet, iii. 2.

WILLIAM SHAKESPEARE

2.1 Phenomenology of hydrogen embrittlement

First, consider hydrogen embrittlement in terms of the phenomenological consequences of hydrogen/metal interactions. It has frequently been established that severe mechanical degradation occurs and is manifested in a decrease of fracture resistance. Even semantically alluding to the term “embrittlement” suggests a kind of ductile to brittle transition (DBT) caused by the mechanical field interacting with hydrogen. Recognizing that a large fraction of aqueous solution interactions might be related to hydrogen embrittlement in structural materials, the incentive in carefully defining “embrittlement” is evident. From a materials classification standpoint, one may distinguish between a microstructurally stable material in which the metal and solute hydrogen interact and those which require attention to phase stability. An example would be hydride formation which may be additionally enhanced by the mechanical field (as in the IVb and Vb metal group – Ti, Zr, Hf and V, Nb, Ta) and will be discussed in section 2.5.1. For the initial overview, only stable microstructural systems involving metal-solute hydrogen effects in the bulk, i.e. no hydrides, are considered.

Commercial non-hydride-forming alloys for structural applications are usually designed to combine high strength with a reasonable high-temperature ductility. The hydrogen influence on the strength is less pronounced and can nearly

be avoided by appropriate alloy design. Even modern super-alloys, which are the most resistant against hydrogen effects, still suffer embrittlement. Figure 2.1 shows a bar diagram which demonstrates the effect of hydrogen on the ultimate tensile strength, σ_{UTS} , the fracture strain, ϵ_f , and the reduction of the fracture area in a tensile test, RA . The damage parameter, for example for σ_{UTS} , is defined by equation 2.1 as:

$$\mathcal{D}_{UTS} = \frac{\sigma_{UTS(Air)} - \sigma_{UTS(Hydrogen)}}{\sigma_{UTS(Air)}} \quad (2.1)$$

The maximum damage is defined as one , zero means no damage. Some sin-

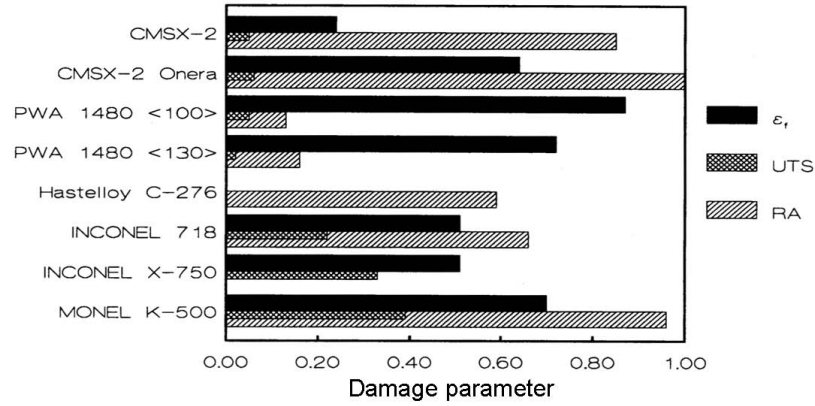


Figure 2.1: Damage parameter, \mathcal{D} , for different single-crystalline and polycrystalline super-alloys [6].

gle crystalline super-alloys, like CMSX-2, show only minor hydrogen effects on σ_{UTS} , but if the ductility at fracture is considered , the relative damage is still nearly one. Similar diagrams can be compiled for other alloy systems [11]. However, a more realistic approach to the effect of hydrogen on mechanical properties would be a fracture mechanical approach. In the schematic of figure 2.2, the stress intensity factor, K_I , and crack growth rate, da/dt , regimes of hydrogen embrittlement are shown. In air below the critical stress intensity factor, K_{IC} , no crack growth occurs. In hydrogen, however, the K_{IC} for propagation of cracks is reduced to K_{TH} . In figure 2.2 three regions must be considered. Region 1 or threshold regime, where the crack starts to propagate and increase very quickly in rate until the rate becomes transport limited by the supply of hydrogen. K_{TH} depends on the equilibrium concentration of hydrogen in the fracture process zone (FPZ) and on the applied stress as was demonstrated by Oriani and Josephic [12]. Region 2 or crack velocity regime, where the crack growth rate is limited by the transport of hydrogen to FPZ, increasing the crack

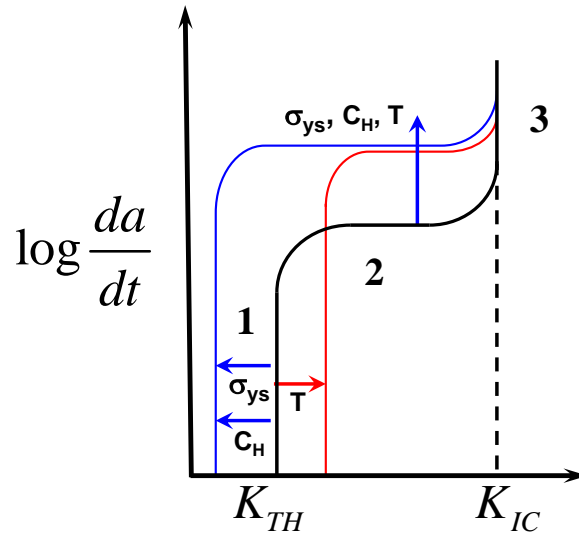


Figure 2.2: Schematic of critical variables affecting the threshold values (K_{TH}) and the crack growth rate da/dt . The solid curve represents baseline crack growth, the blue curve with increasing C_H or yield strength (σ_{ys}) and the red curve with increasing temperature under constant C_H and (σ_{ys}).

driving force by increasing K_I has only a minor influence on the crack growth rate since the crack simply blunts. If K_I is further increased, the crack outruns the hydrogen supply and behaves as is it were in air (region 3). The blue arrows in figure 2.2 are associated with increasing both local hydrogen concentration, C_H , and yield strength (higher applied stress), σ_{ys} . This shifts the whole curve leading to lower thresholds and accelerated growth rates. As quantitatively modeled elsewhere [13, 14], this is simply explained in terms of higher initial concentrations of internal hydrogen, C_0 , or external pressure, P_{H_2} , allowing greater amounts of local hydrogen, C_H , to be collected by the lattice dilation at the crack tip. Due to the tetragonal nature of the lattice distortion, for example hydrogen in iron, Zhang and Hack [15] have recently defined the importance of the off-diagonal stress terms as well. Similarly, an increase in yield strength will increase both dilational and shear components of the stress tensor, increasing the local hydrogen at the crack tip. The effect of temperature is quite different. The dual nature of temperature is to decrease the local hydrogen concentration in the threshold regime but increase kinetics in the crack velocity regime (region 2). For example, in the threshold regime (region 1) the local concentration

decreases with temperature according to:

$$C_H = C_0 \exp \left[\frac{f(\sigma_{ij}, \Delta v)}{kT} \right] \quad (2.2)$$

where $f(\sigma_{ij}, \Delta v)$ is a positive function of mixed-mode loading and atomic volume change, k is Boltzman's constant and T is the temperature. However, in the crack growth regime increasing temperature leads to an enhanced rate of embrittlement as the transport of hydrogen is generally increasing with temperature. Therefore the crack growth rate dependence to temperature for example can be expressed as follow:

$$\frac{da}{dt} \propto \exp \left(-\frac{q_D^{eff}}{kT} \right) \quad (2.3)$$

The transport is in this case controlled by an effective activation energy for diffusion, q_D^{eff} , due to trapped hydrogen. Missing here is any mention of the mechanism of hydrogen entry into the metal lattice as well as a failure criterion which might follow how hydrogen lowers the local stress (or local stress intensity) required for cleavage.

2.2 Entry of hydrogen into metals

The entrance of hydrogen into the metals and alloys is, without a doubt, the first step in the process resulting in hydrogen embrittlement. This process is in itself quite a complicated process that depends on many parameters. Due to the importance of the hydrogen entry in the overall hydrogen embrittlement process, this section is devoted to it.

2.2.1 Gas phase

The overall gas-solid interaction could be considered to be defined in terms of three steps: physisorption, chemisorption, and absorption. Physisorption, the result of van der Waals forces between a surface and an adsorbent, corresponds to the formation of a multilayer fluid. It is completely reversible, generally occurs instantaneously and is accompanied by an enthalpy change which is approximately equal to the heat of condensation of the gaseous adsorbent (20 kJ/mol or less). In the chemisorption step, a chemical reaction between the surface atoms and the adsorbent molecules occurs. Since short-range chemical forces are involved, chemisorption is limited to a monolayer. Chemisorption

is usually slow, activated and either slowly reversible or irreversible. The enthalpy change (heat of adsorption) can be related to the formation of a polarized, one-center covalent bond between an adsorbent atom or molecule and a surface atom. For the dissociative chemisorption of hydrogen on transition metals, the heat of adsorption, is related to the bond energies of a M–H and H–H pair. The results of such calculations indicate that the energies of a Fe–H and Ni–H bond are 282 and 276 kJ/mol, respectively. If we take the bond energy of a metal-metal bond as 1/6 of the heat of sublimation, then the Fe–Fe and Ni–Ni bond energies are approximately 70 kJ/mol. At that point one is tempted to conclude that the formation of a brittle hydride phase, even if the hydride exists only as a surface phase, is both necessary and sufficient for hydrogen embrittlement to occur. However platinum, which is not embrittled by hydrogen has Pt–H and Pt–Pt bond energies of 263 and 94 kJ/mol. Clearly, chemisorption is necessary but is not in itself sufficient for hydrogen embrittlement [1, 16].

The final step in the gas-solid interaction set, absorption, involves the incorporation of the products of chemisorption into the bulk lattice of the metal. There has been a long discussion in the literature regarding the nature of hydrogen dissolved in transition metals. The discussion focuses on whether hydrogen is present as the H atom, H^+ or H^- [5]. The chemical interaction between hydrogen and a transition metal lattice must result in a polarized covalent bond, and the degree of polarization is the topic of the above-mentioned discussion. Opinion generally favors ionicity, but the opinion is split as to the sign. If we apply Pauling's electronegativity concepts, then the state of hydrogen in the lattice is inferred to be essentially H^- . On the other hand, the rigid-band model treats the metal lattice as an electron acceptor and the hydrogen atom as an electron donor, resulting in hydrogen as an electron-shielded proton.

2.2.2 Liquid phase

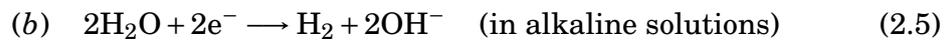
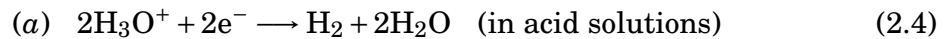
There are many instances in which metals may occlude considerable amounts of hydrogen derived from aqueous environments. The best known, most important and long ago recognized example is the entry of hydrogen into steel during its dissolution in strong acids: a reaction accompanied by hydrogen gas evolution [3]. Less efficient in this respect are reactions that occur between metals and neutral or alkaline solutions; for example, between a metal surface and a thin layer of air-saturated water condensate.

It should be emphasized that the solid metal/aqueous electrolyte boundary is an especially complicated type of interface, much more involved than the

metal/gas boundary. This complication is chiefly caused by the presence of a dense network of water dipoles in the electrolyte, and by the competitive adsorption of different species on the metal surface. Particularly complex conditions exist in the case of corrosive and inhomogeneous materials prone to localized attack, which leads to pitting or cracking and to significant changes in the composition of the metal-adhering layer of the electrolyte. Figure 2.3 shows a schematic diagram of the metal/electrolyte interface, showing fully and partially solvated ions. The idea behind this model is that of a plate condenser. One plate is the metal with its surface excess charge; the other plate is built up by solvated ions at closest approach, held in place by purely electrostatic forces (outer Helmholtz plane). Ions with weakly bound solvation shells (mostly anions) usually lose part of their solvation shell and form a chemical bond with the surface (so-called specific adsorption). Because the chemical interaction between such ions and the electrode surface causes more charge to be accumulated at the surface than that required by electrostatics, counter charge is incorporated in the double layer for charge compensation. The potential drop across the interface in case of non-specific (solid line) and specific (dash line) ion adsorption is also sketched in the figure [17].

2.2.2.1 Mechanism of the cathodic evolution of hydrogen from aqueous electrolytes

The cathodic evolution of hydrogen from aqueous electrolytes is known to proceed in several successive stages. Depending upon the electrolyte, the overall hydrogen evolution reaction (HER) can be written:



It is now generally accepted that two successive steps are essential to the overall HER mechanism. The first step, which is common to all metals, consists in either discharge of hydrated protons (in acid solutions):



or electrolysis of water (in alkaline solutions):



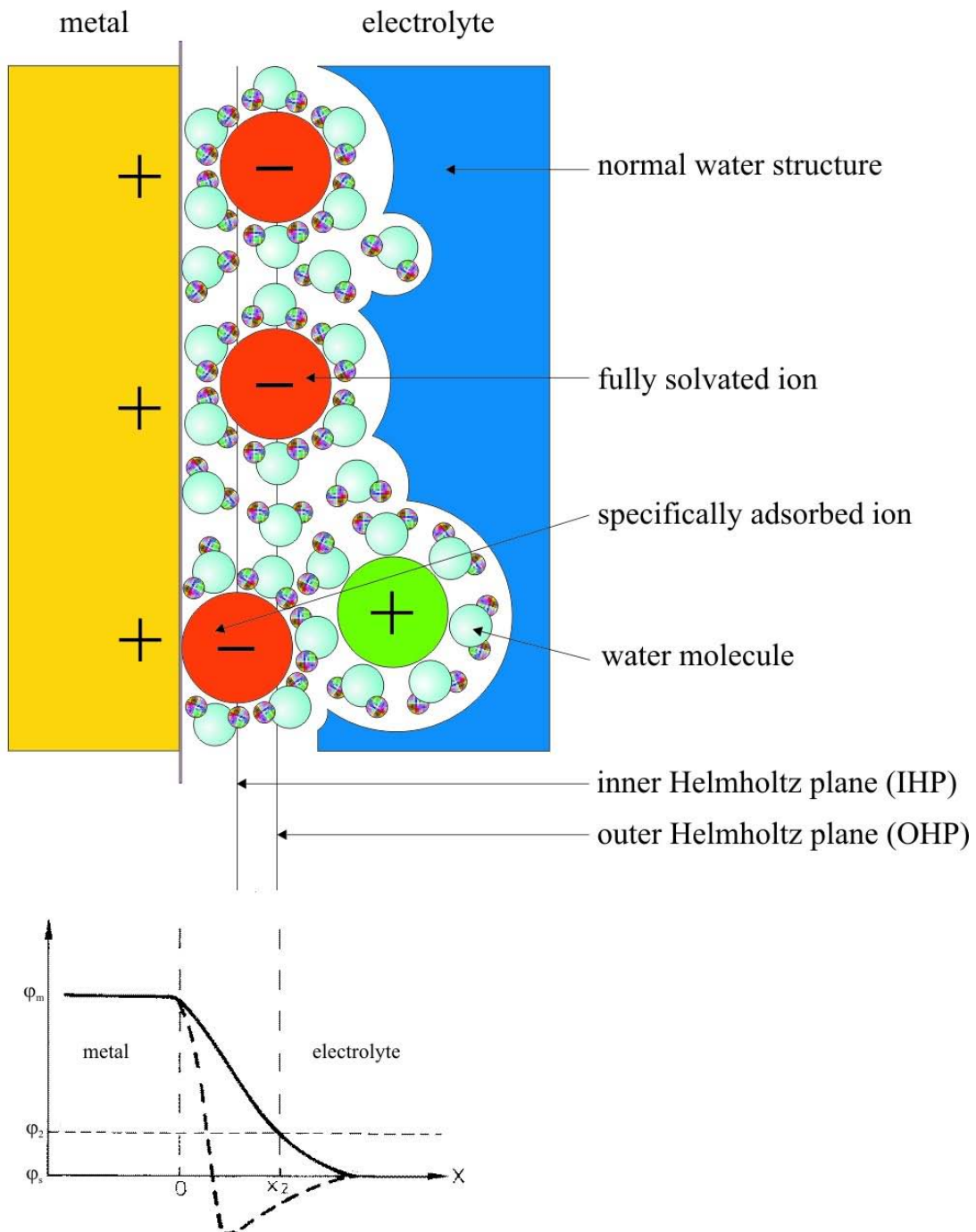
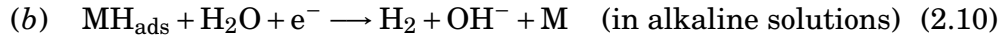


Figure 2.3: Schematic diagram of the metal/electrolyte interface, showing fully and partially solvated ions. The potential drop across the interface in case of non-specific (solid line) and specific (dash line) ion adsorption is also sketched in the figure [17].

where MH_{ads} , represents hydrogen atom adsorbed on the metal surface. The presumed mechanism of the next step of HER depends on the nature of the electrode metal and on the cathodic current density. The detachment of hydrogen atoms from the metal surface is thought to occur by either chemical desorption (also called catalytic recombination), which may occur in both acid and alkaline solutions:



or electrochemical desorption:



The rate of each individual reaction depends upon the experimental conditions. The slowest step controls the rate of the overall process, and is said to be the rate-determining step (RDS). The RDS of the overall HER determines the cathodic current density, i_c , and the overpotential, η :

$$\eta = a - b \log i_c \quad (\text{Tafel's equation}) \quad (2.11)$$

where a and b are constants independent of i_c . The slope of the Tafel curve, b , constitutes one of the criteria that are required to determine the mechanism of the HER. Since different mechanisms involving different RDS often have the same Tafel slope, the measurement of further electrochemical parameters such as the hydrogen coverage, the exchange current density, the transfer coefficient, the reaction order, the stoichiometric number, and the heat of adsorption, permits conclusions to be drawn about the probable mechanism of HER on various metals. The results, however, are affected by many additional factors and are often inconclusive.

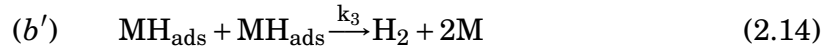
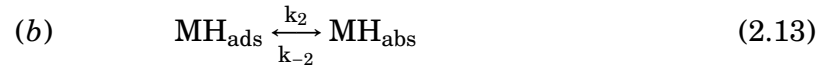
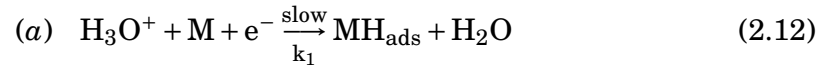
Consequently, the RDS has been identified with reasonable certainty only for a limited number of electrode metals in acid solutions. For example, on “soft” metals characterized by low melting points and high overpotentials, namely mercury, lead and cadmium, the rate of HER has been shown to be controlled by proton discharge, and the next step consists of a fast electrochemical desorption. On the contrary, for nickel, tungsten and gold that exhibit relatively low overpotentials of HER, the proton discharge is rapid and the electrochemical desorption is slow and rate-determining. In the case of metals which have the ability to absorb hydrogen, both the HER and the hydrogen absorption reaction (HAR) occur simultaneously. Consequently, the measurement of the rate of

hydrogen entry can provide diagnostic criteria for the mechanism of the HER.

2.2.2.2 Entry of electrolytic hydrogen into metals

A number of metals can absorb hydrogen, and this absorption provides an alternative reaction path to the chemical or electrochemical desorption of hydrogen atoms. Usually only a small portion of the hydrogen liberated at the cathode enters into the metal. The rate of hydrogen entry depends on many variables: the nature of the metal or alloy, its composition and thermomechanical history, surface conditions, composition of the electrolyte, cathodic current density, electrode potential, temperature, pressure, etc.

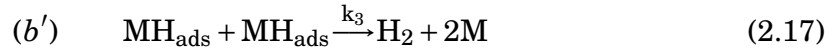
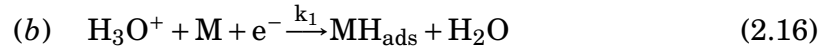
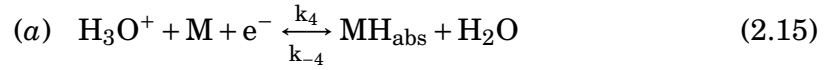
Two models for explaining electrochemical hydrogen entry into the metal have been proposed. The first of these, which was developed by Bockris and others [18, 19, 20, 21], considers that the intermediate stage through which electrolytic hydrogen passes on entry to the metal substrate is the adsorbed state and is identical to that which leads to hydrogen evolution. The reaction sequence at the cathode surface is as follows (in acid):



Where MH_{ads} refers to adsorbed hydrogen on the metal surface, MH_{abs} refers to absorbed hydrogen directly beneath the metal surface, and k_1 , k_2 , k_{-2} and k_3 are the rate constants of the various steps. According to this model the permeation (entry) rate should be proportional to the coverage of the metal surface by adsorbed hydrogen atoms, θ_H

Bagotskaya and Frumkin [22] have postulated that hydrogen enters into the metal in the same elementary act as that in which it is discharged, and that the intermediate state through which hydrogen enters the metal lattice is not identical with the adsorbed intermediate state which leads to hydrogen evolution. In this model, the HAR and the HER occur independently. The reaction

sequence at the cathode surface can be summarized as follows:



where k_4 and k_{-4} are the rate constants.

2.2.2.3 Promoter of hydrogen entry into metals

Several types of compounds have been found to promote the entry of hydrogen into metals from both liquid and gaseous environments. The same types of compounds are known to poison catalysts for hydrogenation reactions in heterogeneous systems, hydrogen recombination poisons. Promoters and poisons show their full effect at relatively very low concentrations. Among the species found to promote hydrogen entry are:

1. Certain compounds of the following elements: phosphorus, arsenic, and antimony belonging to the V-A periodic Group, and sulfur, selenium, and tellurium belonging to the VI-A periodic group.
2. The following anions: CN^- (cyanide), CNS^- (rhodanide), and I^- (iodide).
3. The following compounds of carbon: CS_2 (carbon sulfide), CO (carbon monoxide), CON_2H_4 (urea), and CSN_2H_4 (thiourea).

In the literature there are also scanty and inconsistent indications or assumptions as to the promoting properties of mercury, lead, and tin salts, and also of fluoride and bromide ions, naphthalene derivatives, etc. The most effective promoters are those based on the elements of the V-A and VI-A groups. These promoters have received especially detailed attention to elucidate the nature of their action.

2.3 Hydrogen interaction with defects in metal

The interactions of hydrogen with lattice imperfections are important and often dominant in determining the mechanism of hydrogen embrittlement. Nevertheless, in general, these interactions are far less understood at a fundamental level than the behavior of hydrogen in perfect lattices. As well as reflecting

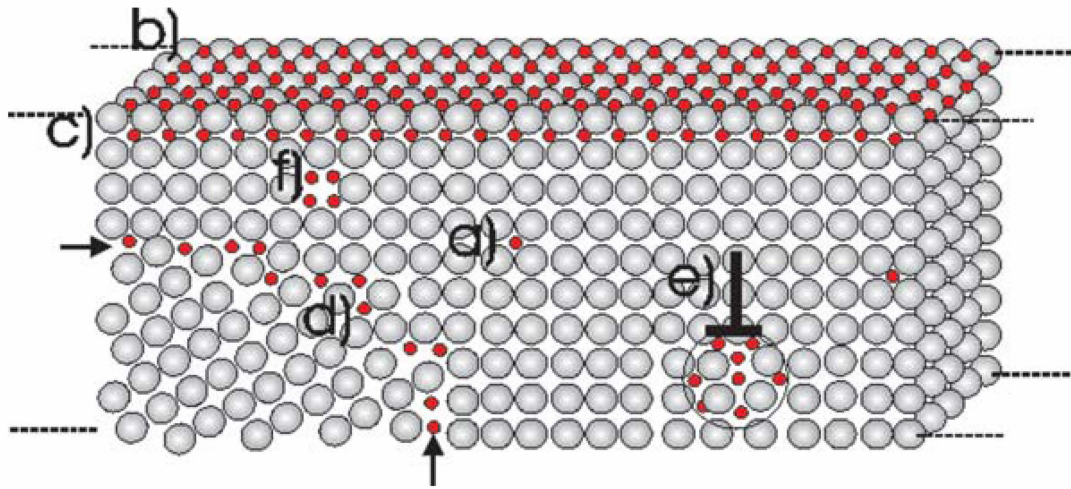


Figure 2.4: Schematic presentation of defects in metal and accumulation of hydrogen atoms in the low-concentration range. Along with the conventional hydrogen solubility in the lattice matrix (a), there are trap sites for hydrogen atoms on the surface (b) and in subsurface (c) sites. At edge dislocations (position indicated by \perp) (e) a cylindrically shaped region of hydrogen segregation is expected. Also, grain boundaries (d) and vacancies (f) solve hydrogen differently than does the matrix [10].

the natural progression of research, this situation results from the variety and complexity of hydrogen-defect interactions and from the experimental and theoretical difficulties that have been encountered in their study. Within the past decade, however, research in the area has been stimulated on a broad front by both technological and scientific developments [10]. Figure 2.4 schematically shows possible defects in pure metal and their interaction with hydrogen [10].

2.3.1 Point defects

The vacancy is arguably the simplest defect in metals, consisting of an empty lattice site with modest peripheral relaxation. Hydrogen is strongly bound to this imperfection in most metals, and the interaction has been investigated in depth using a combination of experimental and theoretical methods [23, 24, 25].

The existence of an attractive interaction between interstitial hydrogen and the vacancy can be inferred from the open-volume character of the defect. In particular, whenever the surface chemisorption state of hydrogen is energetically favored over interstitial solution, as is usually the case. Under this condition the hydrogen is driven to enter the vacancy. Moreover, the local open volume associated with the vacancy is relatively large, being almost sufficient

to appear to the hydrogen atom as a free surface. As a result, the binding energy tends to be large and comparable to that for hydrogen in the chemisorbed state [5].

The occurrence of hydrogen trapping at vacancies has been demonstrated for a number of metals by positron annihilation, a probe specifically sensitive to the presence of vacancies. In the absence of hydrogen, vacancies produced by low-temperature irradiation are observed to disappear when the temperature is raised sufficiently for them to become mobile. This event is generally referred to as recovery stage III, since it follows the onset of interstitial mobility, stage I, and early microstructural evolution of defect clusters, stage II [5]. When hydrogen is present in the lattice, hydrogen-vacancy binding reduces the effective mobility of the vacancy and thereby delays recovery stage III, providing a signature of the trapping reaction.

Recent experiments on hydrogen-metal systems offer clues on the role that vacancies may play in hydrogen embrittlement. One set of experiments has established that hydrogen could induce superabundant vacancy formation in a number of metals [23]. The estimated vacancy concentration, in these systems can reach a value as high as at 23% [25]. A conclusion drawn from these experiments is that hydrogen atoms, originally at interstitial positions in the bulk, are trapped at vacancies in multiple numbers with rather high binding energies. It was speculated that several (three to six) hydrogen atoms can be trapped by a single vacancy, with the highest number (six) corresponding to the number of octahedral sites around a vacancy in either the fcc or the bcc lattice [25].

2.3.2 Solutes and solute-defect complexes

The interaction of hydrogen with solutes in metals is influenced both by the solute's elastic distortion of the lattice structure and by electronic differences in hydrogen bonding between the host and impurity atoms. The resulting behavior is more complicated than in pure metals, and the degree of fundamental theoretical understanding is correspondingly less. Theoretical estimates of the two contributions to the binding have nevertheless been made in a semiempirical manner, making use of such measured properties as phonon frequencies and certain of the measured hydrogen-solute binding energies [5, 10]. These calculations suggest that the binding is predominantly due to elastic distortion in the case of interstitial solutes such as nitrogen and oxygen. For substitutional transition-metal solutes there is a comparable contribution from the electronic effects, with the degree of attraction increasing with the size of the solute and

its number of d electrons. The predicted hydrogen binding energies are usually modest for both the interstitial and substitutional solutes, being typically several tenths of an eV or less.

The hydrogen-solute interactions is exceptionally important from a technological perspective because concerns with hydrogen embrittlement and hydrogen storage usually arise in alloys rather than in metals, and because the use of alloying additions is one of the most accessible means of modifying hydrogen behavior.

2.3.3 Dislocations

An understanding of the interactions between hydrogen and dislocations in metals is of considerable importance due to the influence of these effects on plastic flow and hydrogen mobility. In regions removed from the dislocation core, the energetics of the hydrogen have usually been treated within the framework of continuum mechanics. The formalism describes an elastic energy caused by the interaction between the stress field of the dislocation and the strain field around the interstitially dissolved hydrogen atom. Stresses around edge, screw, and mixed dislocations increase continuously with proximity to the core [26], implying a corresponding range of binding energies. The continuum model breaks down at the dislocation core, necessitating an atomistic treatment.

The strain around hydrogen atoms in fcc metals has cubic symmetry because the hydrogen atoms in solution occupy octahedral sites. The situation is in principle different for the bcc hosts, where the occupation of tetrahedral sites allows tetragonal distortions. In reality, however, from experimental measurements [5] it appears that the tetragonal distortion is absent or very small. Consequently, the interaction energy, being in general the product of a stress and a strain tensor, is simply expressed as [27].

$$\mathcal{E} = \frac{(\sigma_1 + \sigma_2 + \sigma_3)V_H}{3} \quad (2.18)$$

where V_H is the partial molar volume of hydrogen and the σ_i are principal stresses. For an edge dislocation, one can derive the equation [27]

$$\mathcal{E} = \left(\frac{A}{\mathbf{r}} \right) \sin \vartheta \quad (2.19)$$

where \mathbf{r} is the distance from the dislocation core, ϑ is the angle between the glide plane and the position vector \mathbf{r} , and A is a constant that contains the elastic constants of the material together with the Burgers vector of the dislocation

and the partial molar volume of hydrogen. Thus the site energy for a hydrogen atom depends on the coordinates \mathbf{r} and ϑ . In the case of the screw dislocation, the bracketed term in (2.18) is zero, and, as a result, the interaction energy with hydrogen is usually considered to be negligible. This, however, may represent an oversimplification as it assumes the absence of tetragonal distortion, which is not universally accepted [15], and neglects possible trapping at the core. The local hydrogen occupancy of sites in the neighborhood of a dislocation is determined by Fermi-Dirac statistics, reflecting the occurrence of site saturation [28]. From an expression for the interaction energy such as equation (2.19), a distribution of site energies $n(\mathcal{E})$ can be calculated. This then allows a simple formulation of the relation between the average hydrogen lattice concentration and the hydrogen chemical potential;

$$\mu = \mu^0 + \frac{\mathbf{R}T}{2} \ln \left(\frac{P_{\text{H}_2}}{P_{\text{H}_2}^0} \right) \quad (2.20)$$

with P_{H_2} being the external H_2 pressure and $P_{\text{H}_2}^0$ the pressure in the reference state:

$$c = \int_{-\infty}^{+\infty} \frac{n(\mathcal{E})d\mathcal{E}}{1 + \exp[(\mathcal{E} - \mu)/kT]} \quad (2.21)$$

For the case in which almost all of the hydrogen is trapped by edge dislocations, one obtains [5].

$$\mu - \mu^0 = -\frac{A}{2} \sqrt{\frac{\psi \rho \pi}{c}} \quad (2.22)$$

where ψ is the saturation concentration of hydrogen in the neighborhood of the dislocation and ρ is the dislocation density.

When there are large local concentrations of hydrogen in the vicinity of dislocations, H–H interaction must be included in the theoretical treatment. In this case, the predicted segregation of hydrogen atoms to dislocations leads to extended local regions of large concentration. The formation of such high-concentration regions introduces additional energy terms due to elastic accommodation of the hydrogen cloud and the formation of a boundary between the cloud and surrounding matrix. Furthermore, a rearrangement of the matrix atoms could in principle occur, leading to the formation of a new phase, as has been observed for other solutes such as nitrogen in iron and oxygen in silicon [5].

The mobility of hydrogen can be substantially reduced by its attractive interactions with dislocations. These effects are usually treated within the framework of simple trapping models assuming a constant interaction energy [29],

despite the fact that dislocations provide a spectrum of trapping energies. In a generalized trapping model the distribution of site energies around dislocations can be treated rigorously, but at the price of complexity [10].

Experimental characterization of the interactions between dislocations and hydrogen is made difficult by the small volume fraction of the metal which is disturbed by the defect. Even at the highest dislocation densities of 10^{11} cm^{-2} , the cores are typically saturated at average concentrations above about 1 atomic ppm. Electrochemical measurements of uptake and release are applicable in this concentration regime and have been widely used to observe the influence of dislocations on hydrogen solubility and diffusivity. Nevertheless, the mechanical testing methods were not capable to resolve hydrogen-dislocation interaction on small scale. An indirect measurement technique at low hydrogen content is internal friction, which senses the interaction between hydrogen and the moving dislocations. In such experiments, the heights of intrinsic dislocation peaks are decreased by the addition of hydrogen, and a new peak (cold-work or Snoek-Koester peak) appears due to the hydrogen-dislocation interaction. However, the interpretation of the Snoek-Koester peak is not simple. The best approach for such experimental characterization of the interactions between dislocations and hydrogen could be achieved by confining the probed volume of the material to a scale comparable to the defect size. A promising technique for performing such a tests is nanoindentation technique which probes small volumes of material.

2.3.4 Internal boundaries

Grain and phase boundaries constitute the second major class of extended defects in crystalline metals, and the interactions of hydrogen with these entities are central to the influence of hydrogen on mechanical behavior. A predictive understanding of these interactions, however, has proved elusive, primarily for two reasons. First, information on the boundary atomic configurations is incomplete and often imprecise, and without such data the energetics of the hydrogen cannot be quantitatively treated. In addition, boundaries in metals often involve nonmetallic species, as in the case of carbide, nitride, and oxide precipitates, and this can introduce the complication of nonmetallic bonding. The situation is more favorable on the experimental side, where a substantial body of data on hydrogen binding energies has been obtained. Furthermore, better determinations of boundary structures are in prospect with the advent of advanced computer modeling and a new generation of microscopy techniques with

higher resolutions.

Due to their structural complexity, internal boundaries are expected to exhibit multiple hydrogen binding energies. The number of such energies should be small for coincidence grain boundaries and for phase boundaries where there is a well-defined orientational relationship, whereas the energetics of less regular interfaces are probably more complicated. Theoretical modeling of the hydrogen has not progressed to the point of definitively addressing the range of binding energies. The segregation of solutes at internal boundaries is often detected by inducing interfacial separation and analyzing the exposed surfaces. This direct approach is difficult in the case of hydrogen, however, due to the mobility of the solute down to low temperatures. The most extensive information has been obtained indirectly by observing differences in hydrogen concentration and mobility due to the presence of the boundaries, and approximate binding energies have been extracted in several instances.

In addition to their trapping of hydrogen, internal boundaries are believed to provide paths for accelerated diffusion. However, both mechanistic understanding and experimental data are very limited in this area. In the case of substitutionally dissolved impurities, accelerated diffusion is well established and ascribed to a reduced vacancy formation energy in the excess volume of the boundary. In contrast, the diffusion of interstitial hydrogen does not rely on vacancies, so that reduced activation energies at the boundary are presumably necessary to accelerate the transport. Some experimental investigations of grain-boundary diffusion in nickel have yielded rates several orders of magnitude greater than in the crystalline matrix [30, 31].

2.4 Experimental methodologies of HE study

In table 2.1, some compact measure of the experimental and theoretical effort addressing hydrogen embrittlement problem is provided [4, 5, 6, 7, 8, 9, 10, 32, 33, 34, 35, 14, 36, 37, 38, 39, 40, 41, 42, 43, 44, 45, 46, 47, 48, 49, 50, 51, 52, 53, 54, 55, 56, 57, 58, 59, 60, 61, 62, 63, 64, 65, 66, 11, 13, 12, 15]. On the basis of all these experimental and theoretical approaches many different and sometimes inconsistent effects of hydrogen on mechanical properties were observed. For example figure 2.5 shows the scatter in embrittlement index (percent reduction in area at fracture) from 465 tests on 34 different steel grades as a function of yield stress [67]. This inconsistency was mainly resulted from technological shortcomings of instrumentation and measurements techniques available at the time. For example, the effect of hydro-

gen on deformation has mostly been explored through conventional mechanical testing methods, such as tensile and compression tests on relatively large specimens in conjunction with ex situ or in situ hydrogen charging of the samples [68, 69, 70, 71, 72, 73, 74, 75, 76, 77, 78, 79]. First of all, the macroscale samples used in these studies are not fully characterizable in the sense of microstructure, defect density, composition, hydrogen concentration, etc. The results from these macroscale samples show an inherent scatter even without the effect of hydrogen. Although qualitative effects of hydrogen were observed from these experiments, the results are difficult to interpret quantitatively as the hydrogen embrittlement is a phenomenon which is taking place in the atomic scale. There are, however, experimental works enabling mechanistic assessments of hydrogen embrittlement. For example in situ straining experiments in

Table 2.1: Some experimental methodologies, techniques and theoretical investment into hydrogen embrittlement addressing this interactive problem

Experimental	Theoretical
Mechanical characterization and threshold values monotonic or cyclic [38, 14]	Thermodynamically based computations [58]
Sustained load, overloads, slow strain rate [49, 47, 52]	Hydrogen absorption and entry [51, 52, 48]
Fracture mechanic methodology on precracked samples [36, 37]	Discrete dislocation models [51]
Infrared spectroscopy (FTIR) [59]	Strain energy models [60, 61, 62]
Mössbauer, SEM, TEM, SPM, X-ray, Neutron scattering [10, 32, 33, 34, 35, 43, 41, 45, 46, 39]	Hydrogen diffusion and transport [51, 52, 48]
Subcritical crack kinetics [58]	Hydrogen/metal interaction [7, 63]
Interfacial strength [58]	cohesive energy [66, 64, 65, 62]
Time dependent tests [52, 58]	Atomistic models [53, 54, 55, 56, 57, 64, 65]
Internal friction, acoustic emission, phonon dispersion [50]	Hydrogen critical concentration and trapping sites [51, 52, 48]

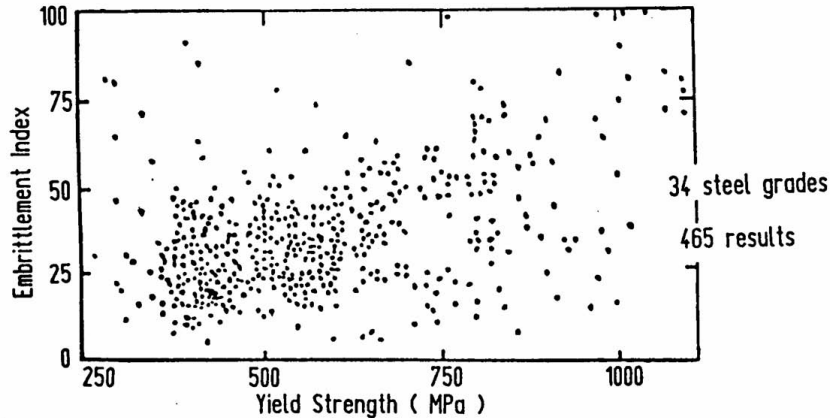
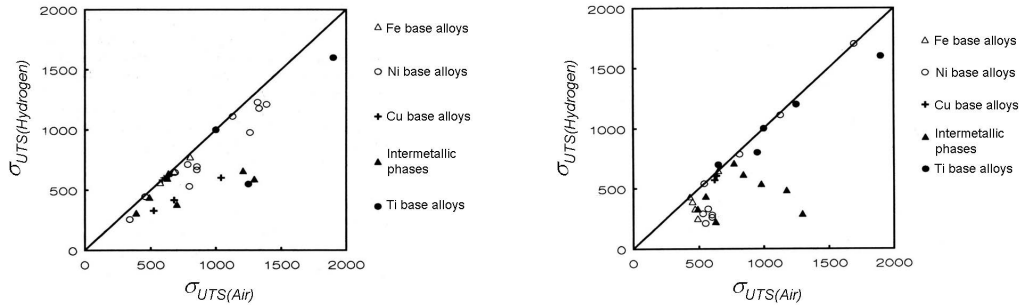


Figure 2.5: Embrittlement index from 465 tests on 34 different steel grades as a function of yield stress [67].

environmental transmission electron microscope [39, 40, 41, 42, 43, 44, 45, 46]. Both experimental approaches to the problem of hydrogen embrittlement will be discussed in the next two sections.

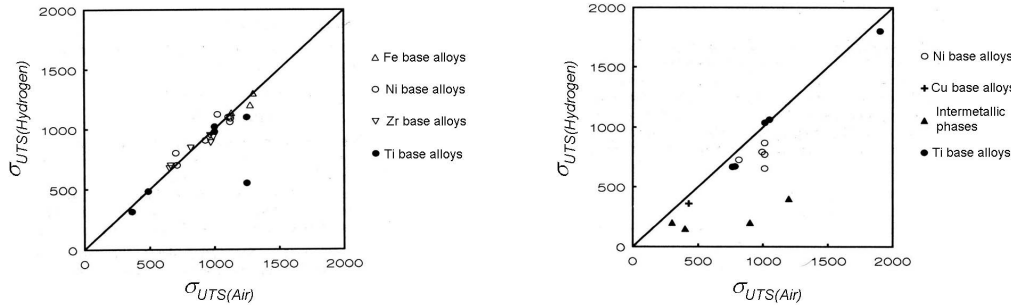
2.4.1 Conventional Methods

The easiest approach to see the effect of hydrogen on mechanical properties is to conduct a mechanical test on a hydrogen charged sample and measure the change in mechanical properties in comparison to an uncharged sample [80, 81, 68, 69, 70, 71, 72, 73, 74, 75, 82, 76, 77, 78, 79, 83, 38]. However, for such a test there is a huge amount of parameters which could be set differently. First of all hydrogen charging may be done in situ during the experiment [74, 52, 71, 73, 70, 68] or ex situ [38, 84]. Hydrogen charging may be done also electrochemically [38, 52, 71, 73, 70, 68], by plasma [74], or from gas phase [14, 37, 36]. The mechanical test can also be conducted under static or cyclic loading. All these differences result in discrepancies observed between different studies on the same materials. Bergmann [11] made a review on the effect of different experimental parameters on ultimate tensile stress, σ_{UTS} , of different alloys. He plotted the measured ultimate tensile stress in hydrogen, $\sigma_{UTS(Hydrogen)}$, versus ultimate tensile stress in air, $\sigma_{UTS(Air)}$. The observed difference in behavior of similar materials depending on the experimental parameters are shown in figures 2.6. Figure 2.6a shows the effect of ex situ electrochemical hydrogen charging at room temperature on different alloys where mostly resulted in reduction of σ_{UTS} . A more drastic effect is observed by in situ electrochemical hydrogen charging as shown in figure 2.6b. In the same alloys no reduction of σ_{UTS} is observed during in situ high pressure hydrogen charg-



(a) Electrochemically precharged samples tensile tested at room temperature

(b) In situ electrochemically charged and tensile tested at room temperature



(c) In situ in high pressure hydrogen gas at room temperature charged and tensile tested samples

(d) High temperature and pressure hydrogen atmosphere precharged samples tensile tested at room temperature

Figure 2.6: The effect of hydrogen charging condition and temperature on ultimate tensile stress in hydrogen, $\sigma_{UTS(Hydrogen)}$, versus ultimate tensile stress in air, $\sigma_{UTS(Air)}$ for different alloys and intermetallics. [11].

ing at room temperature (figure 2.6c), where in contrast ex situ and at high pressure and temperature charged samples show an obvious reduction in σ_{UTS} (figure 2.6d). This is a clear evidence for the complexity of hydrogen degradation of materials. This means a *critical experiments* for mechanistic study of hydrogen embrittlement should be conducted on a fully characterized sample (i.e. microstructure, defect density, composition, impurity concentration, etc) under precisely defined condition (i.e. hydrogen charging, temperature, pressure, stress, etc). Kimura et al. [68, 70, 69] made an attempt to do such a *critical experiment*. They performed tensile tests on different grades of high purity iron and studied the effect of charging, temperature, sample size, and impurities on mechanical behavior. They found that depending on these parameters the hydrogen effect may be observed either as softening or hardening. As an

example, figure 2.7 shows the effect of in situ hydrogen charging on the flow stress of high purity iron at various temperatures, where depending on the temperature either softening or hardening is observed [68]. They discussed several

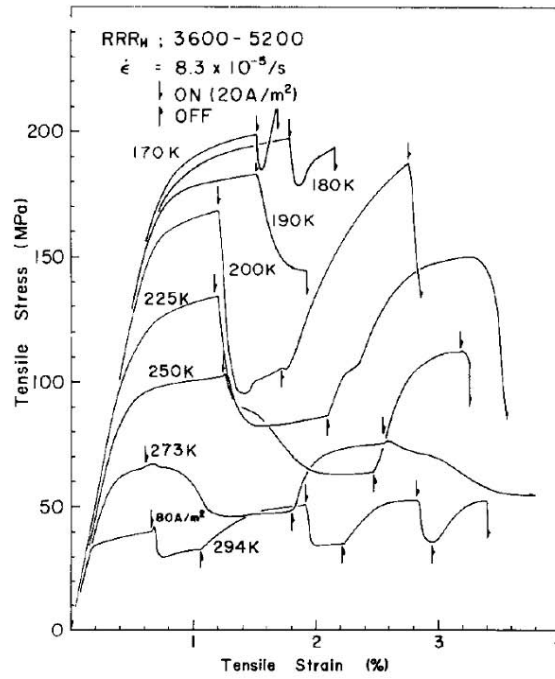


Figure 2.7: The effect of in situ hydrogen charging on the flow stress of high purity iron at various temperatures [68].

mechanisms for the observed effects, and concluded that the softening in high purity iron is due to an interaction between hydrogen and screw dislocations. The hardening below 190°K is due to an interaction between hydrogen and edge dislocations, including kinks on screw dislocations. As the discussion of these results has focused on the methods of charging with hydrogen, no definitive conclusions can be drawn about the effects of hydrogen on plastic deformation. This is mainly due to difficulties in the conventional deformation method (tensile test) they utilized to study the effect, as the details of plastic deformation (i.e. dislocation nucleation, multiplication, and movement) can not be explored with enough precision using such methods. Also the relatively large specimen size in conventional mechanical testing methods makes it almost impossible to fully characterize the samples before and after the experiments. This makes a microscopic comparison between the behavior of different samples from the same material almost impossible, second there is no guarantee that such bulky macro-samples, even if prepared carefully in the same manner, have the same microstructure and defect density. Therefore there is a need for a technique

which is capable of resolving the effect hydrogen has on details of plastic deformation and dislocation activity in metals. Further efforts to conduct such experiments will be discussed in the next sections.

2.4.2 Environmental transmission electron microscopy

One instrument that has been used for dynamic studies since its inception is the TEM. In 1934 Marton reported having gaseous environments in TEM in order to allow observation of hydrated biological samples. [85]. Marton's design included two 0.5 μm aluminum foils as upper and lower windows sandwiching a biological sample to sustain a living environment. The electron transparent windows permitted the confined biological objects to be imaged in TEM mode. Whelan et al. [86] reported observing dislocations moving in Al and stainless steel due to surface stresses induced by the electron beam. Since these observations, specimen holders have been developed that permit the observation of the effect of temperature, deformation, and environment (gaseous and chemical) on materials. A more radical approach was to reconfigure the electron microscope or to attach it to another instrument, essentially dedicating the microscope to a particular type of experiment. One of these approaches was to conduct in situ straining of metals in environmental TEM to allow hydrogen embrittlement to be studied in real time [42, 87, 40, 41, 44, 43, 39, 88, 46, 89, 90, 91]. To be able to perform TEM experiments in a controlled gaseous environment, and maintain operation of the microscope, a method was developed to confine the gas in the sample region and to minimize the electron path length in the gas [42]. Special in situ straining systems were used to strain the samples inside the TEM. Numerous materials, including Fe [92, 88], Ni [40], Al and Al-alloys [89, 44], Ni₃Al [93], Ti and Ti-alloys [91, 46], and 316 stainless steel [90] have been deformed in-situ in the environmental cell TEM. Shih et al. conducted such an in-situ environmental cell TEM test on α -Ti [91]. The series of images presented in figure 2.8 shows the effect of hydrogen gas introduction to TEM chamber on the mobility of dislocations observed in their experiments. The arrangement of dislocations produced by deforming the sample in vacuum is shown in figure 2.8(a). During the introduction of hydrogen gas, the stage displacement was held constant. The dislocation motion induced by the introduction of hydrogen gas (gas pressure 100 torr) can be seen by comparing the positions of dislocations 1–5 in figure 2.8b–d. New dislocations also appear in the field of view, some examples are marked by arrows in figure 2.8d. If the gas is removed from the cell, the dislocations stop moving. Reintroduction of the gas causes the dislocations to

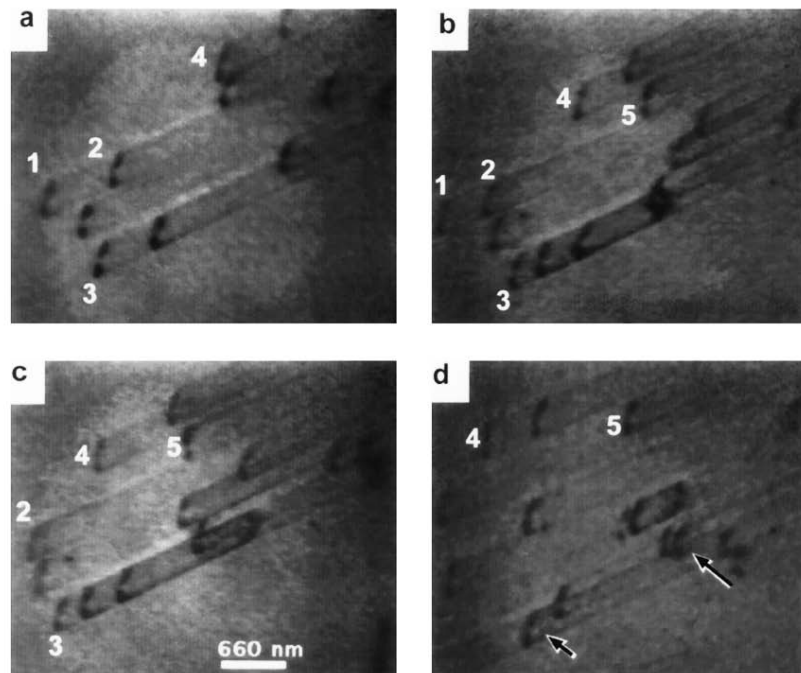


Figure 2.8: The effect of hydrogen on the mobility of dislocations in α -Ti [91]. The numbers identify the same dislocation in successive images and the arrows indicate new dislocations that have appeared in the field of view. Conditions are: (a) vacuum; (b); (c); and (d) 100 torr of hydrogen gas.

move again. Ferreira et al. studied the effect of hydrogen on the interaction between dislocations in 310s stainless steel and high-purity aluminum with the same technique [43, 44]. In 310s stainless steel, the presence of hydrogen in the TEM chamber was observed to reduce the elastic interactions between obstacles and perfect and partial dislocations; thus enhancing the mobility of the dislocations. An example of a decrease in the separation distance between dislocations in a pileup in 310s stainless steel as a result of introduction of hydrogen into the chamber is presented in figure 2.9 [43]. The initial dislocation configuration was created by deforming the sample in vacuum, figure 2.9a. Hydrogen gas was introduced to the system and as the gas pressure increased the dislocations moved closer to the grain boundary and the separation distance between the dislocations decreased. The overall shift in position of the dislocations is more evident in figure 2.9f, which was formed by superimposing a negative image (white dislocations) of figure 2.9e on a positive image of figure 2.9a. Clearly, all of the dislocations have moved closer to the barrier and the distance between the dislocations has decreased. Note that these in situ observations during stepwise hydrogen addition/removal were performed in ultra-thin sections with no plastic constraint. The limited hydrogen pressure which may be introduced to

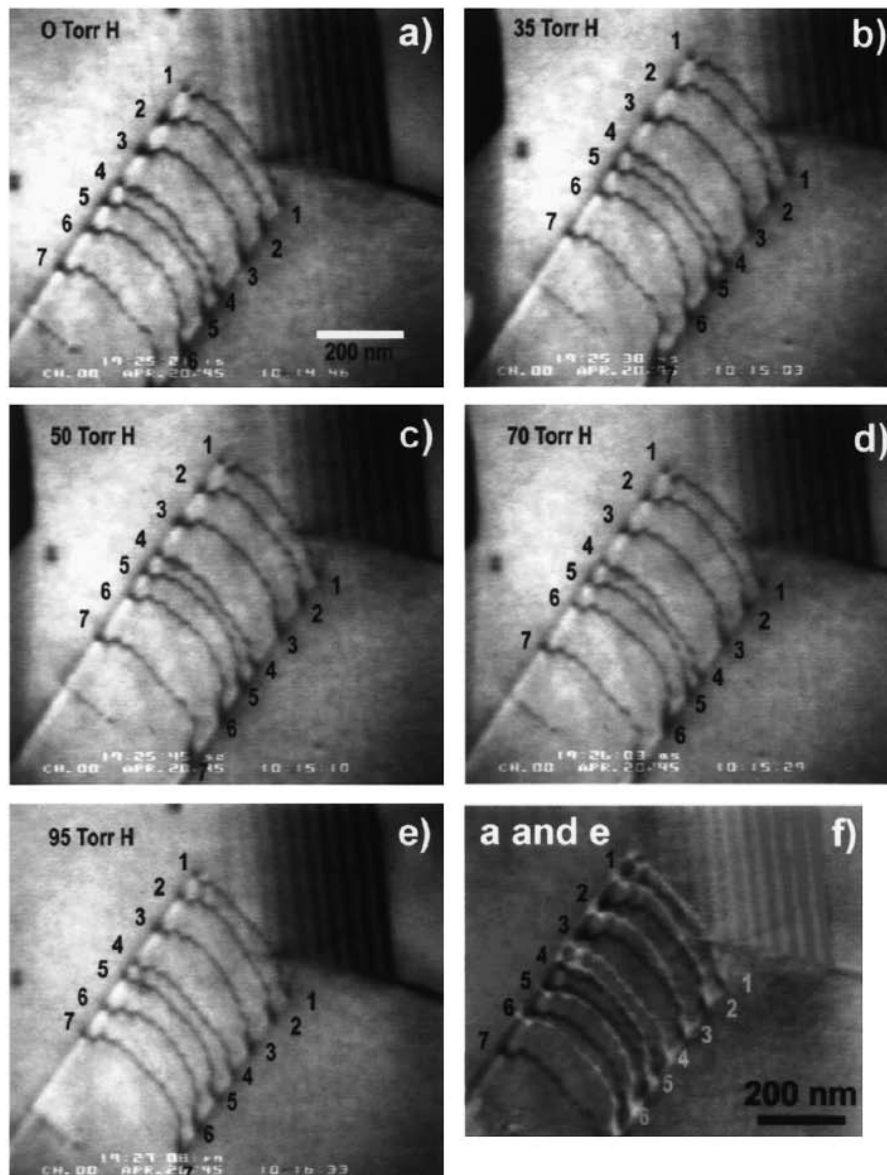


Figure 2.9: Reduction of the separation distance between dislocations in a pileup in 310s stainless steel due to solute hydrogen [43]. The hydrogen gas pressures are indicated. Image f is a composite image made from a positive of image a (black dislocations) and a negative of image e (white dislocations)

the chamber as well as possible surface effects should be taken into account. Also, only dislocation which are pinned on both sides of the thin films are observable in TEM. Therefore interpretation of this kind of in situ environmental TEM experiments should be done very carefully.

2.5 HE mechanisms

The fundamental mechanisms for hydrogen embrittlement in metals have been extensively reviewed [94, 7, 1, 95, 6]. The atomistic mechanism for hydrogen embrittlement is controversial with three major candidates advanced: Hydride-induced embrittlement, hydrogen enhanced decohesion (HEDE), and hydrogen enhanced localized plasticity (HELP). Each of these mechanisms are summarized, and the supporting theoretical and experimental evidence is noted.

2.5.1 Hydride-induced embrittlement

The stress-induced hydride formation and cleavage mechanism is one of the well-established hydrogen embrittlement mechanisms with extensive experimental and theoretical support [6, 42, 46, 96]. The nucleation and growth of an extensive hydride field ahead of a crack has been observed dynamically by Robertson et al. [42, 46] in β -Ti in situ charged from the gas phase in a controlled environment transmission electron microscope. In their observations the hydrides first nucleated in the stress-field of the crack and grew to large sizes not by the growth of individual hydrides but by the nucleation and growth of new hydrides in the stress field of the others. They showed that these small hydrides grew together to form the larger hydrides. This auto-catalytic process of hydride nucleation and growth, together with the brittle nature of them, seems to be the main cause of embrittlement of typical hydride forming elements, i.e. the elements in the group Vb; e.g., V, Nb, Ti and Zr.

2.5.2 Hydrogen enhanced decohesion

The HEDE mechanism was first suggested by Troiano [97, 94, 98], and developed in detail by Oriani and coworkers [99, 29, 100, 101, 12]. In this model, hydrogen accumulates within the lattice and there reduces the cohesive bonding strength between metal atoms. Initially, hydrogen accumulation above the unstressed-lattice solubility was driven by lattice dilation due to elastic hydrostatic stresses [102], while later work recognized that trapping is a potent mechanism for hydrogen segregation [103]. McMahon and coworkers advanced the view that impurity elements segregated to grain boundaries similarly reduced host-metal bond cohesion, adding to the embrittling effect of hydrogen [104]. The HEDE provides the basic notion that hydrogen damage occurs in the crack tip fracture process zone (FPZ) when the local crack tip opening tensile stress exceeds the maximum-local atomic cohesion strength, lowered by the presence

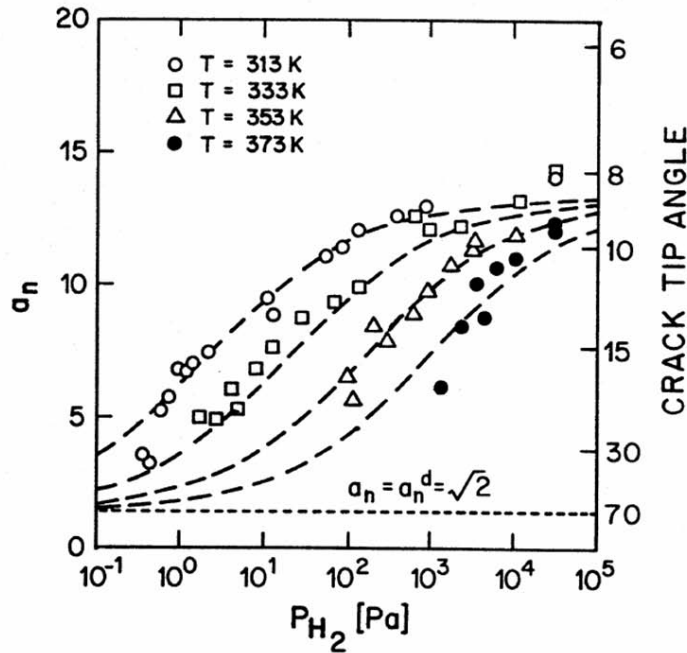


Figure 2.10: The dependence of in situ measured crack tip opening angle, α , on hydrogen pressure for Fe-3wt%Si single crystals stressed at several temperatures. The parameter a_n represents the ratio of incremental crack extension to crack mouth opening; $a_n = \cot(\frac{\alpha}{2})$. The horizontal-dashed line represents crack growth exclusively by crack tip slip, with α as the angle between active slip planes in the single crystal. As decohesion-based growth becomes increasingly important, α decreases. [36]

of hydrogen [100]. In the HEDE scenario, hydrogen damage sites are located at a distance ahead of the crack tip surface where tensile stresses are maximized. Predictions are derived from knowledge of crack tip stress, hydrogen concentration at damage sites, and its relationship with the inter atomic bonding force vs. atom displacement law.

A consensus is emerging that HEDE is the dominant mechanism for internal hydrogen assisted cracking (IHAC) and hydrogen environment assisted cracking (HEAC) in high strength alloys that do not form hydrides [105]. HEDE is likely for several reasons. First, large concentrations of hydrogen should accumulate in the FPZ due to very high crack tip stresses plus hydrogen trapping along a crack path, as suggested by [106] and supported by modern considerations of crack tip mechanics and trapping [8].

Second, experiments show directly that the sharpness of a crack tip in stressed Fe-3wt%Si single crystal increases progressively with increasing H_2 pressure and decreasing temperature; shown by decreasing crack tip angle (α) in figure 2.10 [36, 37]. In this figure, the horizontal-dashed line represents crack

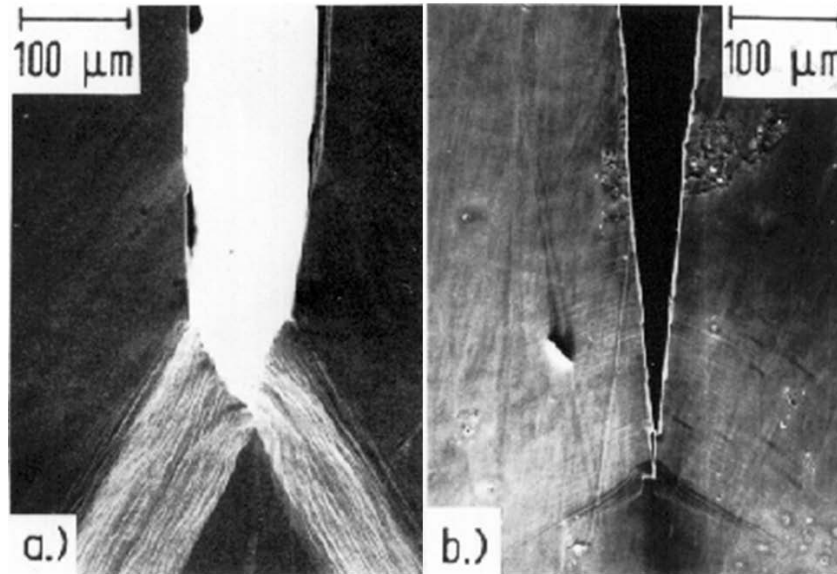


Figure 2.11: Crack tip opening angles obtained in Fe-3wt%Si single crystals after straining in vacuum (a) and hydrogen (b). [36]

growth by slip only, at a crack tip opening angle, α , of 70° that equals the angle between active slip planes in the single crystal (figure 2.11a). This angle will decrease as a second mechanism of crack growth becomes increasingly important (figure 2.11b). Since the crack planes in Fe-3wt%Si were always parallel to 100 and dimples were not resolved on these crack surfaces, the results in figure 2.10 were interpreted to prove that the decohesion mechanism progressively replaced crack tip slip as the advance process. The temperature and hydrogen partial pressure (P_{H_2}) dependencies were argued to be consistent with the amount of hydrogen expected to adsorb on an Fe surface.

Third, atomistic simulations suggest that hydrogen can reduce atomic cohesion [106]. Finally, a wide range of micromechanical models have been derived from the decohesion principle and effectively fit experimental values of K_{TH} and da/dt_H for IHAC and HEAC. These models span the range from continuum fracture mechanics to crack tip dislocation mechanics [13]. The effects of P_{H_2} and T , including rapid pressure or temperature-change experiments, as well as the effects of hydrogen concentration and σ_{YS} , have been predicted reasonably as summarized in [8, 6].

The HEDE mechanism is debated because of weaknesses in the supporting evidence. Foremost, there is still no direct experimental demonstration that atomic hydrogen dissolved in a metal lowers the interatomic force-displacement relationship, or alters elastic properties or surface energy that are derived from

such bonding. The primary problem is that the amount of hydrogen that can be dissolved in a specimen for bulk-property measurement is orders of magnitude less than that projected to accumulate locally within the crack tip FPZ. While theory suggests effects of hydrogen on metal bonding, results are limited by the capabilities of such modeling and necessary assumptions. The theoretical demonstration of hydrogen-sensitive bond strength can similarly support HEDE and HELP [107, 108, 109]. Finally, all HEDE-based models of macroscopic K_{TH} and da/dt properties contain one or more adjustable parameters due to uncertain features of the crack tip problem.

2.5.3 Hydrogen enhanced localized plasticity

The HELP model proposes the notion that solid solution free hydrogen either shields dislocations from interacting with other elastic obstacles, which allows dislocations to move at lower stresses [39, 40, 41, 42, 43, 44, 45, 46] or reduces the stacking-fault energy, which decreases the tendency for cross-slip by increasing the separation distance between partials [110, 43, 44, 84, 80, 111]. Moreover, such enhanced plasticity has been claimed to result in localized softening which enhances plastic failure in contrast to the usual sense of embrittlement. Enhanced ductile processes due to hydrogen interaction was suggested by Beachem [112]. He suggested that hydrogen stimulates dislocation processes that localize plastic deformation sufficiently to result in subcritical crack growth with brittle characteristics on the macroscopic scale. The primary evidence for HELP is in situ environmental TEM (2.4.2) of thinned specimens subjected to plastic deformation during exposure to either vacuum or hydrogen gas [45]. Such observations revealed an increased number of dislocations in a pileup, as well as initiation of dislocation motion or reduction of stacking fault energy (SFE), due to hydrogen gas introduction to the electron microscope. Similar plastic deformation accompanies crack growth in the TEM; however, such growth occurred at lower-applied stresses in the presence of hydrogen gas. For example, a stationary crack formed in vacuum began to propagate after introduction of hydrogen gas to the microscope. Such cracks propagated along a grain boundary and in the matrix volume adjacent to a boundary; with the interface mode prevalent when impurities such as sulphur in nickel were present to augment hydrogen damage.

Studies on the effect of hydrogen on bulk specimens show decreased flow stress [73], increased stress relaxation [84] and altered strain rate sensitivity [83] due to dissolved-bulk hydrogen. However, hydrogen effects on harden-

ing or softening are controversial, with diametrically opposed results reported for the same alloy and debate on experimental differences or artifacts possibly responsible for each trend [45]. While such information can confirm that hydrogen interacts with dislocations to affect plastic flow, the point is moot since the high hydrogen content, highly triaxial stress state, and graded character of the crack tip FPZ are not represented by bulk crystal uniaxial deformation experiments.

The HELP mechanism is debated because of additional weaknesses in the supporting evidence. The TEM studies use a thin foil (< 200 nm) with at best a two-dimensional stress state and substantial possibility for surface effects on dislocation motion. Surface issues may be exacerbated by the high fugacity hydrogen, produced by hydrogen gas dissociation in the electron beam and capable of reducing surface oxide and oxidizing hardening solute such as carbon or oxygen. These changes, rather than a core-hydrogen interaction could cause the observed plasticity and thus be unique to the thinned foil. Studies have not been extensive for complex microstructures with multiple obstacles and very short slip distances typical of high strength alloys. The geometry of localized flow in such high strength microstructures has not been developed. Modeling of dislocation mobility has not included hydrogen drag on the moving-dislocation line. Finally, the HELP mechanism has not been developed to yield semi-quantitative predictions of K_{TH} or da/dt_{II} . As such, the HELP model does not support structural integrity analysis.

2.6 A new approach to HE study

The technical shortcomings regarding experimental investigation of hydrogen embrittlement were mentioned in section 2.4. The two main experimental approaches into the hydrogen embrittlement problem resulted in two atomistic mechanism for this phenomenon. The HEDE model was proposed on the basis of the conventional mechanical tests, whereas the HELP model was mainly based on in situ environmental TEM observations. Since, from the preceding discussion, the both methods have shortcomings for investigation of the hydrogen embrittlement, there is a need for a new method. A desirable method for this purpose should be microscopic as in the case of the in situ environmental TEM, but capable of performing the tests under realistic condition, like conventional mechanical test methods¹.

¹In the environmental TEM strained thin film samples and high energy electrons make the experimental condition quite complex and incomparable to realistic condition of hydrogen

By the invention of the STM in the early 80's a new microscopy technique was born [113]. The so called SPM with a high spatial resolution was of advantage to electron microscopy because of the ability to operate in ambient condition or even inside the fluids. This resulted in a very fast implementation of this technique in various branches of the natural science [113].

One of the most successful SPM techniques in materials science is nanoindentation atomic force microscope (NI-AFM) [114]. A NI-AFM is capable of imaging the surface like an scanning force microscope, positioning the tip on a specific point of the imaged area, and then performing the indentation. The radius of the tips used in a typical NI-AFM system are in the range of 100 nm to 10 μ m. Therefore the probed volume of a material tested with a NI-AFM is also in the same range and additionally can be controlled by controlling the indentation depth. From this point of view the technique seems to be very promising for study of hydrogen embrittlement in small volumes.

Another unique ability of NI-AFM is capability of detecting dislocation nucleation events on well-prepared surfaces [115, 116, 117]. During the initial elastic loading sequence of a nanoindentation experiment, the lateral dimensions of the volume of material that deforms are significantly smaller than the mean dislocation spacing for annealed metals. As a result, the indenter produces shear stresses underneath the tip contact region that approach the theoretical shear strength [118, 119, 120]. A pop-in occurs in the load displacement curves at the onset of plasticity, which correlate to the homogeneous dislocation nucleation¹. Low dislocation densities are required; otherwise the indenter mainly activates existing sources such as Frank-Read sources, and no pop-ins occur. Since nanoindentation involves small volumes of material, additionally multiple tests can be performed within a single sample which has been previously characterized by other methods. The most attractive techniques for characterization of the samples prior to nanoindentation are techniques based on SEM where the surface of the samples can be characterized nondestructively to the probing depth of NI-AFM. For example orientation gradient mapping (OGM) [121], and electron channeling contrast imaging (ECCI) [122] provide useful information from the underlying microstructure and dislocation substructure in the sample. Additionally, the small volume of deformation produced after nanoindentation can be well characterized using the same techniques as mentioned above or by in situ imaging. This small deformed volume is nevertheless large enough to activate multiple slip systems under the indenter. This makes the deforma-

embrittlement (see section 2.4.2)

¹Pop-in phenomena will be reviewed in section 3.6.2.3

tion more realistic compared to other local measurement techniques like in situ straining of thin films in TEM. The in situ imaging capability of NI-AFM allows testing of areas that are either free of defects, i.e. second phases and grain boundaries, or intentional testing near these defects by precise positioning of the tip before indentation [123, 124, 125]. All these capabilities make NI-AFM an outstanding local measurement device for micromechanical characterization of materials.

There have been few attempts to use this technique for probing hydrogen embrittlement [126, 127]. Recently Nibur et al. [32] used nanoindentation to study the effect of dissolved hydrogen on the deformation of small volumes in an austenitic stainless steel. They found that hydrogen reduces the pop-in load at which dislocations are nucleated and it is further shown that this is likely due to hydrogen reducing the shear modulus. Gao et al. [33] used a similar approach to study the effect of hydrogen on dislocation nucleation in iron single crystals. Their results show that the hydrogen enhances dislocation nucleation. In all of these attempts, ex situ methods were used for hydrogen charging. Therefore the actual concentration of hydrogen within the shallow depth probed by nanoindentation was doubtful, as hydrogen outgassing will produce a concentration gradient between the surface and the bulk. Additionally our ex situ tests showed that the nanoindentation results for an ex situ charged sample is suspicious (see 5.1).

The advantage of NI-AFM (like most of the other SPM techniques) compared to electron microscopy is the ability to operate in liquid¹. Therefore the prime motivation of the present work was to perform nanoindentation tests inside electrolytes on in situ hydrogen charged surfaces. The development of the in situ electrochemical NI-AFM (ECNI-AFM) setup makes it possible to perform such experiments on several different metals and alloys. This micromechanical approach enables us to gain new and deeper insight into the hydrogen embrittlement.

¹Not easy but it is possible (see 3.5)

CHAPTER 3

NI-AFM

*And therefore, ere thou enter farther in,
Look down once more, and see how vast a world
Thou hast already put beneath thy feet;*

The Divine Comedy, Paradiso: Canto XXII
DANTE ALIGHIERI

3.1 Nanoindentation

Hardness measurements are one of the most common ways to test the mechanical properties of materials. These tests are quick and easy, repeatable and inexpensive. Since the early 1800's, when Friedrich Mohs [128] first introduced scratch testing, relative hardness has been used to characterize mechanical properties. Almost a century later Johan Brinell [128] introduced a test in which a hard sphere was pressed into a specimen. The ratio of the force applied and the surface area of contact was defined as the hardness, a definition still used today. Many people such as Knoop, Vickers, and Rockwell [129] have all modified this test, but the principle has remained the same.

In today's drive for smaller and smaller parts, we need to understand the mechanical properties of small volumes of material. The reduction in scale may potentially change a material's behavior from that of its bulk form. Nanoindentation is a means of characterizing local properties of small volumes and thin films. In the nanometer regime, atomic scale heterogeneities can have a dramatic effect on hardness tests. Factors such as location of the indent, surface preparation, surface orientation, the radius of the indenter and even the tip material play important role in the information gathered [130, 131, 132]. The mechanical response of small volumes of material is more sensitive

to often-overlooked characteristics such as the surface energy and dislocation density [133]. Also oxides, absorbed species, compositional changes and even exposure to the environment can have significant local influence on the mechanical properties [134]. On the other hand at small enough scales, a single crystal of metal has a structure that can be thought of as a perfect lattice. This means that theoretical property values, based upon idealized atomic interactions, may be attainable. The response to point contacts on the nano-scale may differ greatly from what we observe on a macro scale due to faultless configurations or the isolated influence of a specific defect.

Very low load indents used for nanoindentation are beyond the resolution of optical techniques, and other imaging apparatus such as SEM make the tests no longer convenient. One way to maintain the ease of testing is to use a procedure called depth-sensing indentation or nanoindentation. A probe forms the indent while recording the applied force and the corresponding displacement. These displacement measurements are on the order of nanometers, and the applied force is usually on the order of micro-Newtons. This technique has one significant difference from traditional methods. The whole material response is recorded, both the elastic and the plastic deformation. The measurements are no longer just a measure of residual deformation. Another hundred years after Brinell, the way in which we evaluate the hardness of a material is again redefined.

3.2 Contact Mechanics

Indentation is the act of bringing two bodies into contact; one being a probe, extremely stiff and minimally altered by the interaction, the second is the specimen whose properties we are interested in quantifying. It is the response to the applied load that provides an indication of the mechanical properties. In order to understand and interpret what is measured during indentation testing, we must start with the theories that describe the influence of force on materials. Since nanoindentation records the displacement due to the elastic as well as the plastic deformation we must understand some of the basics of the theories of elasticity and plasticity.

Figure 3.1 is a cross-section of a flat surface and a rigid spherical indenter. The indenter radius is R , the radius of contact is a , and h_t is the total depth of penetration. The other two depths indicated are the distance from the free surface to the radius of contact h_e , and the distance from the radius of contact to the total depth h_p .

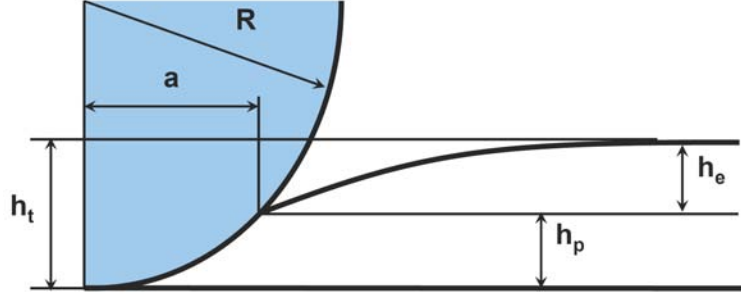


Figure 3.1: Schematic of the interaction between a rigid spherical indenter (with radius = R) and a flat surface. The radius of contact, a , is also indicated. The total displacement of the surface is h_t , which consists of the distance from the free surface to the radius of contact h_e , and the distance from the radius of contact to the total depth h_p .

Hertz first theorized about idealized material contact when working with distortion due to contacting lenses in 1882 [135]. The contact distorted the lenses and caused fringes to be formed in the transmitted light. In order to understand the nonpermanent change in the lens shape he began to investigate elasticity. His theory of elasticity can also be applied to the initial portion of point contact loading. He demonstrated that the radius of contact, a , is related to the combined radius of the objects R , the load applied P , and the materials' elastic properties E_r in the following manner [136]:

$$a^3 = \frac{3PR}{4E_r} \quad (3.1)$$

The combined radius is determined by the following expression:

$$\frac{1}{R} = \frac{1}{R_1} + \frac{1}{R_2} \quad (3.2)$$

where R_1 and R_2 are the radii of the two contacting bodies. In the case of a rigid indentation, the sample surface is usually very flat compared to that of the indenter; therefore the radius of the indenter alone is used. The term E_r is the reduced modulus. It is a composite modulus property used to account for the non-rigid tip interaction, or the elastic interactions of the tip and the surface. An efficient method of combining the two moduli is to assume that the two materials behave as springs in series. The reduced modulus can be expressed:

$$\frac{1}{E_r} = \frac{1 - \nu_m^2}{E_m} + \frac{1 - \nu_i^2}{E_i} \quad (3.3)$$

where E_m and E_i are the Young's Moduli for the sample material and the in-

denter respectively; ν_m and ν_i are the materials Poisson's ratios. The elastic contact is small compared to the overall size of the specimen and the indenter. The displacements of the points on the surface within the area of contact are given by the following expression, in respect to the origin of the specimen free surface:

$$h = \frac{3P}{8aE_r} \left(2 - \frac{r^2}{a^2} \right) \quad r \leq a \quad (3.4)$$

In this equation r is the radial distance from the axis of symmetry. This equation helps to define the total elastic displacement pictured in Figure 3.1.

Hertz was also concerned with the distribution of pressure between these two contacting bodies. The area of the sample in contact with the indenter is important because it determines the load distribution on the material. Some of the basic assumptions are that the two bodies are elastic, semi-infinite, half-spaces, with no friction between them, and the stress is equal to zero far from the point of contact. An elliptical pressure distribution satisfies all the boundary conditions. For a spherical indenter the surface pressure distribution can be expressed by:

$$\frac{\sigma_z}{p_{mean}} = -\frac{3}{2} \left(1 - \frac{r^2}{a^2} \right)^{1/2} \quad r \leq a \quad (3.5)$$

Where σ_z is the stress in the direction normal to contact, p_{mean} is the mean contact pressure, which is defined by the indenter load divided by the projected area of contact:

$$p_{mean} = \frac{P}{\pi a^2} \quad (3.6)$$

Substituting equation 3.1 in for the load, P , leaves an expression that is independent of applied load:

$$p_{mean} = \left(\frac{4E_r}{3\pi} \right) \frac{a}{R} \quad (3.7)$$

This mean contact pressure is also referred to as the "indentation stress". The ratio of the radius of contact over the actual indenter radius is sometimes referred to as the indentation strain. These measures of applied force help to better interpret the material response in familiar terms.

The normal pressure at the center of contact p_0 is also the maximum, and in the case of a spherical indenter is equal to $1.5 p_{mean}$. At the edge of the contact area the pressure falls to zero. The pressure within the area of contact for a

spherical indenter is defined as [128]:

$$p = p_0 \left(1 - \frac{r^2}{a^2}\right)^{1/2} \quad (3.8)$$

Outside the area of contact it is a free surface and therefore the normal pressure is zero. The maximum pressure p_0 is related to the total load by the expression [135]:

$$p_0 = \frac{3P}{2\pi a^2} \quad (3.9)$$

During indentation, the radius of contact is a function of the material properties, the depth of the indent and therefore the radius of the indenter R . Using equation 3.1 and substituting for these known values we derive the expression for maximum pressure independent of contact area:

$$p_0 = \left(\frac{6PE_r^2}{\pi^3 R^2}\right)^{1/3} \quad (3.10)$$

Hertz did not calculate internal stress fields, but did indicate that these could be calculated by interpolating surface solutions along the axis of symmetry. As early as 1885 the shape of deformation derived by Boussinesq [135] and in 1904 a general solution for the stress tensor of Hertzian contact within a solid was proposed by Huber (Huber stress tensor) [137]. In cylindrical coordinates r, θ, z it is given by:

$$\begin{aligned} \frac{\sigma_r}{p_{mean}} &= \frac{3}{2} \left[\frac{1-2\nu}{3} \frac{a^2}{r^2} \left(1 - \left(\frac{z}{\sqrt{u}}\right)^3\right) + \left(\frac{z}{\sqrt{u}}\right)^3 \frac{a^2 u}{u^2 + a^2 z^2} \right. \\ &\quad \left. + \frac{z}{\sqrt{u}} \left(\frac{1-\nu}{a^2 + u} u + (1+\nu) \frac{\sqrt{u}}{a} \arctan\left(\frac{a}{\sqrt{u}}\right) - 2 \right) \right] \\ \frac{\sigma_\theta}{p_{mean}} &= -\frac{3}{2} \left[\frac{1-2\nu}{3} \frac{a^2}{r^2} \left(1 - \left(\frac{z}{\sqrt{u}}\right)^3\right) \right. \\ &\quad \left. + \frac{z}{\sqrt{u}} \left(2\nu + \frac{1-\nu}{a^2 + u} u - (1+\nu) \frac{\sqrt{u}}{a} \arctan\left(\frac{a}{\sqrt{u}}\right) \right) \right] \\ \frac{\sigma_z}{p_{mean}} &= -\frac{3}{2} \left(\frac{z}{\sqrt{u}}\right)^3 \frac{a^2 u}{u^2 + a^2 z^2} \\ \frac{\tau_{rz}}{p_{mean}} &= -\frac{3}{2} \frac{r z^2}{u^2 + a^2 z^2} \frac{a^2 \sqrt{u}}{a^2 + u} \\ \tau_{r\theta} &= \tau_{\theta z} = 0 \end{aligned} \quad (3.11)$$

in these expressions u is the positive root of the equation:

$$\frac{r^2}{a^2 + u} + \frac{z^2}{u} = 1 \quad (3.12)$$

A graphical representation of the Huber stress tensors for a contact radius of $a = 1$ unit of length, a Poisson's ratio of $\nu = 0.3$ are given in figures 3.2–3.5.

From equation (3.11) we have $\tau_{r\theta} = \tau_{\theta z} = 0$ additionally σ_θ is a hooping stress and its trajectories are circles around the z axis. Therefore the solution of the principle stresses of the Huber stress tensor can be reduced to a two dimensional case and can be expressed as follow:

$$\begin{aligned} \sigma_1 &= \frac{\sigma_r + \sigma_z}{2} + \sqrt{\left(\frac{\sigma_r - \sigma_z}{2}\right)^2 + \tau_{rz}^2} \\ \sigma_2 &= \sigma_\theta \\ \sigma_3 &= \frac{\sigma_r + \sigma_z}{2} - \sqrt{\left(\frac{\sigma_r - \sigma_z}{2}\right)^2 + \tau_{rz}^2} \\ \tau_{13} &= (\sigma_1 - \sigma_3)/2 \end{aligned} \quad (3.13)$$

A graphical representation of these principle stresses for a contact radius of $a = 1$ unit of length, a Poisson's ratio of $\nu = 0.3$ are given in figure 3.6, figure 3.7, and figure 3.8.

In figure 3.8 the principle shear stress shows a maximum on the z axis. The solution for this maximum point results in

$$\tau_{max} = 0.31 \left(\frac{6PE_r^2}{\pi^3 R^2} \right)^{\frac{1}{3}} \quad (3.14)$$

$$h_{(\tau_{max})} = 0.48 \left(\frac{3PR}{4E_r} \right)^{\frac{1}{3}} \quad (3.15)$$

where τ_{max} is the value and $h_{\tau_{max}}$ is the position of this maximum shear stress. Interestingly the position of this maximum shear stress ($\tau_{max} = 0.31p_0$) is below the surface ($h_{\tau_{max}} = 0.48a$). Since in crystalline materials the shear stress is responsible for the deformation, the most important conclusion to be taken from these data is that the position of the first plastic deformation is just at this point below the surface. This has a great advantage for material characterization because it shows that it is possible to probe the properties of the bulk material with the NI-AFM technique, and not surface effects.

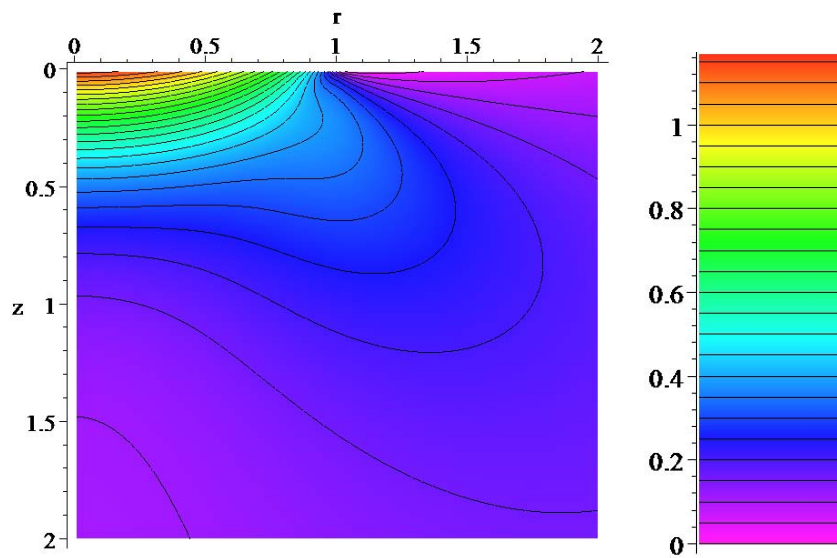
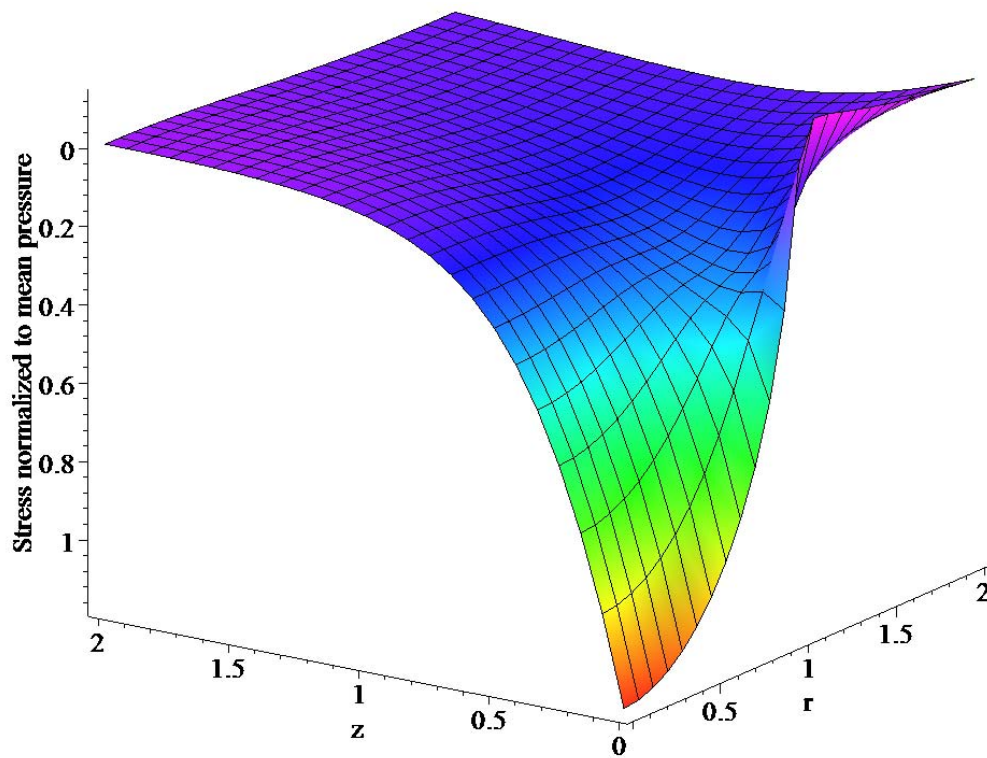
(a) Stress contours of the σ_r below the surface(b) Three dimensional representation of σ_r below the surface

Figure 3.2: Graphical representation of the σ_r in Huber stress tensor below the surface, as a result of the elastic Hertzian contact between a flat surface and a spherical indent with a contact radius of $a = 1$ and $\nu = 0.3$ (z is the axis of symmetry).

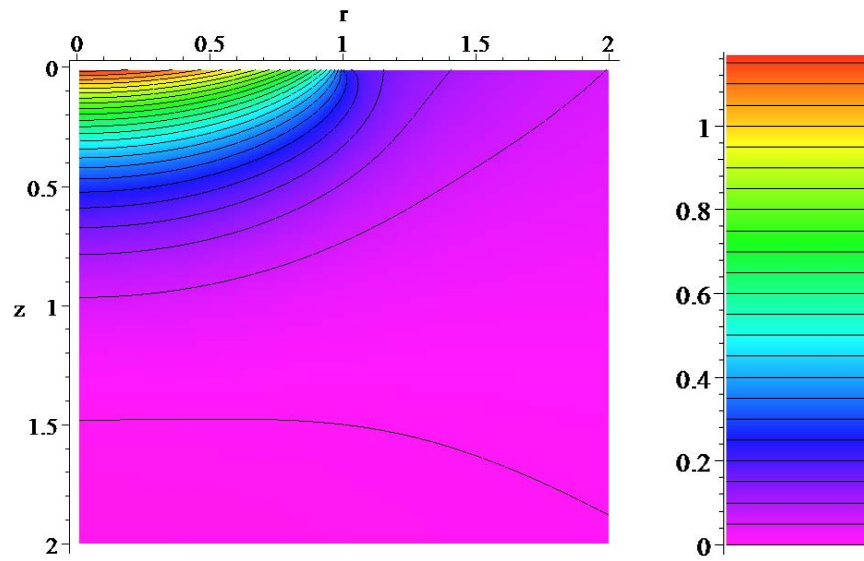
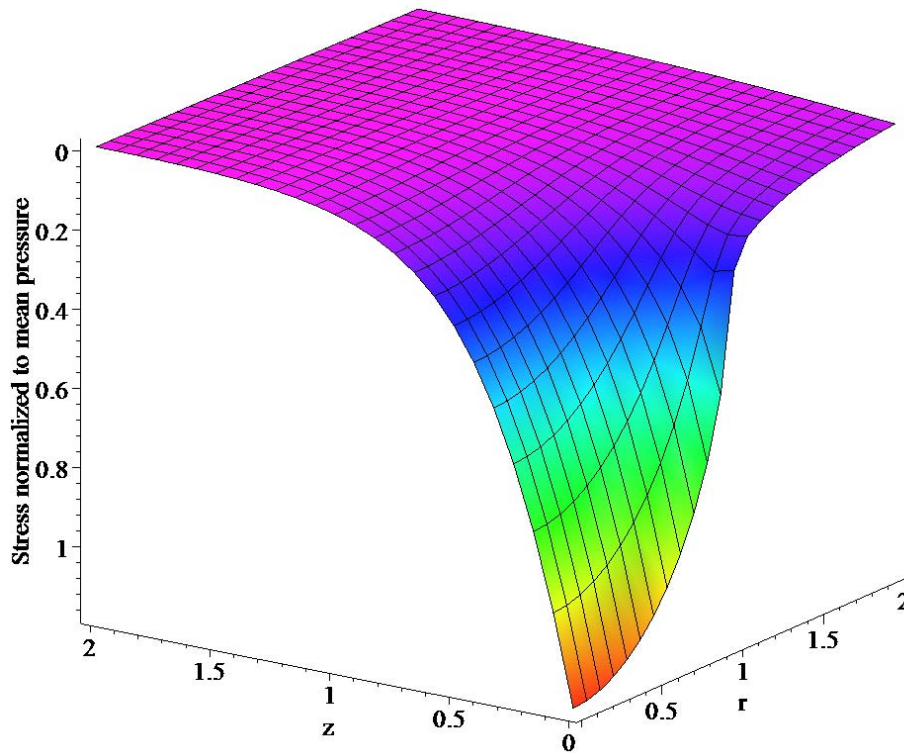
(a) Stress contours of σ_θ below the surface(b) Three dimensional representation of σ_θ below the surface

Figure 3.3: Graphical representation of the σ_θ in Huber stress tensor below the surface, as a result of the elastic Hertzian contact between a flat surface and a spherical indent with a contact radius of $a = 1$ and $\nu = 0.3$ (z is the axis of symmetry).

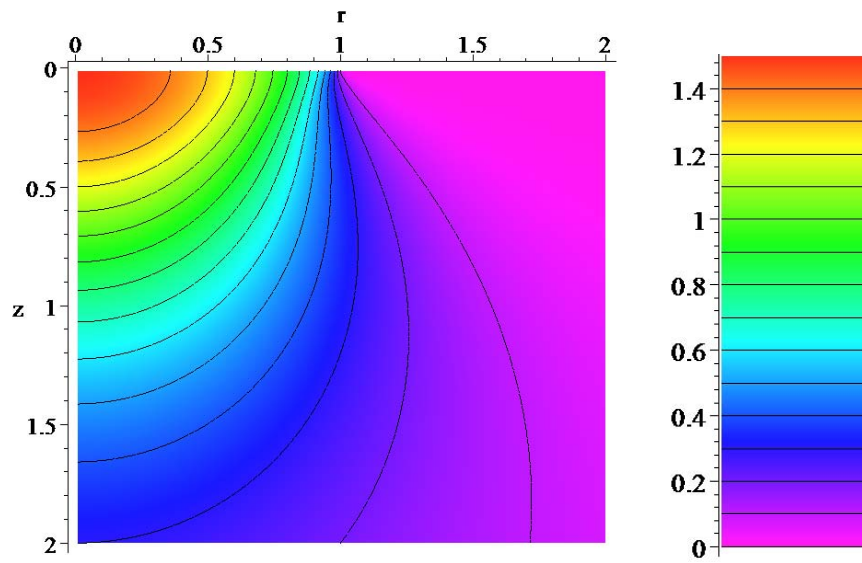
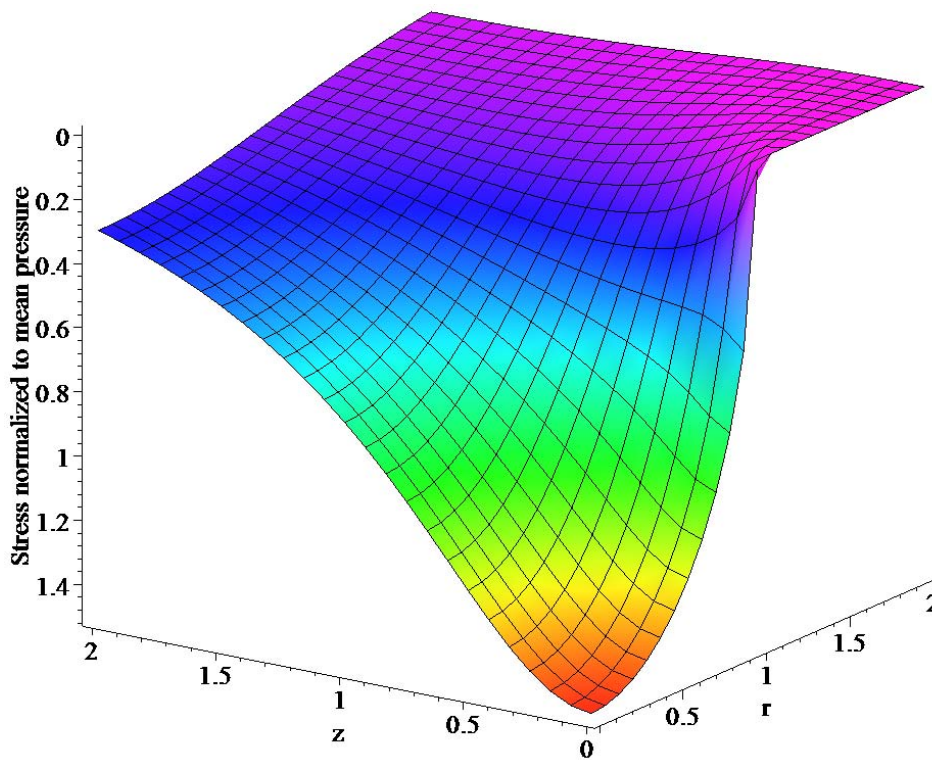
(a) Stress contours of the σ_z below the surface(b) Three dimensional representation of σ_z below the surface

Figure 3.4: Graphical representation of the σ_z in Huber stress tensor below the surface, as a result of the elastic Hertzian contact between a flat surface and a spherical indent with a contact radius of $a = 1$ and $\nu = 0.3$ (z is the axis of symmetry).

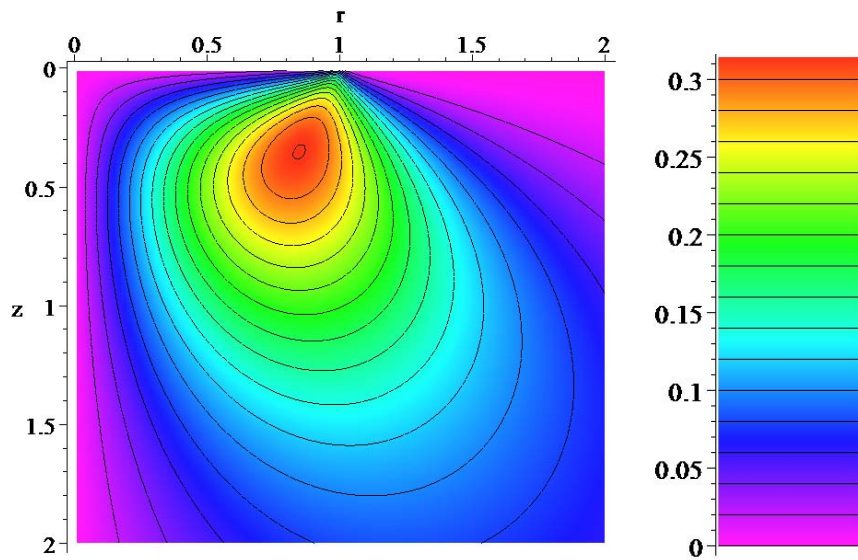
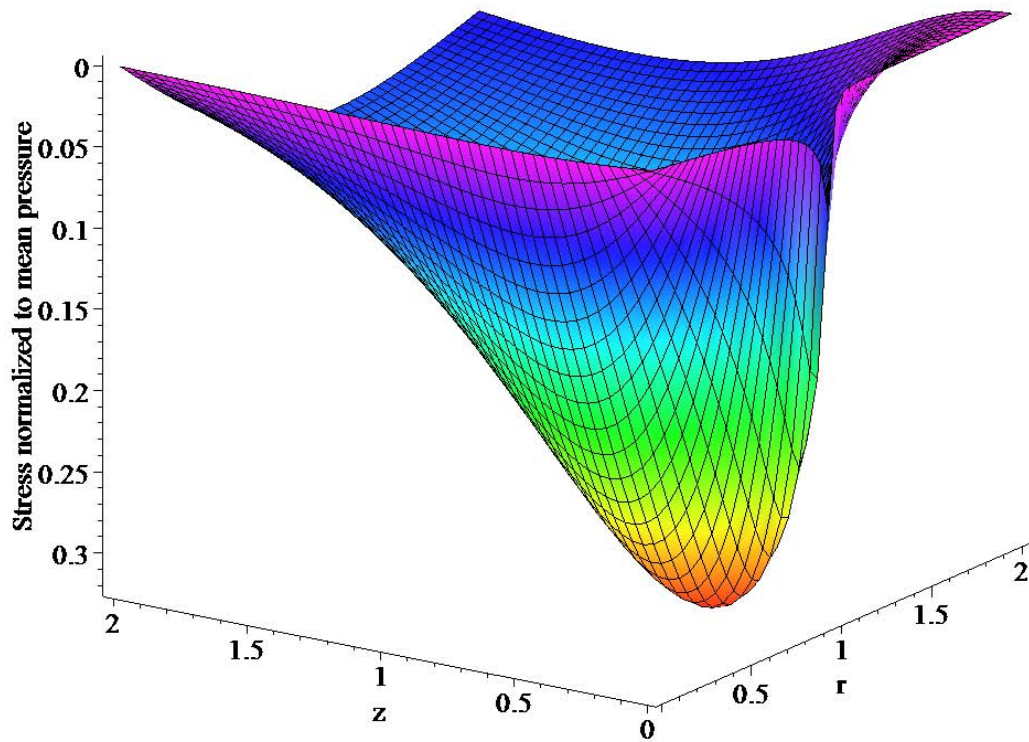
(a) Stress contours of the τ_{rz} below the surface(b) Three dimensional representation of τ_{rz} below the surface

Figure 3.5: Graphical representation of the τ_{rz} in Huber stress tensor below the surface, as a result of the elastic Hertzian contact between a flat surface and a spherical indent with a contact radius of $a = 1$ and $\nu = 0.3$ (z is the axis of symmetry).

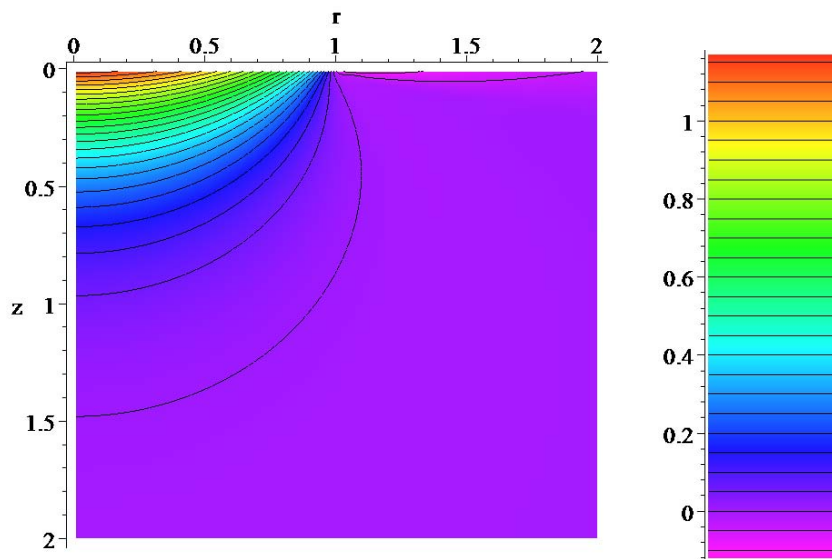
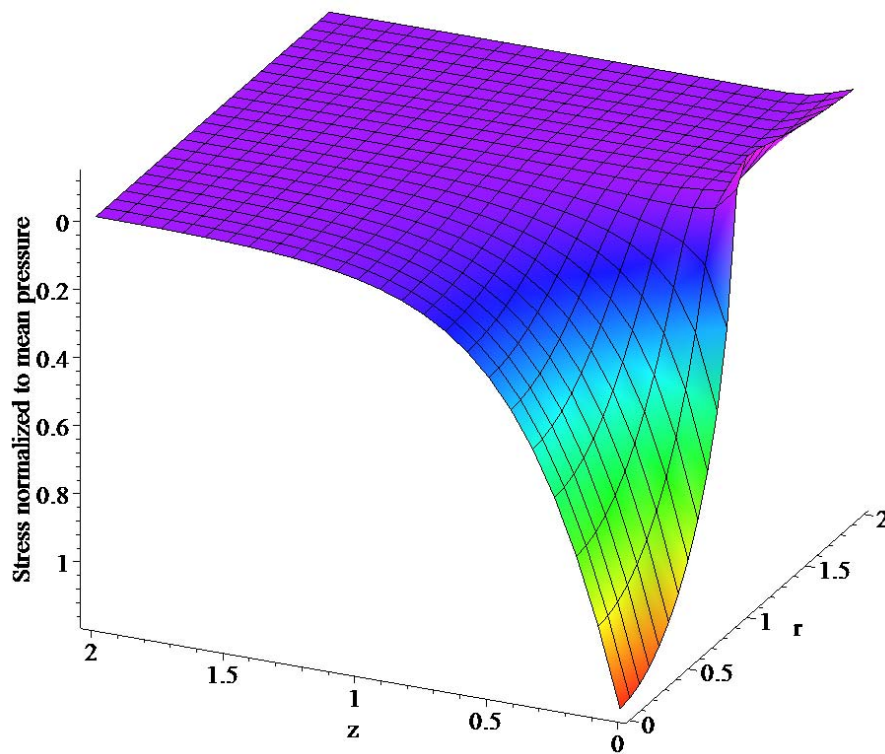
(a) Stress contours of the σ_1 below the surface(b) Three dimensional representation of σ_1 below the surface

Figure 3.6: Graphical representation of the σ_1 principle stress below the surface, as a result of the elastic Hertzian contact between a flat surface and a spherical indent with a contact radius of $a = 1$ and $\nu = 0.3$ (z is the axis of symmetry).

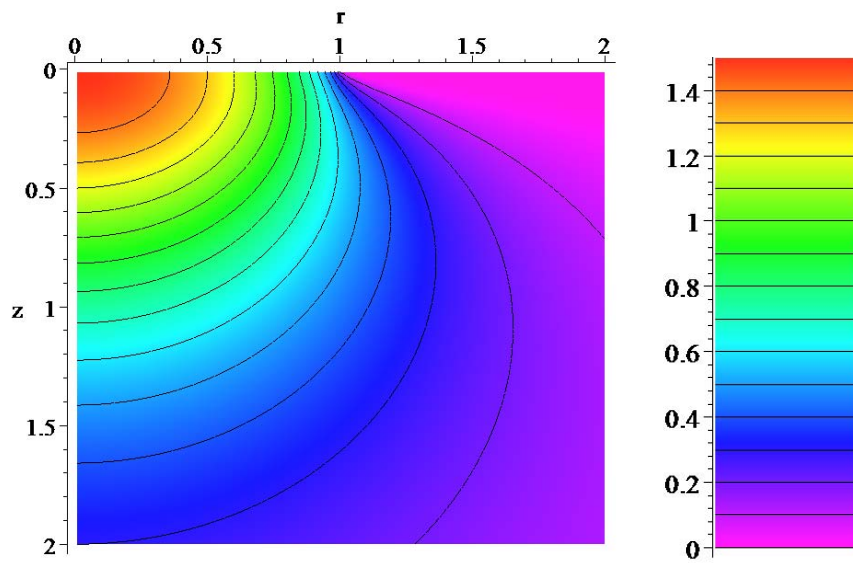
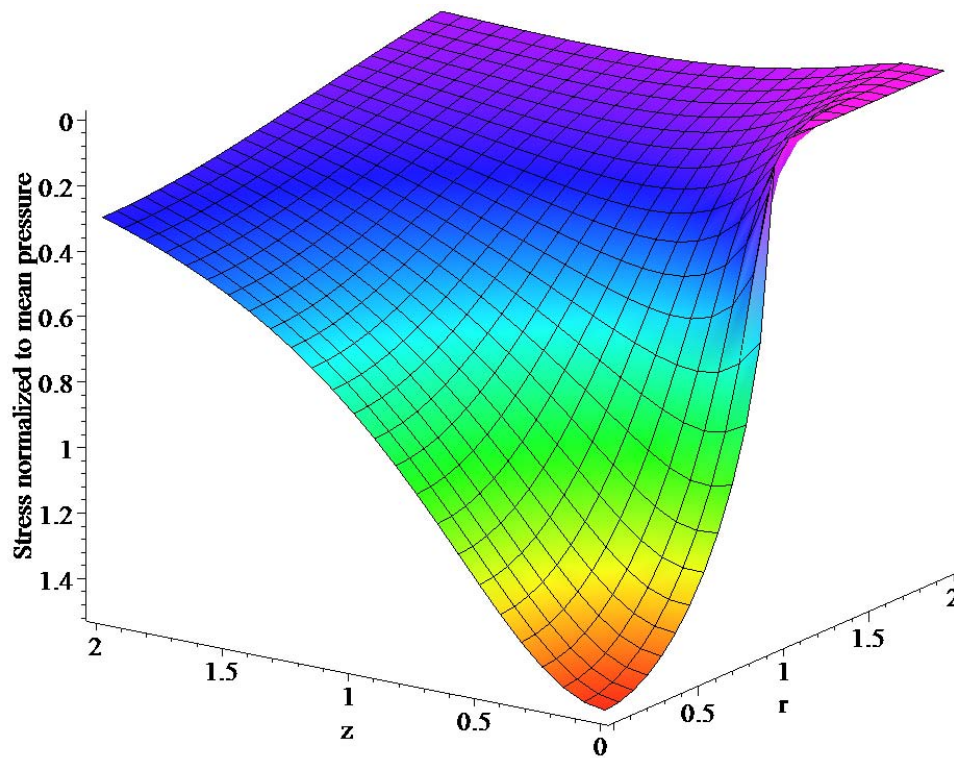
(a) Stress contours of the σ_3 below the surface(b) Three dimensional representation of σ_3 below the surface

Figure 3.7: Graphical representation of the σ_3 principle stress below the surface, as a result of the elastic Hertzian contact between a flat surface and a spherical indent with a contact radius of $a = 1$ and $\nu = 0.3$ (z is the axis of symmetry).

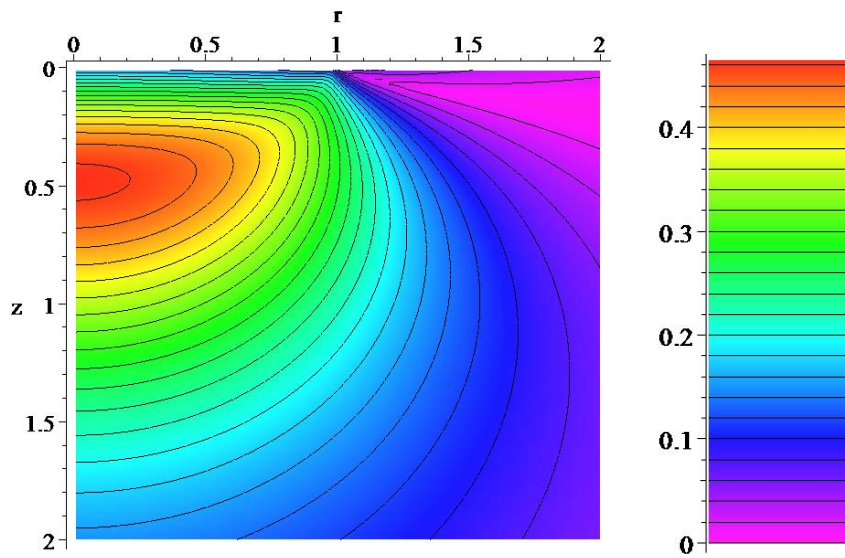
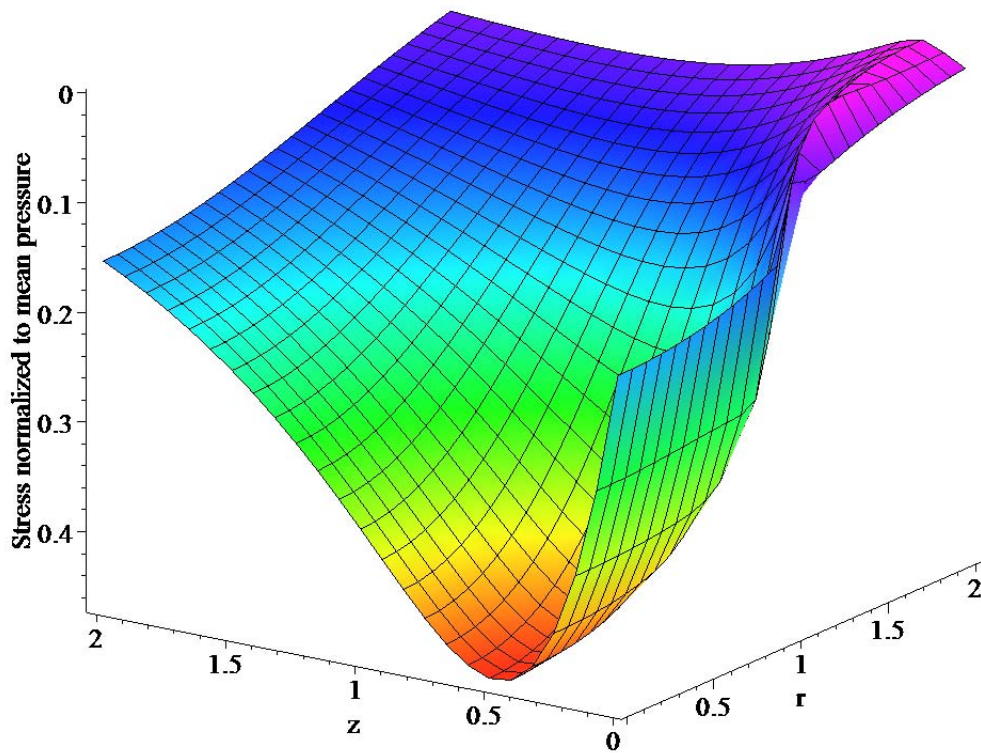
(a) Stress contours of the τ_{13} below the surface(b) Three dimensional representation of τ_{13} below the surface

Figure 3.8: Graphical representation of the τ_{13} principle shear stress below the surface, as a result of the elastic Hertzian contact between a flat surface and a spherical indent with a contact radius of $a = 1$ and $\nu = 0.3$ (z is the axis of symmetry).

3.3 Depth sensing nanoindentation

The value most commonly sought in indentation tests is a material's hardness. Hardness tests started as a way of comparing materials, testing their quality, and quantifying their properties. While traditional hardness tests and nanoindentation measure slightly different things, the purpose remains the same. In macroscopic testing a load is applied and the residual imprint left by that load is optically measured to determine the contact area. The ratio of applied load $P_{applied}$ to residual contact area $A_{residual}$ gives the hardness H_{macro} :

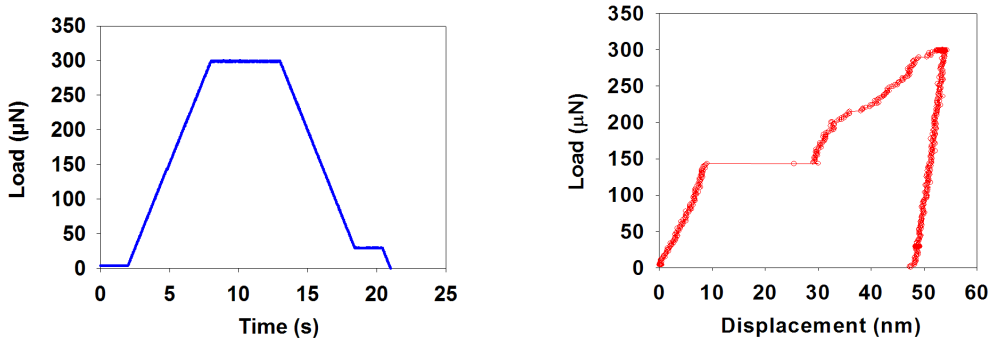
$$H_{macro} = \frac{P_{applied}}{A_{residual}} \quad (3.16)$$

This hardness value is the plastic response of the material to applied load. The measurements of the residual contact area are only as good as the resolution of the imaging technique. There becomes a size scale beyond the capabilities of optical microscopy, where SEM or SPM would be necessary to image the indent. On the nanometer scale it is no longer convenient or time efficient to make measurements in this manner with either of these techniques.

One of the reasons nanoindentation was developed was to test the mechanical properties of thin films. Microindentation available in the early 1980's did not allow for loads low enough to isolate the properties of the film. The guideline within the field is that indentation depth should only be about 10% of the total film thickness to ensure that only the film is tested without influence from the substrate. An optical technique at this scale is not viable. It is difficult to accurately apply such small loads and the uncertainty in the measured area is too high. For a 1 μm indent this uncertainty could be as high as 100% [138]. New methods of testing, that accurately apply loads and measure the displacement, meant that visual inspection of the indented area was no longer necessary. With the old analysis techniques only the residual plasticity was measured. Now the initial elasticity as well as the elastic recovery that occurs during unloading are recorded. In order to determine the desired material properties such as hardness, new analysis techniques must be developed.

Nanoindentation utilizes continuous measurement of the displacement as the load is applied and then removed. Figure 3.9a shows a typical loading profile. The corresponding load displacement curve for this load function is given in figure 3.9b. Before the indentation test begins the imaging¹ gains are removed and no load is applied to the tip, in order to measure any drift in the transducer. The

¹for details of imaging capability of instrumented nanoindentation systems see section 3.4.1



(a) Loading profile for typical indentation test. (b) Load displacement curve made by using the load function in (a).

Figure 3.9: Loading profile and the resulted load displacement curve. (a) In loading profile the transducer drift is observed in the first 5 seconds, followed by loading, then a hold at maximum load for few seconds, and finally gradual unloading to 10% of the maximum load. (b) Load displacement curve on electrochemically polished nickel made by using the given load function of (a).

displacement is measured as a function of time, and the remainder of the test is corrected by this measured drift rate. The indentation test will only begin if the probe drift is below a specified level (typically <0.1 nm/s). The loading portion of the curve measures the material's resistance to penetration. The loading slope is primarily dependent upon the sample material and the shape and size of the indenter. The hold segment at maximum load is used to determine if there is time dependent plasticity or creep in the material. The second holding time at 10% of the maximum load is to separate the displacement due to the creep from the thermal drift. The creep rate in metals is usually depending on the stress, given by the following equation:

$$\frac{\partial \epsilon}{\partial t} = C \sigma^m e^{-\frac{Q}{kT}} \quad (3.17)$$

where C is a constant dependent on the material, microstructure and the particular creep mechanism, exponent m is dependent on the creep mechanism, Q is the activation energy of the creep mechanism, σ is the applied stress, k is Boltzmann's constant, and T is the temperature. In the equation 3.17 the value of m is in the range between 2 to 6 depending on the mechanism of the creep. That is, the creep rate decreases exponentially with decreasing the applied load (stress). Therefore if the penetration at maximum load (stress) is due to the creep, obviously at the 10% of the maximum load (stress), the value of the dis-

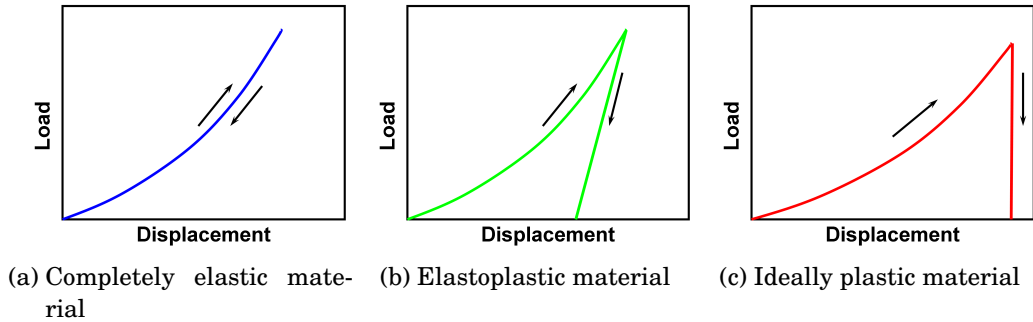


Figure 3.10: Representative load-displacement data demonstrating differences in elasticity (a) Completely elastic material. (b) elastoplastic material. (c) ideally plastic material.

placement should be exponentially smaller. Whereas in the case of the thermal drift the amount of displacement is independent of the applied load (stress). In this way by comparison of the displacement at this two holding times, it is possible to exclude the thermal drift from creep. Time dependent plasticity will be discussed further in Section 3.6.

An elastically deformed material will retrace the loading curve upon unloading (Figure 3.10a). An elastoplastic material response is shown in Figure 3.10b, the material displays a mixture of elastic and plastic behavior. A primarily plastically deformed material will have almost no elastic recovery (Figure 3.10c). A material that behaves in an entirely elastic manner, rubber for example, will have an indeterminate hardness using traditional indentation methods, because there would be no residual impression. Depth sensing indentation on the other hand will provide valuable information on the elastic properties of the material. Since measuring the entire response of the material gives a more complete picture of its mechanical behavior.

Different analysis techniques have been developed for each segment of the loading profile. The loading portion requires models that include both elasticity and plasticity. The hold portion is commonly used to investigate creep behavior. The unloading portion of the curve can be treated as the elastic recovery of the material. In practice, analysis of the loading and holding portions of the curve require numerous assumptions about the relationship between plasticity and contact area. The most common analysis techniques utilize the unloading portion of the indentation data, primarily because they are the least model dependent.

Nanoindentation analysis is based upon the assumptions that the radius of curvature of the indenter is small compared to that of the specimen's surface

and the dimensions of these objects are large compared to the contact area. By establishing that the size of the indent is small compared to the whole system, we can isolate the stresses and strains caused by indentation from those of the specimen, such as attachment of the sample, surface constraints (boundaries), and geometry. We also assume that the contacting bodies are frictionless, that only the normal force is transmitted to the sample.

Over the years the methods of interpreting load-displacement data have been improved. The investigation of the role of elasticity in material deformation began well before the reduction in component scale demanded a new testing method. In 1961 Stillwell and Tabor were looking at elastic recovery of conical indentations and how they are related to mechanical properties [135]. Armstrong and Robinson were measuring materials' combined elastic and plastic deformation during indentation testing in 1974 [138]. In 1981 Lawn and Howes utilized elastic recovery in hardness measurements [139]. The first researchers to utilize the unloading portion of the load-displacement curve as a means of determining the contact area were Bulychev, Alekhin, Shorshorov, and Ternovskii in 1975 [138]. Doerner and Nix [138] were the first to use this technique in the millinewton load range, where the indents become too small to measure accurately by optical means. Oliver and Pharr slightly modified this technique in 1992. A similar analysis technique was developed by Field and Swain that concentrated on spherical indenters [138]. In 1993 these last two techniques were shown to be equivalent [138].

All these techniques start by examining the idealized elastic contact of a rigid sphere and a flat surface. In 1965 Sneddon [135] published the derivation of an expression for the contact between a rigid indenter of various geometries and an isotropic elastic half space. He defined the contact stiffness S as the increment of load δP divided by the increment of displacement δh :

$$S \equiv \left. \frac{\delta P}{\delta h} \right|_{elastic} \quad (3.18)$$

This ratio can be related to the initial unloading portion of the force displacement curve, with the assumption that the initial unloading is entirely elastic. Although most materials deform in both an elastic and plastic manner, most recovery upon unloading is thought to be elastic in nature. The residual deformation is the plastic response, related to the final depth h_f . The tip is also assumed to be ideally rigid; any elastic response is accounted for in the reduced modulus E_r . The contact stiffness can be written as a function of modulus and

projected contact area A_c at maximum load [135]:

$$S = \frac{2}{\sqrt{\pi}} E_r \sqrt{A_c} \quad (3.19)$$

This relationship is called the conical Sneddon stiffness equation. The area of contact is based upon the tip shape¹. From this equation we see that the unloading slope is directly related to the modulus of the material and the square root of the area of contact.

Doerner and Nix [138] were the first to establish a commonly used method for determining hardness and modulus from force displacement curves on the nanometer scale based on these principles. They assumed that the initial unloading was linear, and the intercept depth h_i was found by extrapolating the tangent at P_{max} to zero load. Hardness measurements based upon this linear extrapolation are more closely correlated to experimental data and finite element analysis for materials of well-known hardness, as compared to values attained using the depth at peak load h_{max} or the final depth h_f . Although this was a better approximation, there were still some problems with the interpretation. Oliver and Pharr [138] found that the initial unloading more closely resembled the behavior of the power law, and not necessarily linear unloading. They fit the initial portion of the unloading curve with the relation:

$$P = \alpha (h - h_f)^m \quad (3.20)$$

Where α and m are curve fitting parameters. The derivative of this power law relation with respect to h , is taken at the maximum load $P = P_{max}$, the resulting slope is equal to the contact stiffness $dP/dh = S$ of the material.

Sneddon's analysis for elastic displacement outside the contact perimeter gives the following relation:

$$h_{max} - h_c = \epsilon \frac{P_{max}}{S} \quad (3.21)$$

Where h_{max} is the maximum indentation depth, h_c is the contact depth, and ϵ is a constant that depends on the shape of the indenter. For a spherical indenter $\epsilon = 0.75$. Pharr and King [138] have both shown that this relationship holds for a number of geometries: any that can be described with a function of revolution, with pyramidal shaped indenters having a very small error. Therefore, when using a three-sided pyramidal Berkovich indenter, a spherical indenter is a sufficient approximation.

¹For further information regarding the relation between the shape of the tip and the area of contact see section 3.4.2

The maximum load over the stiffness term in Equation 3.21 can be rewritten in terms of displacement:

$$h_c = h_{max} - \epsilon(h_{max} - h_i) \quad (3.22)$$

Where h_i is the intercept depth, determined by extrapolating the initial unloading slope to $P = 0$. The intercept depth is an underestimate for the contact depth. Figure 3.11(a) is a schematic of the indenter and material cross-section and Figure 3.11(b) is the corresponding load displacement image.

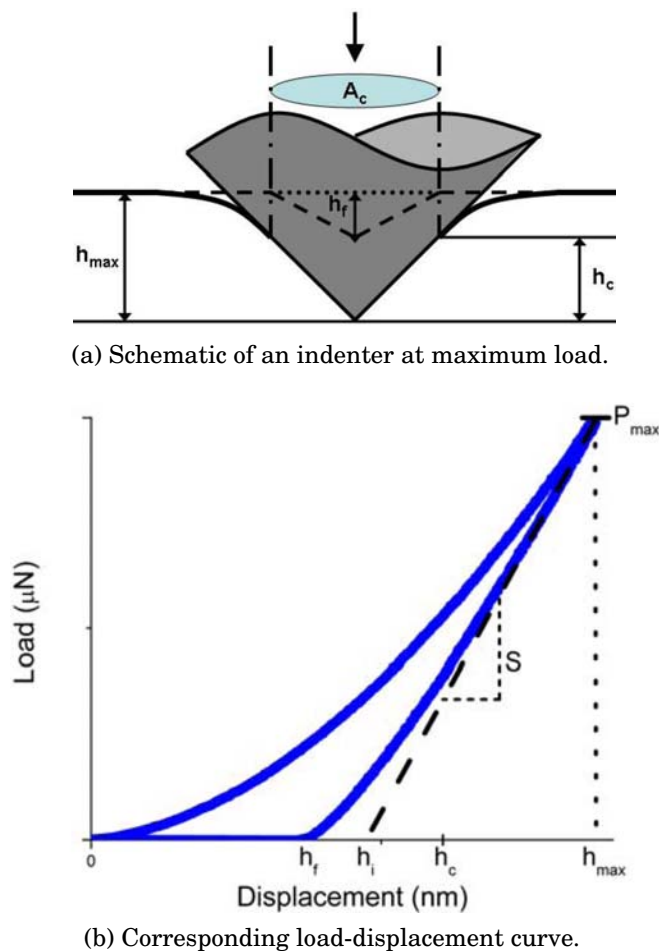


Figure 3.11: Schematic of an indenter at maximum load P_{max} with an associated total depth of h_{max} . The contact between the indenter and the surface at maximum load is defined by depth h_c , with a corresponding projected area of contact A_c . The dashed line, with a final depth of h_f , indicates the sample profile after the load has been removed (a). Corresponding load-displacement curve, indicating the final depth h_f , the intercept depth h_i , the contact depth h_c , and the maximum depth. The slope of the tangent at maximum load is the dashed line. The stiffness S is the slope of this line (b).

In order to make these calculations, a very accurate description of the tip's projected area of contact, as a function of depth, is necessary. The tip area function is experimentally determined. The particulars of these measurements will be discussed in the next section (Section 3.4.2). The projected area of contact for each indent is the solution to the area function at $h = h_c$. Using the power law relationship for unloading and a well-defined function for the tip area, the hardness of the material can be defined as:

$$H_c = \frac{P_{max}}{A_c} \quad (3.23)$$

Where H_c is the hardness, P_{max} is the maximum indentation load, and A_c is the projected area of contact at depth h_c . It is evident from this definition that any inaccuracies in determining the depth of contact might dramatically influence the calculated hardness value. Miscalculations in the area of contact influence the applied stress, and can therefore dramatically change the calculated hardness. Section 3.6 discusses some of the ways in which the contact area can be misinterpreted.

The other material property often sought in indentation testing is the modulus of the material. There is one major assumption in the calculation of the indentation modulus: that it remains constant over all depths. The reduced modulus is calculated using the area of contact and the stiffness:

$$E_r = \frac{\sqrt{\pi}}{2\sqrt{A_c}}S \quad (3.24)$$

From here the modulus of the material can be calculated using Equation 3.3 and accepted values for the Young's Modulus and Poisson's ratio of the indenter. In the case of a diamond indenter these values are $E_i = 1140$ GPa and $\nu_i = 0.07$ respectively [140].

During indentation testing, at all scales, materials demonstrate widely varied responses to the same load, characteristic of the materials and their preparation. Small quantities of materials can behave strangely due to the unique microstructures of the size regime. Grain size, film thickness, and epitaxial stresses are a few of the scale specific features that can influence hardness testing. The size scale of nanoindentation changes some of the ways to interpret load-displacement data. A fundamental understanding of the mechanical response of a material to point contacts is necessary for further advancement of nanotechnology.

3.4 Instrumentation

Over the past 20 years a number of systems have been developed to monitor displacements of fractions of nanometers as a load is applied, held, and released. Commercially available systems are purchased by universities, research labs, and an increasing number of corporate product development labs. Most systems are load controlled. This means that there is no specified minimum depth for most instruments, the depth of penetration is material dependent. The force and displacement resolution are also important, but they can not be controlled. They are dependent upon the instrument and the location of that instrument. The resonant frequency of a building, the ability to control the temperature, even air humidity can influence the consistence of measurements. The term nanoindentation is often applied to three slightly different size scales, based upon the instrument capabilities. Starting with the largest, there are indentation tests that apply loads of milli-Newtons, causing displacements on the order of hundreds to thousands of nanometers. This is just beyond the low end of what is referred to as micro indentation. The next range, which is the group our instrument belongs to, applies loads in the range of 10's to 1000's of micro-Newtons, measuring total displacements up to 100's of nanometers. There is an even smaller scale method of indentation testing that utilizes a specialized Atomic Force Microscope cantilever as its probe tip¹. This final scale is sometimes referred to as interfacial force microscopy, but falls under the family of nanoindentation because it is making mechanical property measurements on the nanometer scale. Each of these different scales of testing has their own specific applications and instrumentation. The measurements investigate slightly different aspects of a material's mechanical response, primarily determined by the scale. There are surface features, assumptions in calculation, and other possible distortions unique to each size regime. Together they bridge the gap from microindentation to nearly the scale of atomic simulations.

3.4.1 Hysitron Triboscope

The Hysitron Triboscope is a unique and powerful instrument because it is a quantitative nanoindentation system and it has the ability to image the surface before and after indentation. It does not utilize the piezo feedback nor the Atomic Force Microscope (AFM) cantilever to perform its tests. The nanoindenter is an attachment (accessory) to a scanning probe microscope. The whole

¹The mechanical properties of the cantilever defines the available maximum force and displacement within such system

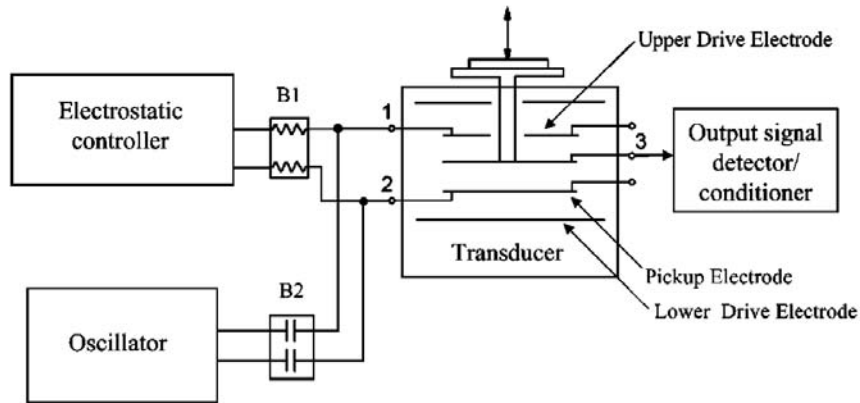


Figure 3.13: Schematic circuit diagram of the Hysitron TriboScope transducer assembly.

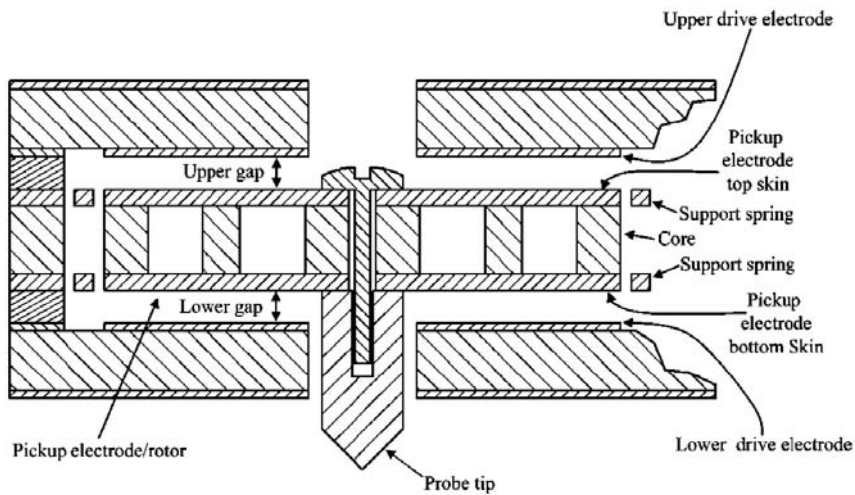


Figure 3.14: Schematic of a three plate capacitor force-displacement transducer of the Hysitron Triboscope. Voltage applied to the drive plates creates an electrostatic force with the pick-up electrode. The displacement is monitored by changes in capacitance.

electrode (the middle plate) which is spring mounted (figure 3.14), and therefore free to move up and down in the region between the two drive plates. This middle plate has a screw, which is where the tip attaches. To perform an indentation an electrostatic force is generated between the drive plates and the pickup electrode when a voltage is applied to the drive plates. The terminals labeled “1” and “2” are used to provide force that is electrostatically generated by the transducer. The electrostatic force F_{el} is proportional to the square of the Voltage V applied to the drive plate:

$$F_{electrostatic} = k_e V^2 \quad (3.25)$$

Where k_e is an electrostatic force constant (determined by the manufacturer and supplied with the transducer). The area of the plates and the distance between them determines this electrostatic force constant. Once calibrated the instrument determines the appropriate voltage profile to apply the required force profile for the specified indentation test. For displacement sensing, the two outer electrodes are driven by AC voltage that is 180° out of phase. This results in an electrostatic field whose potential varies linearly with lateral displacement, due to the close proximity of the plates. In the center this field is zero, because the two fields cancel each other out. At the location of either plate the field is proportional to the voltage applied. The middle plate or pick-up electrode assumes the potential of the position relative to the drive plates. The displacements are measured by changes in the capacitance of the stack of plates. This enables the displacement and applied load to be measured simultaneously.

In order to use the force displacement data, there are a few corrections that must be made. The electrostatic force consists of both the force applied to the surface and the force required to move the indenter further into the surface. In order to determine the applied force the spring displacement must be subtracted from the total electrostatic force.

$$F_{applied} = F_{el} - k_s h \quad (3.26)$$

The spring constant is k_s and h is the displacement of the middle plate. This spring constant can be determined simply by doing an indent in air, where the force on the sample is equal to zero.

Every instrument has a certain amount of inherent deflection occurring during testing that is directly proportional to the load. It is measured as penetration into the surface and must be corrected for. The compliance of the machine C_m consists of deflection due to the load frame, the indenter shaft and the specimen mount. At large loads for materials with a high modulus, this can account for a large portion of the displacement. The total compliance of the system C_t is the machine compliance plus that of the indented material, which is equal to one over the material stiffness:

$$C_t = \frac{dh}{dP} = C_m + \frac{1}{S} = C_m + \frac{\sqrt{\pi}}{2E_r \sqrt{A}} \quad (3.27)$$

This expression demonstrates that the total compliance can be considered as springs in series, simply adding the separate components. Combining equa-

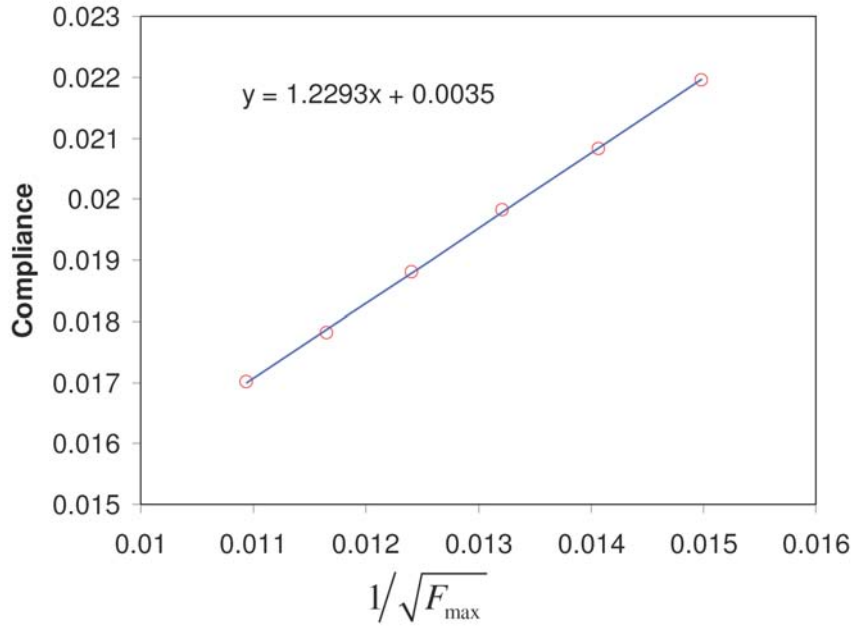


Figure 3.15: Graph of $1/S$ versus $1/\sqrt{P_{\max}}$ for a series of indents performed in fused quartz. The machine compliance is the intersection of fitted line with y axis.

tions (3.16) and (3.27), the following relationship is found:

$$C_t = C_m + \frac{\sqrt{\pi H}}{2E_r \sqrt{P_{\max}}} \quad (3.28)$$

For fused quartz, it is a fair assumption that hardness and reduced modulus are constant at large indentation depths ($h_c > 1/3$ tip radius) when indented with a Berkovich indenter, and no cracks are formed. If this assumption is made, a graph of $1/S$ versus $1/\sqrt{P_{\max}}$ for a series of indents performed in fused quartz will yield a straight line with a y intercept of the machine compliance, as shown in figure 3.15.

3.4.2 Nanoindentation tips

The probe tip is a very important part of indentation testing. The geometry and the material it is made from can dramatically influence the raw data. The material is important because of how the stiffness influences the reduced modulus and because of local adhesion that might occur between the sample and the tip. The most common shapes of indenters are spheres, flat punches, cones, and pyramids. Three types, Berkovich, Cube Corner and Conical, and their pro-

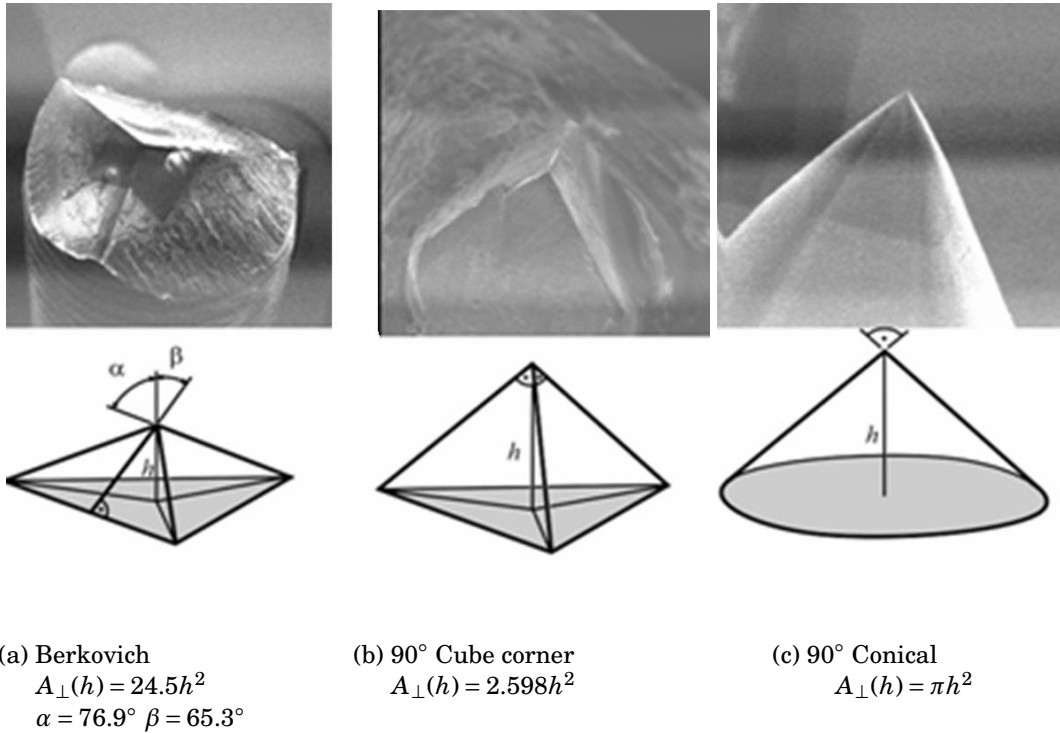


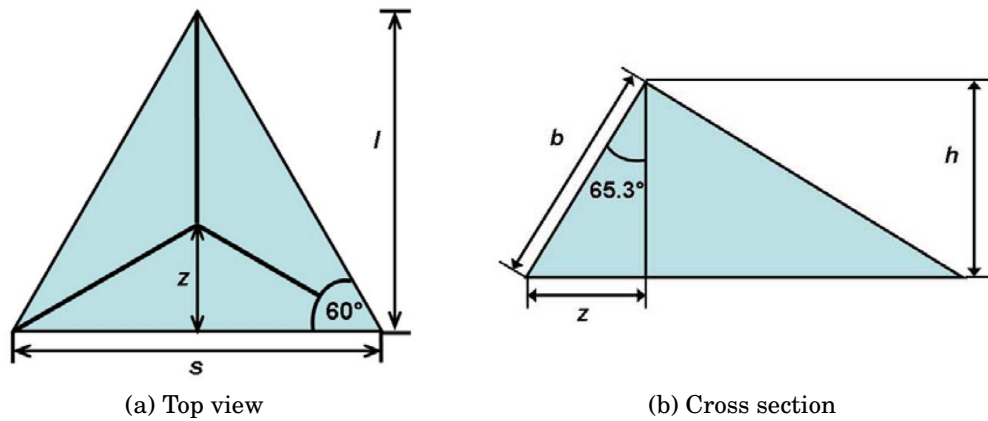
Figure 3.16: Schematic of nanoindentation probe tips and their projected ideal area A_c related to the depth h . (a) Berkovich; (b) Cube Corner; (c) Conical.

jected ideal area A_c related to the depth h are shown in figure 3.16. Each of these has its own pressure distributions, and therefore different load requirements for deformation.

In this work, a Berkovich tip is always used unless stated otherwise. Figure 3.17 is a sketch of the three sided pyramidal indenter. The Berkovich indenter has a face angle of 65.3° , which results in an equivalent cone angle of 70.32° . The face angle was chosen to give the same projected area to depth ratio of a Vickers indenter. The radius of the apex for the tips is critical because it dictates the contact area. A typical new Berkovich indenter has a radius on the order of 50–300 nm which will increase with continues use of the indent.

For depth sensing indentation accurate knowledge of the area of contact is crucial. No tip is perfect, which is why we experimentally determine the area of contact as a function of depth. The first step is the idealized function relating the projected area of contact to the contact depth, based on the equivalent cone angle. For a Berkovich indenter this is:

$$A = 24.5h_c^2 \quad (3.29)$$



$$s = 2\sqrt{3}h \tan 65.3^\circ$$

$$z = \frac{s}{2} \tan 30$$

$$l = \frac{\sqrt{3}}{2}s$$

$$b = \frac{s}{2\sqrt{3} \sin 65.3^\circ}$$

$$h = \frac{s}{2\sqrt{3} \tan 65.3^\circ}$$

$$A_{proj} = 3\sqrt{3}h^2 \tan^2 65.3^\circ = 24.56h^2$$

Equivalent cone angle: 70.32°

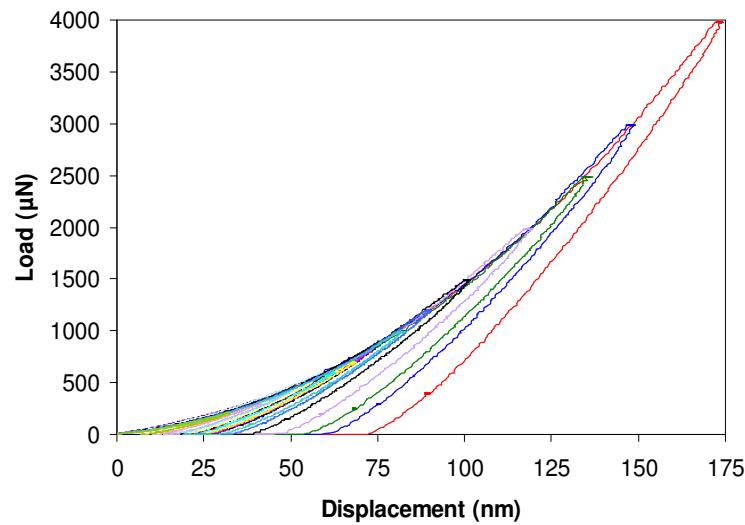
(c) Equations for dimensions of tip

Figure 3.17: Schematics of a Berkovich indenter with dimensions. (a) Top view, (b) Cross Section, and (c) Equations for dimensions of tip indicated in schematics.

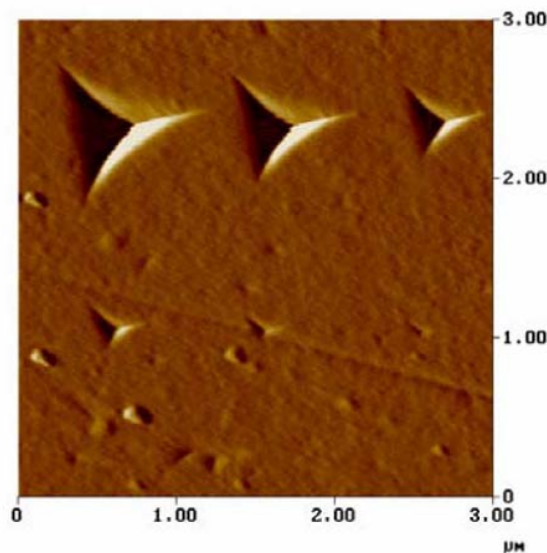
The area of contact is related to the material contact stiffness. Equation 3.19 can be rewritten as:

$$A_c = \frac{\pi}{4} \left(\frac{S}{E_r} \right)^2 \quad (3.30)$$

This enables the contact area to be determined based upon measured stiffness of a material with a known reduced modulus. Fused quartz is the sample material used in tip calibrations. It is used because it has an extremely consistent measured modulus of 72 GPa. The reduced modulus for a diamond indenter and



(a) Load displacement curves



(b) Indents with different loads in fused quartz

Figure 3.18: Indentation tests on fused silica, done at numerous loads (a). Surface image of fused quartz, done by indentation probe after testing, showing indents of a variety of sizes (b). Tests like these are used to create a tip area function.

fused quartz is 69.6 GPa. Its amorphous structure enables the consistent deformation behavior of the material. Fused quartz does not display some of the discrepancies between the actual and the calculated contact area, sometimes displayed in metals. For example it does not experience distortion in the contact area that is caused by piling-up or sinking-in. Figure 3.18a shows numerous load-displacement plots done on fused quartz, and Figure 3.18b is an image of

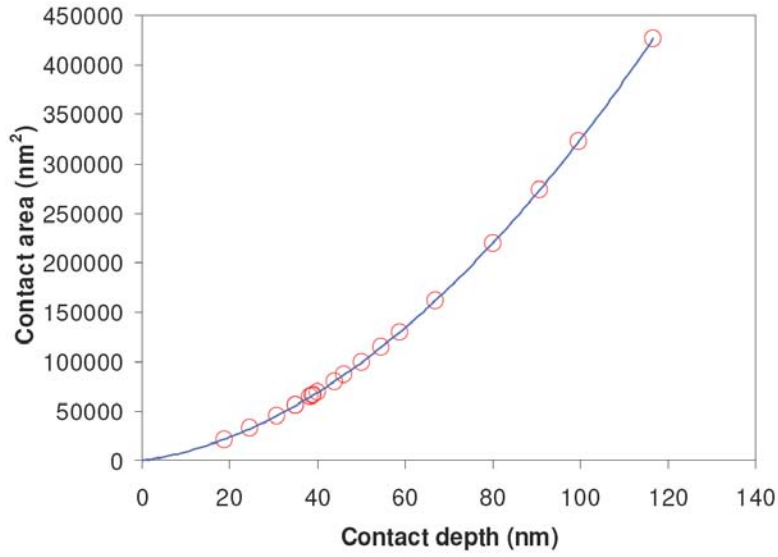


Figure 3.19: Area function curve determined from load displacement curves given in figure 3.18b.

a typical fused quartz surface after indentation testing. Figure 3.18a demonstrates the load displacement behavior of this well behaved material. There are numerous indents made at each load (2000, 1000, and 500 μN). Some of the tests were even run on different days. The material is extremely repeatable; the loading behavior is identical in every trial and the depth of penetration is consistent for a given load. This demonstrates the consistent nature crucial for accurate tip shape calibration. Indentation tests are done over the desired range of contact depth. The stiffness is taken from each of these indents and a corresponding projected area of contact is calculated using equation 3.30. The computed projected area of contact is plotted as a function of contact depth. The points are then fit to a fifth order polynomial given by the following equation:

$$A_c = C_0 h_c^2 + C_1 h_c + C_2 h_c^{1/2} + C_3 h_c^{1/4} + C_4 h_c^{1/8} + C_5 h_c^{1/16} \quad (3.31)$$

Where C_0 is equal to 24.5, and the rest are curve fitting parameters. The resulted area function curve for the load displacement curves given in figure 3.18b is shown in figure 3.19.

3.5 NI-AFM in liquid

One of the reason for great success of different SPM techniques in different fields of science and technology, was the ability of these techniques in imaging

surfaces under ambient condition with very high spatial resolution [113]. While previously adopted high resolution techniques like SEM and TEM work only in vacuum or very restricted pressures, the SPM is able to work even inside a fluid. Sonnenfeld et al. made the first STM experiments in liquid [141] and electrolyte under electrochemical control [142] only five years after the invention of the first STM by Gerd Binnig and Heinrich Rohrer [143]. Today electrochemical STM (EC-STM) is a widely used standard method. Development of AFM in liquid [144] and the electrochemical AFM (EC-AFM) [145] also happened shortly after introduction of first AFM [146].

High spatial nanometric resolution of SPM's, in conjunction with possibility to use them in ambient condition or even immersed in liquid makes them a perfect candidate for environmental degradation studies like corrosion [147, 148] and hydrogen embrittlement [10].

Since invention of NI-AFM [149, 150] only some attempts were made to perform nanoindentation inside solution. Seo et al. used NI-AFM in conjunction with an electrochemical setup to study the mechanical properties of passive films on iron [151, 152, 153, 154], titanium [155, 156, 157] and tantalum [158].

In the next sections, the complexities in conducting NI-AFM inside liquid will be described.

3.5.1 Complexities of NI in liquid

In 1961 Kramer and Demer reported the first microhardness measurements inside liquid [159] however due to the low resolution of the technique it was not become popular. By introduction of instrumented nanoindentation technique Venkataraman et al. [160] made the first indentation experiments in liquid, by putting a drop of dilute HCl on the surface of iron. Mann and Pethica [161] made the first indentation experiments on fully immersed samples. However since the exact measurement of the force is a requirement during NI-AFM experiments there are several points which should be considered during a nanoindentation experiment inside solution. In contrast to EC-AFM where due to the remote force sensing method the whole tip could be immersed in the solution, in NI-AFM the complex force transducer (figure 3.14) should be protected from the solution. Therefore only a part of the tip would be immersed in the solution. Usual nanoindentation tips are made of a sharp diamond tip with a known geometry brazed to a steel shaft. For nanoindentation in fluid there are special fluid cell tips available. These tips have an extended shaft (4mm in length, figure 3.20) made out of titanium that allows the end of the tip to be completely

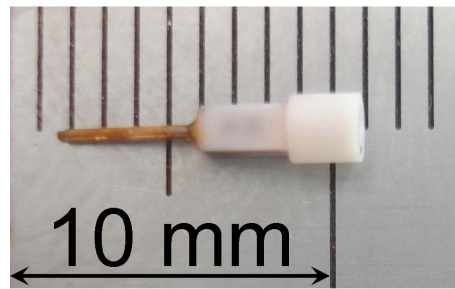


Figure 3.20: Special fluid cell tip for nanoindentation inside liquid

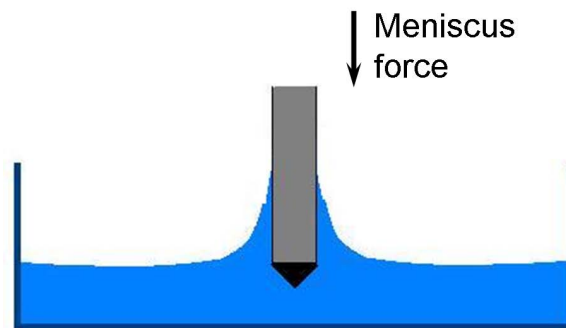


Figure 3.21: Meniscus force acting on the nanoindenter shaft during nanoindentation inside the liquid

immersed in a fluid, while the tip holder and transducer remain in the air. This will result in different variable forces acting on the tip during the experiment. These forces, which will be explained in the next sections, should be considered during the experiments and compensated.

3.5.1.1 Meniscus force

The meniscus force is the force that arises due to the surface tension in a liquid-meniscus, which spans and connects the tip shaft and surface of the solution. The meniscus force in NI-AFM inside a liquid is schematically shown in figure 3.21. This force is depending on the contact angle (wetting angle) shown in figure 3.22. The wetting of a solid with a liquid, where a gas is the surrounding medium, is dependent on the relation between the interfacial tensions (liquid/gas, liquid/solid and solid/gas). The ratio between these tensions determines

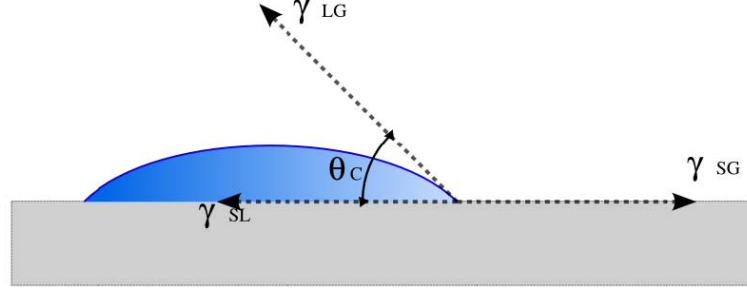


Figure 3.22: Representation of wetting angle and its dependence on interfacial energies

the contact angle θ_c between a liquid and a given surface as follows:

$$\cos\theta_c = \frac{\gamma_{SL} - \gamma_{SG}}{\gamma_{LG}} \quad (3.32)$$

where γ_{SL} is the solid-liquid interfacial energy, γ_{SG} is the solid-gas interfacial energy, and γ_{LG} is the liquid-gas interfacial energy or the liquid surface tension. The meniscus force acting on the nanoindenter tip shaft could be calculated as follows:

$$F_m = \gamma_{LG}L \cos\theta_c \quad (3.33)$$

where F_m is the meniscus force, L is the circumference of the tip shaft. The manufacturers of nanoindentation tips are reducing the diameter of the tip shaft as much as possible to minimize the meniscus forces that will be present where the tip penetrates the fluid. Considering 700 μm shaft diameter, and $72 \times 10^3 \text{ N/m}$ surface tension of the pure water we can calculate the meniscus force as a function of contact angle, which is shown in figure 3.23. Figure 3.23 shows that the value of the meniscus force can drastically influence the nanoindentation experiment.

3.5.1.2 Buoyant force

When a rigid object is submerged in a fluid, there exists an upward force on the object that is equal to the weight of the fluid that is displaced by the object. This force is called buoyant force. For an immersed volume of V the buoyant force is given by:

$$F_b = \rho_L V g \quad (3.34)$$

where ρ_L is the density of the liquid, and g is the gravity acceleration constant. In the case of the NI-AFM inside liquid the buoyant force acting on the tip is depending on the immersion depth of the tip, and the density of the electrolyte.

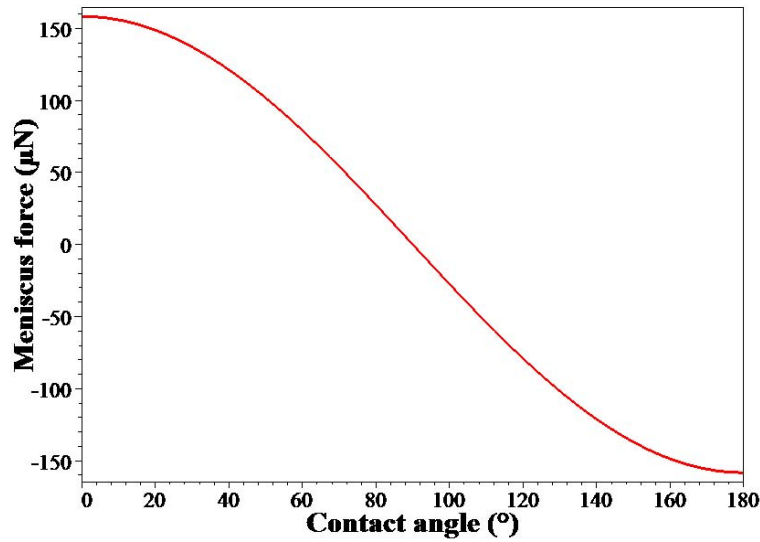
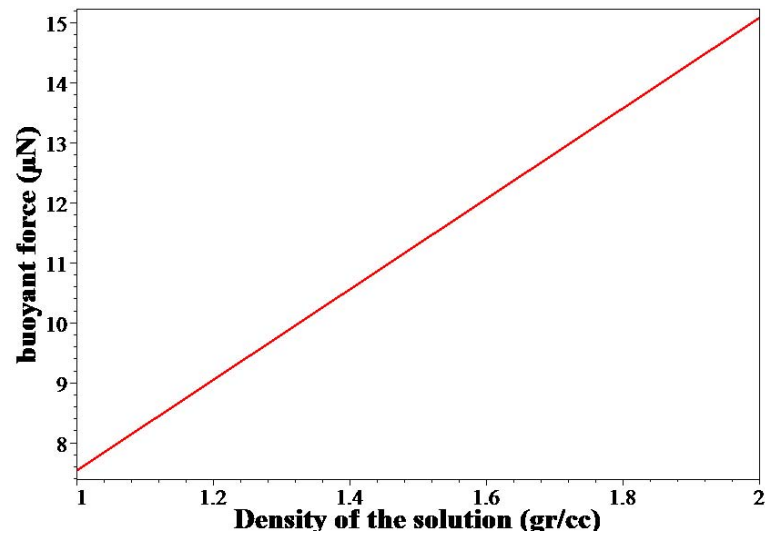


Figure 3.23: Change in the meniscus force with contact angle, calculated for the case of pure water and shaft radius of 700 μm .

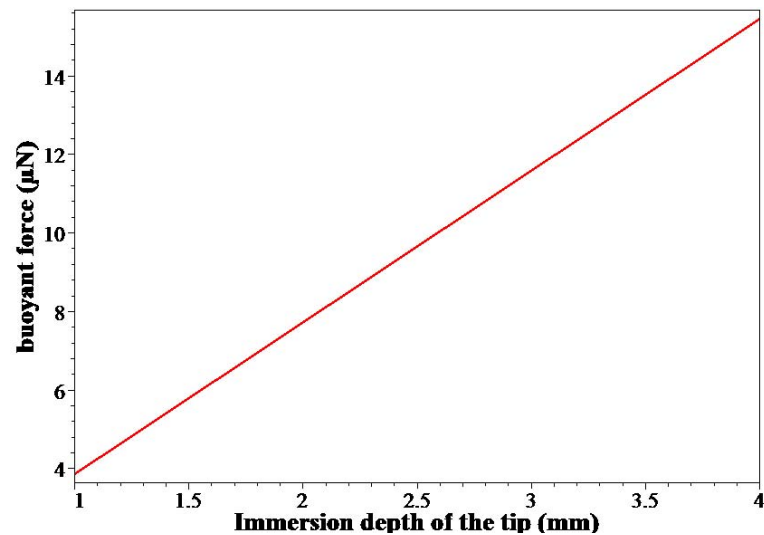
The dependence of the buoyant force on the density of the solution is shown in figure 3.24a for 2 mm immersed length of the tip. For a constant density of 1 gr/cc (ρ_{water}) the relation between the buoyant force and the immersion depth of the tip is shown in figure 3.24b. Here our attempt is not to measure the exact meniscus or buoyant force but only to have a feeling of their approximate values and their dependence on different parameters.

3.5.2 Controlling the forces acting on the tip

Under the static condition buoyant and meniscus forces acting on the tip can be balanced by the springs holding the tip. However they are resulting in a large displacement of the center plate of the transducer (figure 3.14) which should be set back to the equilibrium position by adjusting the controller of the system. This is the easy part of the job however during the engaging process of the tip there is large vertical movements of the tip which disturb the equilibrium of the forces acting on the tip. They should be dynamically controlled during the engaging process by interrupting the procedure and adjusting the controller several times. During the performance of the NI-AFM inside liquid, evaporation or changes in concentration of the liquid as well as any change in the surface condition of the tip shaft results in the variation of these forces which will respectively influence the experiment. This sometimes may result in crashing of the tip into the surface or losing the contact to surface. Therefore, sometimes it is necessary to stop the experiment in intervals and re-zero the forces on the tip.



(a) Buoyant force as a function of the solution density for 2 mm tip immersion depth



(b) Buoyant force as a function of the tip immersion depth for a solution density of 1 g/cm^3

Figure 3.24: Dependence of the buoyant force on the density of the solution (a) and the immersion depth of the tip (b).

3.6 Indentation phenomena

In the previous section we have discussed idealized elastic and plastic behavior and the analysis methods used to calculate material properties from the displacement that occurs as a load is applied. A description of the tools necessary to make these measurements has also been given. Many different things, however, can happen under an indenter. Many of these violate the rather restrictive

assumptions of the previously mentioned models used to interpret nanoindentation load-displacement data. Many are related to phenomena in the sample that we wish to investigate. Others may, for any given test, be phenomena that prevent us from obtaining the information we seek. In order to interpret nanoindentation data, familiarity with the pertinent phenomena for a given sample is an absolute necessity. In this section, many of the important phenomena which may arise in a sample during nanoindentation are described. We have (somewhat arbitrarily) divided these phenomena into two categories, geometry-based and material-based phenomena, which will be discussed in next sections.

3.6.1 Geometry-based phenomena

Geometry-based phenomena are those which arise from the shape of the sample or the indenter. Another source of the geometry-based phenomena is the superposition of different materials in the sample. Usually we can control to some extent the geometry-based phenomena during preparation of the sample or selection of the tip. Three main geometry-based phenomena which are extensively discussed in literature are surface roughness, inhomogeneities in material, and size effect. They will be briefly reviewed in the next sections.

3.6.1.1 Surface roughness

Real surfaces are never ideally flat. Often there are even a variety of scales to the surface modulations. On a macroscopic scale, roughness has little effect on indentation testing, provided the indent is large compared to the asperity size as shown in figure 3.25a. However in the opposite case, when the asperity size is large compared to the indent, no statements about the mechanical properties are possible. This is due to the lack of a well defined contact geometry as shown in figure 3.25b. Traditionally this has meant that the finish of the surface and the indenter have not been a significant concern. In the nanometer regime care must be taken to identify the influence of roughness of different frequencies. Many of the surface modulations are significantly larger than the area of interest; hence locally it can be approximated as flat. But there are often surface features on the same order and even smaller that influence the images or experiments being performed. The contact between two bodies is not only controlled by the material properties (elastic modulus and hardness) but by topographical properties as well. Three parameters of the surface also play an important role in the contact of two engineering samples. These are the surface density of the asperities, the standard deviation of the height distribution, and the mean ra-

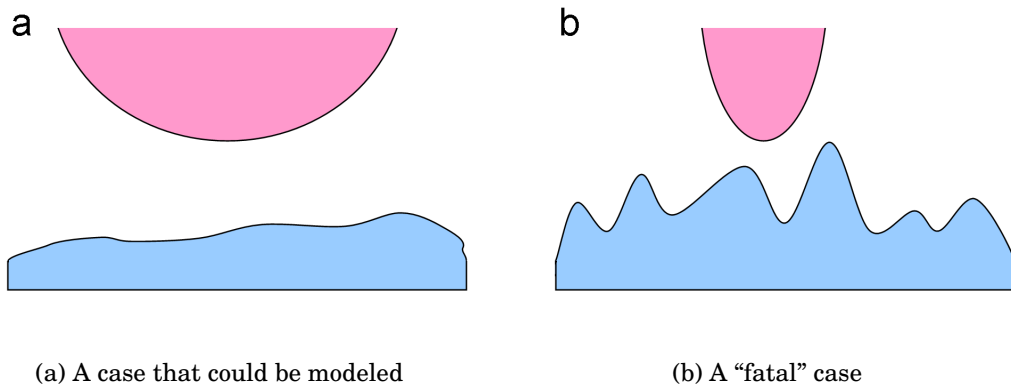


Figure 3.25: Different cases of ratio of lateral dimension of tip to the lateral dimension of surface roughness. (a) represents a case that could be modeled; whereas (b) represents a “fatal” case in which no statements about the mechanical properties are possible due to the lack of a well defined contact geometry.

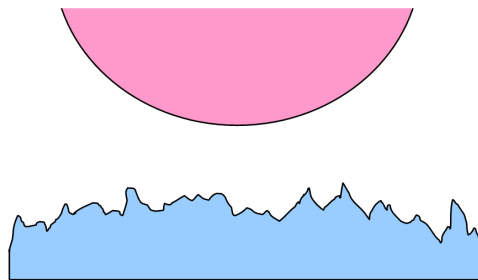


Figure 3.26: Schematic of the non-uniform contact between an indentation tip and a rough surface. The over estimate in contact area compared to that assumed based on displacement will lead to increased localized stress, generating greater deformation, resulting in an underestimate of hardness.

dus of the asperity [135]. In nanoindentation the roughness can lead to significant errors in the calculated contact area. Depth sensing indentation analysis techniques are based on Sneddon elastic contact model, which states that there is a single point of contact [135]. Figure 3.26 demonstrates how a rough surface can cause numerous points of contact with an indenter. The non-uniform contact increases the localized stress at the points of intersection. Therefore the plasticity starts from the surface with inhomogeneous dislocation nucleation¹

¹see section 6.1 for more information on homogeneous dislocation nucleation

deforming the material to a greater depth at relatively low loads. This can result in a greater displacement and lower calculated hardness for a rough surface compared to a smooth one.

SPM is a very powerful tool, in part due to the digital nature of the data. The digital format enables extensive statistical analysis of the surface. Quantification of the surface can be achieved through height distribution analysis and identification of periodic feature wavelengths. Any mathematical method used to calculate hardness will be influenced by imaging artifacts in the data collection. The tip radius is often sighted as a filter for high frequency component of surface topography. There is also usually a planar artifact caused by the fact that the tip and surface are almost never perfectly perpendicular. There are also instrumentation issues such as drift and non-linearity in the motion of the piezoelectric scanner. Kiely and Bonnell [162] have done a comparison of different mathematical treatments that quantify surface topography, pointing out many of the attributes and limitations, as well as the influence of data collection issues. They suggest many ways to ensure that the calculated roughness values are truly representative. Roughness characterization needs a description of the length scale, the size of the image in relation to the largest feature size, and the processing performed on the image, in order to have a complete picture of what the value means.

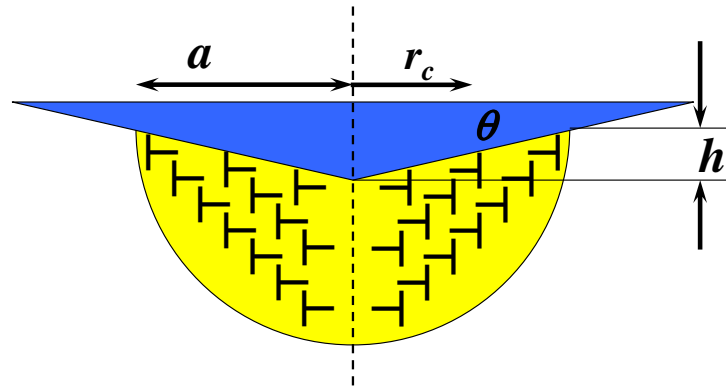
3.6.1.2 Inhomogeneities

In principle the term “inhomogeneities” covers a large number of cases. In fact all deviations from the ideal homogeneous half-space fall in this category. Examples are: Samples that show a contamination layer, a simple thin film, a multi-layered structure, a gradient layer, samples that consist of a multi-phase material or a material that has particles embedded in a matrix. Durst et al. [120] did extensive finite element simulations of conical indentations in two-phase elastic-plastic materials to investigate the influence of the shape and the aspect ratio of particles embedded in a matrix material on the deformation behavior and hardness during depth-sensing indentation. The simulations were compared with indentation experiments in precipitation hardened nickel-base superalloy. In the studied alloys, the matrix formed channels with a thickness of about 100 nm around the precipitates with diameters of about 500 nm. The simulations explained an experimentally observed transition from particle to matrix deformation behavior during indentation. Depth limits in hardness testing in particle-matrix systems were evaluated. Depending on the aspect ratio, soft and hard particles were tested reliably up to a normalized contact radius of

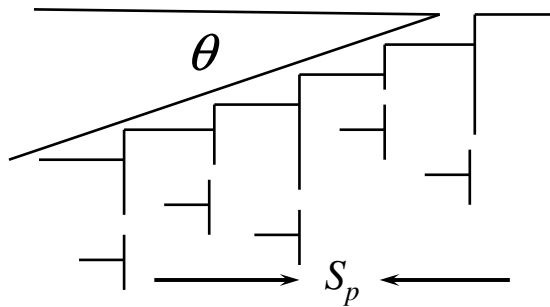
about 70% particle diameter.

3.6.1.3 The indentation size effect

That the hardness decreases with increasing indentation size is known as the indentation size effect (ISE), which has been observed in numerous nanoindentation experiments on various materials [163]. This decrease is believed to be associated with the geometrically necessary dislocations (GNDs) induced by imposed strain gradients. Nix and Gao [164] successfully modeled the ISE for crystalline materials by considering the density of GNDs around a conical indenter. The Nix and Gao's model has become one of the commonly cited treatments of the ISE. In the Nix and Gao's model, it is assumed that the indentation



(a) Simplified plastic zone during nanoindentation



(b) Relation between the GNDs and the indentation depth

Figure 3.27: Geometrically necessary dislocations created by a rigid conical indentation. The dislocation structure is idealized as circular dislocation loops. a is the contact radius, r_c the radius of the circular loops, θ the angle between the surface of conical indenter and the plane of the surface, h the indentation depth, s_p the spacing between individual slip steps on the indentation surface [164].

is accommodated by circular loops of GNDs with Burgers vector normal to the surface, as shown schematically in figure 3.27. Assuming that the individual dislocation loops are spaced equally along the surface of the indentation gives

$$\tan\theta = \frac{h}{a} = \frac{b}{s_p} \quad (3.35)$$

$$s_p = \frac{ba}{h} \quad (3.36)$$

where s_p is the spacing between individual slip steps on the indentation surface, b the magnitude of the Burgers vector, h the indentation depth, a the contact radius, and θ the angle between the surface of the indenter and the plane of the sample surface, as shown in figure 3.27. The total line length λ of dislocation loops necessary to form the shape of the conical indenter is

$$\lambda = \int_0^a \frac{h}{ba} 2\pi r_c dr_c = \frac{\pi ha}{b} = \frac{\pi \tan\theta}{b} a^2 = \frac{\pi}{b} \cdot \frac{h^2}{\tan\theta} \quad (3.37)$$

It is also assumed that all of the injected loops remain within a hemispherical volume V_d defined by the contact radius

$$V_d = \frac{2}{3}\pi a^3 \quad (3.38)$$

So the density of the GNDs ρ_G is given by

$$\rho_G = \frac{\lambda}{V_d} = \frac{3h}{2ba^2} = \frac{3\tan^2\theta}{2bh} \quad (3.39)$$

By taking Tabor's factor to be 3 and applying the von Mises flow rule and the Taylor relation, the relation between hardness and dislocation density is expressed as:

$$H = 3\sigma = 3\sqrt{3}\tau = 3\sqrt{3}\alpha_1\mu b\sqrt{\rho_G + \rho_s} \quad (3.40)$$

where σ is the normal stress, τ the shear stress, α_1 a constant, μ the shear modulus, and ρ_s the density of statistically stored dislocations which determines the hardness H_0 in the absence of any GNDs:

$$H_0 = \alpha_1\mu b\sqrt{\rho_s} \quad (3.41)$$

From these equations, the measured hardness H related with the indentation depth h can be described as

$$\frac{H}{H_0} = \sqrt{1 + \frac{\rho_G}{\rho_s}} = \sqrt{1 + \frac{h_0}{h}} \quad (3.42)$$

where h_0 is a length scale depending on ρ_s through H_0 . Rewriting this equation as

$$H^2 = H_0^2 \left(1 + \frac{h_0}{h}\right) \quad (3.43)$$

a linear relationship would be found in the plot of H^2 vs. h^{-1} .

In the Nix and Gao's model, it is assumed that all the GNDs are contained in a hemisphere, namely the plastic zone, with a radius equal to the contact radius a . However, GNDs will spread beyond the hemisphere assumed due to the strong repulsive force between GNDs for very small indentation depth [163]. It means the actual plastic zone is larger than that described in the Nix and Gao's model. This has been confirmed by the overestimation in hardness by the Nix and Gao's model at small indentation depths observed in several experiments [163, 165], where the radius of plastic zone was taken to be $f \cdot a$, $f \geq 1$ to correct the model at small indentation depths.

3.6.2 Material-based phenomena

Material-based phenomena are those which arise from the intrinsic behavior of the material being tested. Aspects of the material and its fabrication method may significantly influence the observed mechanical behavior during nanoindentation. Material-based phenomena may be used to extract further information about mechanical behavior of materials. Since invention of the nanoindentation technique lots of experimental works has been done to use nanoindentation technique for characterization of materials using material-based phenomena [166, 167, 168, 134, 169]. In the next sections material-based phenomena will be briefly reviewed and some of experimental efforts on using them for further characterization of materials will be cited.

3.6.2.1 Pile-up and Sink-in

At a particular depth of penetration the contact area is dependent not only upon the tip shape, but also on the elastic properties of the material. Materials with limited elasticity accommodate the volume of the indenter by plastic flow of the material, eventually piling-up around the tip. Elastic materials accommodate

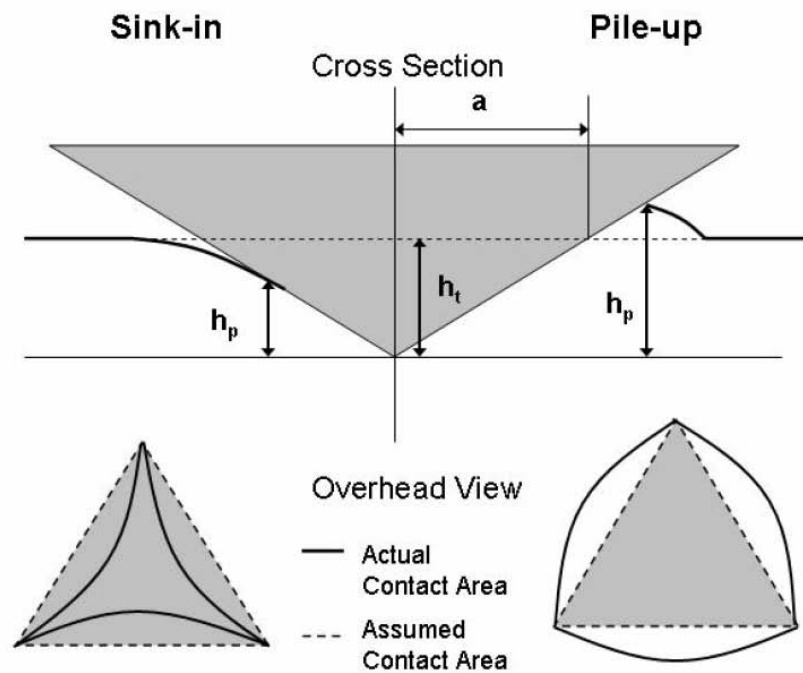


Figure 3.28: Schematic representation of pile-up and sink-in. Top picture is a cross-section of the indenter at maximum load. The radius of the projected area of contact a based upon displacement is an overestimate in the case of sink-in and an underestimate for materials that pile-up. This is easily visualized by the overhead view, where the assumed contact area is indicated by dotted lines while the actual contact area is indicated by the solid lines.

the volume of indenter by longer range elastic deformation. In such cases the material appears to sink-in around the tip. Figure 3.28 is a schematic of these two situations shown in cross section and a top view. The left-hand side of the image shows sink-in, or a reduction in contact area, while the right side shows pile-up which can significantly increase the contact area. These figures demonstrate that the extent of elastic deformation can dramatically change the contact area from that predicted by the total displacement of the probe. The Oliver and Pharr method produces reasonable mechanical property values for most materials [170]. Since the analysis technique is based on idealized elastic contact, which predicts material to be drawn downward during contact, the Oliver and Pharr method is a good approximation for materials that experience sink-in. The influence of pile-up is more pronounced on property calculations.

Bolshakov and Pharr [171] did extensive finite element analysis on the influence of material properties on the shape of deformation zone during simulated indentation testing. In systems that demonstrated pile-up they measured differences of up to 60% between the calculated contact area and the actual contact area. They found that only materials that did not work-harden (pre-work hardened materials for example) experienced pile-up. In order to quantify the amount of elastic recovery in a system they utilized the ratio of the final depth h_f over the maximum depth h_{max} . For entirely elastic material the ratio would be equal to zero, and for a purely plastic response the ratio would be equal to one. All materials with a ratio below 0.7 experience sink-in, regardless of their ability to work-harden. Materials with an h_f/h_{max} value above 0.7 experienced pile-up. The amount of pile-up corresponds to the size of the plastic zone, or the load applied.

Materials that do not experience significant strain hardening, for examples those that have already been strain hardened, have a plastic zone that is hemispherical in shape. The deformation zone is dependent upon the ratio of the elastic modulus to the yield stress E/σ_Y [138]. When E/σ_Y is large the plastic zone often extends beyond the area in direct contact with the tip. When additional plasticity occurs near the indenter, pile-up occurs. When the E/σ_Y ratio is small the deformation to accommodate the tip is more localized. In materials that do experience strain hardening, the yield strength changes as a function of deformation. This is why in strain hardening materials the plastic zone extends into the material, and the radius of deformation is reduced. The change in yield strength means the material at the edge of the plastic zone is softer than directly under the tip. The additional volume of the tip then can be accommodated without plastic flow.

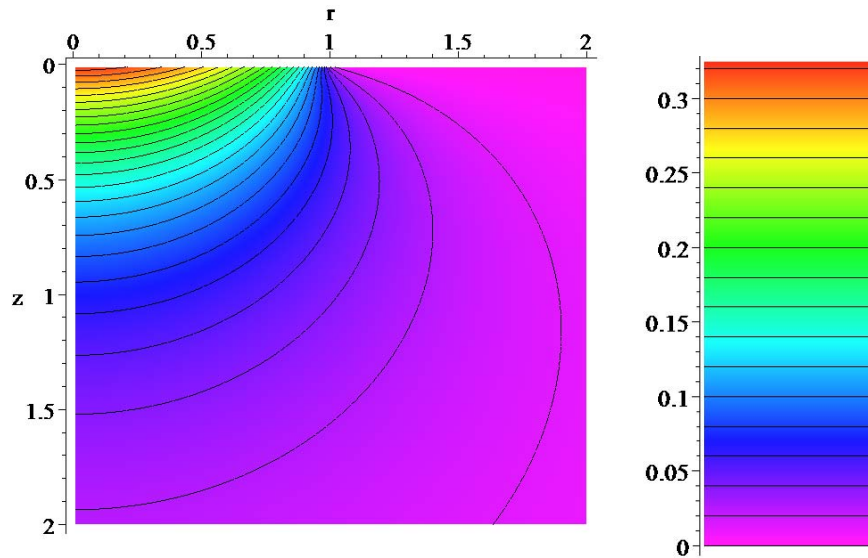
It is a common misconception that soft metals such as gold and copper experience significant pile-up all of the time. Many soft metals work-harden readily and are often seen to pile-up around an indenter in such cases. Soft fcc metals are also commonly used as a representative soft film for investigation of substrate effects on indentation data [172]. The problem of pile-up is often extreme in situations of a soft film on a hard substrate, for the indents often penetrate well into the substrate. The discontinuity in materials creates an extreme case for plastic flow of the soft film. The dramatic increase in the contact area can cause overestimations in hardness as large as 100%. Pile-up is not a function of being a soft material, but rather is closely correlated to whether the material is work hardened or annealed.

3.6.2.2 Phase transformation

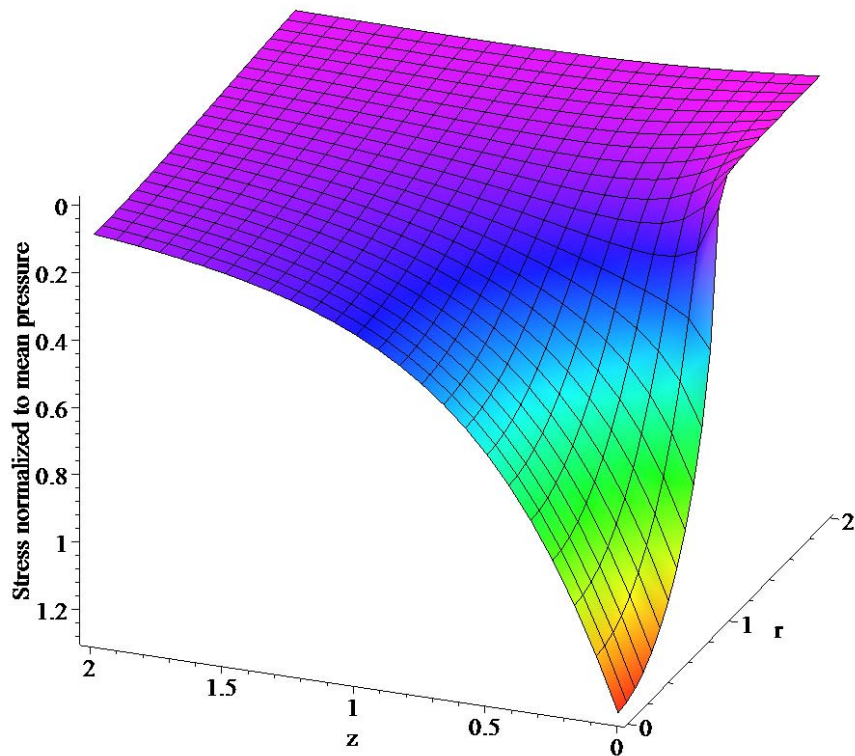
There are observations where materials undergo a pressure induced densification or phase transformation process during indentation. As demonstrated in the section 3.2 Hertzian contact model and Huber stress tensors could be used to calculate the principle stresses beneath a spherical indent (equation 3.13). These principle stresses may be used further to calculate the hydrostatic pressure below the indent according to the following equation: For the case of a spherical indent the resulted hydrostatic pressure under the tip may be calculated using equation 3.13. Figure 3.29 shows the contour of the equi-pressure areas under an spherical indent according to the Hertzian contact model. This high hydrostatic pressure as well as non-hydrostatic pressure existing below the indenter may result in a phase transformation or amorphisation in material underneath the indent. This phenomenon has been observed in materials, such as Si [173, 174], SiC [175, 176], quartz [175], Ge [177], GaAs [178]. The continuous or abrupt phase transformation of the tested material is often loading-rate dependent as shown by Kailer et al. [179]. This phase transformation results in a volume change of the material below the tip and influences the load-displacement curve in different manners as shown in figure 3.30 [180]. Recently Frick et.al. [181] reported the stress-induced martensitic transformations and shape memory effect in nickel-titanium (NiTi) shape memory alloys during nanoindentation.

3.6.2.3 Pop-in

Crystalline materials often show a discrete transition from elastic to plastic deformation, which is referred to as pop-in behavior (figure 3.9). Before the pop-in event these materials show an extraordinarily high strength, which is close to the theoretical strength of the crystal itself. This behavior can be related to the nucleation of dislocations. The pop-in behavior was initially observed by Gane and Bowden [182]. The process of bringing a tungsten carbide tip into contact with an electropolished and annealed gold surface was observed in a scanning electron microscope while the load on the tip was monitored. For very low loads no indentation was observed upon removing the tip from the surface. Upon reaching some critical load, the tip rapidly penetrated into the sample, leaving an impression of the indentation on the gold surface. This was a significantly different phenomena than had been suggested by Hertz in 1881 [136]. Rather than observing a transition from elastic to plastic deformation at applied shear stresses which meet either the Tresca or von Mises yield criteria, the authors



(a) Contours of the hydrostatic pressure, σ_h , below the surface



(b) Three dimensional representation of the hydrostatic pressure, σ_h , below the surface

Figure 3.29: Graphical representation of the hydrostatic pressure below the surface calculated from Huber stress tensor due to the elastic Hertzian contact between a spherical punch and a flat surface with a contact radius of $a = 1$.

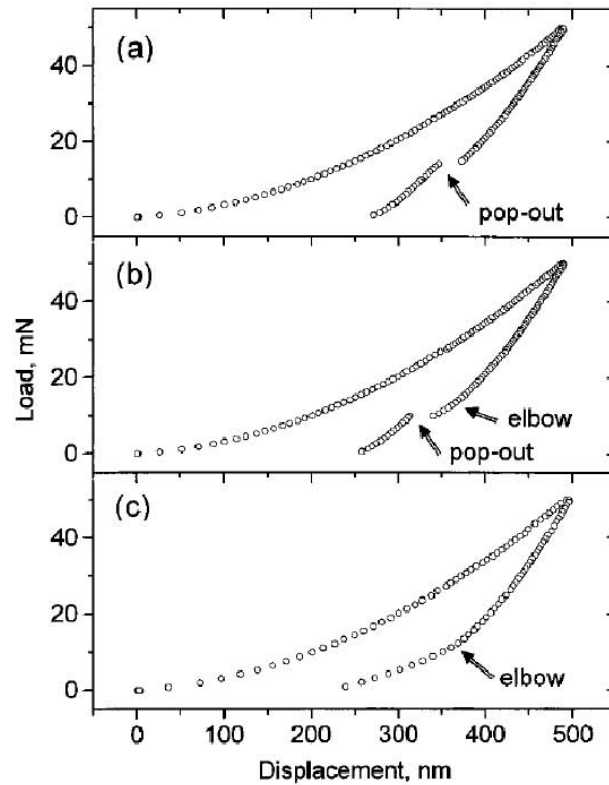


Figure 3.30: Effect of phase transformation on load displacement curves observed during nanoindentation of silicon [180]

suggest that the stresses being applied to the gold sample approach the theoretical shear strength of the material, even though it is likely that the stress field around the indenter will encounter a dislocation prior to the onset of plasticity.

Pethica and Tabor [183] applied a load to a clean tungsten tip in contact with a nickel (111) surface in an ultra high vacuum environment while monitoring the electrical resistance between the tip and surface. The nickel had been annealed, sputtered to remove contaminants, and then annealed again to remove surface damage from the sputtering process. When an oxide was grown on the nickel to thicknesses of greater than 5 nm loading was largely elastic while the electrical resistance remained extremely high, with only minimal evidence of plastic deformation. However, past some critical load the resistance between the tip and sample dropped dramatically, with continued loading suggestive of largely plastic deformation.

These two sets of experiments have been the basis for further discussion regarding the onset of plasticity during indentation. With the development of nanoindentation systems further examples of this phenomena have been ob-

served. Sudden excursions in depth at low loads during nanoindentation have been observed in aluminum [132, 131, 163], tungsten [184, 185], gold [117, 116, 186] platinum [187, 188], stainless steels [32, 189, 190], nickel [124, 125, 191, 134], intermetallics [192, 193, 119], etc. These excursions were ascribed to either oxide film failure or the onset of plasticity.

Göken and Vehoff determined that there is purely elastic contact between a diamond tip and sample surface for loads lower than pop-in load [119]. The authors utilized Hertzian contact mechanics to estimate the shear stress under the indenter tip according to equation, and found that it approached the theoretical shear stress of the material.

Leipner et al. [173] studied the deformation of semiconductor crystals using nanoindentation techniques coupled with SEM and TEM. By imaging the structure of indentations into GaAs using SEM and TEM, the authors find no residual impression when the load-depth curve from the indentation data shows no residual depth upon unloading. TEM observations of indents past this “pop-in” show dislocation loop structures have developed underneath the indentation. The authors also mention that the observed displacement during pop-in will be an upper bound to the product of the number of dislocation loops and the Burgers vector.

Gaillard et al. [194] studied the pop-in phenomena in MgO and LiF crystals and observed dislocation etch pits around the indents with atomic force microscope (AFM) only after pop-ins.

A study of the effects of the passivating film on the loading behavior of an iron-3 weight percent silicon (Fe-3wt.%Si) single crystal was carried out by Venkataraman et al. [160]. In this study, it was shown that electropolished Fe-3wt.%Si has the same general behavior as tungsten, exhibiting elastic loading at low loads followed by a sudden excursion in the load-depth curve. By adding a drop of HCl to dissolve the passive film, it was shown that removing the oxide film on Fe-3wt.%Si removes the ability to support elastic loading. When the liquid evaporated and the sample repassivated, the ability to sustain elastic loading and the subsequent excursion was recovered. A subsequent study has shown that some of the conclusions drawn regarding softening of material without the passive film were actually caused by metal dissolution [195].

The lack of plasticity prior to the excursion, followed by the sudden penetration of the indenter corresponded to either the oxide breaking or dislocation nucleation. Two schools of thought were developed regarding the mechanism occurring during this pop-ins. It was suggested by Gerberich et al. [196] that dislocations actually were generated prior to the pop-in, and that the pop-in is

indicative of the failure of a passive oxide film on the surface. This model requires dislocation loops to nucleate upon loading, move under the indenter tip, cross slip to planes leading back to the free surface, and then break through the oxide and escape to the free surface. There is direct evidence using TEM that dislocations do cross slip under an indenter tip and travel back to the surface in Fe-3wt.%Si [197].

The second school of thought regarding the nature of these loading excursions attributed the excursion to only dislocation nucleation, and that the oxide breaking is not the controlling factor in the process. Bahr et al. [184] showed that the pop-in have been attributed to the onset of plasticity in tungsten and Fe-3wt.%Si single crystals. The load at which the first pop-in was observed in these studies varied with crystal orientation, oxide thickness and dislocation density. The shear stress under the indenter tip corresponding to the first displacement burst was also found to be equal to the theoretical shear stress [185, 186, 116]. Similar works on single and polycrystalline gold, where no oxide film is existing on the surface, lend more creditability to the theory of dislocation nucleation. Further on, recently in situ nanoindentation of aluminum in transmission electron microscope (TEM) provided direct proof for observation of the dislocation nucleation underneath the indent [198, 199, 200](figure 3.31).

Additionally computer simulation of the nanoindentation shows that the pop-in corresponds to the homogeneous nucleation of dislocation loops [201, 202, 203] as shown in figure 3.32. The simplest way to interpret the pop-in is that once the shear stress underneath the indenter has reached a critical value given by the theoretical strength of the material, dislocation nucleation and spreading must occur. A pop-in event is then found in the load-displacement data [204]. This theoretical strength was calculated for the first time by Frenkel in 1926 [205]. Figure 3.33 shows that the atom movement is periodic in direction of b and can be approximated as sinusoidal. Therefore, the applied shear stress, τ , is given by the expression

$$\tau = \frac{\mu b}{2\pi \mathbf{d}} \sin \frac{2\pi x}{b} \quad (3.44)$$

where μ is the shear modulus of the material, b is the spacing of the atoms in the direction of applied shear stress, \mathbf{d} is the spacing of the rows of atoms, and x is the shear translation of the two rows of atoms away from their initial low-energy equilibrium position. The maximum value for τ is the theoretical shear

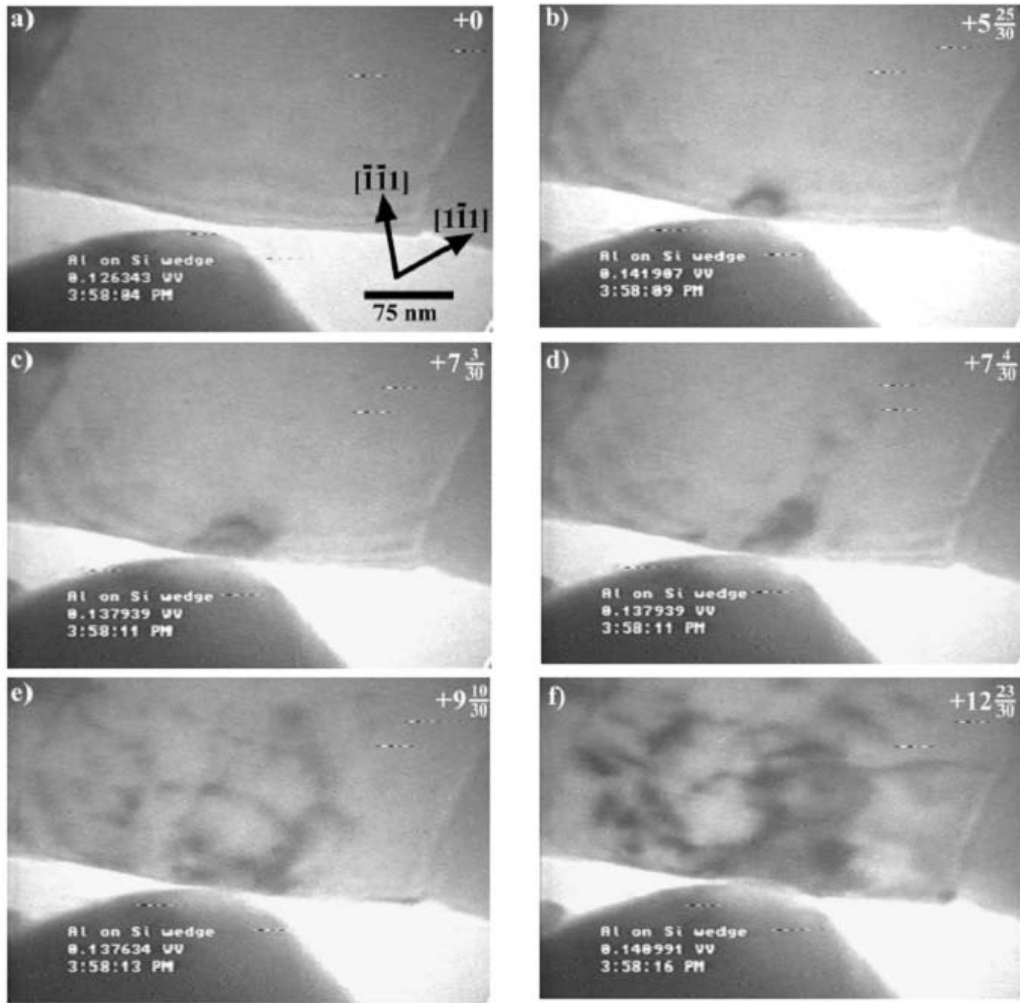


Figure 3.31: (a)–(f) The time-series TEM images of an Al grain showing the evolution of elastic-plastic deformation during an in-situ nanoindentation experiment. The direction of indentation is close to $[1\bar{1}1]$ in the indented grain. The time elapsed from image (a) is given in seconds in the upper right corner of each frame [200].

stress, and can be expressed as follows:

$$\tau_{th} = \frac{\mu b}{2\pi \mathbf{d}} \quad (3.45)$$

Since b is comparable in size to \mathbf{d} , the theoretical shear stress is often considered a fraction of the shear modulus. Numerous researchers have used different mathematical treatments that have resulted in theoretical shear strengths that range from $\mu/5$ to $\mu/30$ [206]. The approximation of $\mu/5$ is most likely an overestimate because the attractive forces between atoms fall off more quickly than

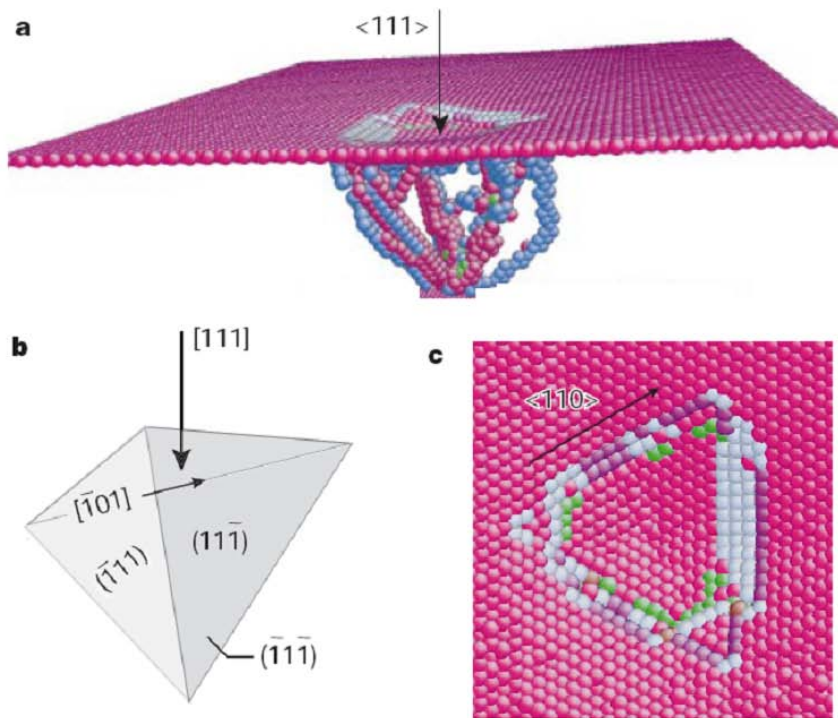


Figure 3.32: Homogeneous defect nucleation in $\langle 111 \rangle$ spherical indentation of Al. (a) MD simulation of spherical indentation ($R=12$ nm) normal to the $\langle 111 \rangle$ surface of Al results in a sessile structure derived from homogeneously nucleated glide loops on three equivalent $\{111\}$ planes. The simulation comprises 326592 atoms and periodic boundary conditions. Atom color indicates coordination number N : light pink, surface coordination, $N=9$; atoms with perfect coordination $N=12$ are made invisible. Other colors (green, blue and light pink interior atoms) indicate under- or over-coordinated atoms, which are atoms comprising defects. (b) Diagram of the $\{111\}\langle 111 \rangle$ slip systems available for indentation in the $\langle 111 \rangle$ direction. (c) Top view of the MD simulation surface showing the $\langle 111 \rangle$ orientations of three slip steps (surface ledges) that result from the initial nucleation event. The surface ledge corners then act as stress concentrators for further heterogeneous nucleation events [202].

is predicted by the sinusoidal model. This model also fails to take into account other low energy configurations such as twins. The low end approximation of $\mu/30$ was calculated by Mackenzie [206] using central forces for close packed metal. This is most likely an underestimate because it ignores thermal stresses and directional forces.

As mentioned before in section 3.2 the position of this maximum shear stress is in a depth equal to $0.48a$ below the surface and its value is $0.31p_0$ (equa-

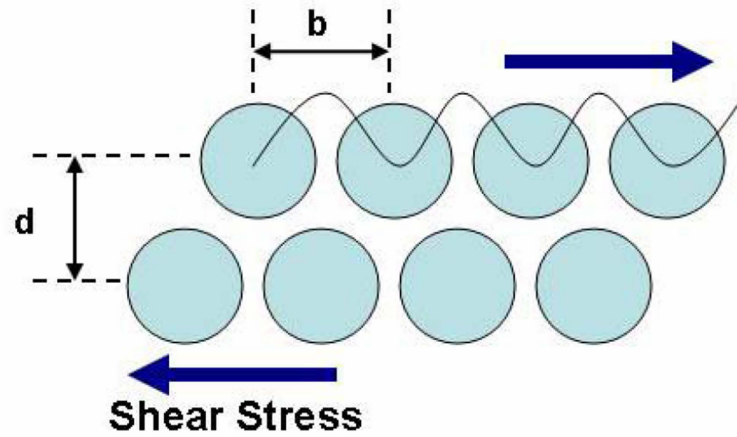


Figure 3.33: Schematic of the theoretical shear stress, the force required to slide one row of atoms over another, to a location of perfect registry.

tion (3.15)). With only knowledge of the tip radius, R and Young's modulus this is possible to calculate the maximum shear stress below the tip for loads below the pop-in load (elastic regime). The load displacement curve below the pop-in load can be fitted by a Hertzian behavior. Hence this is possible to estimate the tip radius from the Hertzian load displacement curve given by equation

$$P = \frac{4}{3}E_r\sqrt{Rh^3} \quad (3.46)$$

which is deduced from equations (3.4) and (3.1).

3.6.2.4 Creep

Creep is the term used to describe the tendency of a material to move or to deform permanently to relieve stresses. Material deformation occurs as a result of long term exposure to levels of stress that are below the yield or ultimate strength of the material. The rate of this damage is a function of the material properties and the exposure time, exposure temperature and the stress. There are four primary mechanism of creep deformation. These are dislocation glide, dislocation creep, diffusion creep, and grain boundary sliding. Usually more than one mechanism is happening at a time. Dislocation glide usually occurs at very high stress levels. The rate of creep is correlated to the ease of dislocation motion, in other words the distribution and influence of barriers such as precipitates and other dislocations. Dislocation creep is the glide of dislocation assisted

by the presence of vacancies. Diffusion creep is the flow of vacancies and interstitials under applied stress. It is the primary mechanism at low stresses and high temperatures. Grain boundary sliding is not a significant portion of steady state creep, but is important in keeping the material together during the other creep mechanisms. Vacancies play an important part in these creep mechanisms. Because vacancy concentration is exponentially dependent on temperature, it is no surprise that increasing the temperature has a dramatic influence on creep behavior.

The high displacement resolution of the nanoindentation system is capable of resolving material creep under the indent at the constant load. Special attention, however, should be paid to exclude thermal drift from creep displacement (see section 3.3).

3.6.2.5 Fracture

In an inhomogeneous tensile stress field, fracture cannot occur until the stored elastic energy is sufficient to supply the surface energy demand of a growing crack, as was pointed out by Roesler [207]. As mentioned in 3.2 a tensile component, however small, is unavoidable in all indentation fields. This raises the issue of brittleness, for cracking will then certainly occur if suitable initiating sources are present. It is also necessary to identify some important test variables. For instance, to establish the nature of the indentation stress field one specifies details of the contact geometry, load rate, etc. Similarly, to take into account extraneous influences on the fracture properties one specifies the temperature and state of the environment. These and other factors are responsible for a complex diversity in general indentation fracture behavior, a diversity which is not easily accommodated within a rational descriptive framework.

Nevertheless, recent developments in depth sensing nanoindentation make the quantitative evaluation of indentation processes possible and opened up the way to a broad view of the problem. Moreover, apart from providing the basis of a model system for discussing the applied phenomena, these developments have shown the indentation test to be a potentially valuable tool in the measurement of intrinsic fracture parameters of brittle solids. In particular, basic information on fracture-surface energies and crack-velocity functions may be extracted from the experimental observations.

The fracture toughness of brittle thin films, an important measure of the resistance of these materials to fracture and crack propagation, used to be evaluated through conventional microindentation using a microindenter [208]. However, because of the bluntness of the microindenter tip, large forces are neces-

sary to produce the cracks necessary for analysis. As hardness and modulus of thin films cannot be measured with microindentation without tedious work in correcting for the substrate effect on the results, the fracture toughness of thin films cannot be determined easily with the microindentation method. The applicability of nanoindentation to the measurement of the fracture toughness of thin films and very small volumes of bulk materials become very interesting. Because of the remarkable improvement in the sharpness of the nanoindenter tip with respect to the microindenter tip, the low loads associated with nanoindentation equipment may be high enough to overcome the threshold of cracking, which is the primary concern of employing the nanoindentation method. To do this usually very sharp tips like cube corner tips (figure 3.16) are utilized. Nanoindentations are carried under varying peak loads on properly prepared specimens. The fracture toughness can be calculated from the lengths of the cracks formed on the surface by using the following equation[209, 210, 211, 212]

$$K_{\mathcal{C}} = \alpha \left(\frac{E}{H} \right)^{\frac{1}{2}} \left(\frac{P}{\mathcal{C}^{\frac{3}{2}}} \right) \quad (3.47)$$

where, $K_{\mathcal{C}}$ is the fracture toughness, E is the Young's modulus, H is the hardness, P is the peak applied load, \mathcal{C} is the length of the radial cracks, and α is an empirical constant depending on the tip shape, in the case of a cube-corner tip α is 0.032.

CHAPTER 4

Experimental

*This proud one wished to make experiment
Of his own power against the Supreme Jove,
My Leader said, whence he has such a guerdon.*

The Divine Comedy, Inferno: Canto XXXI

DANTE ALIGHIERI

4.1 General aspects of sample preparation

Single crystalline nickel samples were produced by a modified Bridgman technique from high purity nickel samples under high vacuum in an alumina crucible. The copper single crystal was produced by the Czochralski method in a protective atmosphere in a graphite crucible. Iron aluminum single crystal is provided by Easo P. George from Oak Ridge National Laboratory, Oak Ridge, Tennessee. All single crystals are oriented using laser reflection patterns of etched surfaces as described in [213]. The etching solution, time, and temperature used for preparation of laser reflection patterns are given in table 4.1. The oriented samples with the goniometer transferred to electrical discharge machine (EDM). In the EDM they were cut into a circular shape with a diameter of 12 mm and a thickness of a few millimeters. Orientations were double checked in SEM using electron backscatter patterns (EBSD) as shown in figures 4.1 and 4.2. To minimize the defect density all samples were annealed at $0.8T_{melting}$ in a vacuum of 10^{-6} mbar for one day and cooled in the furnace, except where otherwise is noted. Further information regarding the preparation of polycrystalline samples (i.e. aluminum, Fe-3wt.%Si, austenitic stainless steel (SS), and superduplex stainless steel (SDSS)) will be provided in the appropriate sections.

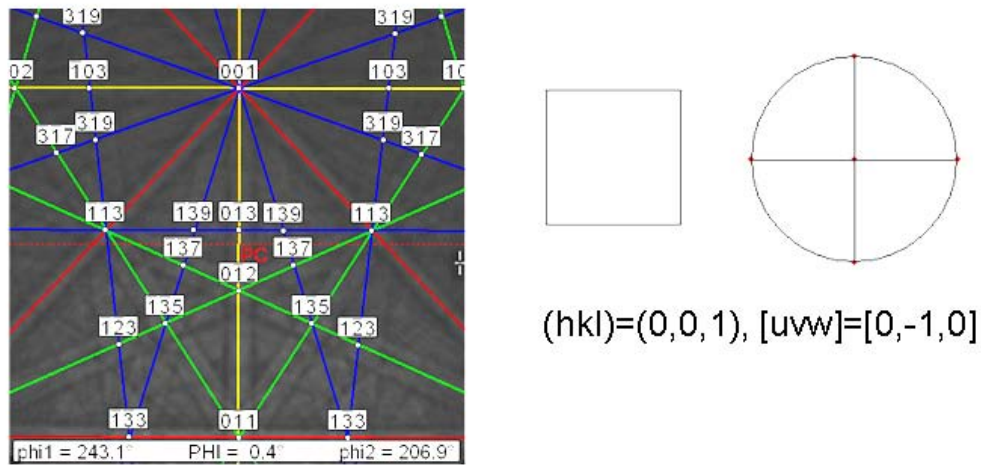


Figure 4.1: EBSD pattern showing the orientation of a FeAl single crystal after orienting with laser reflection pattern from etched surface (see table 4.1).

One of the most important points in nanoindentation experiments is the preparation of high quality sample surface as mentioned in section 3.6.1.1. This can be achieved only through careful mechanical and electrochemical polishing. The sample preparation step has a very distinct effect on the later measurements. Different parameters like contamination of electropolishing solution, time between electropolishing and measurements, air humidity, etc may change the experimental results. Figure 4.3 shows the effect of electropolishing solution quality as well as time between electropolishing and test on pop-in load distribution in nickel. The electrochemical polishing is material dependent. The optimum electropolishing parameters are material specific and should be found through electrochemical experiments. This is reviewed in section 4.1.1. For mechanical polishing the same method was used for all of the samples. Starting with silicon-carbide grinding papers at grade 800, 1000 and 1200, the samples

Table 4.1: Etching solutions and parameters used for achieving proper laser reflection patterns in single crystal samples.

Material	Solution	Temperature (°C)	Time (s)
Nickel	63% HNO ₃	20–35	5–15
Copper	1 M (NH ₄) ₂ S ₂ O ₈	40–60	30–60
FeAl	37% HCl, 63% HNO ₃ and H ₂ O in 1:1:2 ratio	20–45	5–10

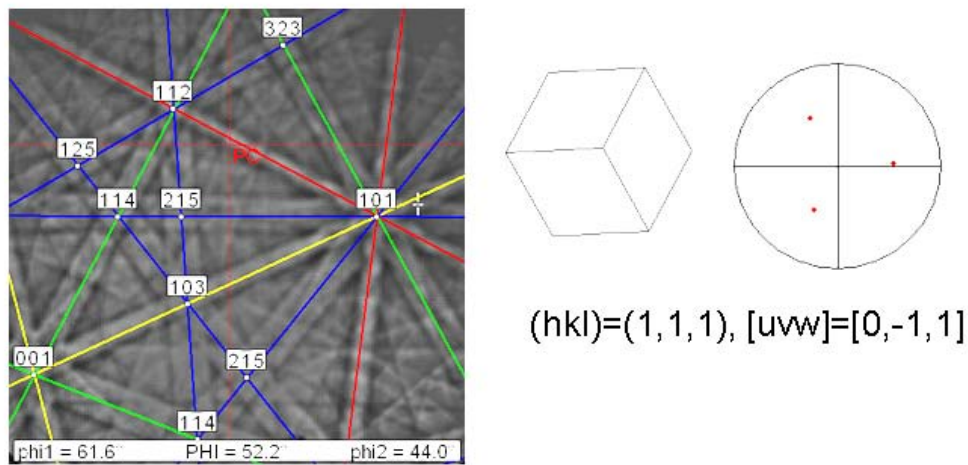


Figure 4.2: EBSD pattern showing the orientation of a nickel single crystal after orienting with laser reflection pattern from etched surface (see table 4.1).

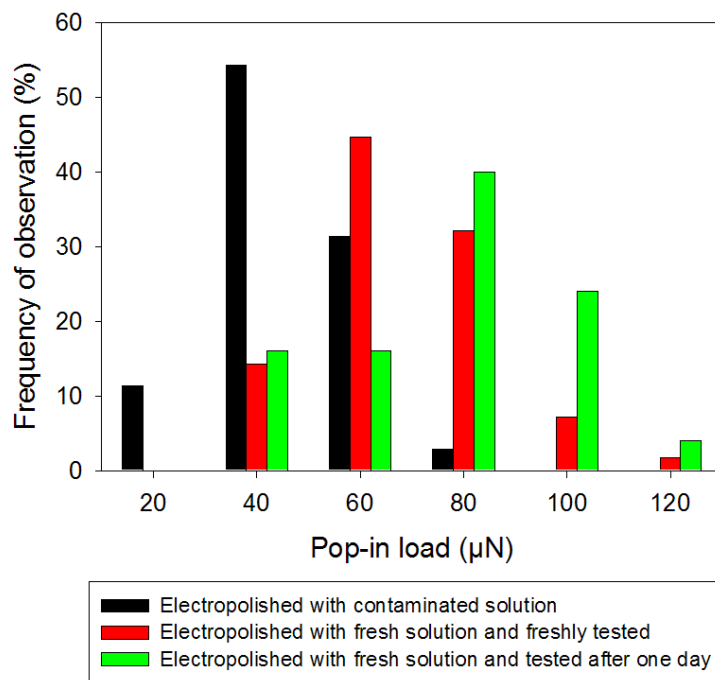


Figure 4.3: Dependence of pop-in load on surface preparation.

were ground. Afterward they were mechanically polished with diamond suspensions at 6 μm, 3 μm and 1 μm.

4.1.1 Electropolishing procedure

A unified theoretical explanation for electropolishing has not yet been developed, since several mechanisms may be involved, and the relative importance of each of them may vary depending on the metal being electropolished and the electrolyte used. According to Jacquet's initial idea, differences in resistance in the the anolyte layer over projections versus that over depressions is the key factor. Therefore a desirable electrolyte characteristics include the following:

- i. Should be a somewhat viscous solution
- ii. Should be a good solvent during electrolysis
- iii. Should not attack the sample with current off
- iv. Should contain one or more large ions, e.g., PO_4^{3-} , ClO_4^{1-} , or SO_4^{2-} , or large organic molecule
- v. Should be simple to mix, stable and safe
- vi. Should be operable at room temperature and be insensitive to temperature changes.

The operating condition of a particular sample-electrolyte combination can be evaluated by preparing a plot of the applied voltage versus the current density. The resulting curves will approximate one of the two shapes shown in figure 4.4. Curve I is typical of electrolytes that either polish over a very wide range or does not polish at all. Curve II is characteristic of electrolytes that form an ionic film. The dotted portion of the curve is added in recognition of certain published data and the observation that the formation of a polishing film requires a finite time. Polishing will occur between B and C and is usually best slightly before C. In order to find a proper solution and condition for electropolishing the samples used in this study, different solutions have been tested. The available electropolishing solutions could be divided in two main categories; aqueous and organic. It has been shown that the resulted electropolished surface in aqueous solutions is covered by a thin oxide layer. This phenomena has been observed and reported in early publications and is believed to be resulted from presence of water molecules [214]. For the purpose of this work, there was a wide range of choices of organic electropolishing solutions, but due to the ease of preparation and use, the solutions based on methanol, ethanol, and isopropanol were chosen. These alcohols together with sulfuric, phosphoric, or perchloric acids

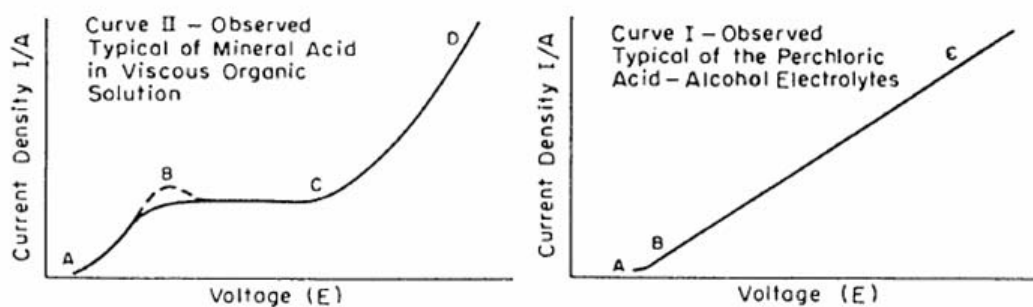


Figure 4.4: Typical curves for determining conditions for electropolishing, Curve I is typical of electrolytes that either polish over a very wide range or will not polish at all. Curve II is characteristic of electrolytes that form an ionic film

with different concentrations were used to prepare different electropolishing solutions. The polarization curves of the samples in the different electrolytes were recorded by using the potentiodynamic polarization technique. Figure 4.5 shows such polarization curves for nickel in different concentrations of sulphuric acid in methanol. The polarization curves made it possible to find the optimum electropolishing solution for the samples. Further on these solutions were used in a set of experiments to find the best parameters for electropolishing using the commercial electropolishing machine from Struers, LectroPol-5. Table 4.2 summarizes the electropolishing solutions and parameters used in this study for electropolishing different materials.

To obtain defect-free surfaces, the deformed layer produced by mechanical grinding and polishing must be removed. Since most electropolishing solutions have low metal removal rates, it is clear that long electropolishing times are required to produce deformation free surfaces if one start with a roughly ground surface. On the other hand, a long electropolishing time may result in a wavy surface or local overheating of the sample. Therefore the mechanical polishing was always continued to a finer state, for example 1 μm diamond paste, to produce deformation free electropolished surfaces in short time.

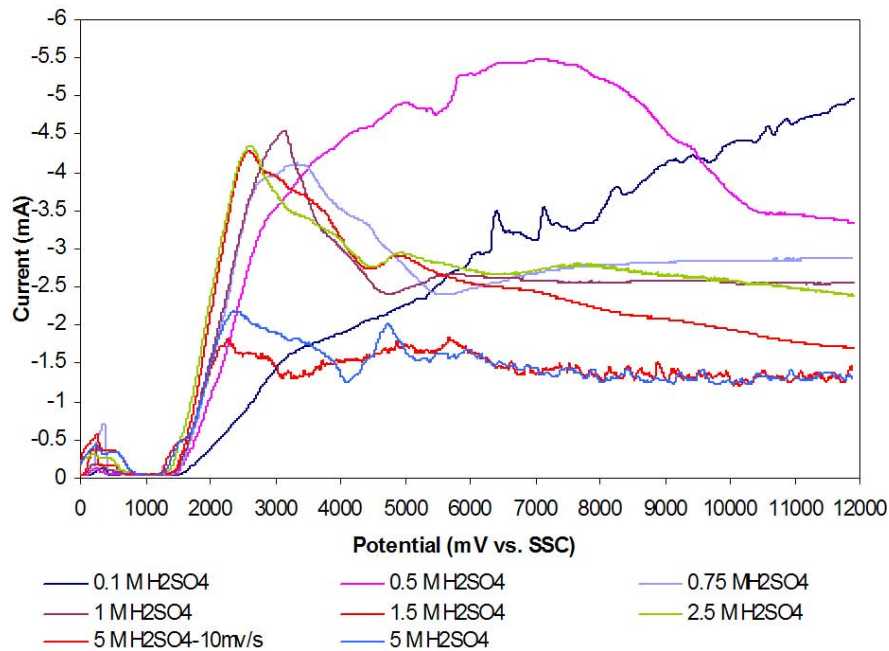


Figure 4.5: Potentiodynamic polarization curves for nickel in different concentration of sulphuric acid in methanol (scan rate 20mV/s).

Table 4.2: Electropolishing solutions and parameters used for different materials.

Material	Solution	Pot. (V)	Temp. (°C)	Time (s)	Flow rate
Nickel	H ₂ SO ₄ /Methanol	28-35	16-22	20-120	6-10
Copper	H ₃ PO ₄ /Ethanol	22-28	20-30	10-50	8-14
Fe-3wt.%Si	H ₂ SO ₄ /Methanol	8-14	10-15	30-120	5-10
304 SS	H ₂ SO ₄ /Methanol	8-14	10-20	30-120	5-10
FeAl	H ₂ SO ₄ /Methanol	38-44	0-10	30-120	5-10
Duplex SS	H ₂ SO ₄ /Methanol	8-14	10-20	30-120	5-10
Aluminum	HClO ₄ /Ethanol	38-44	0-10	30-120	5-10

4.2 Mechanical property measurements

4.2.1 Microindentation

Microindentation experiments were made with a Vickers hardness testing machine (*Leica-VWHT-MOT*). All experiments were performed at room temperature. Different maximum loading forces from 49 mN to 19 N are available. The maximum loading force is always kept 15 s before unloading. At least five in-

dents were performed for each test.

4.2.2 Nanoindentation

All nanoindentation experiments were conducted using a Hysitron, Inc. Tribo-Scope[®], as an attachment to a Digital Instruments Nanoscope II[®] SPM. One of the main advantages of the Hysitron system is the ability to image before and after indentation, using a specially designed force transducer and the AFM imaging software. The indenter tip is used as the imaging probe in contact mode. The imaging capabilities make it possible to indent on specific surface features, and avoid any sites with deformation due to a previous impact. This also enables post indent imaging that facilitates identifying the relative location of the indent. It is also a fully quantifiable system. The indentations were made with a Berkovich Diamond indenter (see section 3.4.2 for more information). The instrumentation was calibrated in the manner described in Section 3.4.2

All indentation tests had a loading function like the one given in figure 3.9 except when otherwise is noted. The set point for imaging of the surfaces was 2 nA, which is equivalent to 2 μ N. All hardness values were derived by the Hysitron software, utilizing the equations detailed in section 3.3 and following the standard method proposed by Oliver and Pharr [215, 170]. The pop-in load were determined using self written VisualBasic code given in appendix A.

4.3 In situ electrochemical NI-AFM

In order to be able to perform the in situ electrochemical NI-AFM (ECNI-AFM) experiments, the first step was to make NI-AFM experiments inside a fluid. However, operating a NI-AFM even in air is not an easy task. Changing from operation in air to fluid brings new complications which have been discussed in section 3.5. In addition to these practical problems in performing NI-AFM inside liquid, there is problems due to the implementation of electrochemical control. Most of the electrochemistry related problems are material specific and will be discussed case by case for each material used in this study. However one omnipresent problem during in situ electrochemical nanoindentation is dissolved oxygen in liquid which can influence the electrochemical processes. In the first set of tests, where this problem was not considered, reproducible results were not obtained due to the unstable surface and corrosion as shown in figure 4.6. In electrochemical experiments the usual practice is to bubble an inert gas, e.g. argon or nitrogen, inside the solution to remove the oxygen and

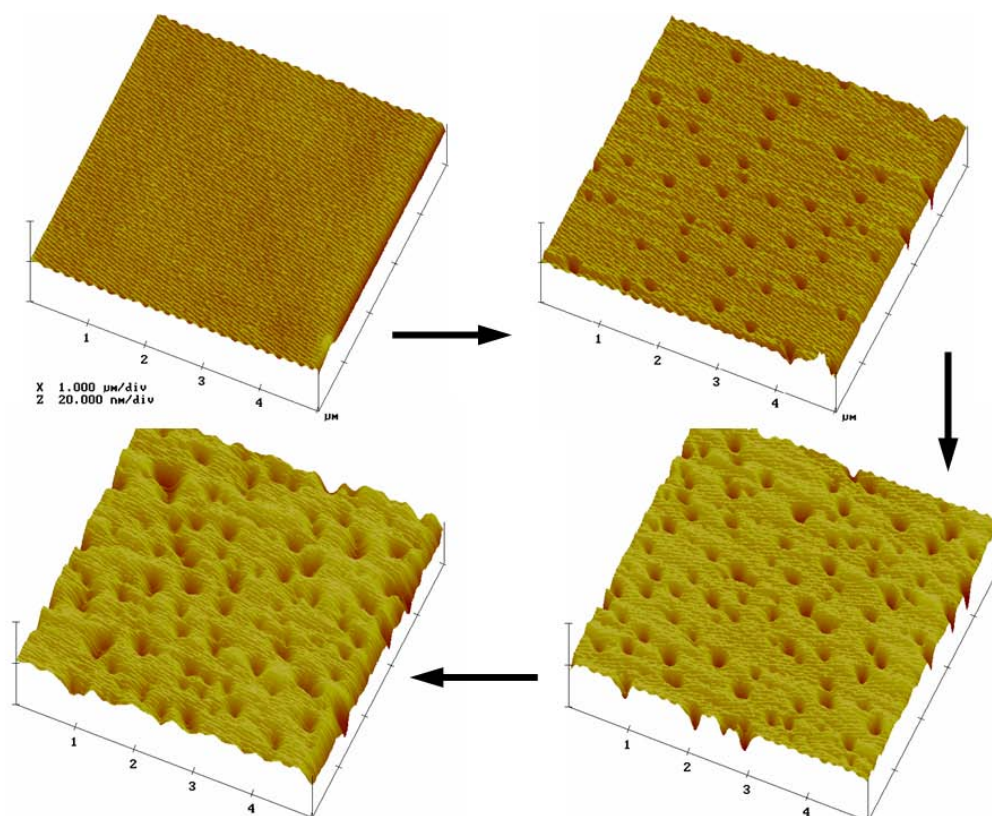


Figure 4.6: Localized corrosion process happening on the surface of nickel single crystal. Increase in the number and depth of pits with time. pH 3, 0.05 M Na_2SO_4 solution.

inhibit the dissolution of oxygen. As in our experiments, no bubbling of an inert gas was possible; the whole system was put inside a protective atmosphere. The electrolytes were deaerated externally before each experiment. Figure 4.7 shows the experimental setup developed for conducting in situ ECNI-AFM. The whole setup was suspending on four springs which are acting as a passive system for vibration isolation. A three electrode electrochemical cell was designed to be fitted to the DI Multimode sample holder (figure 4.8). Nanoindentation was conducted inside this electrochemical cell while the sample was covered with approximately 2 mm of electrolyte. A platinum wire was used as a counter electrode and the reference electrode was an Ag/AgCl electrode. Consequently all the electrochemical potentials for in situ experiments are reported against an Ag/AgCl reference electrode. A Bank Elektronik TG 97 potentiostat was used to control the electrochemical potentials. The electrochemical data was recorded on a PC using an AD-DA interface. Special tubing was used to inject a deaerated solution from the outside and into the electrochemical cell inside the protective



Figure 4.7: Experimental setup for in situ electrochemical nanoindentation. Protective atmosphere chamber and vibration control.

atmosphere, as shown schematically in figure 4.9. All electrolytes were prepared from analytical grade compounds and double distilled water. Prior to the tests, the electrochemical cell was cleaned in piranha acid, which is a warm mixture of three parts sulphuric acid (H_2SO_4) and one part hydrogen peroxide (H_2O_2). Because the mixture is a strong oxidizer, it will remove most organic matter, and it will also hydroxylate most surfaces (add OH groups), making them extremely hydrophilic and water compatible. The tip was also cleaned carefully before each test in a mixture of ethanol and isopropanol and then in double distilled water. This high cleanliness for this type of nanoscale experiment is a requirement. Only $3.85 \times 10^{-7} \text{ cm}^3$ impurity inside the electrolyte results in deposition of a 10 nm layer of deposit. Figure 4.11 shows topography images taken during in situ NI-AFM in a contaminated solution. The impurities were deposited on the surface of the sample and resulted in artifacts (figure 4.11a). Scanning the surface of the sample resulted in removal of these sediments as shown in figure 4.11b. Conducting a nanoindentation test on such a surface usually results in artifacts in load displacement curves as shown in figure 4.10.

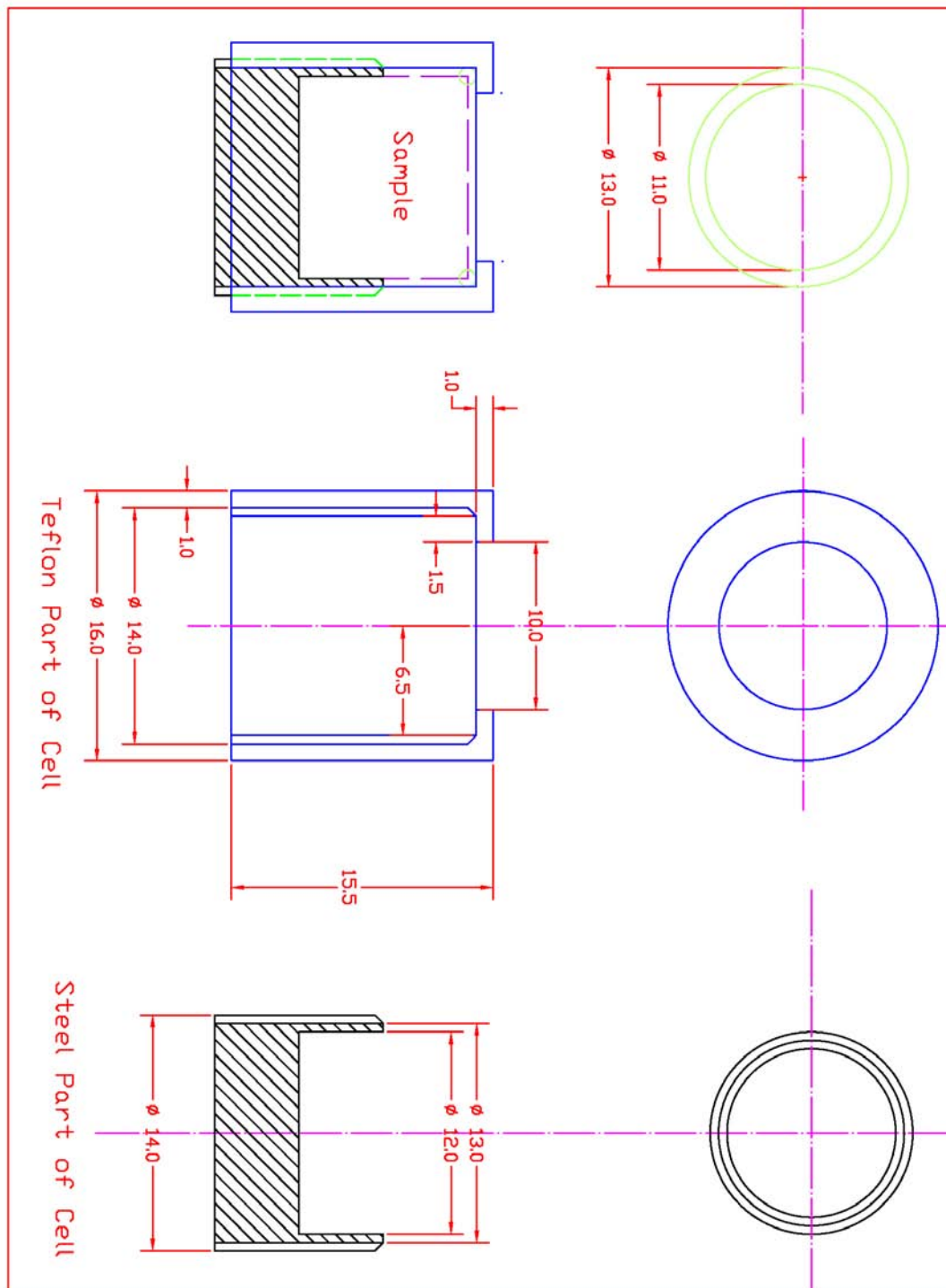


Figure 4.8: Drawing of the special cell designed for performing in situ electrochemical nanoindentation experiments.

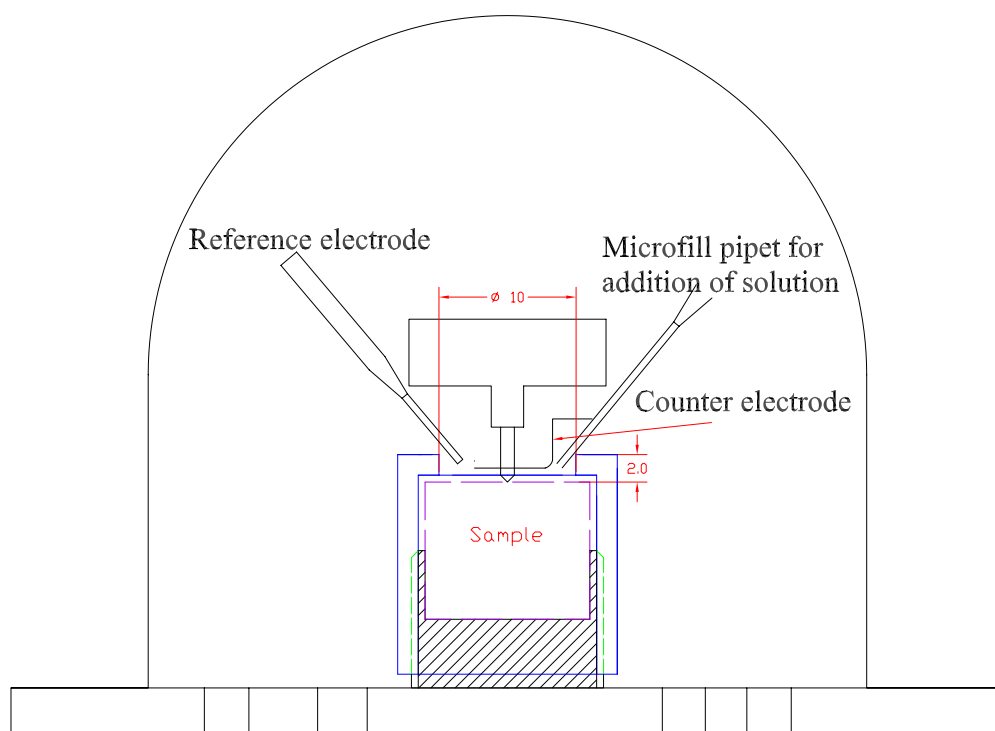


Figure 4.9: Schematic representation of the experimental setup for in situ ECNI-AFM experiments.

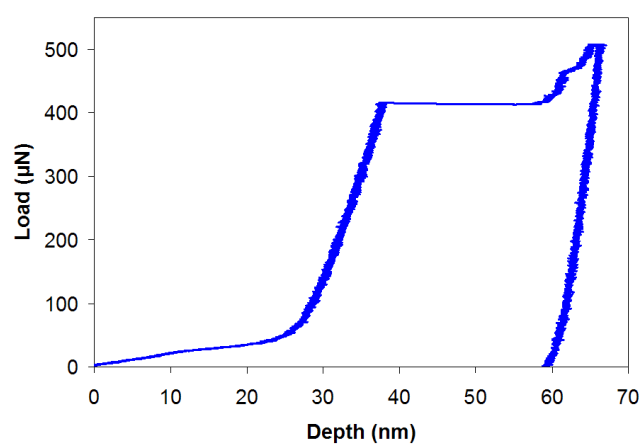
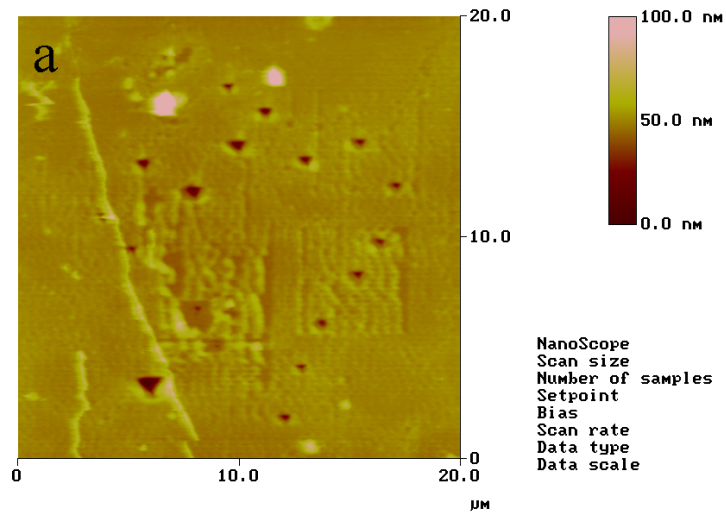
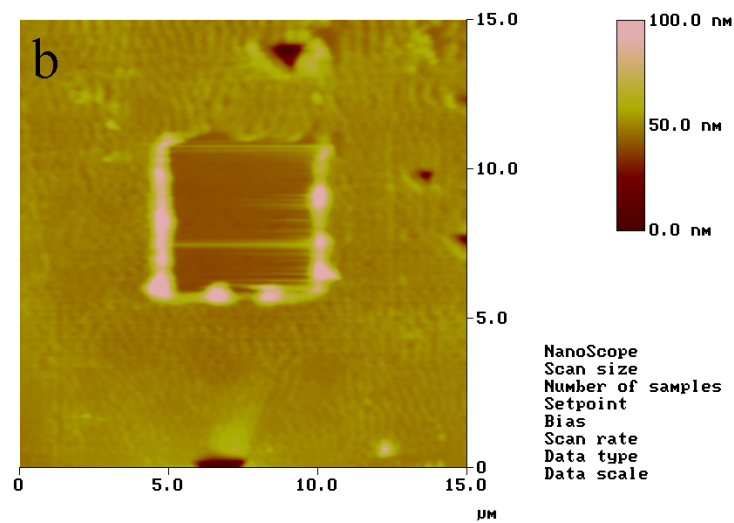


Figure 4.10: Artifact in load displacement curve resulted from impurities inside the electrolyte absorbed on the sample surface during in situ ECNI-AFM



(a) Deposition of impurities on the surface



(b) Removal of the deposits by scanning the surface with a higher contact load

Figure 4.11: Impurities in the solution start to deposit on the surface during in situ electrochemical nanoindentation and influence the imaging and nanoindentation measurements. Scanning the surface with higher contact load removes this deposits.

CHAPTER 5

Results

*O Muses, O high genius, now assist me!
O memory, that didst write down what I saw,
Here thy nobility shall be manifest!*

The Divine Comedy, Inferno: Canto II
DANTE ALIGHIERI

THE experimental setup designed and used in this work is a new unique method which, to the knowledge of the author, has been used for the first time in hydrogen embrittlement studies. Therefore different metals, alloys, and an intermetallic alloy were studied with this novel method. This has been done to be sure about the consistency of the observed effects. The choice of some of these materials were done upon previous knowledge from hydrogen interaction with them. For example copper is known to be immune against hydrogen embrittlement. Therefore it was one of the choices as a comparison to become sure if the observed effects in other sensitive metals were due to the hydrogen. The other selected metals were aluminum, ferritic and austenitic iron alloys, nickel and an iron aluminum intermetallic which all are technically important materials and prone to hydrogen embrittlement.

The problems of performing NI-AFM tests inside fluid and under electrochemical control have been reviewed in [3.5.1](#). But why is it necessary to perform in situ charging for probing hydrogen effects by NI-AFM? In the next section the reasoning will be given. In the following sections the results of in situ electrochemical tests on the candidate materials will be presented and discussed.

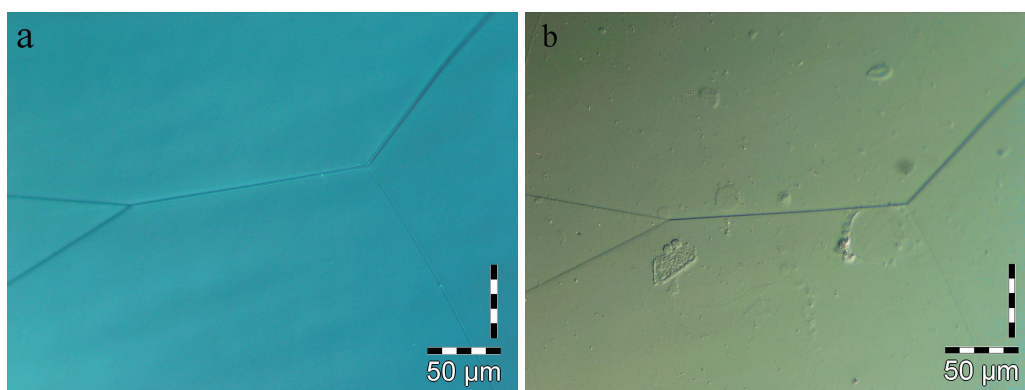
5.1 Why not ex situ tests?

In order to show the shortcomings of ex situ hydrogen charging, tests were conducted on ex situ hydrogen charged nickel samples. Two different methods of hydrogen charging were employed, electrochemical charging, and high pressure and temperature charging in autoclave.

5.1.1 Ex situ electrochemical hydrogen charging

5.1.1.1 Nanoindentation measurements on ex situ charged nickel

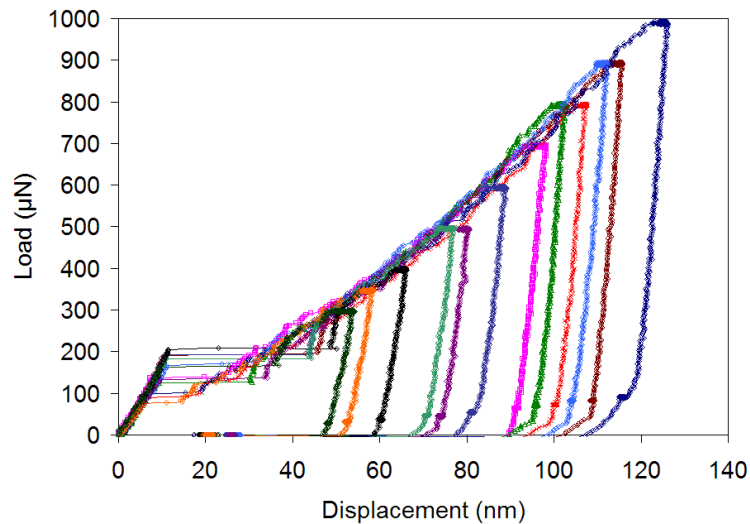
A high purity zone refined nickel sample with grain size in the range of a few millimetres was carefully prepared according to the given procedure in 4.1. Figure 5.1a shows an optical micrograph image of the sample surface after electropolishing. The ex situ hydrogen charging was performed in 0.1 molar Na_2SO_4 solution. The pH of the solution was set to 2 by addition of excess H_2SO_4 . As a hydrogen evolution poison 0.5 mg/lit Na_2S was added to the solution. The charging was continued for 6 days in order to get a uniform hydrogen concentration within the surface layer of the sample. During the hydrogen charging, the potential of the sample was controlled by a potentiostat at -1000 mV against an Ag/AgCl reference electrode. A platinum wire was used as a counter electrode. The first problem that was encountered during the ex situ tests, was the surface damage caused by the hydrogen charging, as shown in figure 5.1b. This increased the roughness of the surface and therefore it was necessary to



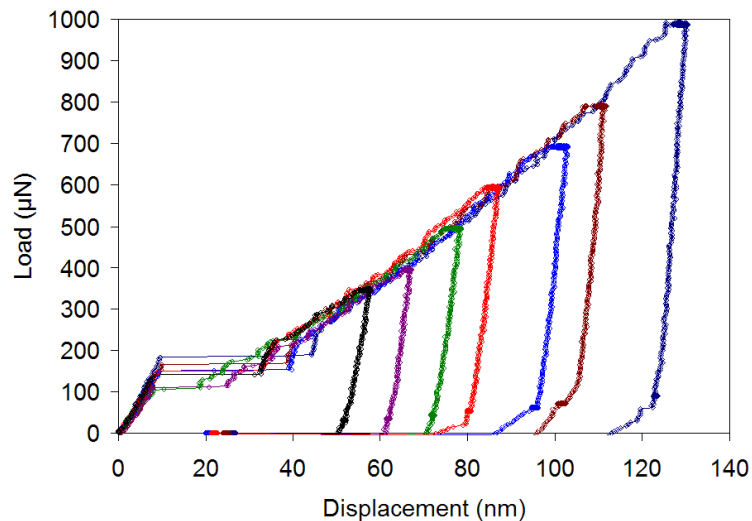
(a) Freshly electropolished nickel surface (b) Nickel surface after hydrogen charging

Figure 5.1: Light microscope micrograph of nickel surface in freshly electropolished condition (a), and the same position after electrochemical hydrogen charging in pH 2, 0.1 M Na_2SO_4 solution at -1000 mV versus Ag/AgCl reference electrode (b).

electropolish the sample before nanoindentation. The resulting load displacement curves for the sample before and after hydrogen charging are given in figure 5.2. Figure 5.3 shows the effect of ex situ hydrogen charging on measured nanohardness. The pop-in distribution for hydrogen charged and hydrogen free samples are given in figure 5.4. The results presented in figure 5.2 and



(a) Before hydrogen charging



(b) After ex situ hydrogen charging

Figure 5.2: Load displacement curves of nickel (a) before hydrogen charging, (b) after ex situ hydrogen charging, with different maximum load and a constant 100 $\mu\text{N/s}$ loading rate.

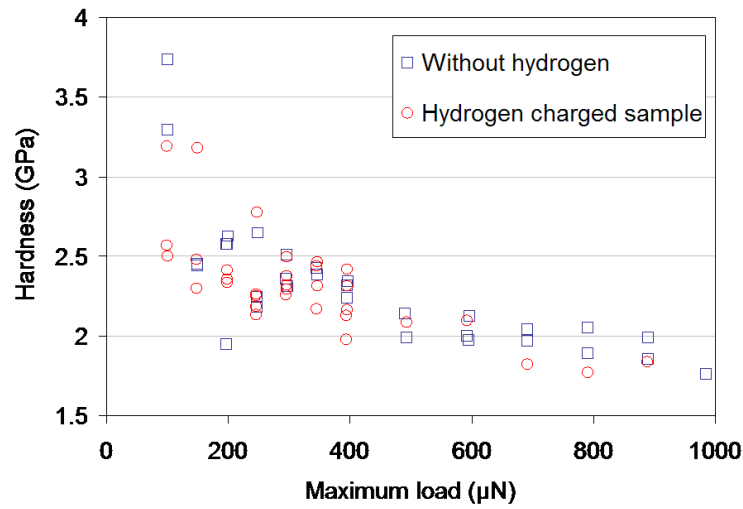


Figure 5.3: Comparison of nanohardness measurement on ex situ hydrogen charged and uncharged nickel sample.

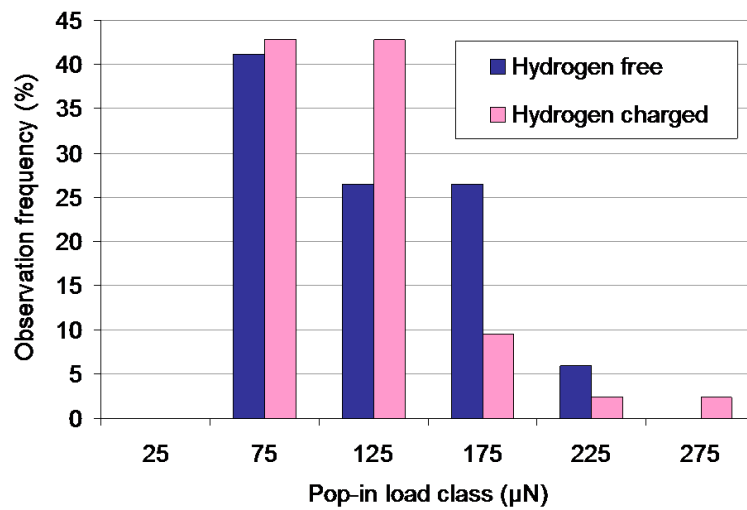


Figure 5.4: Distribution of the pop-in load for hydrogen free and ex situ hydrogen charged situations in nickel.

figure 5.4 clearly show no change in load displacement, dislocation nucleation (pop-in load) and hardness of the nickel sample after hydrogen charging.

5.1.1.2 Microhardness measurements on ex situ charged nickel

The above mentioned results of the ex situ hydrogen charging experiments, where no distinct effect of hydrogen was observed, was the motivation for microhardness tests on the ex situ hydrogen charged samples. Figure 5.5 shows the result of microhardness measurements on a single crystal nickel after 100 hours ex situ charging under a similar condition as the nanoindentation tests. According to the geometry of the Vickers indent, shown in figure 5.7, it is possible to estimate the depth of the indents as a function of the mean value of the projection diagonal d_m ¹

$$h_{Vickers} = \frac{d_m}{2\sqrt{2}} \tan 22^\circ \quad (5.1)$$

In figure 5.8 the increase in the microhardness of the sample as a result of hydrogen charging is plotted versus estimated depth of indentation from equation (5.1). The increase in the microhardness by hydrogen charging is in agreement with reported results in the literature [216, 217].

A simple semi infinite diffusion model according to figure 5.6 was assumed in

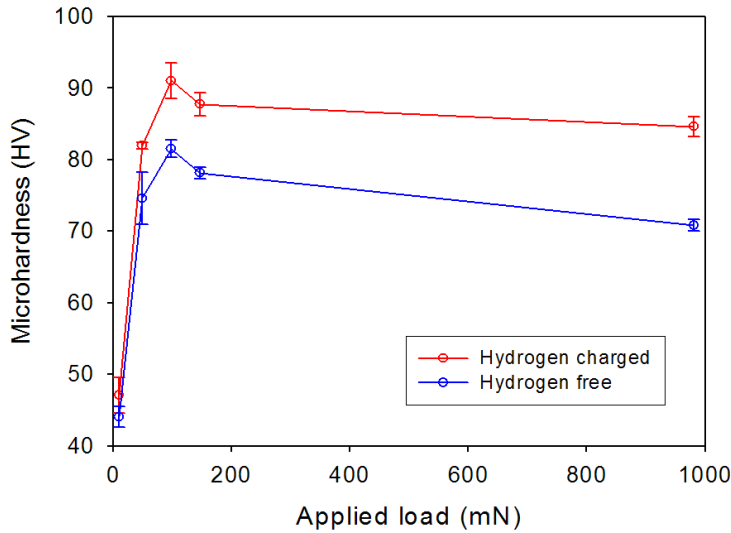


Figure 5.5: Comparison between the microhardness of the hydrogen free and the ex situ hydrogen charged single crystal nickel as a function of the applied load used to perform the indentations

¹ d_m is the mean value of the projection diagonal, d_1 and d_2 , as shown in figure 5.7

order to analyze the outgassing of hydrogen from the sample

$$\frac{C(x,t) - C_S}{C_0 - C_S} = \operatorname{erf}\left(\frac{x}{2\sqrt{Dt}}\right) \quad (5.2)$$

where $C(x,t)$ is the concentration of hydrogen in position x and time t , C_S is the surface concentration of hydrogen, C_0 is the bulk concentration of hydrogen, and D is the hydrogen diffusion coefficient. The following boundary conditions were used for the solution of equation (5.2)

$$\text{Boundary conditions} \begin{cases} x = 0 & t = 0 \Rightarrow C = C_0 \\ x = 0 & t > 0 \Rightarrow C = C_S \\ x \rightarrow \infty & t \geq 0 \Rightarrow C = C_0 \end{cases}$$

Hydrogen concentration profile in the sample was calculated, using hydrogen diffusion data given by Robertson [218]. In figure 5.8 the hydrogen concentra-

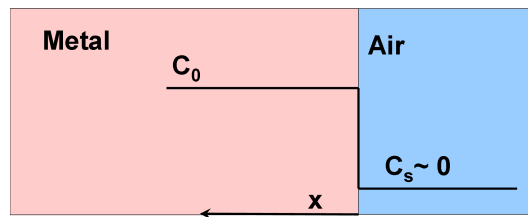


Figure 5.6: Schematic of hydrogen outgassing model used for analysis of hydrogen outgassing from the sample

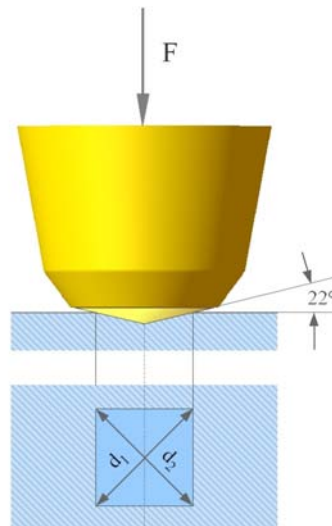


Figure 5.7: Schematic of a Vickers indenter utilized for microhardness measurement

tion profile after 90 seconds is drawn (red curve). The increase in hardness fit perfectly to the hydrogen profile in the sample. This proves the validity of the hydrogen outgassing model used for estimation of the hydrogen profile.

The penetration depth during nanoindentation of nickel (see figure 5.2) is limited to 100 nm. Also it should be noted that the first dislocation nucleation (i.e. pop-in) usually happens in a displacement range of 10 nm. According to the Hertzian contact theory (see section 3.2) the position of the maximum shear stress resulting in dislocation nucleation (see section 3.6.2.3) is $0.48a$ below the tip. Where a is contact radius and given by equation(3.1). Combining the equation(3.1) the equation (3.4) results in:

$$a = \sqrt{Rh} \quad (5.3)$$

where R is the tip radius and h is the displacement of the surface on the axis of symmetry. Therefore, for a tip radius about 500 nm, the position of the maximum shear stress during the pop-in is about $0.48 \times \sqrt{500 \times 10} = 34$ nm below the surface. In the figure 5.8 there is a green region about 50 nm. This shows the probing depth of nanoindentation. The comparison of this green region with the hydrogen concentration profile clearly shows why during nanoindentation on ex situ hydrogen charged nickel no effect was observed. Therefore, in or-

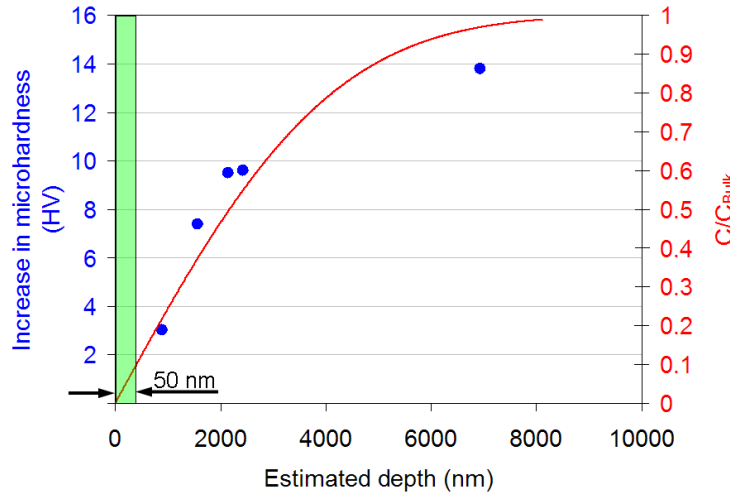


Figure 5.8: Increase in nickel microhardness as a result of hydrogen charging versus depth of indentation estimated using equation (5.1) (Blue points). Hydrogen concentration profile after 90 seconds of hydrogen outgassing (Red curve).

der to study the effect of hydrogen on dislocation nucleation by NI-AFM, it is necessary to use an in situ hydrogen charging method.

5.1.2 Ex situ hydrogen hydrogen charging in autoclave

In order to charge the sample at higher temperature and pressure an autoclave was used. This high pressure charging, however, resulted in a heavily damaged surface, as shown in figure 5.9 which was not appropriate for nanoindentation tests [219].

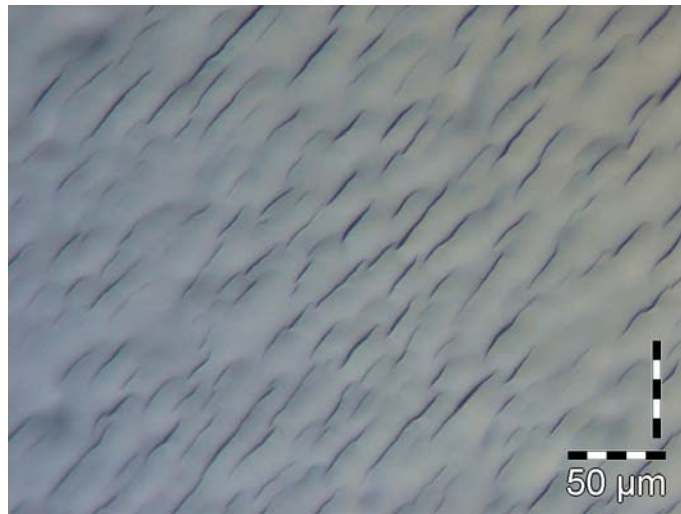


Figure 5.9: Surface damage in nickel as a result of ex situ hydrogen charging in an autoclave at 300 °C and 200 bar.

5.2 In situ ECNI-AFM tests on copper

Copper is known for its very low hydrogen solubility and diffusivity [220]. DeWulf and Bard [221] showed that without hydrogen recombination poisons e.g. As_2O_3 no detectable hydrogen concentration develops in copper. This makes the copper a proper calibration material for in situ electrochemical nanoindentation tests, where no effect of cathodic charging should be observed.

The electrochemical behavior of copper has been studied vastly [222, 223, 224, 225, 226]. In combination with electrochemical polarization, ellipsometry, and X-ray photoelectron spectroscopy (XPS), Brusic et al. [227] showed that the air formed copper oxide could be reduced under cathodic potentials and stable oxides of copper could be formed reversibly in the pH range of 8–12. At pH values below 7, the dissolution of copper becomes significant. This is especially the case at pH values below 5, at which the formation of stable surface oxides is not possible [147]. In weakly acidic and alkaline solutions, the thickness of this anodic oxide film does not exceed 6 nm. In borate buffer, pH 8.4 at 250 mV, it has a thickness of less than 2 nm [224]. Therefore, in situ ECNI-AFM tests on the copper sample were performed in Borate buffer solution containing 0.02 M H_3BO_3 and 0.005 M $\text{Na}_2\text{B}_4\text{O}_7 \cdot 10\text{H}_2\text{O}$. Figure 5.10 shows the potentiodynamic polarization curve of a copper (111) single crystal in a Borate buffer solution measured during an in situ NI-AFM experiment. Using the procedure given in 4.1, the copper sample was prepared and put into experimental setup (fig-

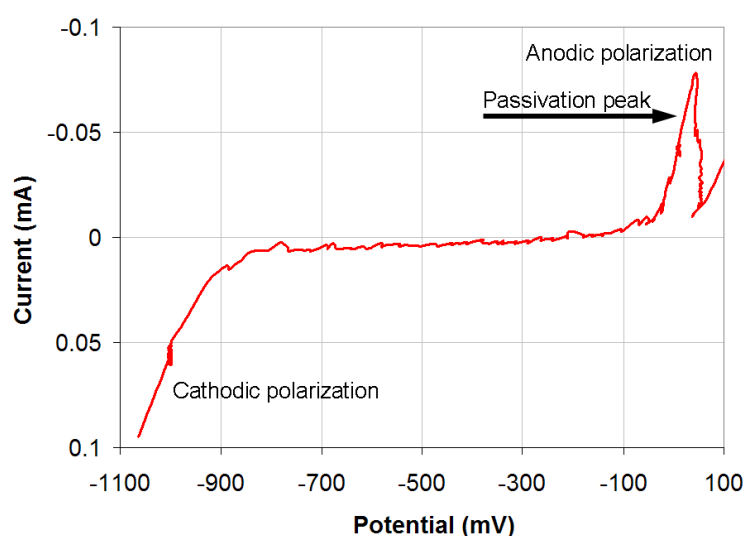
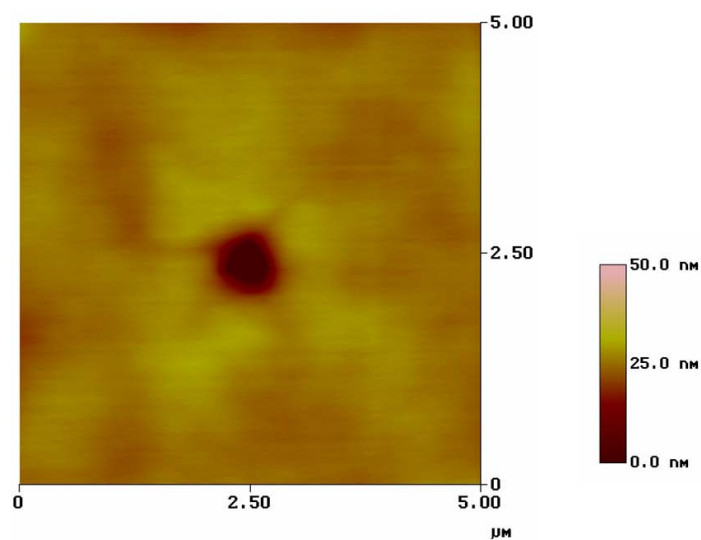
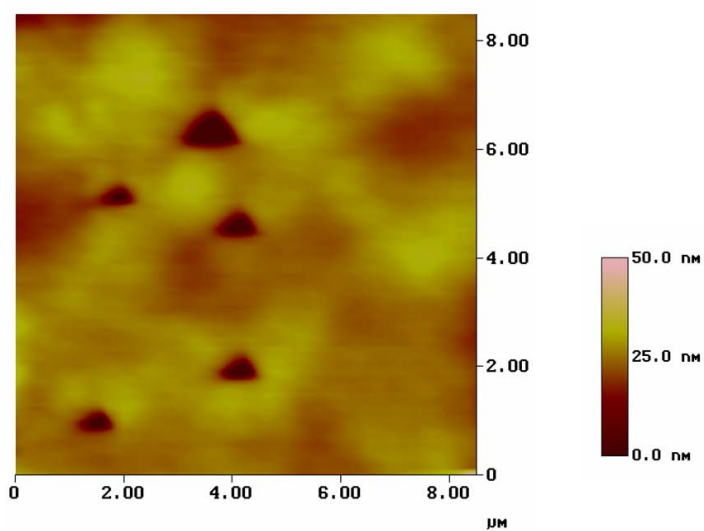


Figure 5.10: Potentiodynamic polarization curve of copper (111) single crystal in Borate buffer (0.02 M H_3BO_3 and 0.005 M $\text{Na}_2\text{B}_4\text{O}_7 \cdot 10\text{H}_2\text{O}$).

ure 4.9). Figure 5.11a shows the topography and the quality of the surface achieved after electropolishing. The solution was injected from outside and into the electrochemical cell while the electrochemical potential was kept at -1000 mV (figure 5.10). As mentioned before, under these circumstances the air formed oxide film on the surface will be reduced. However, in our experiments the removal of this oxide film did not change the topography, as can be seen in figure 5.11b. The resulting load displacement curves under cathodic and anodic potentials are given in figures 5.12 and 5.13 respectively. The first part of the load displacement curves, before pop-in, is fitted with the Hertzian contact model given by equation (3.4). This resulted in a tip radius of 3 μm as fitting parameter. The presented results clearly show no effect of cathodic polarization on the pop-in load. This means that the cathodic charging of the copper resulted in no change in dislocation nucleation behavior. This is in good agreement with the electrochemical hydrogen charging studies on copper, where no hydrogen absorption in to the metal was observed [221].



(a) In air



(b) In Borate buffer solution polarized to -1000 mV

Figure 5.11: Surface topography of electropolished copper (111) single crystal.

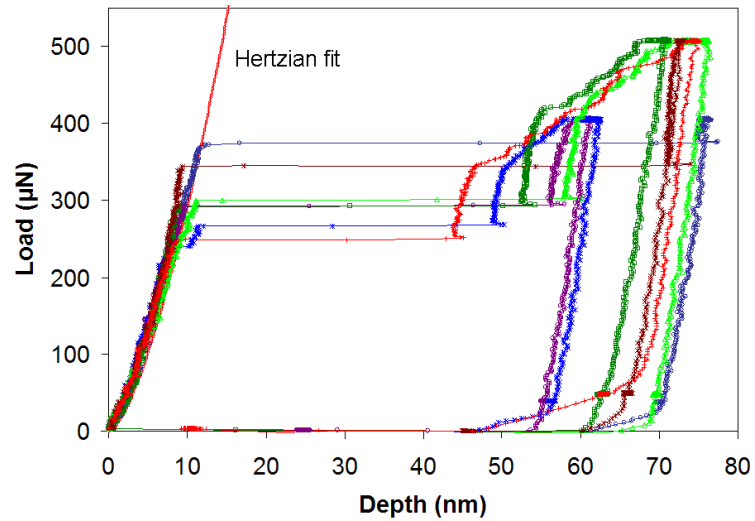


Figure 5.12: Load displacement curves of in situ ECNI-AFM on copper (111) single crystal under cathodic polarization.

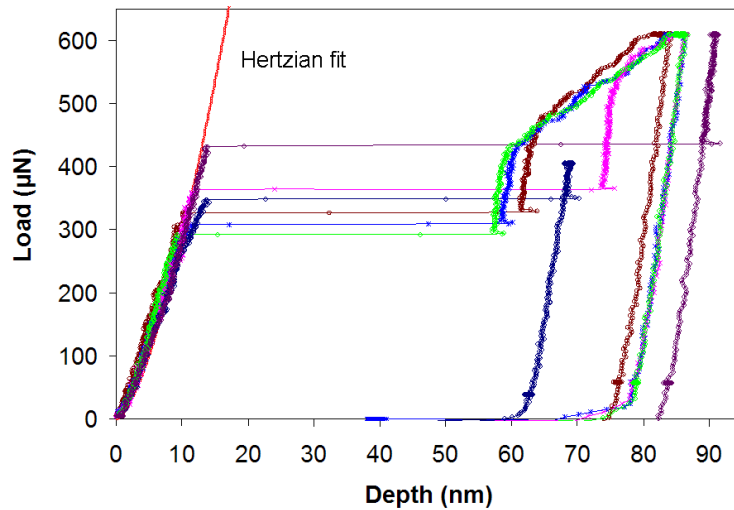
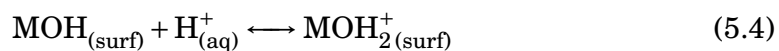


Figure 5.13: Load displacement curves of in situ ECNI-AFM on copper (111) single crystal under anodic polarization.

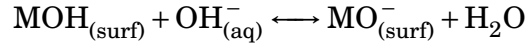
5.3 In situ ECNI-AFM tests on aluminum

Aluminum is a reactive metal protected with a thin stable oxide layer with semi-conductive properties [228]. This gives the metal its exceptional corrosion resistance. It is known that this oxide layer in *aluminum / oxide film / electrolyte* systems exhibit rectification [229]. This means that anodic polarization of aluminum electrodes covered with oxide films gives rise to small currents, while cathodic polarization results in large currents. This oxide film is not reducible inside an aqueous electrolyte. At potentials cathodic to the open circuit potential (OCP) of aluminum, cathodic hydrogen evolution due to the reduction of hydrogen ions and water occurs simultaneously with anodic oxidation and dissolution processes. In this potential region, corrosion rates are greater than at potentials near the OCP [230]. Cathodic enhancements of corrosion are viewed by some investigators to be caused by an increased solution pH near the metal surface, resulting from the production of hydroxide ions [231]. Others, however, attribute cathodic corrosion of aluminum to hydration of the surface oxide film at cathodic potentials, which decreases the resistance of the film toward ionic transport [232, 233]. This of course makes the electrochemical hydrogen charging of aluminum without damaging the surface difficult. This was the motivation to find an alternative method.

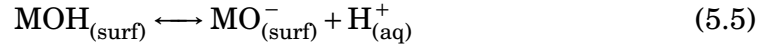
In aqueous solutions, the oxide film is amorphous, and its composition continuously changes from a highly hydrated outer layer to aluminum oxide at the interface of the metal and the oxide film. This oxide layer actively interacts with the solution environment, it grows, transforms, and incorporates solute ions. These transformations are highly dependent upon the composition of the solution. Among several key parameters, the solution pH has one of the largest influences on several processes, both at the interface and interphase levels. Specifically, pH affects the dissolution of aluminum and its oxide film, adsorption on the passive film, and surface charge on the oxide. Little is known, however, about how the pH affects the composition, such as the ion content and structure of the film [234]. It is well known that oxide surfaces or oxide-covered metals exposed to either the ambient environment or immersed in aqueous solutions terminate in an outermost layer of hydroxyl groups due to their interaction with water molecules [235]. In aqueous solutions, the surface hydroxyl groups will remain undissociated if the pH of the aqueous solution is the same as the isoelectric point (IEP) of the oxide. If the pH is less than the IEP, the surface will acquire a positive charge



If the pH is greater than the IEP, the surface will acquire a negative charge



or



This means that, with selection of a proper pH in solution it is possible to promote hydrogen absorption even without external polarization.

A contact angle method has been employed recently, and by using this method it has been determined that the surface's IEP for the air-formed oxide film on aluminum has the value 9.5 [236, 237, 238]. According to the equations (5.4) and (5.5) the pH can greatly effect the hydrogen absorption during immersion of the sample in electrolyte under OCP the tests on aluminum were performed in two different solutions, pH 8.9 Borate buffer containing 0.02 M H_3BO_3 and 0.005 M $\text{Na}_2\text{B}_4\text{O}_7 \cdot 10\text{H}_2\text{O}$ and pH 6, 0.05 M Na_2SO_4 .

The polycrystalline high purity (99.99%) aluminum sample was cut by EDM and then heat treated at 600 °C in order to achieve grains at about 1 mm in size, as can be seen in figure 5.14. Electropolishing of aluminum (see table 4.2) resulted in a very smooth surface, as shown in the surface topography image in figure 5.15a. However, there were defects on the surface which, can be seen both in SEM (figure 5.16) and higher magnification NI-AFM images (figure 5.15b) taken from the surface. The backscatter electron (BE) image (5.16b) taken from the same area shows no underlying defects below the surface within the resolution limits of this technique. During nanoindentation tests, all indents have been done on defect free parts of the surface, identified by in situ imaging of the surface prior to indentation. The procedure of testing was as explained before in section 5.2. Typical load displacement curves of aluminum in air are shown in figure 5.17. A clear pop-in was observed between 200 μN to 300 μN for all indentations. The elastic part of the load displacement curves are fitted with the Hertzian model for elastic contact (3.4) and shown in figure 5.17. There is a long lasting discussion on the origin of the pop-in load (see section 3.6.2.3), specially in the case of aluminum, where the thickness of the film and its mechanical properties are favorable for the film break down hypothesis [239]. Consequently, the observed effect on pop-in load under different conditions in this work may be related to the surface effect and not the effect of hydrogen. To reject this hypothesis, nanoindentation experiments were performed on a similar sample which was cut from a tensile fatigue test sample of the same material, after fracture in the fatigue test. Special care was taken to prepare the sam-

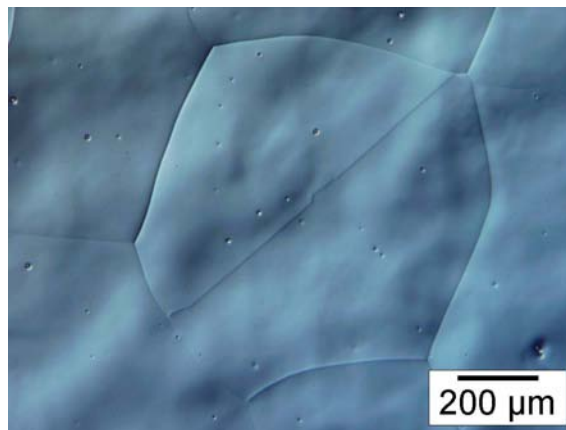
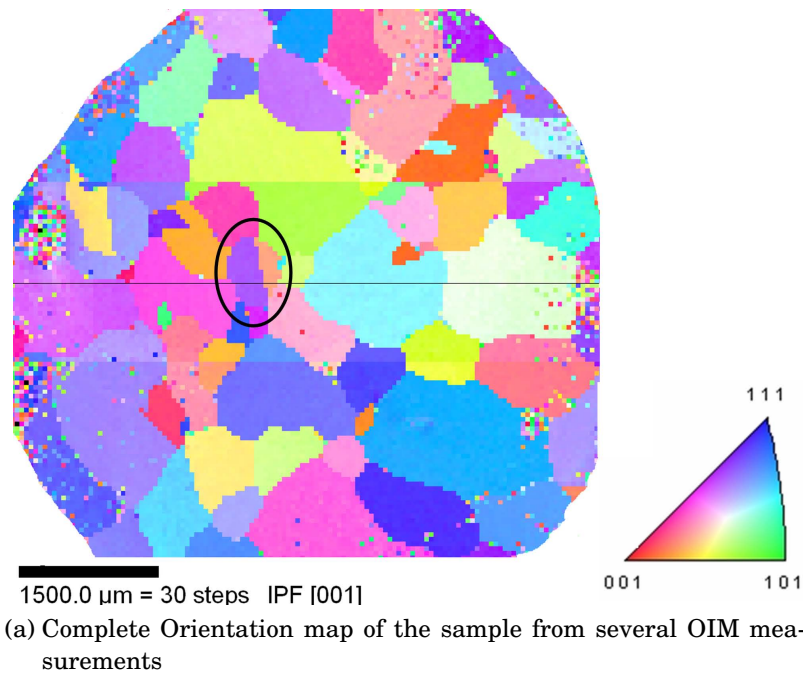
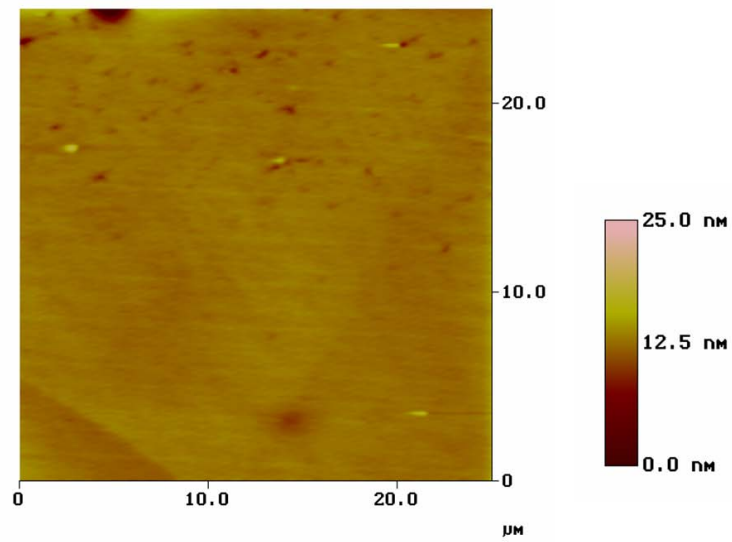
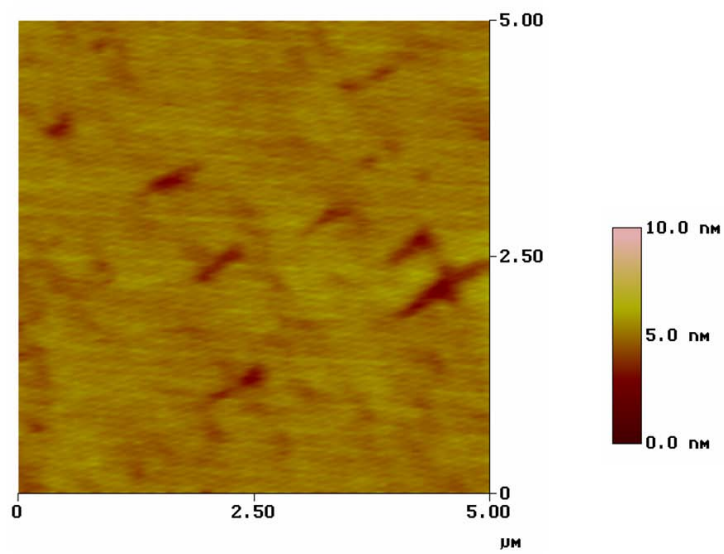


Figure 5.14: OIM and optical microscope images of annealed pure aluminum with grains about 1 mm diameter. The grain in optical micrograph is marked on the OIM image.

ple with the similar surface preparation procedure to have the same surface condition as on the annealed sample. Figure 5.18 shows a secondary electron micrograph (topography) of this sample after electropolishing. Figure 5.19 also shows a topography image taken during nanoindentation of this sample. The topography and roughness of the cyclic deformed sample scarcely showed any difference to the annealed sample. However, by using the ECCI, the underlying dislocation structure of the sample was revealed. As shown in figure 5.20 by



(a) Big area scan



(b) Small area scan, where fine defects are observable

Figure 5.15: Surface topography of electropolished pure aluminum sample.

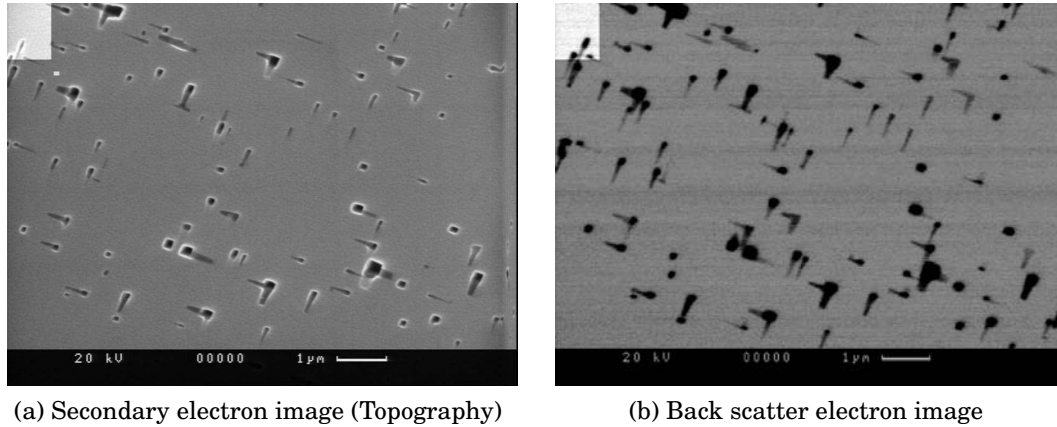


Figure 5.16: SEM image of the freshly electropolished pure aluminum sample. The defects on the surface of the sample are observable in the SE image (a) and no lattice distortion due to the underlying dislocation substructure is observable in BE image (b).

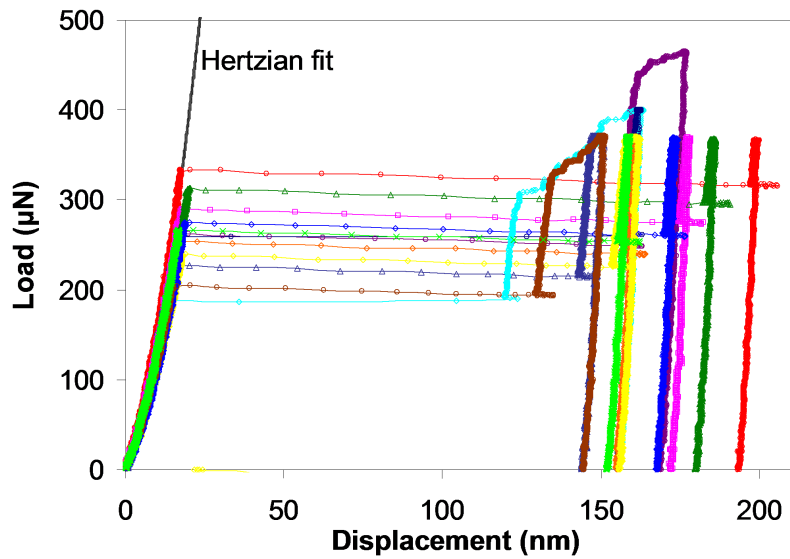


Figure 5.17: Typical load displacement curves of aluminum in air

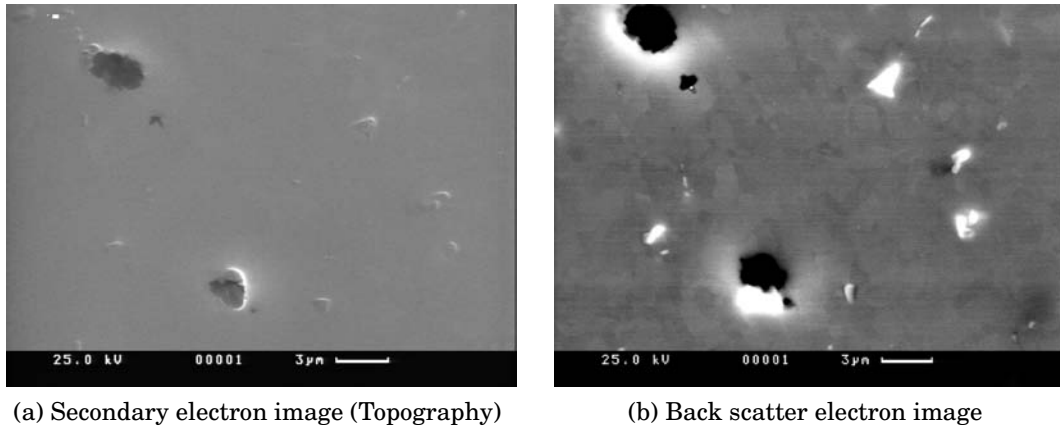


Figure 5.18: SEM image of the freshly electropolished pure aluminum sample, which was cyclically deformed during fatigue test. The defects on the surface of the sample are observable in the SE image (a) and lattice distortion due to the underlying dislocation substructure is observable in BE image (b).

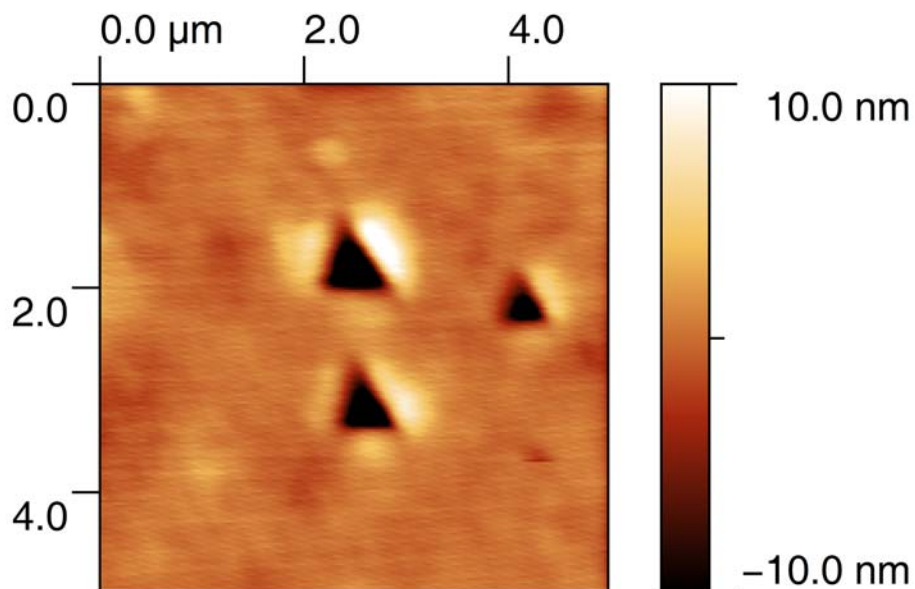


Figure 5.19: Surface topography image taken from electropolished cyclically deformed pure aluminum sample during nanoindentation tests.

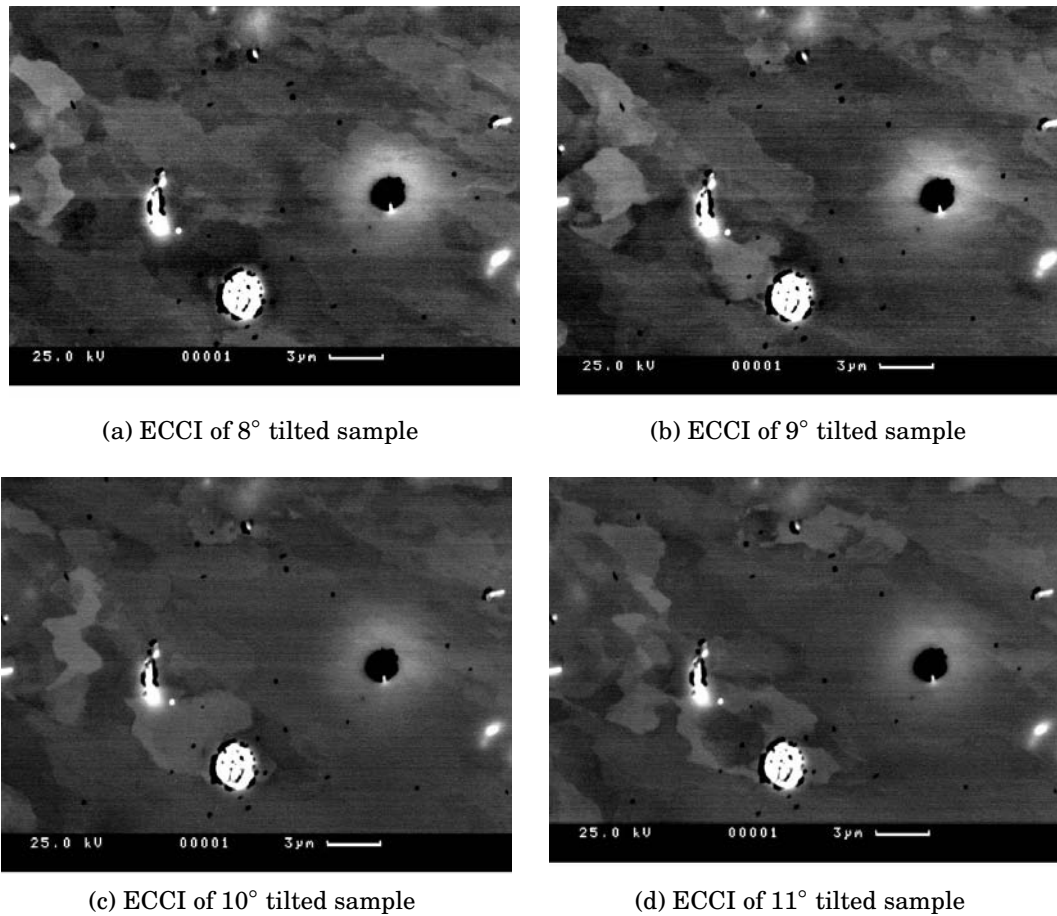


Figure 5.20: ECCI from electropolished pure aluminum sample cyclically deformed during a fatigue test. The underlying dislocation cell structure in metal formed during fatigue test resulted in a change of the electron channeling contrast by tilting the sample.

tilting the sample at different angles the channeling contrast is changing overall in the sample. This shows a high dislocation density distributed uniformly in the sample. However, in the case of annealed sample there was no change in the BE contrast (figure 5.16b), as a result of dislocation substructure (lattice distortion) observable.

Nanoindentation of the cyclically deformed sample with high dislocation density (figure 5.20) resulted in a completely different load displacement curves without any pop-in events (figure 5.21). The high dislocation density in this sample resulted in activation of the existing dislocation sources in the sample during each indentation test. This high dislocation density decreased the chance of hitting a dislocation free region in the sample which is necessary for observation of pop-in (homogeneous dislocation nucleation). This indentation results proved that pop-in in aluminum is originate from homogeneous dislocation nu-

cleation and not the surface film break down.

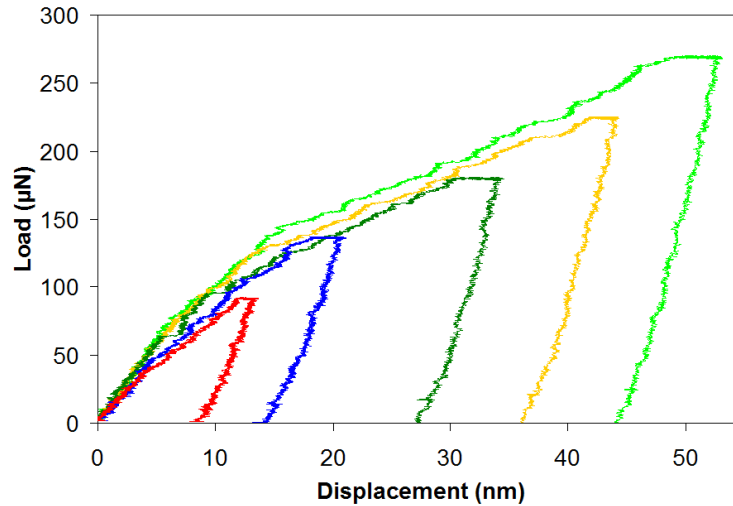


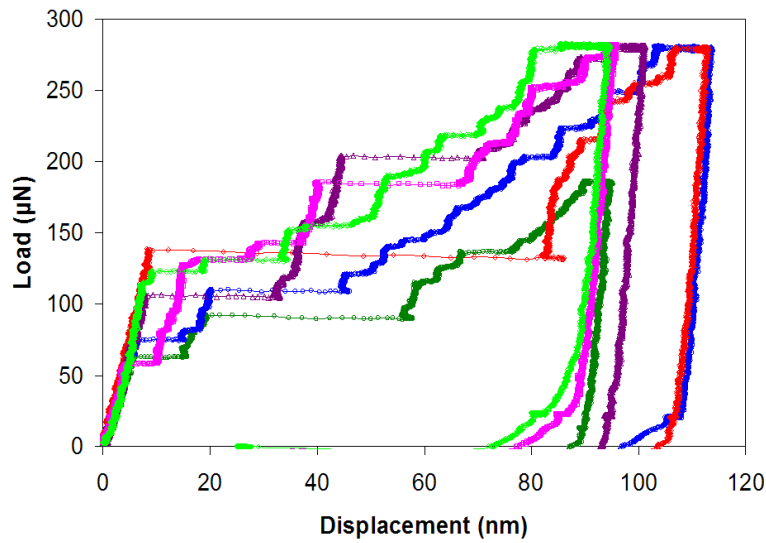
Figure 5.21: Load displacement curves of electropolished pure aluminum sample cyclic deformed during a fatigue test.

5.3.1 ECNI-AFM of aluminum in pH 6, sulfate solution

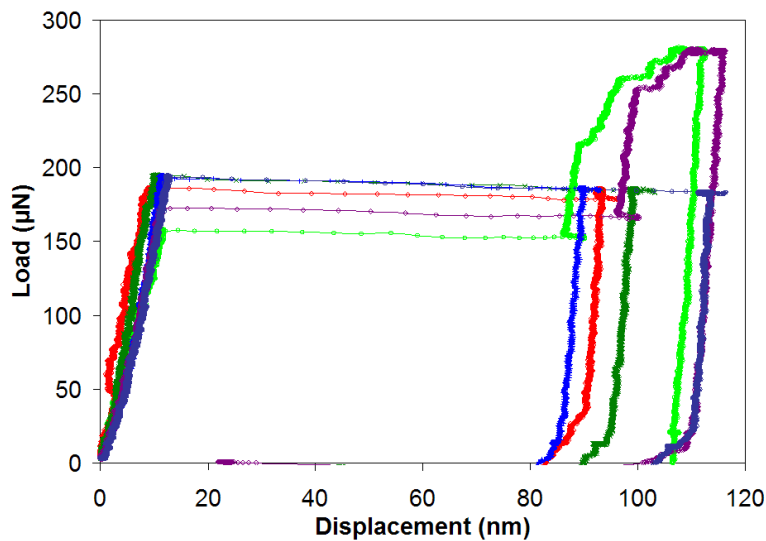
In the experiments done in the pH 6, 0.05 M Na_2SO_4 solution, a drastic change in the pop-in behavior was observed at the OCP. As shown in figure 5.22a, the pop-in load was decreased to lower values than in air (figure 5.17). Multiple pop-ins were always observed during nanoindentation at the OCP. The load displacement curves did not change in slightly more cathodic potentials. Polarization of the sample to anodic (250 mV), however, increased the pop-in load and resulted in disappearance of the multiple pop-ins (figure 5.22b). This resulted in observation of load displacement curves similar to the ones in air. Figure 5.23 shows the surface topography of the sample under OCP and cathodic potentials. No surface roughening was observed, i.e. the change in pop-in behavior at the OCP cannot be attributed to a change in the surface topography.

5.3.2 ECNI-AFM of aluminum in pH 8.9, borate buffer

A completely different nanoindentation behavior was observed at the OCP in pH 8.9 borate buffer as shown in figure 5.24b. The behavior was similar to the one in air and in solution with pH 6 under anodic potential (figure 5.17 and figure 5.22b). The load displacement curves in this solution did not change under



(a) OCP potential

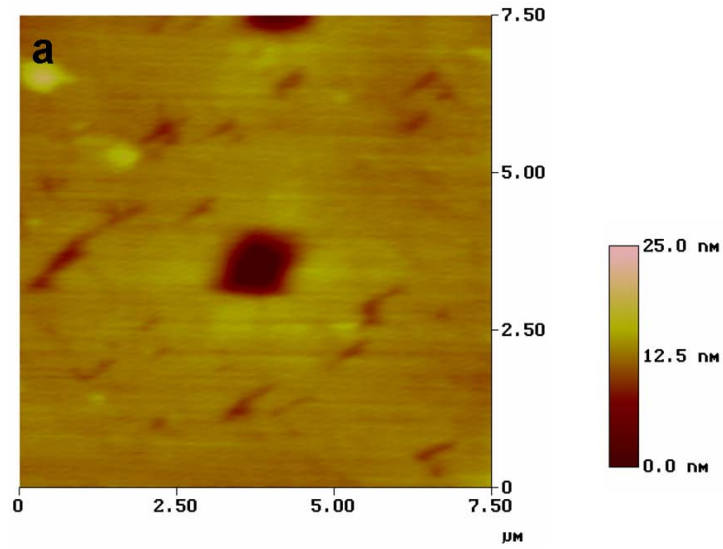


(b) Anodic potential (250 mV).

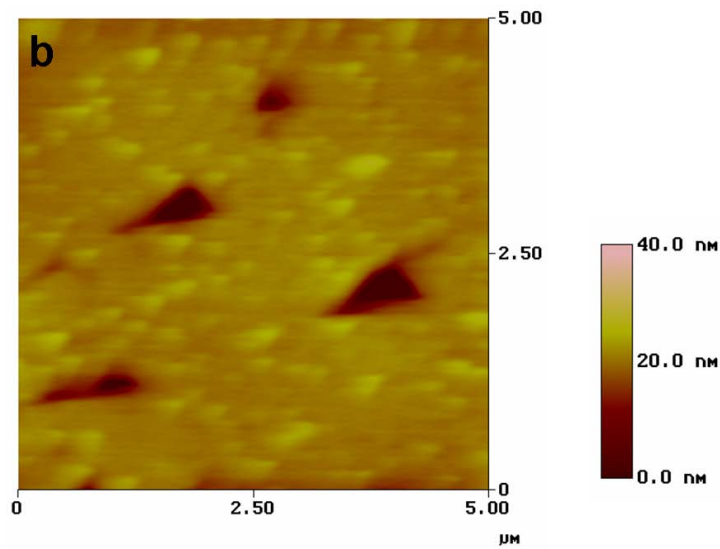
Figure 5.22: Typical load displacement curves of aluminum in pH 6, 0.05 M Na₂SO₄ solution.

anodic polarization. However, cathodic polarization changed the load displacement curves. As shown in figure 5.24c the curves became similar to the curves in pH 6 solution at the OCP. This means that pop-ins occurred at a lower load than before, and there were multiple pop-in events for each nanoindentation.

The surface topography of the sample under different conditions is shown in



(a) OCP



(b) Cathodic potential

Figure 5.23: Surface topography of the aluminum sample in pH 6, 0.05 M Na_2SO_4 solution.

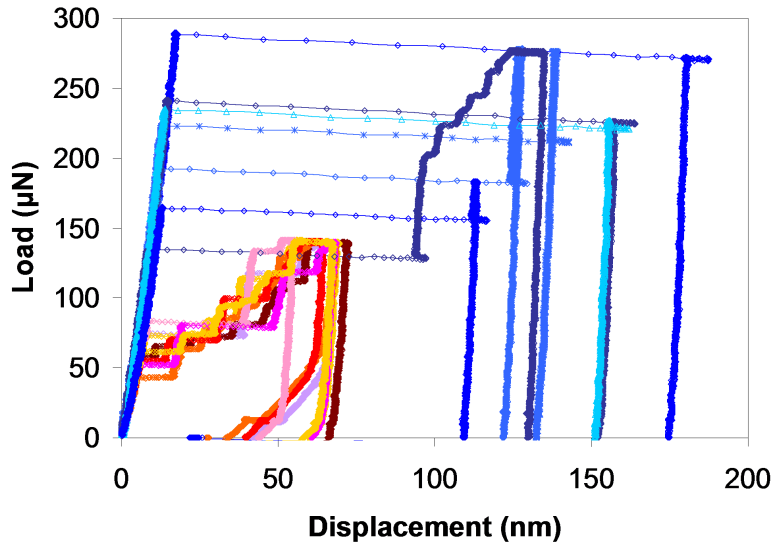
figure 5.3.2. Comparison of the surface topography in air (figure 5.25a) with the ones at the OCP (figure 5.25b), anodic (figure 5.25c), and cathodic (figure 5.25d) shows no surface roughening due to the applied potentials.

Table 5.1 summarizes the mean values of pop-in load, maximum shear stress and its position below the surface for the aluminum sample under different con-

ditions. The maximum shear stress, τ_{max} , and its position below the surface, $h_{\tau_{max}}$, were calculated according to the Hertzian contact model presented in section 3.2 (equation (3.15)). For comparison the theoretical strength ($\mu/10$) according to the Frenkel's model (equation (3.45)) is also given in the table 5.1.

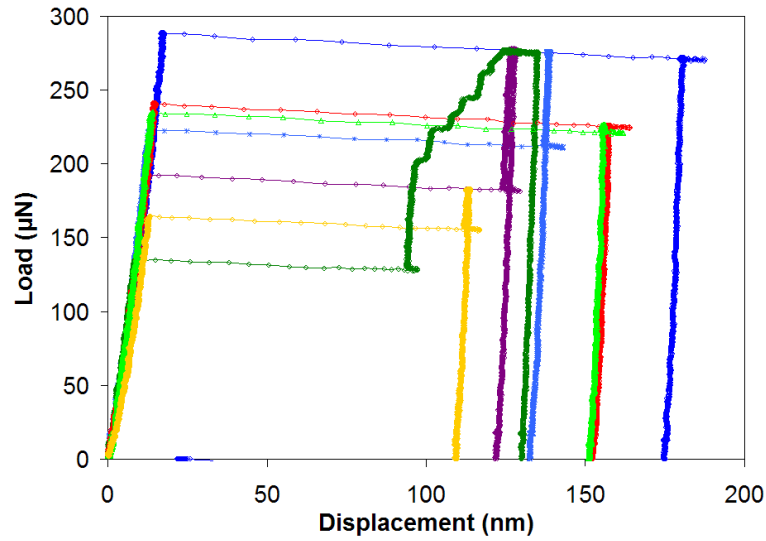
Table 5.1: Effect of hydrogen charging on mean values of pop-in load, maximum shear stress, τ_{max} , and its position below the surface, $h_{\tau_{max}}$, for the aluminum sample under different conditions. which are calculated according to the Hertzian contact model and equation (3.15).

Condition	pH	Pop-in load (μN)	Tip radius (μm)	τ_{max} (GPa)	$h_{\tau_{max}}$ (nm)	$\mu/10$ (GPa)
Air		280	3	0.95	100	2.3
OCP	6	120	3	0.67	83	2.3
	8.9	212	3	0.9	90	2.3
Anodic	6	205	3	0.85	90	2.3
Cathodic	8.9	80	3	0.6	65	2.3

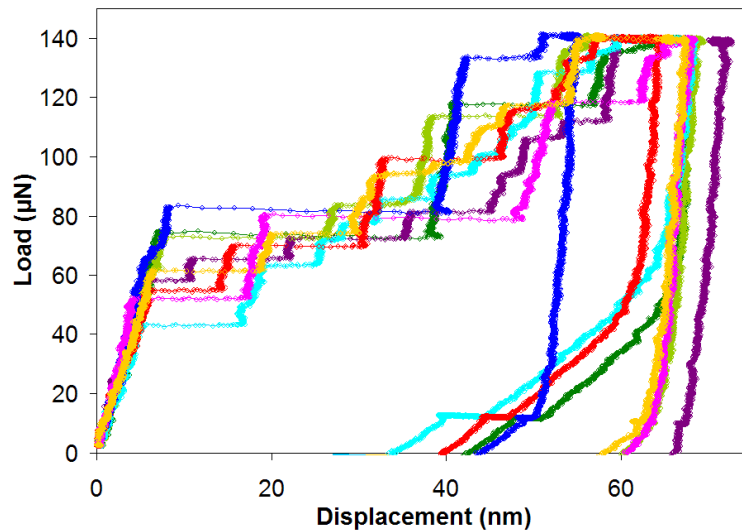


(a) OCP(blue) and cathodic (Red) together for comparison

Figure 5.24: Typical load displacement curves of aluminum in pH 8.9 Borate buffer solution (continued on next page).



(b) OCP potential



(c) Cathodic potential

Figure 5.24: Typical load displacement curves of aluminum in pH 8.9 Borate buffer solution (continued from next page).

5.3.3 pH effect on pop-in load in aluminum

The pH of 0.05 M Na_2SO_4 solution (pH=6) was lower than IEP for aluminum (pH=9.5). Therefore, according to the reaction (5.4) H^+ ions were adsorbed on the sample surface. First of all, semiconductive properties of the aluminum oxide, existing on the surface of the sample, results in a rectification effect. This

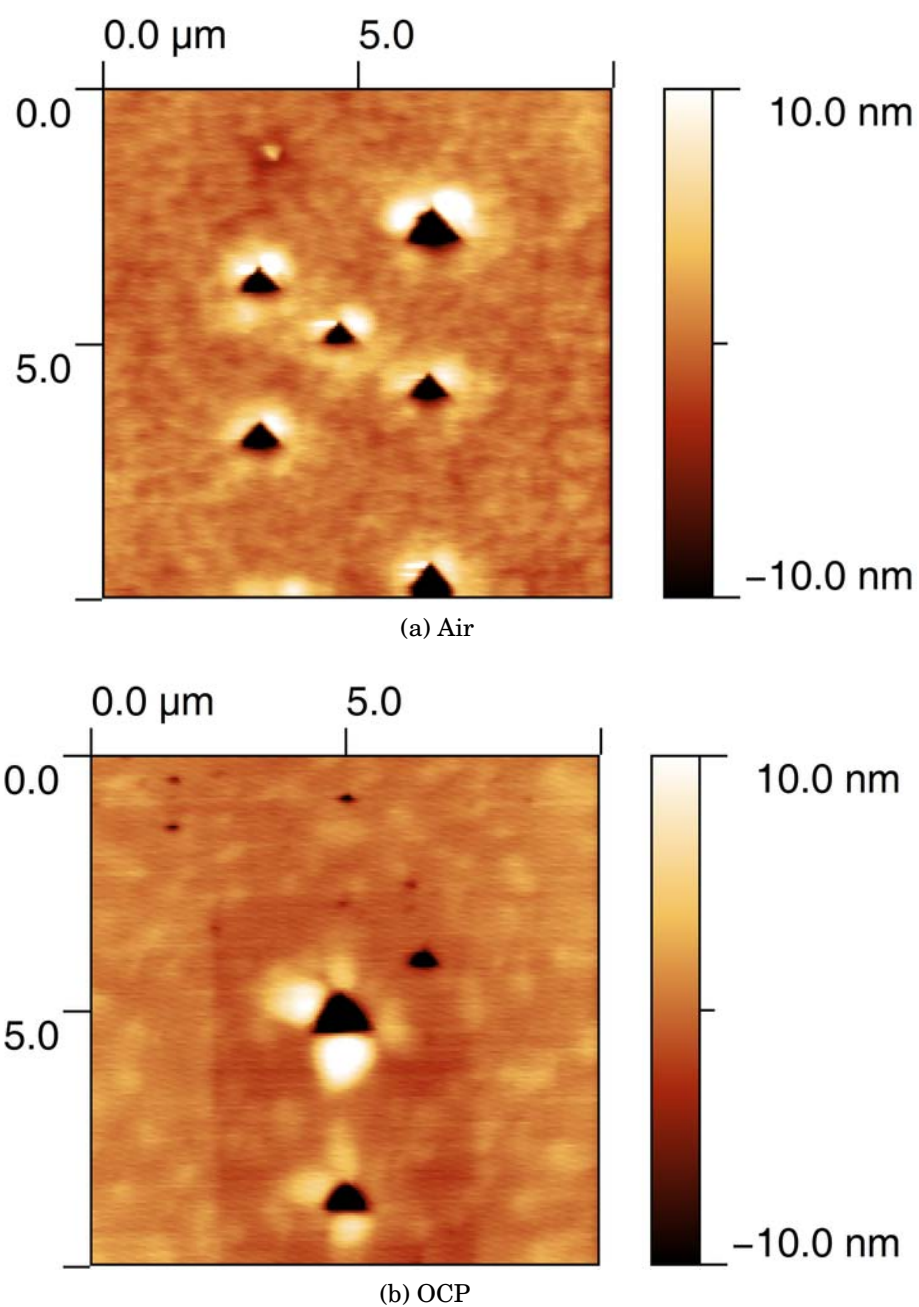


Figure 5.25: Typical surface topography images of aluminum in pH 8.9 Borate buffer solution taken under different conditions (Continued on next page).

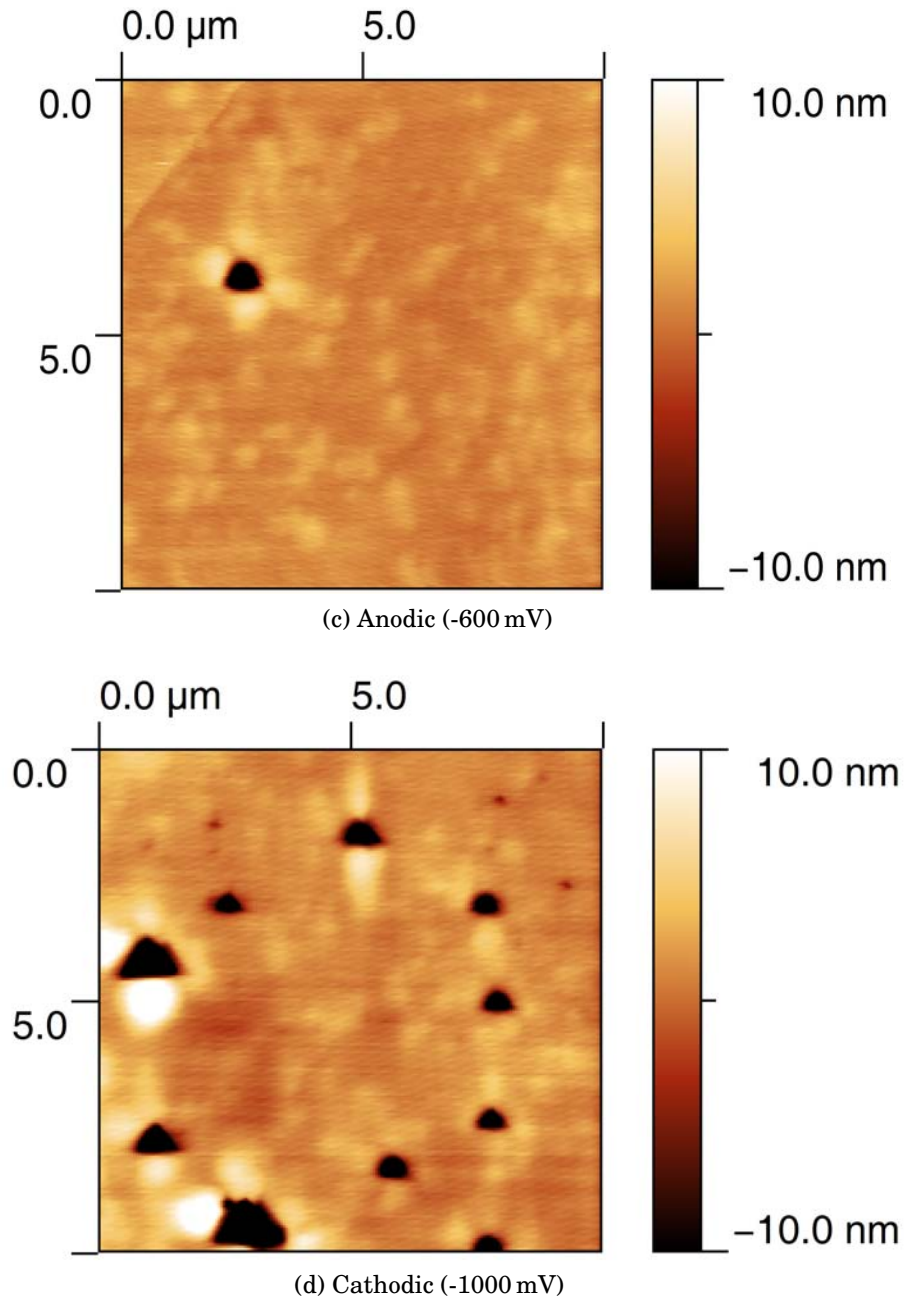
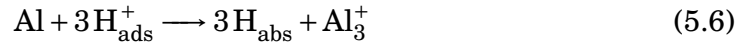


Figure 5.25: Typical surface topography images of aluminum in pH 8.9 Borate buffer solution taken under different conditions (continued from previous page).

means easy movement of current carriers (i.e. electron and protons, H^+) from *oxide/electrolyte* in direction of *metal/oxide* interface. On the other hand, as shown in figures 5.16 and 5.15b, the oxide film on the sample surface is not defect free. Aluminum is a highly reactive metal and H^+ is an extremely mobile ion. Therefore, the absorbed H^+ ions can easily react with the aluminum substrate in defect sites, oxidize the aluminum and thereby self become reduced



The hydrogen atoms reduced according to the equation (5.6), were absorbed in to the metal as described in section 2.2.2.2. These hydrogen atoms then can influence the mechanical behavior of metal as shown in figure 5.22a. Polarization to anodic potentials inhibited the adsorption of H^+ ions. Therefore again the same pop-in behavior as in the air was observed (figure 5.22b). In the case of the experiments in borate buffer, the solution pH was quite near to the IEP. Therefore, the surface condition of the sample did not changed. Accordingly no change was observed in the load displacement curves. However applying cathodic potentials to the sample promoted the adsorption, reduction and absorption of H^+ ions. The absorbed hydrogen consequently contributed in the change of mechanical properties, as can be seen in figure 5.24c.

5.4 In situ ECNI-AFM tests on Fe-3wt.%Si

The Fe-3wt.%Si alloy was received in the coil form with 1 mm thickness. The composition of the alloy is given in table 5.2 provided by the producer. A circular Fe-3wt.%Si sample was cut from the coil by EDM and heat treated at 1200 °C for one week in order to achieve big grains in the range of few millimeters, as shown in figure 5.26. The grain boundaries were marked by microindentations according to the OIM results presented in figure 5.27. This made optical positioning of the NI-AFM tip on a specific grain possible. By using this procedure, it was possible to be confined to a single grain and thereby exclude orientation effects from the indentation results. The Fe-3wt.%Si alloy is a single phase bcc crystal which has been used as a model material in materials mechanic [14], as well as hydrogen embrittlement studies [36]. The electrochemical behaviour of this metal is quite similar to the pure iron and has a very low aqueous corrosion

Table 5.2: Composition of Fe-3wt.%Si alloy used in this study

Element	C	Si	Mn	P	S	Cr	Ni	Mo	Cu	Al	Ti	Nb	V	B	Zr	Ce
Weight%	0.003	2.383	0.202	0.013	0.012	0.033	0.048	0.015	0.020	0.365	0.005	0.020	0.002	0.0008	0.005	0.009

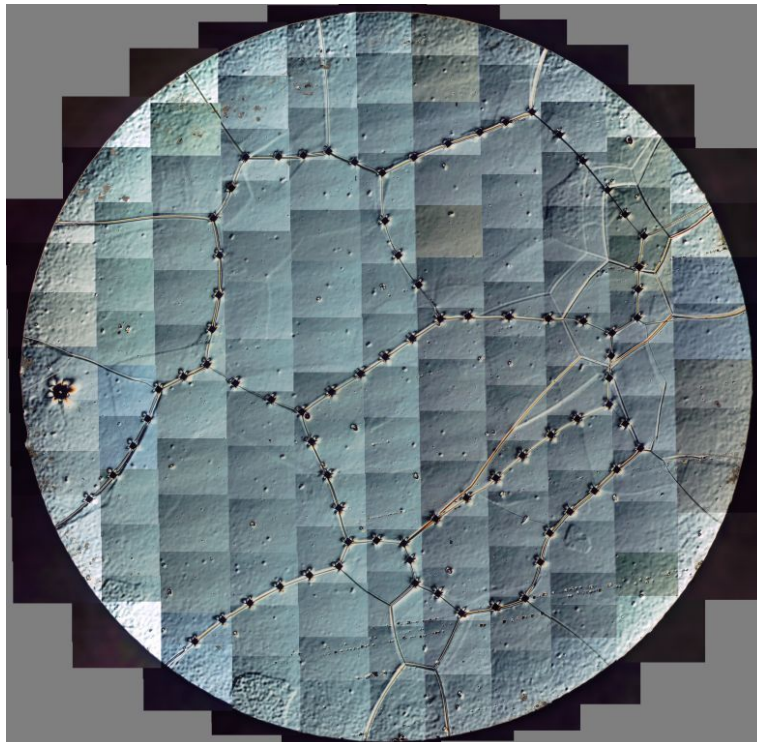


Figure 5.26: Optical microscope images of Fe-3wt.%Si alloy after heat treatment paste together to reproduce a complete image of the sample with the marked grain boundaries according to the OIM results (figure 5.27)

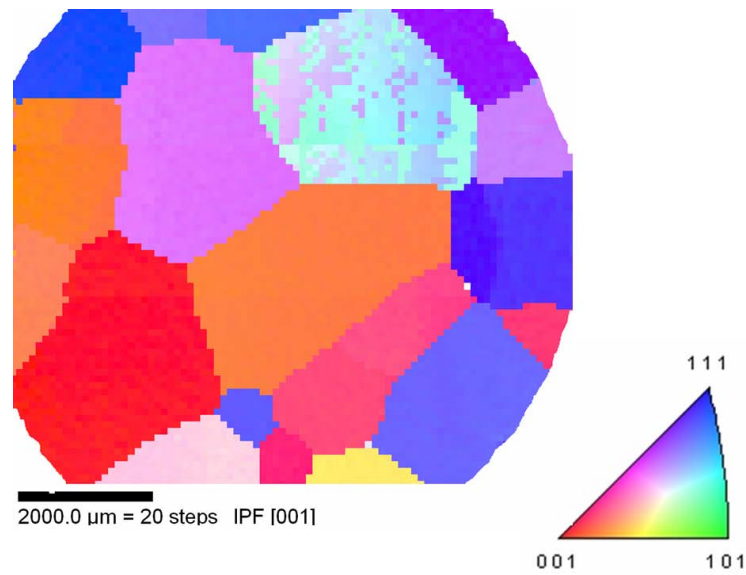


Figure 5.27: Complete orientation map of the Fe-3wt.%Si sample after heat treatment reproduced by pasting several OIM images together. This map is used to mark the grains with microindents as shown in figure 5.26.

resistance in solutions with low pH, as shown in Pourbaix diagram of iron (figure 5.28). Therefore, in situ ECNI-AFM tests were performed in a pH 8.9 borate

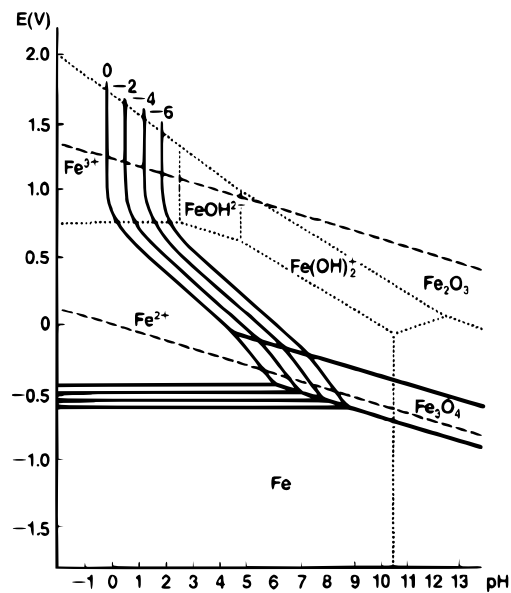


Figure 5.28: Pourbaix diagram of iron

buffer solution. This electrolyte has been preferred because of the possibility of both controlled cathodic removal of prior oxide films and highly efficient anodic passivation [240]. Since little or no iron dissolution occurs during anodic treat-

ment in borate buffer, roughening of the electrode surface does not occur. This enables subsequent nanoindentations. The borate buffer solution has become a standard electrolyte for studying the anodic behavior of iron and its alloys [241]. However, it is known that very limited amounts of chloride ions in borate buffer solutions results in a break down of the passivity [242]. During the in situ electrochemical nanoindentation experiments, due to the limited volume of the electrochemical cell (figure 4.8) and use of Ag/AgCl reference electrode, contamination of electrolyte with Cl^- ions was unavoidable. Figure 5.29 shows the polarization curve for the Fe-3wt.%Si sample in borate buffer solution measured inside the ECNI-AFM setup. The cyclic voltammetry curve measured at the same time is shown in figure 5.30. The low passivation breakdown potential, as well as low repassivation potential observed in this curve, clearly shows the effect of chloride contamination. Therefore, all attempts for producing a stable passive layer was defeated and resulted in a corroded surface which was not suitable for nanoindentation experiments. Figure 5.31 shows the chronoamperometry curves measured during an experiment made to produce a stable passive film under -300 mV anodic potential predicted from polarization curve in figure 5.29. As can be seen from the figure, the anodic current increased with time, which shows the breakdown of the passivation with time. The resulting topography image of the surface is shown in figure 5.32. The surface roughening and localized corrosion due to chloride contamination can clearly be seen. Therefore, in

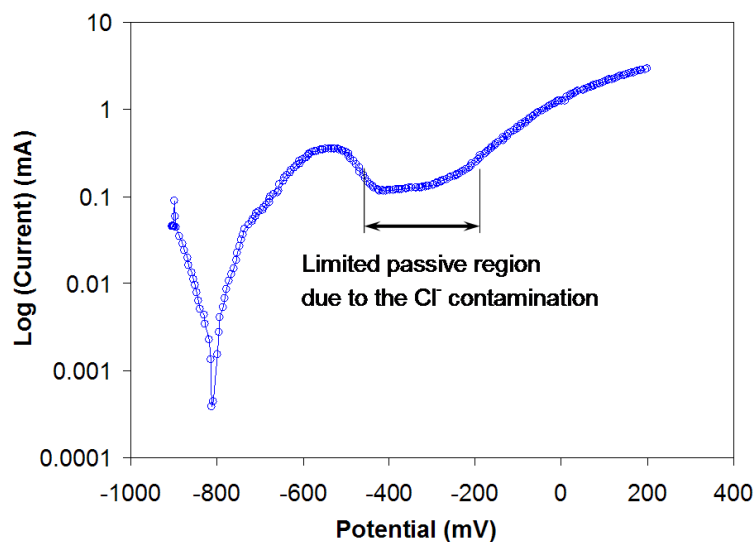


Figure 5.29: Polarization curve of Fe-3wt.%Si sample measured inside ECNI-AFM setup. As a result of electrolyte contamination with Cl^- ions very limited passive region is observed.

the case of the Fe-3wt.%Si sample, the nanoindentation results under cathodic potential will be compared with the results in air. Figure 5.33 shows typical load displacement curves during nanoindentation of the Fe-3wt.%Si sample in air. The same sample was indented in the same grain under a cathodic potential of -1000 mV. This resulted in the load displacement curves shown in figure 5.34.

Imaging of the surface topography under cathodic polarization revealed no surface roughening, as shown in figure 5.35. Table 5.3 summarizes the effect of cathodic polarization on mean values of the pop-in load, maximum shear stress and its position below the surface for the Fe-3wt.%Si sample. The maximum shear stress, τ_{max} , and its position below the surface, $h_{\tau_{max}}$, were calculated according to the Hertzian contact model presented in section 3.2 (equation (3.15)). For comparison the theoretical strength ($\mu/10$) according to the Frenkel's model (equation (3.45)) is also given in the table 5.3.

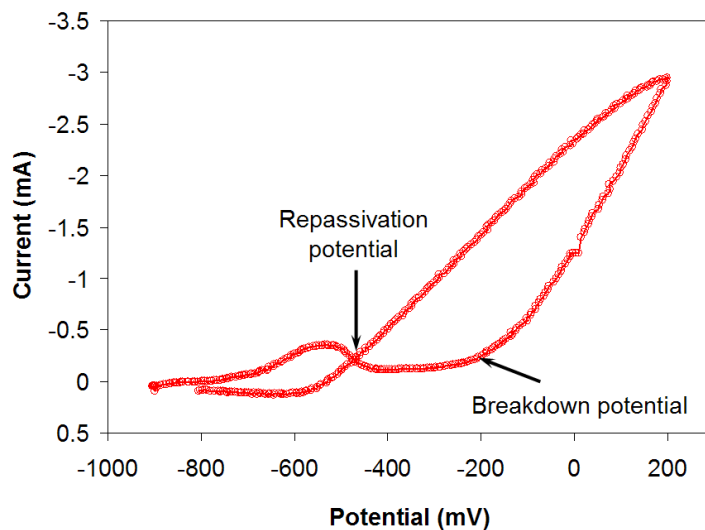


Figure 5.30: Cyclic voltammety curves of Fe-3wt.%Si sample measured inside ECNI-AFM setup. Low passivation breakdown potential and repassivation potential is due to Cl^- contamination electrolyte.

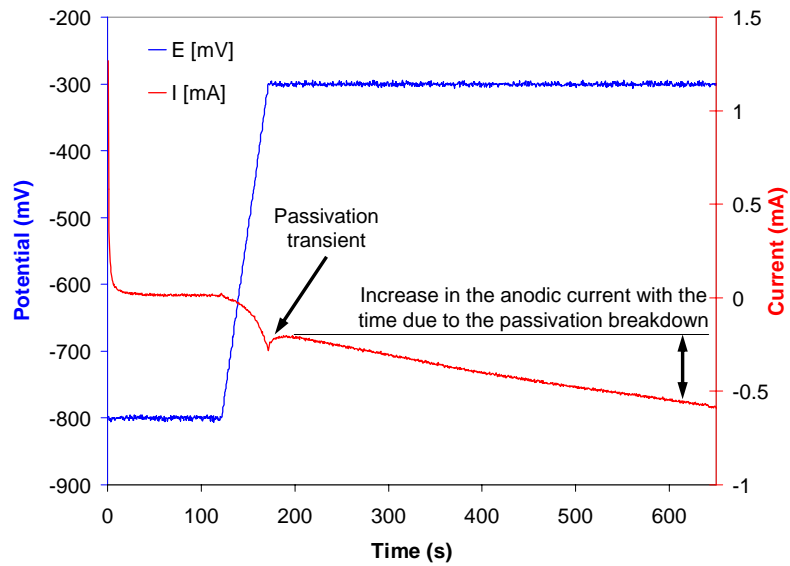


Figure 5.31: Chronoamperometry curve measured during anodic polarization of the Fe-3wt.%Si sample under passive potential of -300 mV in buffer borate where increase in the passive current with the time as a result of chloride contamination is observable.

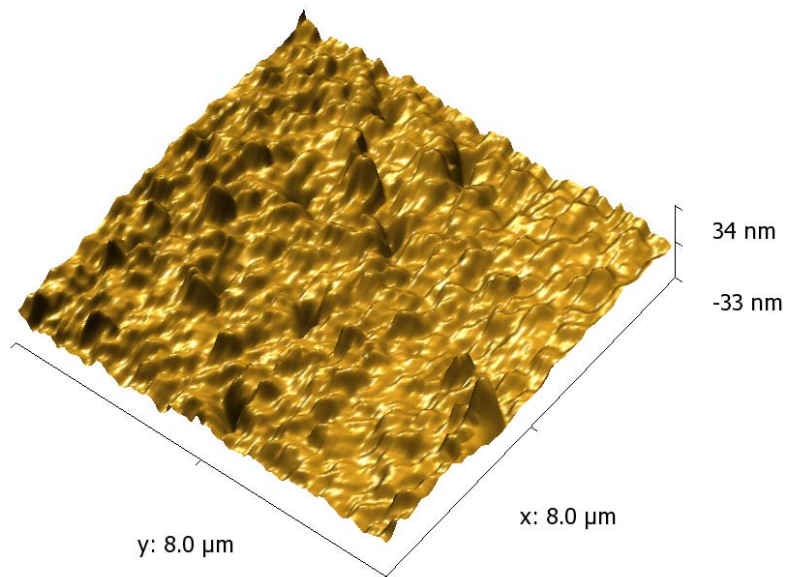


Figure 5.32: Topography image of the Fe-3wt.%Si sample after a short time of anodic polarization in side borate buffer solution. The localized corrosion started on the sample surface due to chloride contamination and passive film breakdown.

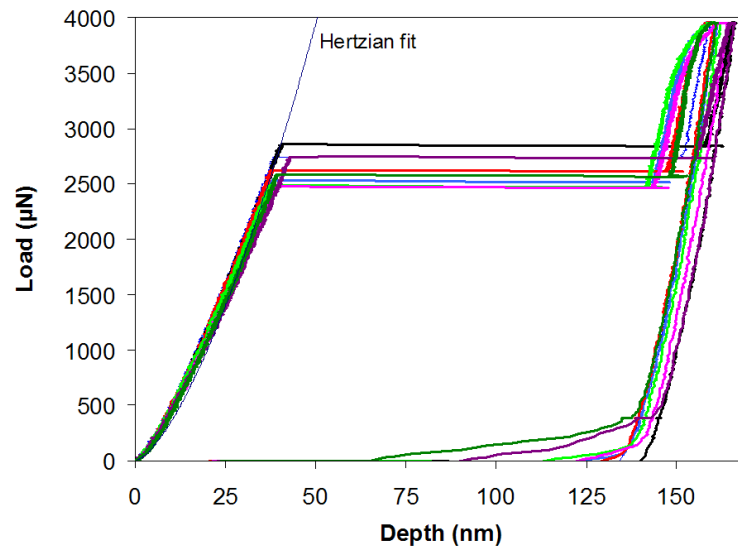


Figure 5.33: Load displacement curves of in situ ECNI-AFM on Fe-3wt.%Si sample in air

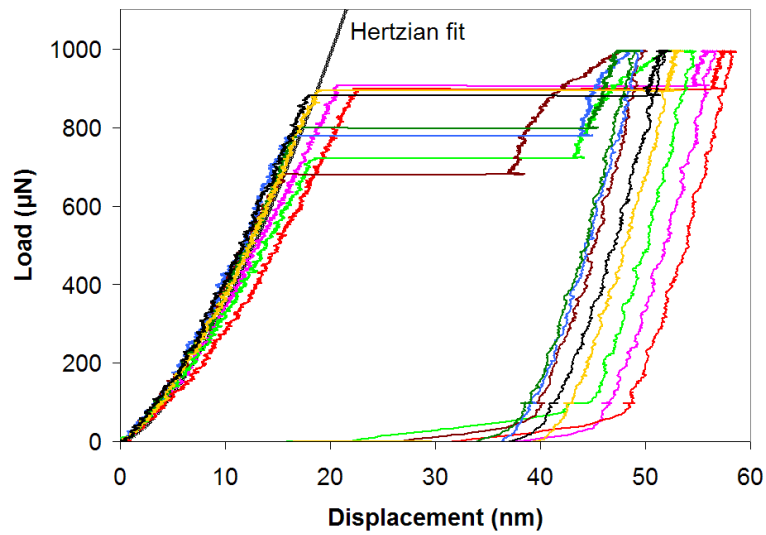


Figure 5.34: Load displacement curves of in situ ECNI-AFM on Fe-3wt.%Si under cathodic polarization of -1000 mV (hydrogen charged).

Table 5.3: Effect of hydrogen charging on mean values of pop-in load, maximum shear stress, τ_{max} , and its position below the surface, $h_{\tau_{max}}$ for the Fe-3wt.%Si sample, which are calculated according to the Hertzian contact model and equation (3.15).

Condition	Pop-in load (μN)	Tip radius (μm)	τ_{max} (GPa)	$h_{\tau_{max}}$ (nm)	$\mu/10$ (GPa)
Air	2600	2	6	122	8.5
Cathodic	840	2	4.32	82	8.5

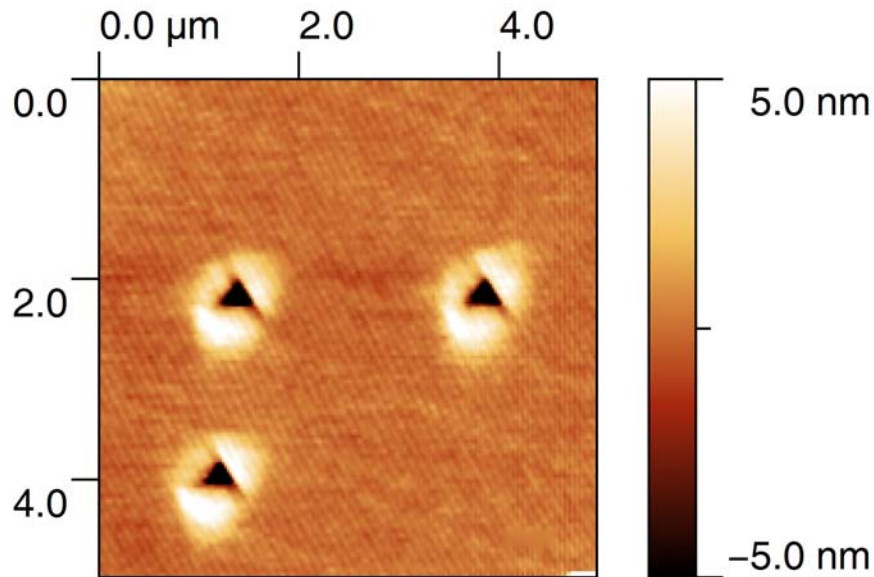


Figure 5.35: Surface topography of the Fe-3wt.%Si sample under cathodic polarization of -1000 mV (hydrogen charged).

5.5 In situ ECNI-AFM tests on a FeAl intermetallic alloy

Iron aluminides are candidate high-temperature and corrosion resistance materials. The phase diagram of the Fe-Al system reveals that several intermetallic compositions exist in this system (figure 5.36). The intermetallic alloys considered for structural applications are based on compositions centered around Fe_3Al and FeAl. The intermetallics with a higher percentage of Al are suitable for coating applications. FeAl possess a B2 crystal structure, as shown in figure 5.37. The unit cell contains two atoms, i.e., the same number as in bcc. In reality, it consists of two interpenetrating primitive cubic cells and it is sometimes referred to as the CsCl type. The aluminum atoms occupy the cube corners of one sublattice and the iron atoms occupy the cube corners of the second sublattice. The commercial importance of iron aluminides for high temperature structural applications has been well established [243]. Iron aluminides contain two of the most easily available metals, namely Fe and Al. They offer low material cost, conservation of strategic materials and lower density than stainless steels. The importance of these iron aluminides is due to their excellent oxidation and sulfidation resistance. The oxidation resistance of Fe-Al alloys increases with increasing Al content. The critical amount of Al for external alumina oxide formation has been determined to be about 14 at.% at 800 °C. The

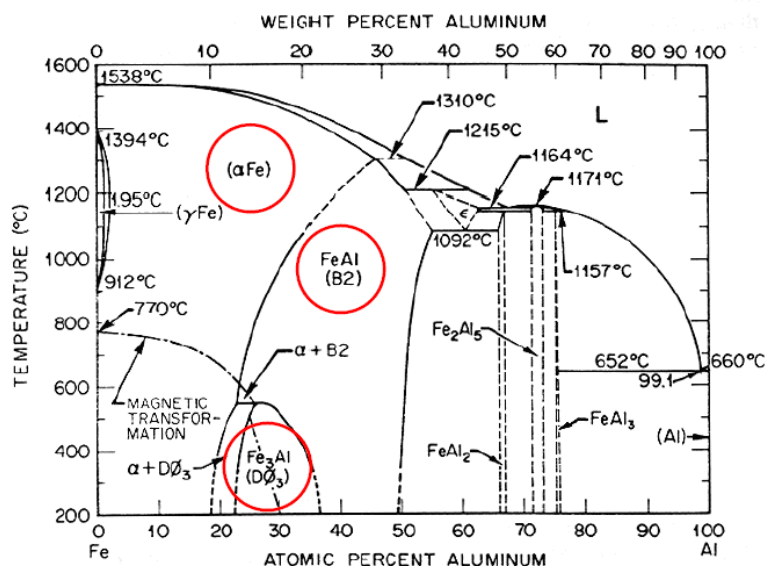


Figure 5.36: Fe-Al equilibrium phase diagram showing the disordered iron solid solution (α) and the ordered intermetallic phases (Fe_3Al and FeAl) that are present from approximately 11–35wt.%Al.

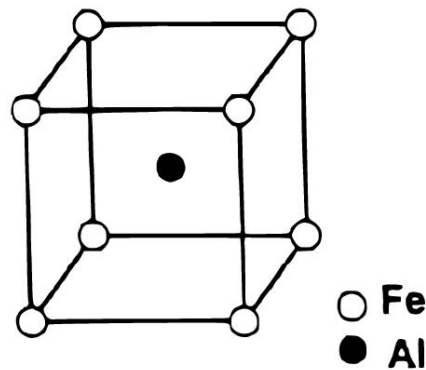


Figure 5.37: B2 crystal structure of ordered FeAl alloy

formation of a stable adherent oxide of alumina is responsible for the excellent oxidation resistance of the iron aluminides. Additionally, iron aluminides possess excellent sulphidation resistance. This is an important property as iron aluminides are considered to be used as structural materials for fossil-based energy conversion systems, where a relatively high amount of sulfur is encountered. Other possible engineering applications include jet engine compressor blades and housings, structural members in aircrafts, heating elements, furnace fixtures, heat exchangers, piping and tubing in automotive equipment, food handling equipment, chemical processing equipment, magnetic and electronic parts and nuclear reactor components [243, 244]. In spite of all these inherent advantages, the binary iron aluminides suffer from hydrogen embrittlement. It has recently been recognized that the poor ambient temperature ductility is due to hydrogen embrittlement [245, 244]. The hydrogen embrittlement behavior of iron aluminides has been the subject of very few works [246, 244, 247], although this topic should be of interest for a reliable development of this class of intermetallics. Therefore in situ NI-AFM experiments were performed on Fe-40wt.%Al (100) oriented single crystal iron aluminides. The passivity and passivity breakdown of FeAl-based iron aluminides in borate buffer solution (pH 8.4) have been studied by De Cristofaro et al. [248]. They showed that the addition of aluminium to iron enables the formation of a passivating layer.

Surface films grown on the intermetallic B2-FeAl alloy after wet-mechanical polishing and after a wide range of anodic polarization conditions have been analyzed by XPS by Frangini et al. [249]. Their results clearly indicate a remarkable enrichment of aluminum within all the films regardless of the growth conditions. Their observations on the passive film thickness and its composition is summarized in table 5.4. The in situ ECNI-AFM experiments on (100) oriented FeAl single crystal were performed in a pH 8.9, borate buffer solution,

Table 5.4: Thickness and cationic fraction of aluminum ($\text{Al}_{\text{ox}}/(\text{Al}_{\text{ox}}+\text{Fe}_{\text{ox}})$) in the oxide films formed on FeAl under different conditions according to XPS analysis [249].

Sample	Oxide film thickness (nm)	$\text{Al}_{\text{ox}}/(\text{Al}_{\text{ox}}+\text{Fe}_{\text{ox}})$
Air oxidized	3.47	0.69
V_{corr} (-0.6 V)	2.62	0.72
Passivated at 0.5 V	2.44	0.73
Passivated at 1.0 V	4.95	0.72
Passivated at 1.5 V	3.03	0.72

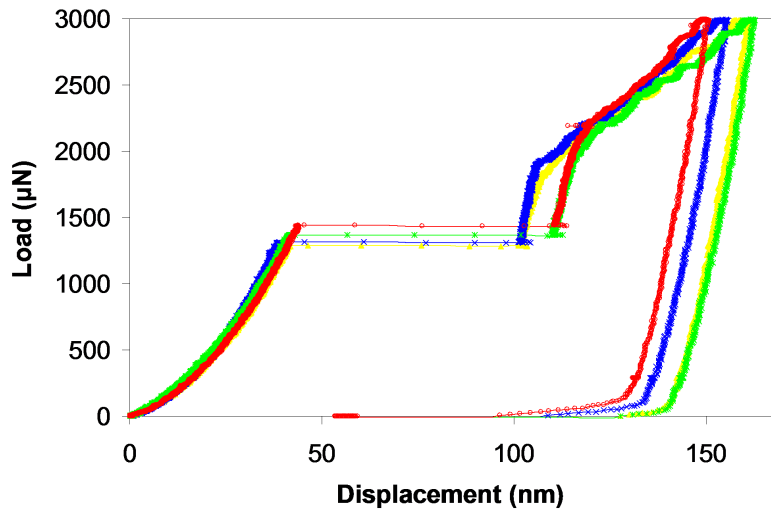


Figure 5.38: Load displacement curves of in situ ECNI-AFM on FeAl (100) single crystal under anodic polarization.

containing 0.02 M H_3BO_3 and 0.005 M $\text{Na}_2\text{B}_4\text{O}_7 \cdot 10\text{H}_2\text{O}$. A conical indenter with a cone angle of 90° was used to perform the indentations. The resulted load displacement curves under an anodic potential of 100 mV are given in figure 5.38. Polarization of the sample to -900 mV did not change the load displacement curves, as shown in figure 5.39. By increasing the cathodic potential, however, the load displacement curves changed and a clear reduction in pop-in load was observed. Figure 5.40 shows the resulting curves under -1100 mV cathodic polarization. To check the reproducibility of this behavior, the potential was switched back to 100 mV anodic again. Figure 5.41 shows that the pop-in load

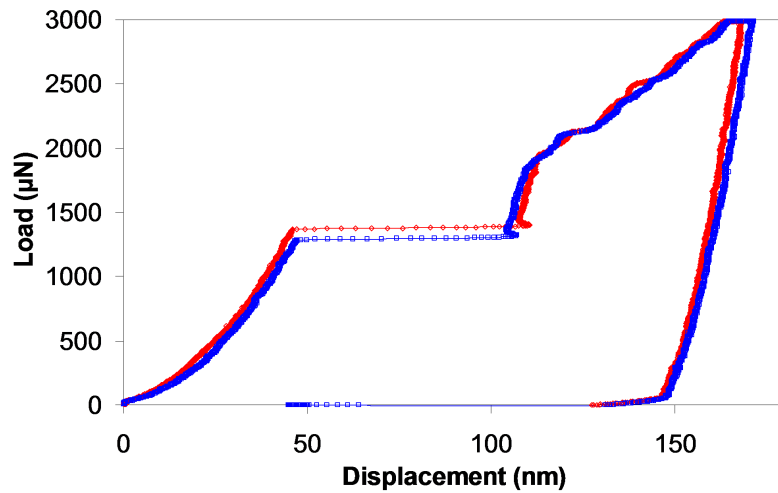


Figure 5.39: Load displacement curves of in situ ECNI-AFM on FeAl (100) single crystal under -900 mV cathodic polarization.

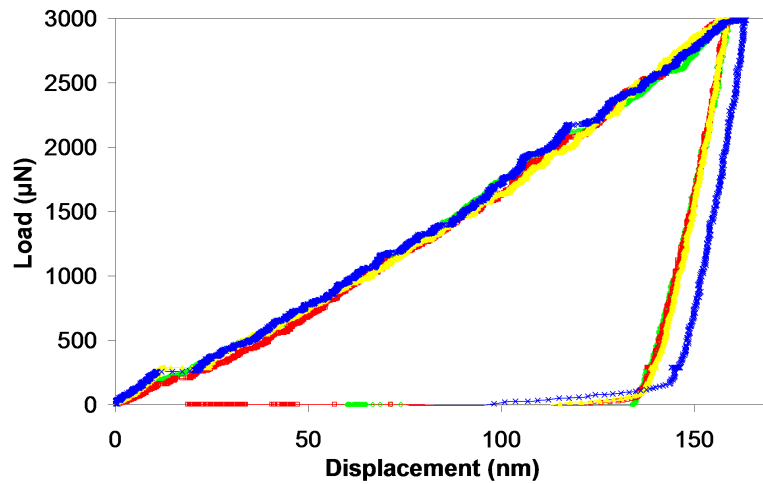


Figure 5.40: Load displacement curves of in situ ECNI-AFM on FeAl (100) single crystal under -1100 mV cathodic polarization.

and load displacement behavior changed and became the same as before (figure 5.38). The observed changes in pop-in behavior under different electrochemical polarizations are summarized in figure 5.42, where the mean value of the pop-in loads under different electrochemical potentials are presented. The surface topography of the sample in air (figure 5.43a), under anodic po-

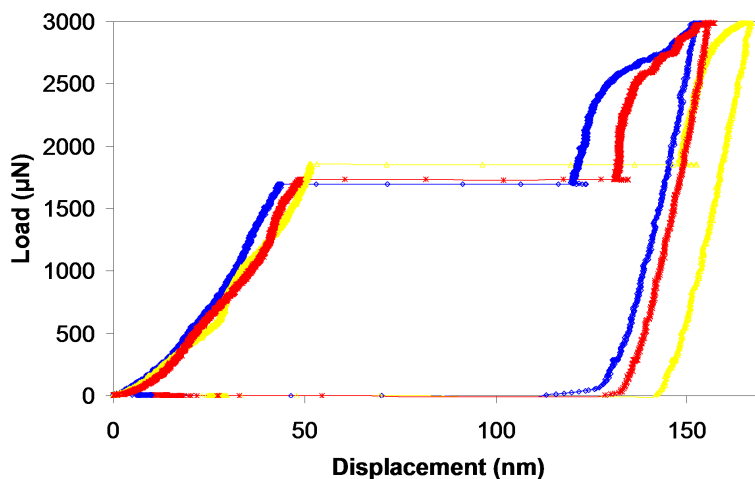


Figure 5.41: Load displacement curves of in situ ECNI-AFM on FeAl (100) single crystal after switching back the potential to 100 mV anodic polarization from -1100 mV cathodic polarization.

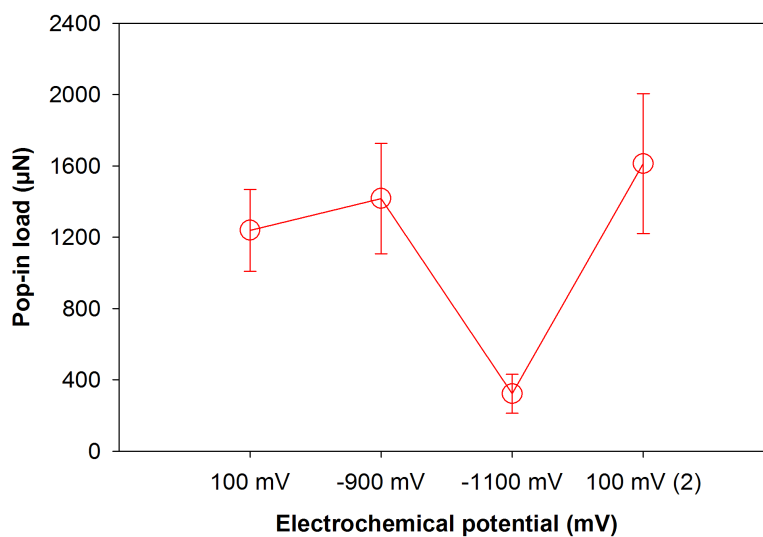
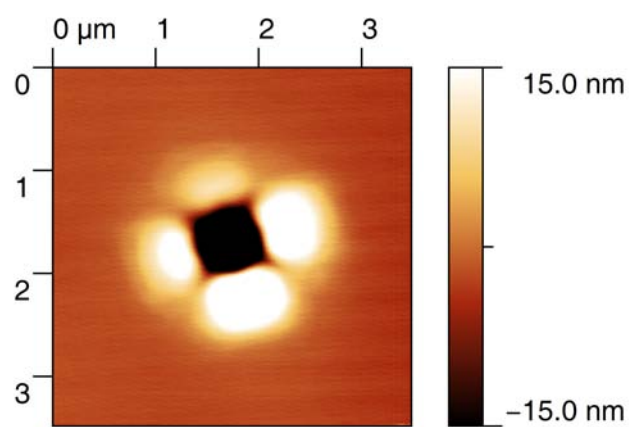


Figure 5.42: The mean value of the pop-in loads observed during in situ nanoindentation of FeAl (100) single crystal under different electrochemical polarization conditions.

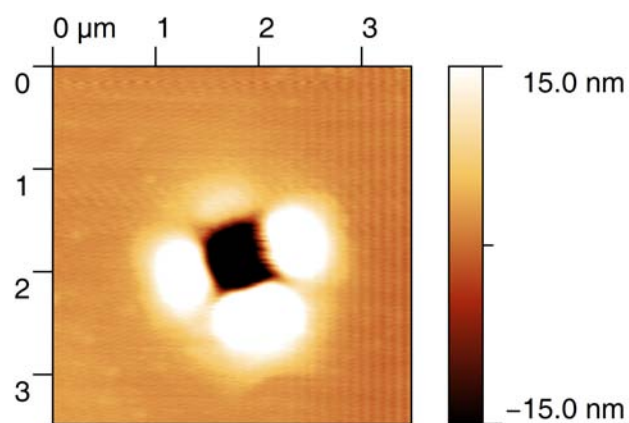
tential (figure 5.43b) and cathodic potential (figure 5.43c) were imaged using imaging capability of the system as shown in figure 5.43. There was no observable change in the surface roughness due to the electrochemical polarization. Table 5.5 summarizes the effect of cathodic polarization on mean values of pop-in load, maximum shear stress and its position below the surface for the FeAl sample. The maximum shear stress, τ_{max} , and its position below the surface, $h_{\tau_{max}}$, were calculated according to the Hertzian contact model presented in section 3.2 (equation (3.15)). For comparison the theoretical strength ($\mu/10$) according to the Frenkel's model (equation (3.45)) is also given in the table 5.5.

Table 5.5: Effect of hydrogen charging on mean values of pop-in load, maximum shear stress, τ_{max} , and its position below the surface, $h_{\tau_{max}}$, for the FeAl sample, which were calculated according to the Hertzian contact model and equation (3.15).

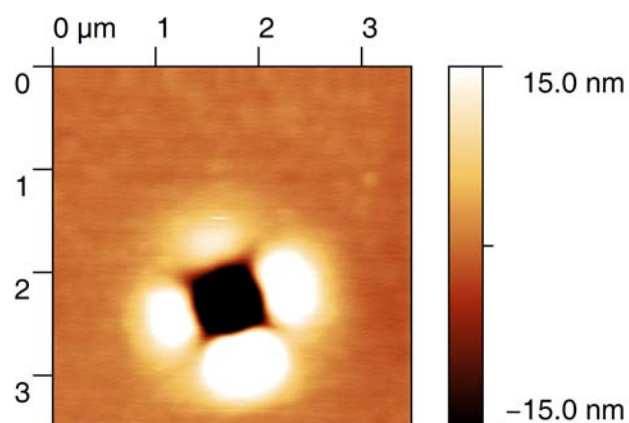
Condition	Pop-in load (μN)	Tip radius (μm)	τ_{max} (GPa)	$h_{\tau_{max}}$ (nm)	$\mu/10$ (GPa)
Anodic	1240	1	7	77	9.4
Cathodic	280	1	4.2	46	9.4



(a) In air



(b) Under anodic potential



(c) Under cathodic potential

Figure 5.43: The surface topography of the FeAl sample in air (a), under anodic potential (b), and cathodic potential (c)

5.6 In situ ECNI-AFM tests on Nickel

Nickel has been the subject of many studies for investigation of hydrogen phenomena [216, 80, 40, 83, 37]. This has resulted in very different explanations of the hydrogen embrittlement mechanisms in nickel. McInteer et al. [80] used slip line observations to compare the slip character of hydrogen-charged and uncharged nickel in compression specimens tested at room temperature. They proposed enhanced plasticity mechanism due to slip localization for hydrogen embrittlement in nickel. Kimura et al. [216] studied the effects caused by the electrochemical hydrogen charging of nickel and nickel-carbon alloys. They found that cathodic charging can cause both softening and hardening of nickel depending on the charging current density, temperature, and strain rate. Dislocation injection due to near surface stresses as a result of charging and hydride formation was suggested by them. Robertson and Birnbaum [40] performed in situ straining experiments in a high-voltage electron microscope equipped with an environmental cell. They observed an increase in the generation rate and velocity of dislocations and in the crack propagation rate by the presence of hydrogen. They proposed hydrogen enhanced plasticity as the hydrogen degradation mechanism of Nickel. Vehoff and Klameth [37] examined hydrogen assisted crack growth in cyclically hardened and notched nickel single crystals. They compared the crack growth rates in electrochemically and in hydrogen gas charged samples and estimated the effective hydrogen activity at the crack tip for various overpotentials and pressures. Their examinations show that in a hydrogen atmosphere the cracks in nickel single crystals grow by a mixture of slip and brittle fracture due to hydrogen enhanced decohesion. These diverse observations, which were obtained with different experimental approaches, was the motivation for performing in situ electrochemical nanoindentation tests on nickel.

The freshly electropolished nickel has a thin (0.6–0.8 nm) film of NiO with a somewhat expanded lattice parameter (by ca. 2%) [250]. Early electrochemical studies showed that this native oxide layer can be reduced by sufficient cathodic polarization in Na₂SO₄ solution with pH lower than 8 [251, 252, 240]. This has later been proved with modern techniques like STM, and in situ X-ray scattering [148]. Anodic polarization of nickel inside a Na₂SO₄ solution produces a new passive layer which is a 0.9–1.2 nm film of NiO, with a normal lattice parameter. This film can not be any more reduced in a neutral solution. This fact was used during in situ ECNI-AFM experiments to exclude surface effects from the effects of hydrogen. Additionally in situ electrochemical nanoindentation tests

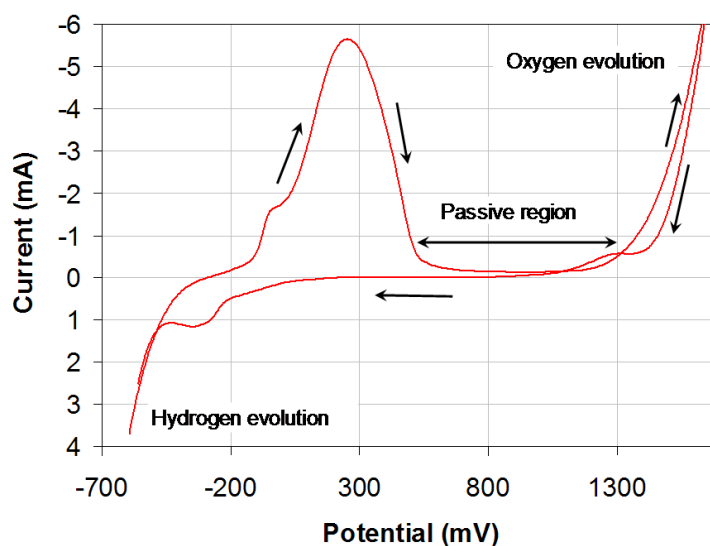


Figure 5.44: Cyclic polarization curve nickel single crystal in pH 6, 0.05 M Na₂SO₄ solution.

were performed on (111) oriented single crystal to remove the orientation effect on both mechanical and electrochemical properties of the surface, which otherwise exist for a polycrystalline sample. The choice of densely packed (111) surface was due to its high thermodynamic stability.

The freshly electropolished nickel sample was installed in the NI-AFM setup (figure 4.9) whereupon the chamber was then filled with a mixture of nitrogen and helium to avoid oxygen affecting the electrochemical reactions. The specimen was kept at a cathodic potential of -1000 mV while the electrochemical cell was being filled with the pH 6, 0.05 M Na₂SO₄ solution. The air-formed oxide film was removed by keeping the sample at this potential for 15 minutes [251]. The sample was then swept with a scan rate of 10 mV/s to an anodic potential of 500 mV in order to passivate the surface and produce the stable passive oxide film. Figure 5.44 shows a cyclic polarization curve for the nickel sample in the test solution. This curve were used to find the hydrogen charging (-1000 mV) and passivation potentials (500 mV). The sample was kept at anodic potential for 15 min before switching to cathodic potential in order to stabilize the anodic passive film. The current transients recorded after switching the potential and during reduction of air formed oxide layer (first step in the test) are shown in figure 5.45. These curves clearly shows the stability of the passive film and reducibility of the air formed oxide film. This stable passive oxide film guarantees that all results reported here are not due to the film effects.

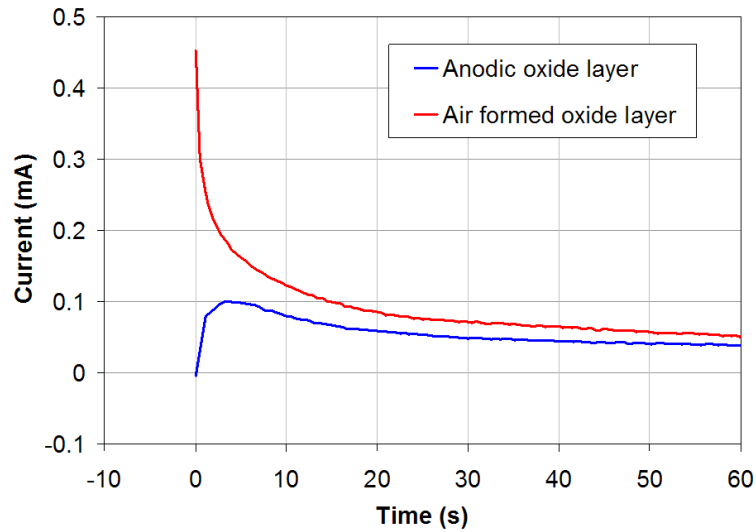


Figure 5.45: Chronoamperometry curves for reduction of two different NiO oxide layers, anodic oxide and air formed oxide, polarized to -1000 mV in pH 6, 0.05 M Na_2SO_4 solution.

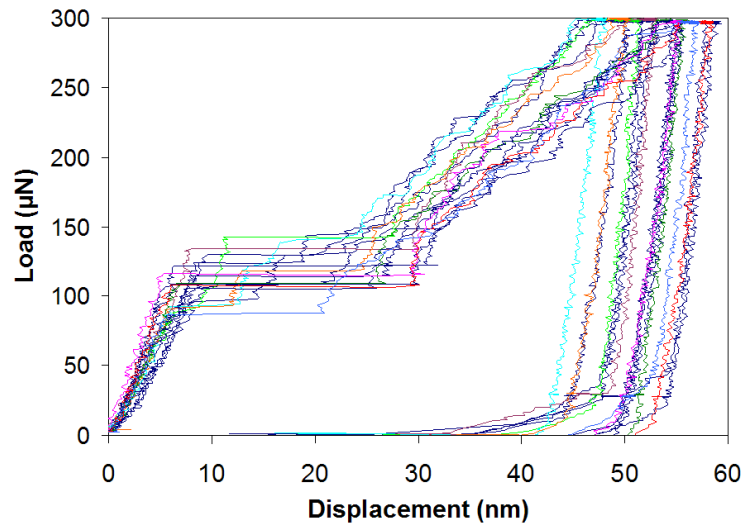


Figure 5.46: Load displacement curves of in situ ECNI-AFM on nickel (111) single crystal under cathodic polarization (hydrogen charged).

The nanoindentation tests were started after approximately one minute of hydrogen charging at cathodic potential. Typical load displacement curves obtained under cathodic potential are shown in figure 5.46. After several indentations, the potential was again switched to anodic potential and maintained for several seconds before indentation. Figure 5.47 shows typical anodic load

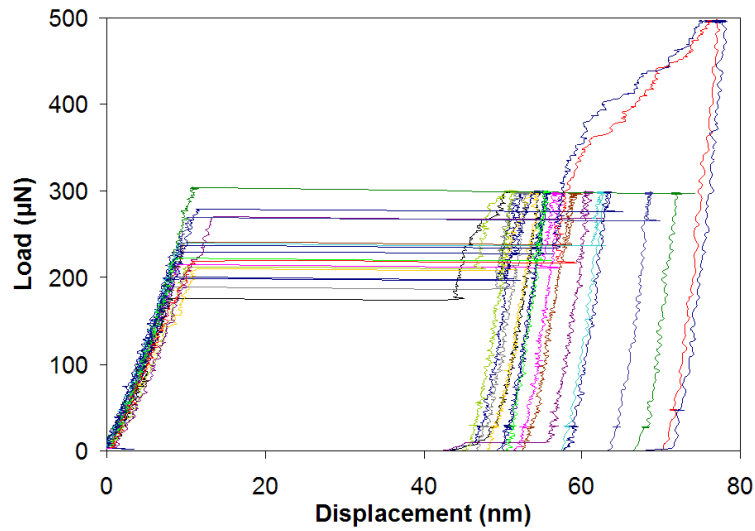


Figure 5.47: Load displacement curves of in situ ECNI-AFM on nickel (111) single crystal under anodic polarization (hydrogen free).

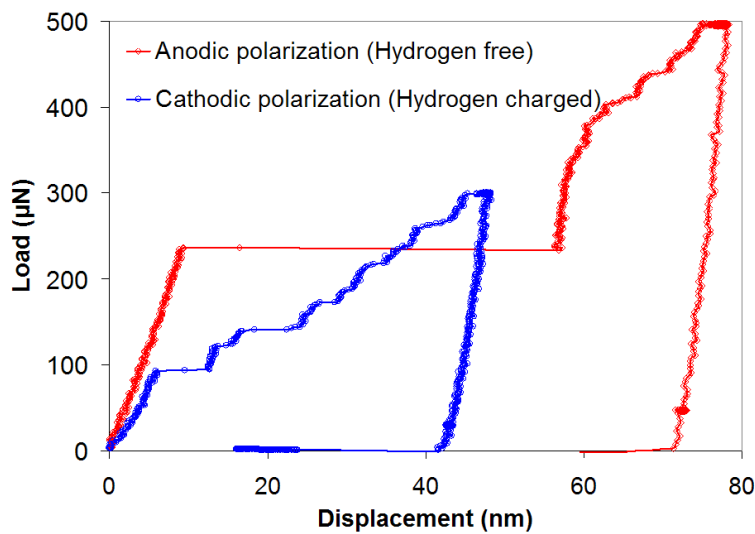


Figure 5.48: Comparison between two load displacement curves of in situ ECNI-AFM on nickel (111) single crystal under anodic polarization (hydrogen free) and cathodic (hydrogen charged) conditions.

displacement curves with pop-in loads that are considerably higher than those at cathodic potential (figure 5.48). This sequence was performed several times in order to check the reproducibility of the observations for each polarization condition. The mean values of the pop-in loads under each condition are shown in figure 5.49. The reproducibility of the results obtained under these cycli-

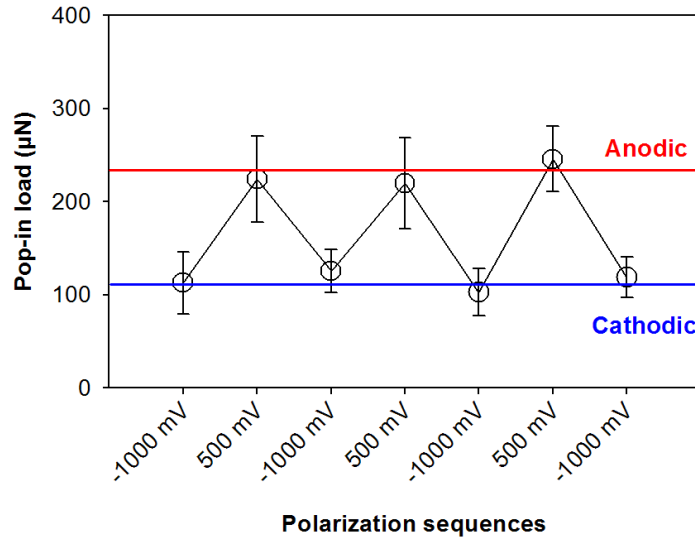


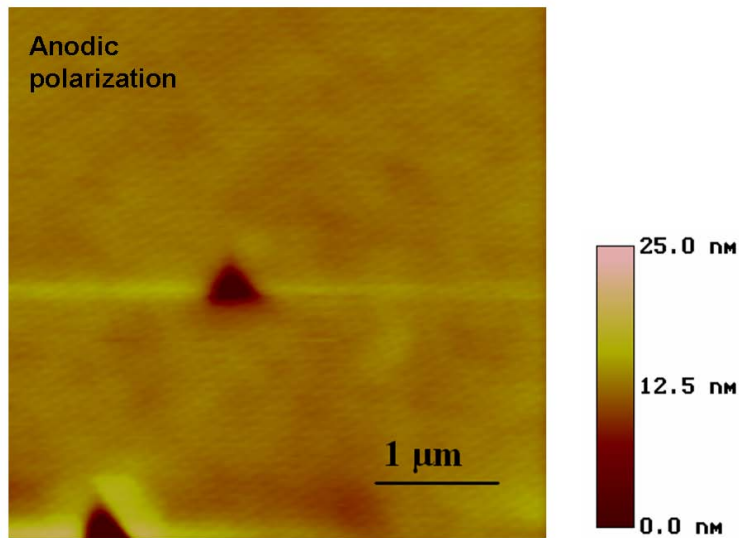
Figure 5.49: Mean values of the pop-in loads in nickel under cyclically changed electrochemical polarization to anodic (hydrogen free) and cathodic (hydrogen charged) potentials.

cally changing polarization conditions ensures that the observed effect was not a surface roughening effect. Additionally, the surface topography of the sample, which was imaged by using the in situ imaging capability of the NI-AFM, shows no surface roughening. This can be seen for both anodic and cathodic polarization in figure 5.50a and figure 5.50b respectively.

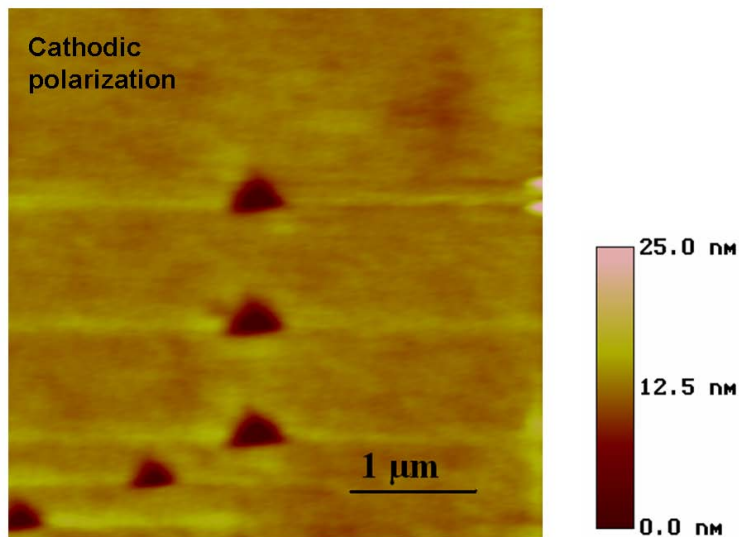
Table 5.6 summarizes the effect of cathodic polarization on mean values of pop-in load, maximum shear stress and its position below the surface for the nickel sample. The maximum shear stress, τ_{max} , and its position below the surface, $h_{\tau_{max}}$, were calculated according to the Hertzian contact model presented in section 3.2 (equation (3.15)). For comparison the theoretical strength ($\mu/10$) according to the Frenkel's model (equation (3.45)) is also given in the table 5.6.

Table 5.6: Effect of hydrogen charging on mean values of pop-in load, maximum shear stress, τ_{max} , and its position below the surface, $h_{\tau_{max}}$, for the nickel sample, which were calculated according to the Hertzian contact model and equation (3.15).

Condition	Pop-in load (μN)	Tip radius (μm)	τ_{max} (GPa)	$h_{\tau_{max}}$ (nm)	$\mu/10$ (GPa)
Anodic	220	0.5	6	37	7.8
Cathodic	100	0.5	4.3	27	7.8



(a) Surface topography under anodic polarization

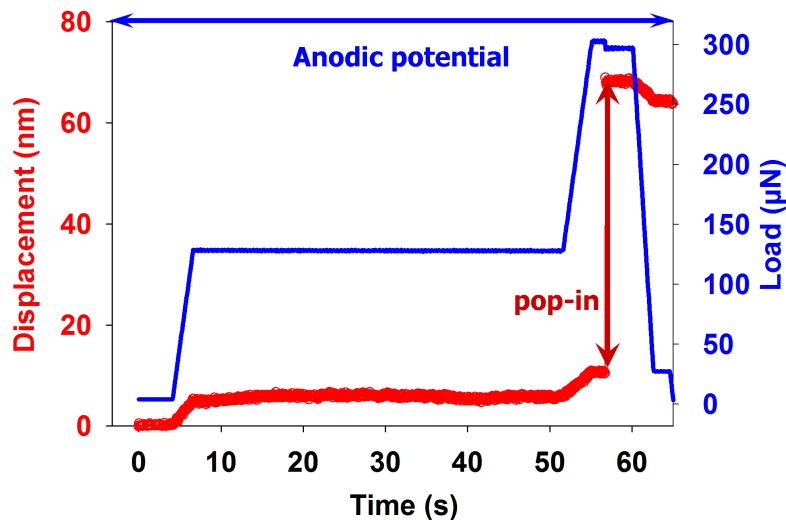
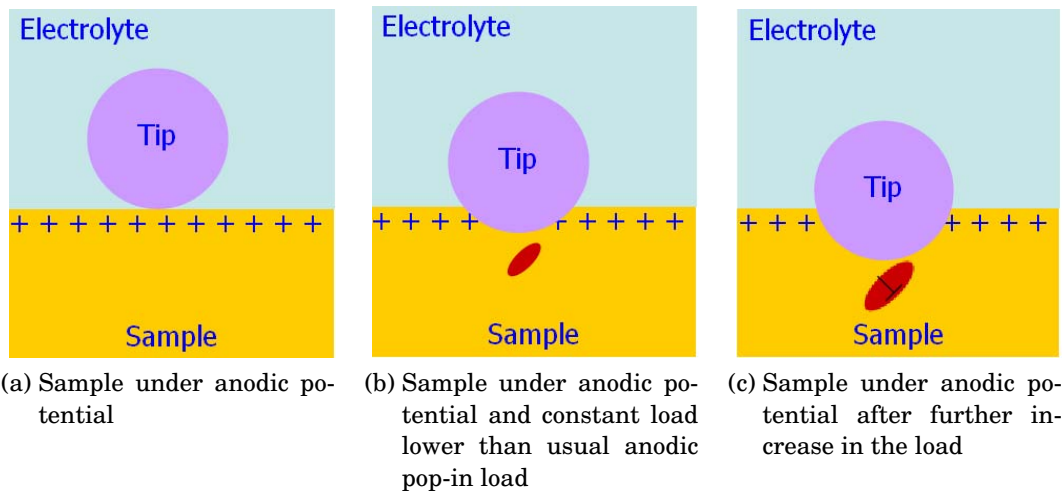


(b) Surface topography under cathodic polarization

Figure 5.50: Surface topography during in situ ECNI-AFM on the nickel (111) surface under different electrochemical polarization.

5.6.1 Time delay experiments

Another set of experiments so-called time delay experiments, was designed in which a hold time was introduced in order to demonstrate the effect of hydrogen on pop-in load. In these experiments the sample was kept under anodic potential to stabilize a hydrogen free metal lattice under the indenter as shown

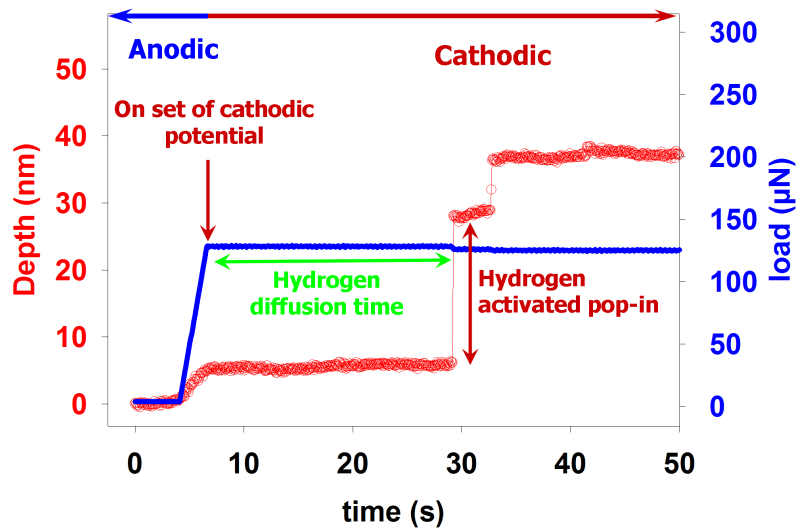
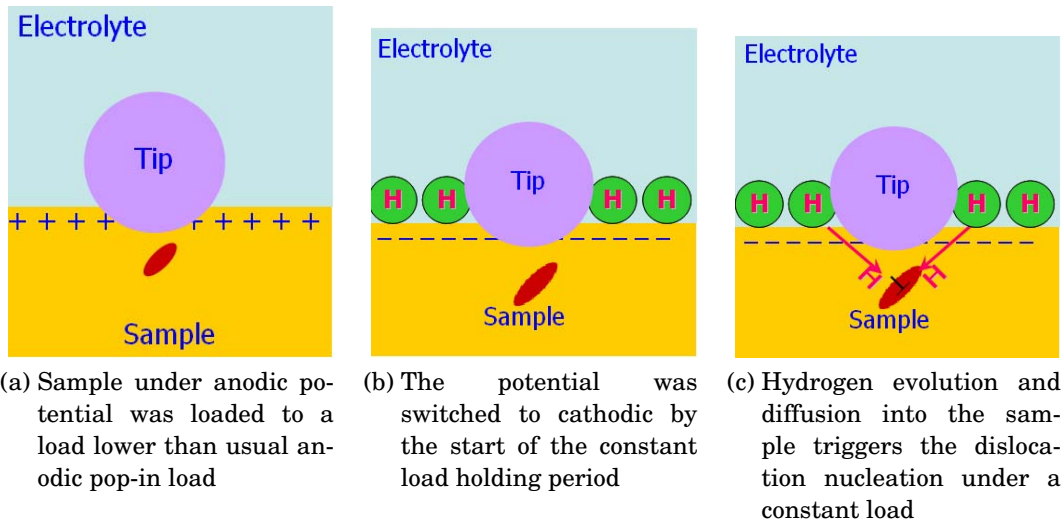


(d) Typical load-time and displacement-time curves under anodic potential for the time delay experiments at 130 μN and 45 seconds hold time

Figure 5.51: Typical time delay experiment under anodic potential.

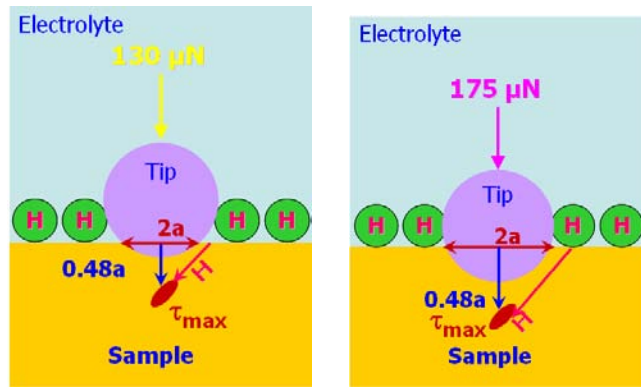
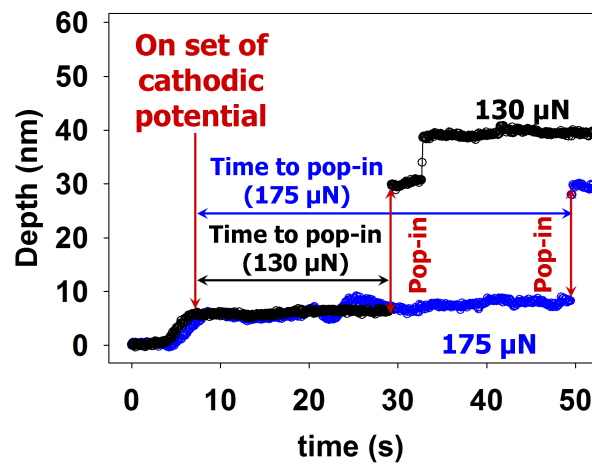
schematically in figure 5.51a. Then the specimen was loaded to a load between the pop-in loads under cathodic and anodic potentials. This load was kept for a specific time while the potential was either anodic or switched at the start of holding time to cathodic. In the first case the pop-in occurs only after further load increase (figure 5.51). In the second case, however, a pop-in occurs during the holding time (figure 5.52). The first part of loading procedure was completely elastic and does not alter the surface film; therefore the observed effect

should be only due to subsurface hydrogen lattice interactions. This procedure guarantees that the condition at the indenter specimen interface is not altered during the potential change, since this region is covered with the tip and does not have any contact with the electrolyte. By increasing the hold load the time to pop-in increased as shown in figure 5.53. There are several papers on a time activated pop-in phenomenon, which report that pop-ins, are occurring after a sufficient hold time at constant loads below the usual pop-in load (see section 6.1). Nevertheless in our experiments as confirmed by several nanoindentations (figure 5.54) the selected load and time range was too small to observe time activated pop-ins under anodic potential. Additionally in so called time activated pop-ins by increasing the hold load time to pop-in increases, while in the current study an opposite effect was observed. Therefore in our case the time activated pop-ins observed under cathodic potential are due to hydrogen. Hence they were called *hydrogen activated* pop-ins.

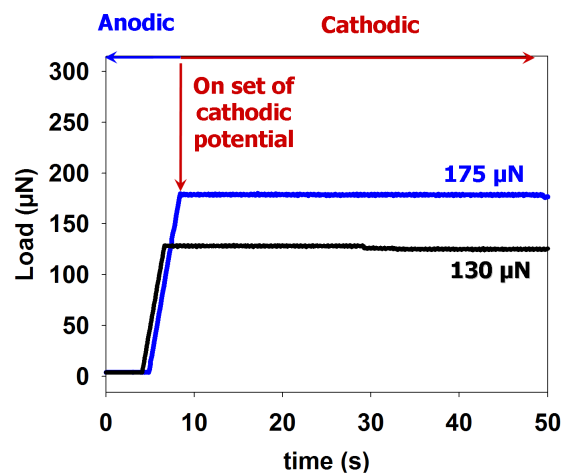


(d) Typical load-time and displacement-time curves with switching to cathodic potential during hold at 130 μN

Figure 5.52: Typical time delay experiment with switching to cathodic potential during hold.

(a) Time delay experiments with $130 \mu\text{N}$ hold load(b) Time delay experiments with $175 \mu\text{N}$ hold load

(c) Displacement-time curves



(d) Load-time curves

Figure 5.53: Typical time delay experiment with switching to cathodic potential during hold. Effect of hold load on time to pop-in

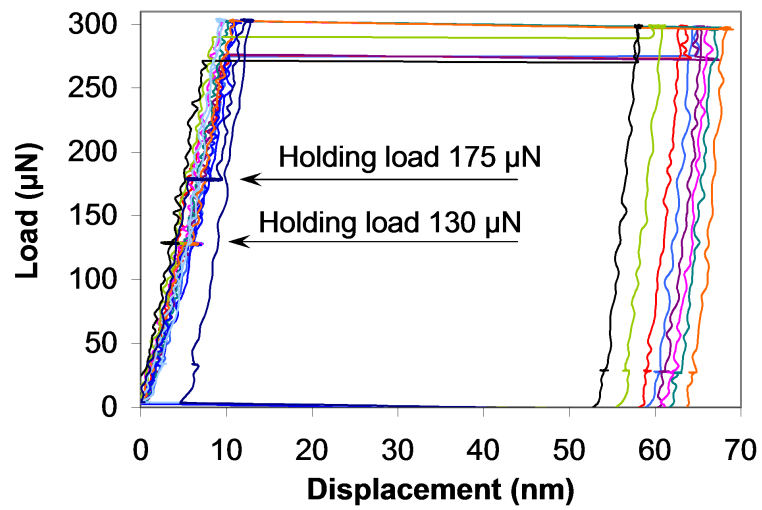


Figure 5.54: Reproducibility of the load-displacement curves for the time delay experiments under anodic potential.

5.7 In situ ECNI-AFM tests on stainless steels

To show the capability of the developed system in probing the effect of hydrogen in complex alloy system, stainless steels are chosen to be examined. Stainless steels represent the most diverse and complex family of all steels. The list of their applications is endless: from the harsh environments of the chemical, oil production and power generation industries to street furniture or automotive trims without forgetting most cutlery, they are used either for decorative purposes and/or for their excellent resistance to corrosion.

Stainless steels are stainless because a protective layer spontaneously forms on their surfaces and reduces the rate of corrosion to almost negligible levels. Under normal conditions, this layer heals very rapidly if scratched, so that if stainless steels only suffered from uniform corrosion, they could survive for literally millions of years [253]. It is generally agreed that stainlessness is obtained for additions of about 12wt.% of chromium or more, although corrosion rates continuously reduce with increasing chromium contents from 0 to this limit. Corrosion resistance can be greatly enhanced above that of a basic 12wt.% Cr steel by further addition of Cr and/or use of other alloying elements such as Ni, Mo, N etc. The number of stainless steel grades is therefore seemingly infinite, with a large number of standard compositions to which manufacturers add their proprietary variants. These are usually divided in four classes on the basis of their microstructures:

1. Martensitic or transformable stainless steels
2. Ferritic stainless steels
3. Austenitic stainless steels
4. Duplex stainless steels

Regardless of the outstanding corrosion resistance of the different grades of stainless steels, they all are suffering from hydrogen embrittlement. Therefore, on two different grades of stainless steels, namely Austenitic and super duplex stainless steel (SDSS), *in situ* electrochemical nanoindentation tests were performed to probe the effect of hydrogen on their mechanical behavior.

5.7.1 Austenitic Stainless steel

Austenitic stainless steels are alloys which exhibit high corrosion resistance combined with high mechanical properties, especially ductility. It is, however,

Table 5.7: Composition of austenitic stainless steel used in this study

Element	Fe	Cr	Ni	Mn	Si
Wt.%	71.5	17.8	8.7	1.6	0.5
Atom%	71	18.8	8.1	1.6	1

well established that when they are exposed to cathodic charging or gas environments of low or high hydrogen pressures, a possible degradation of mechanical properties with a more or less pronounced brittleness can occur [84, 254, 98, 90, 32, 47, 255, 38]. The formation of brittle martensite or hydride phases, as a possible source for hydrogen embrittlement, has been discussed extensively. X-ray diffraction studies on cathodically hydrogen-charged austenitic stainless steels have been performed to investigate possible phase transformations due to hydrogen charging [256, 257].

The sample was prepared from the commercial V2A type austenitic stainless steel, received in the form of plates. The alloy composition measured by energy dispersive x-ray analysis (EDX) analysis for the main alloying elements is given in table 5.7. The sample was solution annealed at 1300 °C in a helium atmosphere for 6 days and quenched in water. This solution annealing treatment of the sample resulted in a coarse grain structure, as shown in figure 5.55. In order to differentiate between the twin boundaries and large angle grain boundaries a special program written by Henning [258] was used to analyze the OIM data. The resulted corrected OIM image is shown in figure 5.56. This coarse grained microstructure made it possible to exclude the orientation effect from nanoindentation results by performing indents on a single grain. Typical load displacement curves of the sample in air are given in figure 5.57. The sample did not show a distinct pop-in. This was due to the quench annealing process performed on this sample. The quenching resulted in an increase in defect density in the sample (i.e. dislocations and vacancies). Therefore, during nanoindentation, the existing dislocation sources were activated and multiplied. The in situ ECNI-AFM tests were performed in the same grain where the air indents had previously been done. The electrochemical potential applied to the sample during these tests, as well as the resulting chronoamperometry curve, are given in figure 5.58. For the in situ tests a pH 6, 0.05 M Na₂SO₄ solution was added to the electrochemical cell while the sample was kept at a cathodic potential of -800 mV. After few minutes the first indents were performed inside the solution under cathodic potential. The resulting load displacement curves are provided

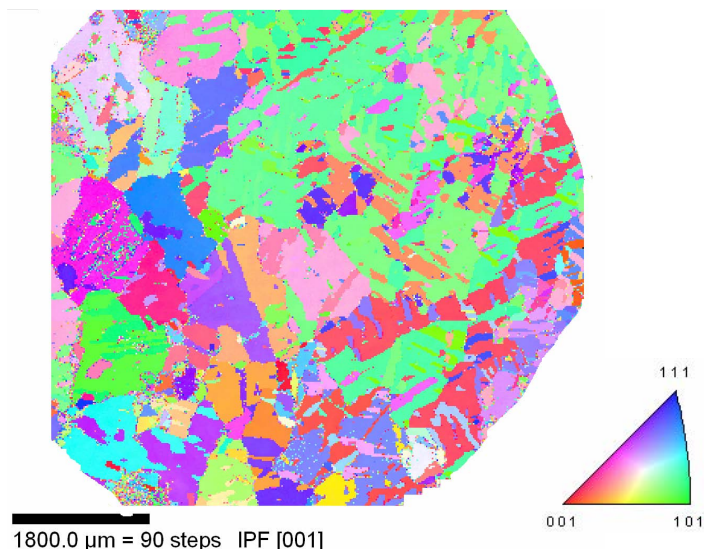


Figure 5.55: Complete orientation map of the solution annealed austenitic stainless steel sample after heat treatment reproduced by pasting several OIM images together.

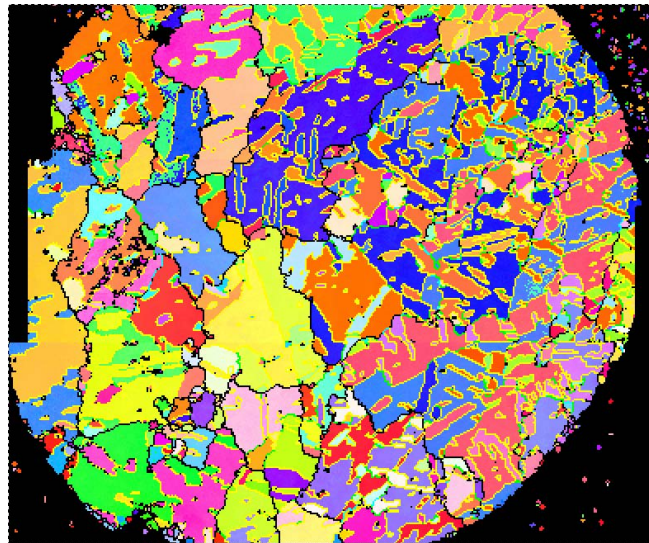


Figure 5.56: Orientation map in figure 5.55 is further analyzed to distinguish between twin boundaries (yellow lines) and large angle grain boundaries (black lines) [258].

in figure 5.59a. The electrochemical hydrogen charging resulted in observation of a clear pop-in behavior. This was due to the trapping of hydrogen atoms by existing defects and dislocations in sample, as mentioned in 2.3. In the next step the sample was polarized to 500 mV anodic potential with a 10 mV/s potential

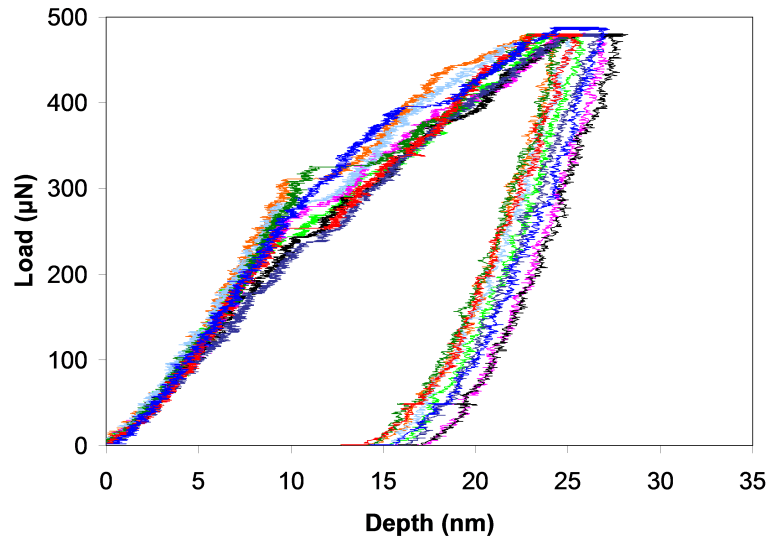


Figure 5.57: Load displacement curves of solution annealed austenitic stainless steel sample in air.

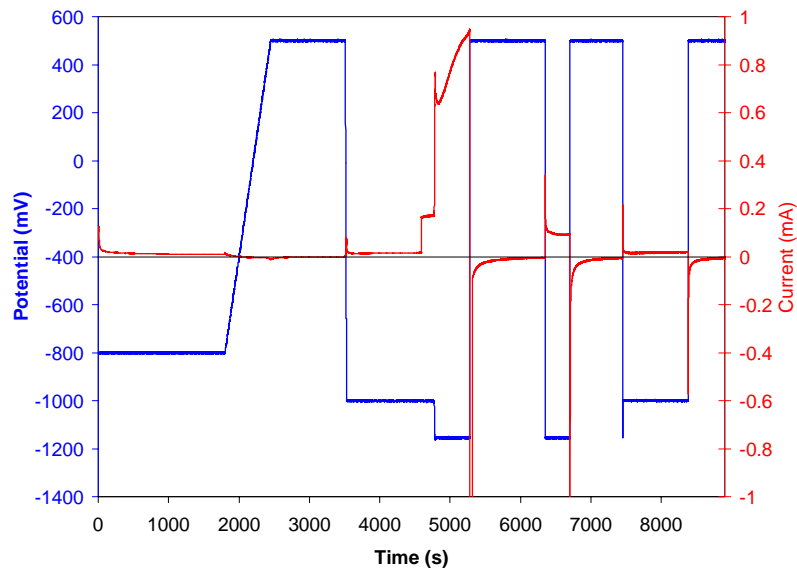
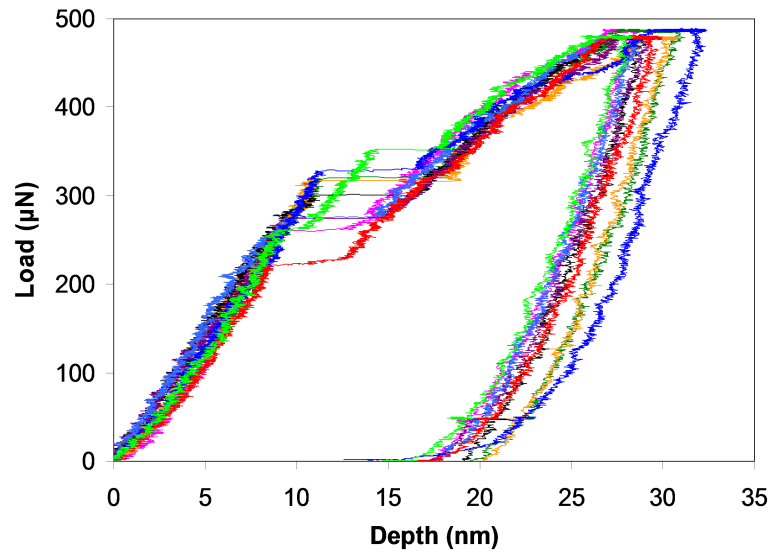


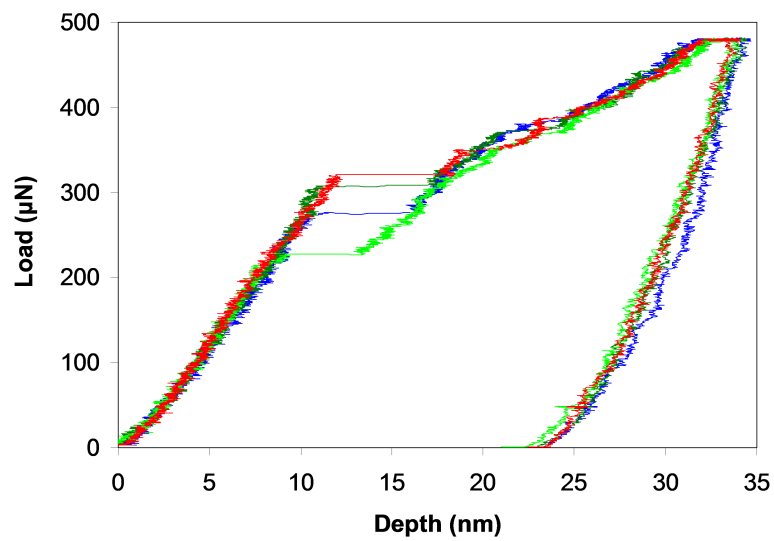
Figure 5.58: Electrochemical potential applied to the solution annealed austenitic stainless steel sample and chronoamperometry curve recorded during in situ ECNI-AFM tests on this sample.

sweep rate. The indentation of the sample started after few minutes of anodic polarization. Typical load displacement curves under 500 mV anodic potential are shown in figure 5.59b. An obvious decrease in strain hardening (i.e. the

slope of the curve in the loading section) and an increase in indentation depth under anodic condition is observable. Switching the potential back to cathodic potentials resulted in an increase in the strain hardening rate, as can be seen in figure 5.59c-d, where load displacement curves for -1000 mV and -1150 mV cathodic potentials are given. The hydrogen effect on the load displacement curves was only to some extent reversible. This can be seen in figure 5.60, where the effect of switching back to anodic polarization on the nanoindentation curves is presented. The hardness of the sample under different electrochemical polarizations is given in figure 5.61. The obvious effect of hydrogen on hardness, which to some extent is reversible can be seen in this figure. During the tests no change in the surface topography of the sample was observed. Figure 5.62 shows the surface topography of the sample in air (figure 5.62a), under anodic potential (figure 5.62b) and cathodic potential (figure 5.62c) imaged using in situ imaging capability of NI-AFM.

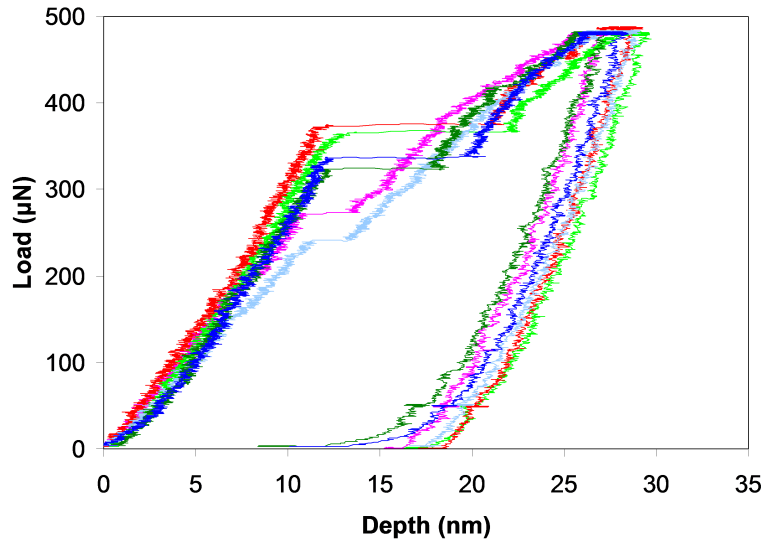


(a) -800 mV cathodic potential (see figure 5.58)

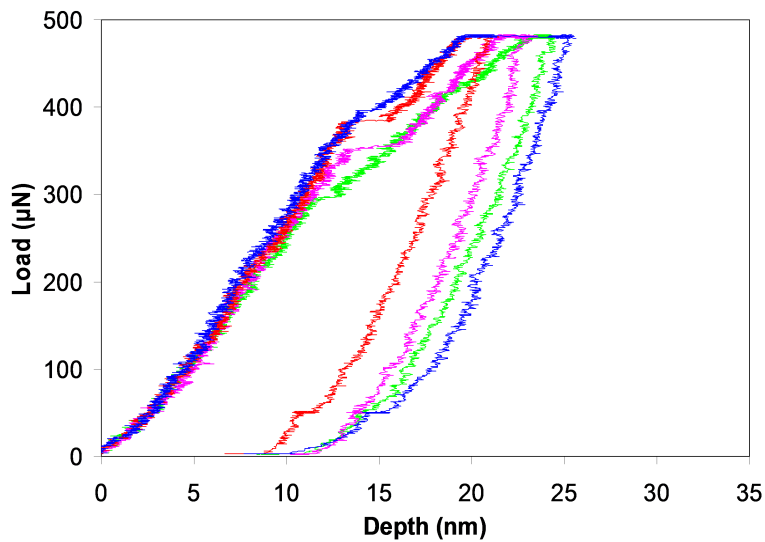


(b) 500 mV anodic potential (see figure 5.58)

Figure 5.59: Effect of the electrochemical potential on load displacement curves of the solution annealed austenitic stainless steel sample (continued on next page).



(c) -1000 mV cathodic potential (see figure 5.58)



(d) -1150 mV cathodic potential (see figure 5.58)

Figure 5.59: Effect of the electrochemical potential on load displacement curves of the solution annealed austenitic stainless steel sample (continued from previous page page).

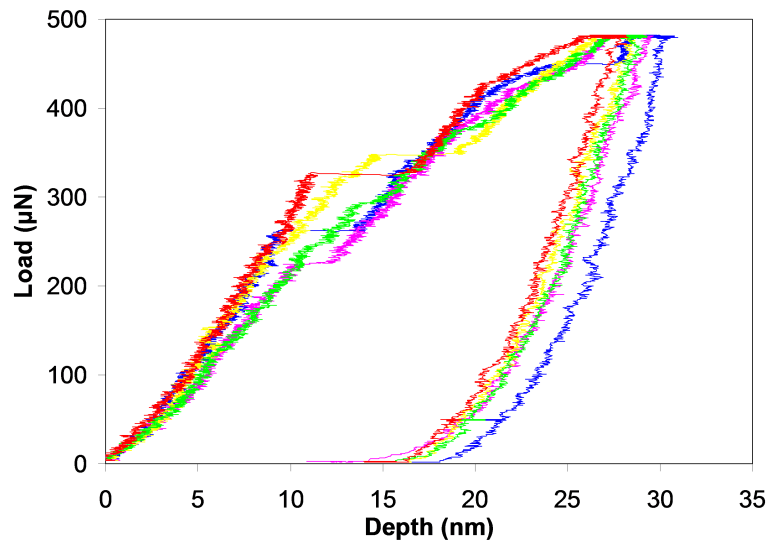


Figure 5.60: Effect of switching back to anodic polarization, from -1150 mV (figure 5.59d) to 500 mV, on load displacement curves of solution annealed austenitic stainless steel sample (see figure 5.58).

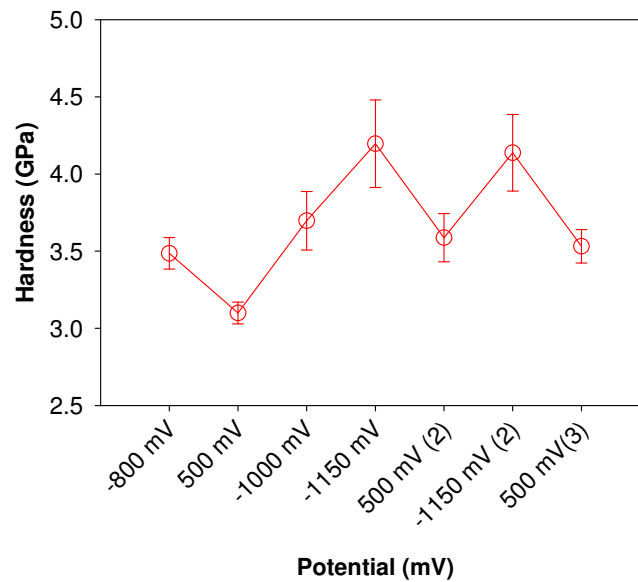


Figure 5.61: Mean values of the hardness under different electrochemical polarization, observed during electrochemical nanoindentation of austenitic stainless steel in solution annealed condition.

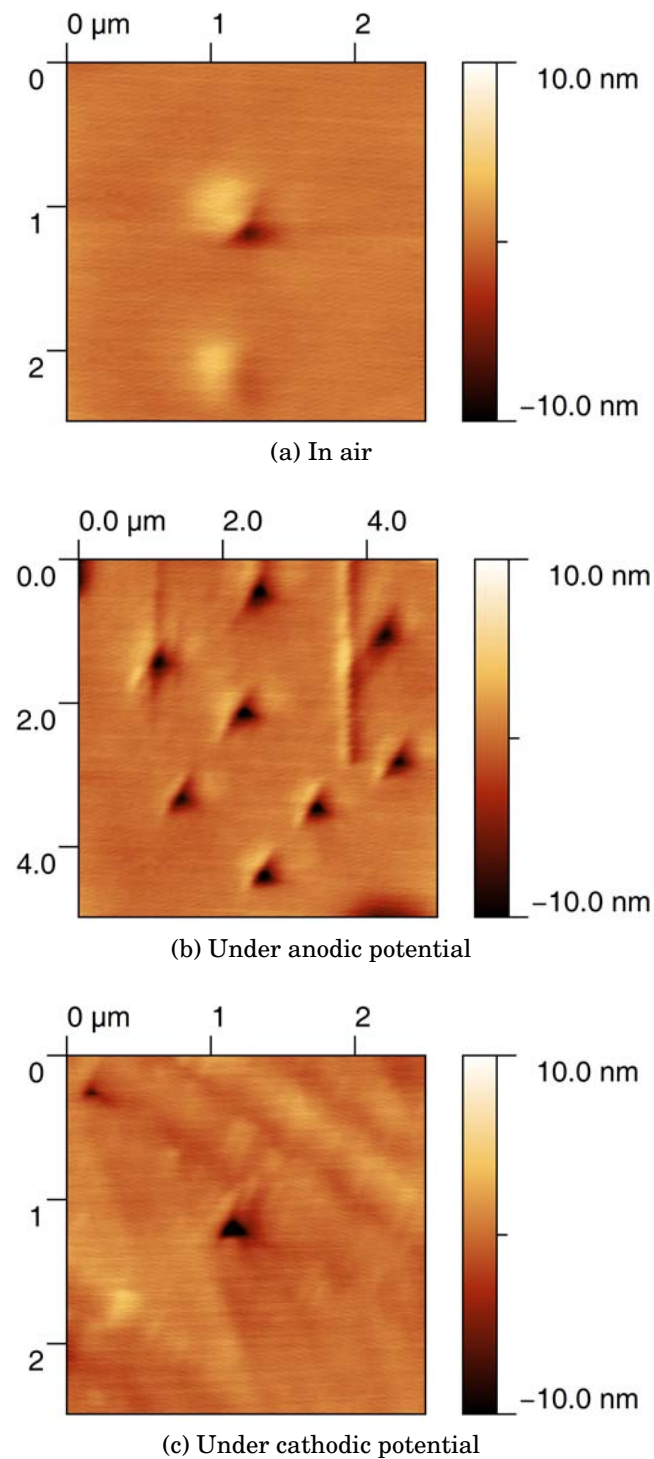


Figure 5.62: The surface topography of austenitic stainless steel sample in air (a), under anodic potential (b), and cathodic potential (c)

5.7.2 Super Duplex Stainless steel

Super duplex stainless steels (SDSS) are highly alloyed two-phase steels with excellent resistance against localized corrosion. They are used in especially demanding environments like chemical industry and oil and gas industry. However, in spite of the very favorable properties of SDSS when exposed to hydrogen, the SDSS tends to fail due to hydrogen embrittlement.

The SDSS sample was a SAF 2507[®] provided by OUTOKUMPU¹. The composition of the sample provided by the supplier is given in table 5.8. The sample was in the solution annealed condition². The ferrite content of the sample was 46% according to the supplier's test results. The chemical composition of the main alloying elements in sample was measured by using EDX and is shown in table 5.9. As expected, the ferrite stabilizing elements chromium and molybdenum are enriched in the ferrite, and the austenite stabilizing element nickel is enriched in the austenite.

The nanoindentation behavior of the austenite and ferrite phases in air were studied in detail to have a basis for further in situ analysis [259]. In situ tests were performed on both an as received sample and a sample aged in vacuum at 500 °C for one hour and cooled in furnace. Fine grain SDSS samples with microstructure as shown in figure 5.63 were used. The topography resulted from electropolishing made it easy to distinguish between ferrite and austenite phases, as shown in figure 5.64. Because of the different surface binding energies of α and γ , the connected grains of both phases can be distinguished easily

Table 5.8: Composition of SDSS used in this study provided by the supplier

Element	C	Si	Mn	P	S	Cr	Ni	Mo	Cu	N
wt.%	0.016	0.23	0.79	0.021	0.001	25	6.98	3.82	0.32	0.27

Table 5.9: Composition of SDSS used in this study measured by EDX

Element (Wt.%)	Fe	Cr	Ni	Mo
Mean	62.2	26	7	4.8
Ferrite	61.5	27	5.7	5.8
Austenite	63.5	24.7	8.2	3.7

¹This grade is equal to the American UNS S32750 and European EN 1.4410 grades

²Heat treated at 1120 °C for 45 minutes and quenched in water

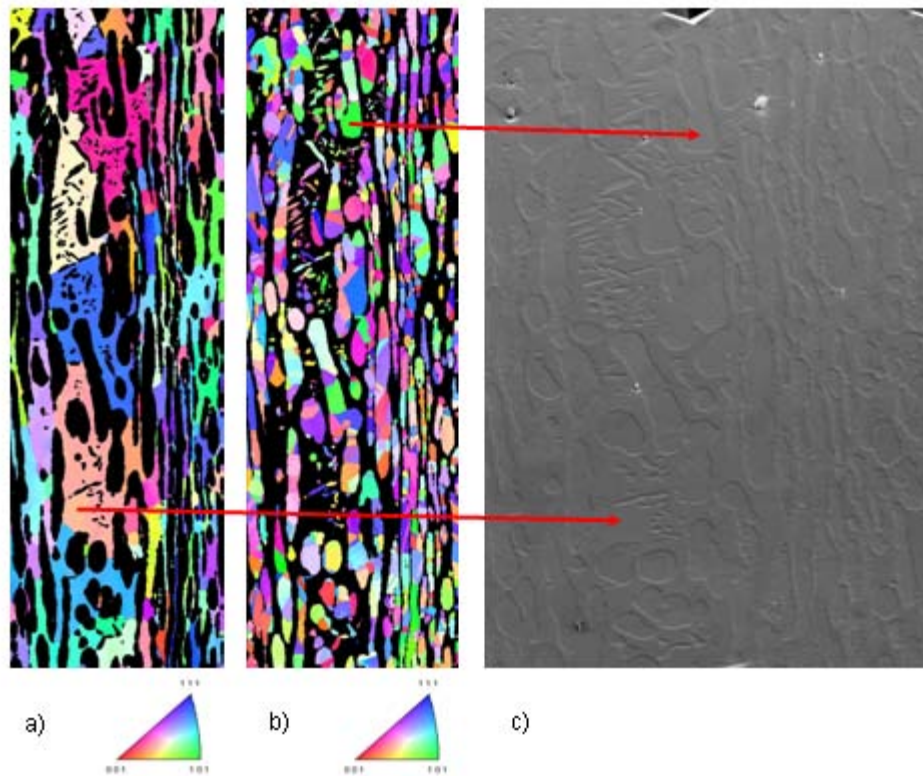


Figure 5.63: OIM and SEM images of SDSS sample used for in situ ECNI-AFM tests. OIM image of ferrite phase (a), austenite (b), SEM image (c)

from each other by their shape. The austenite grain clusters are preferentially convex, whereas the ferrite grains fill the space between these grain clusters.

The in situ electrochemical nanoindentation tests on SDSS were performed in a pH 8.9 borate buffer solution. The electrolyte was added to the electrochemical cell as the sample was held at a potential of 300 mV anodic. After indentation on both phases under anodic potential, the potential was switched to -1100 mV cathodic. The resulting load displacement curves under anodic and cathodic potentials for both austenite and ferrite phases are given in figures 5.65a–d.

Figure 5.66a shows the surface topography of an austenite grain inside the solution under anodic potential. The image was taken in gradient mode to show only the sharp changes in the topography (e.g. grain boundaries and slip lines). Figures 5.66b–e show the changes in the surface topography of the austenite grain with time, after switching the potential to -1100 mV cathodic. After 15 minutes of hydrogen charging the first slip lines were observed on the surface of the austenite grain (figure 5.66c). Another slip system was activated after 30

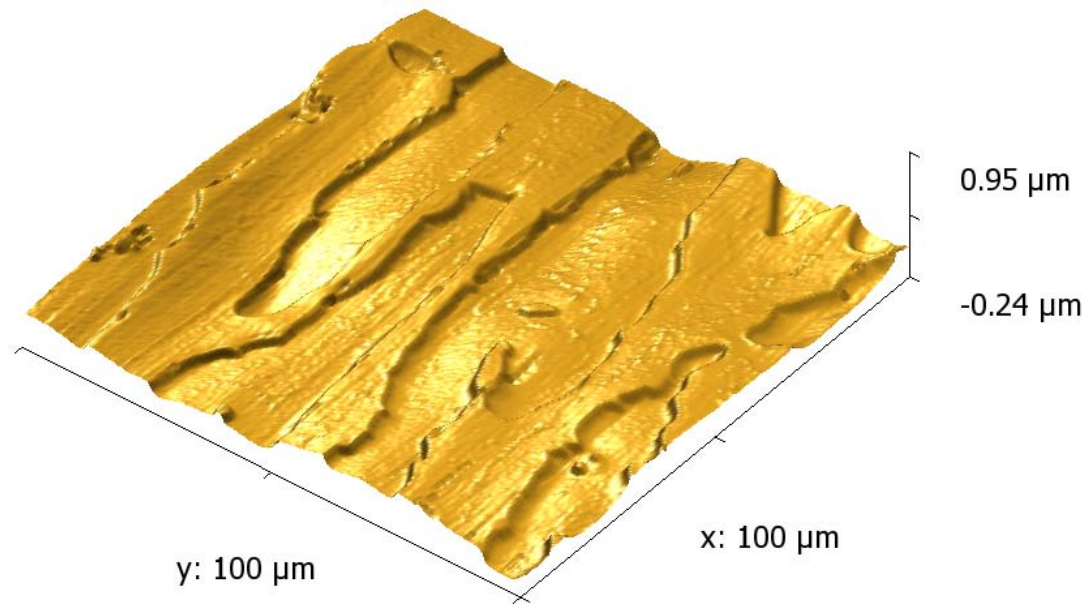


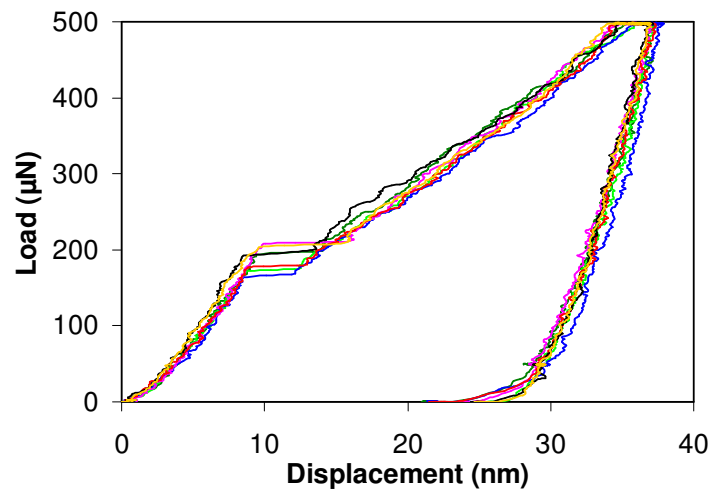
Figure 5.64: Contact mode AFM surface topography of electropolished SDSS. Austenite phase with convex grain boundaries is electropolished deeper.

minutes of hydrogen charging (figure 5.66d). The activity on both of the slip system increased after a longer hydrogen charging time (figure 5.66e). There was no change observed in surface topography of ferrite during hydrogen charging.

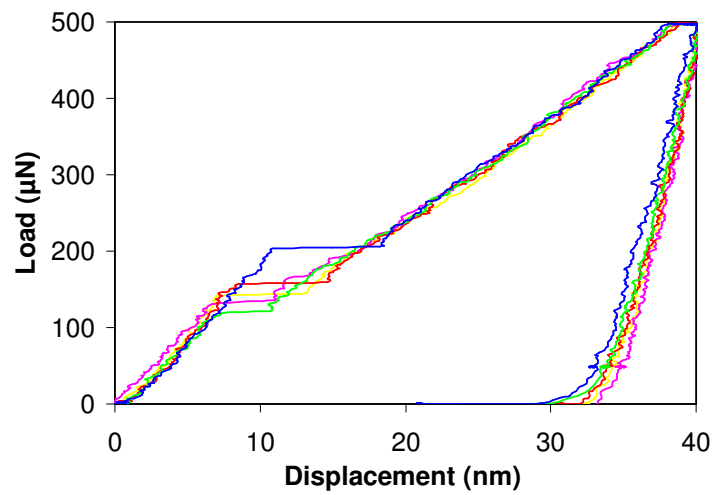
The pop-in event frequencies¹ under cathodic and anodic potentials for both phases are shown in figure 5.67a. The pop-ins were not observed for each indentation. This was due to the relatively high dislocation density of the sample in as received condition². The electrochemical hydrogen charging resulted in a drastic reduction of pop-in events for austenite, whereas did not affect the pop-in events for ferrite (figure 5.67a). This means, that hydrogen charging of austenite results in an increase of the dislocation density. This was in agreement with the observation of the surface topography for austenite during the hydrogen charging, as shown in figures 5.66a–e. Figure 5.68 summarizes the effect of hydrogen on pop-in load distribution in as received SDSS. While a reduction in pop-in load for hydrogen charged ferrite was observed. For the austenite the

¹Since the pop-in happens only when a dislocation free region of metal is indented, therefore in a set of indentations the number of pop-ins observed is depending directly to the dislocation density in the sample. In a metal with a very high dislocation density there is no chance for observation of pop-in (see for example figure 5.21)

²As in the case of solution annealed austenitic stainless steel in 5.7.1 the thermal shock during quenching results in a higher dislocation density in comparison to the annealed and in furnace cooled samples reported in preceding sections.

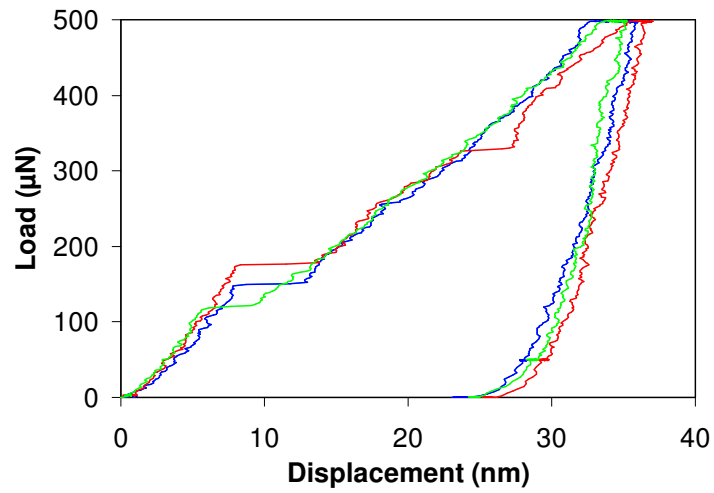


(a) Austenite (300 mV anodic)

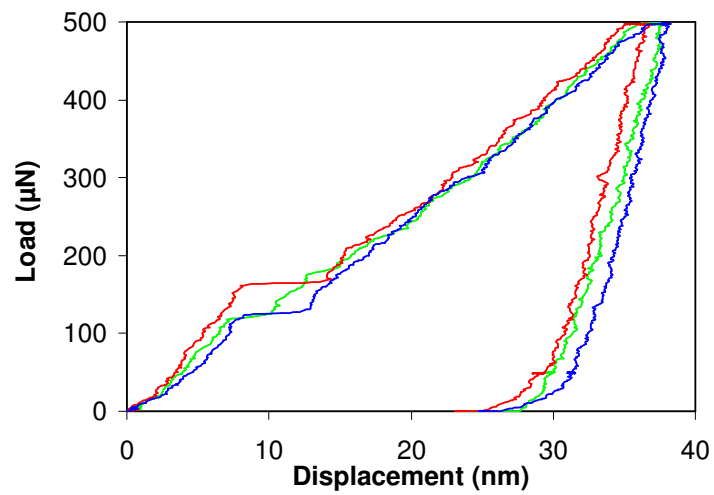


(b) Ferrite (300 mV anodic)

Figure 5.65: Load displacement curves of as received SDSS sample in pH 8.9 borate buffer solution (continued on next page).

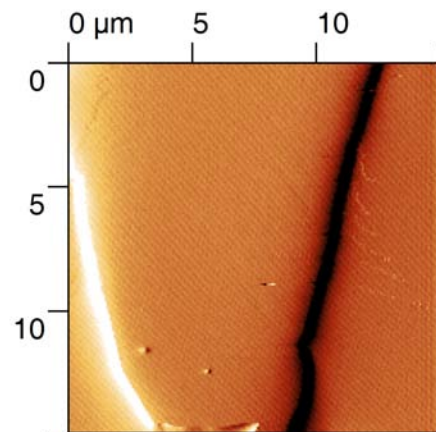


(c) Austenite (-1100 mV cathodic)

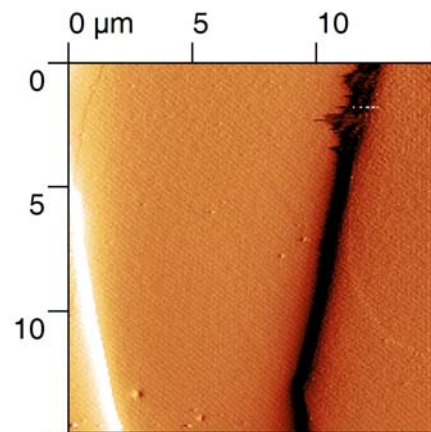


(d) Ferrite (-1100 mV cathodic)

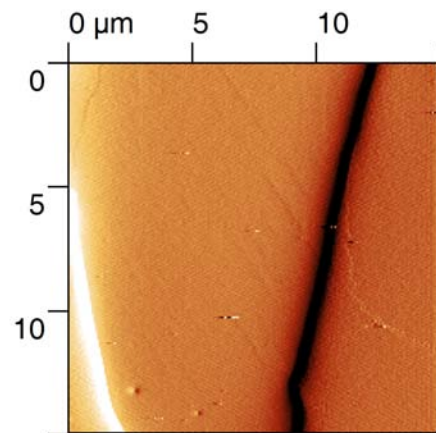
Figure 5.65: Load displacement curves of as received SDSS sample in pH 8.9 borate buffer solution (continued from previous page).



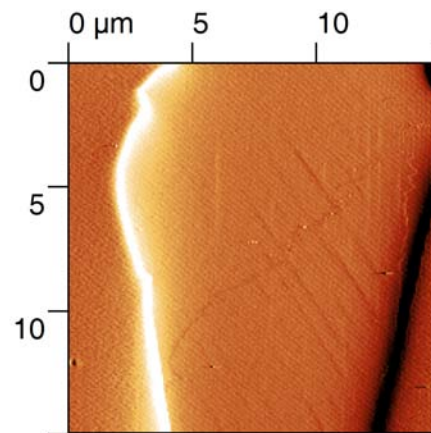
(a) Austenite under anodic potential



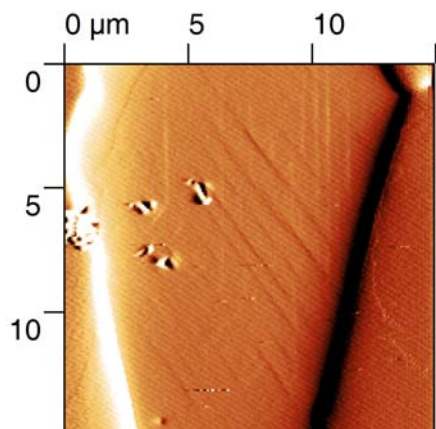
(b) Austenite at the moment of switching potential to cathodic



(c) Austenite under cathodic potential ca. 15 min after hydrogen charging

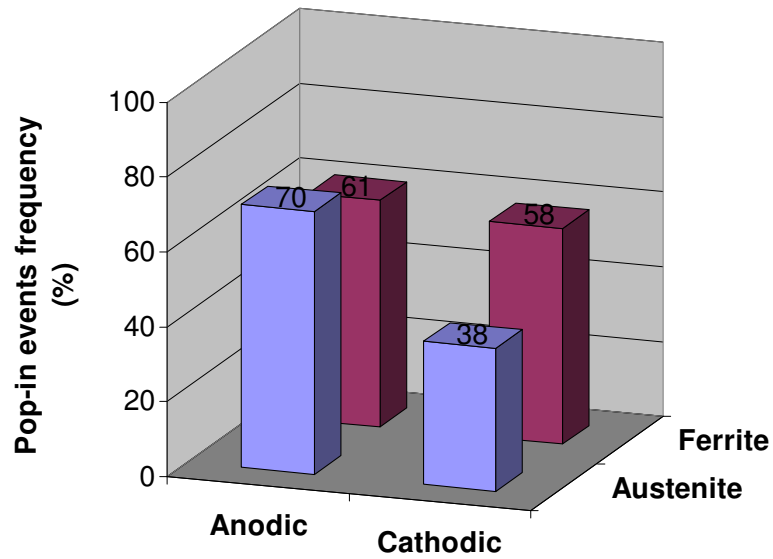


(d) Austenite under cathodic potential ca. 30 min after hydrogen charging

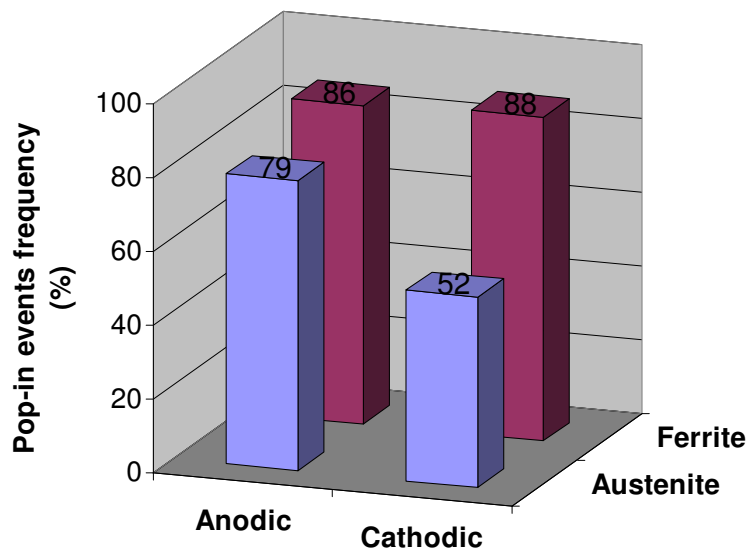


(e) Austenite under cathodic potential ca. 60 min after hydrogen charging

Figure 5.66: Gradient images taken during in situ ECNI-AFM on as received SDSS sample. The formation of slip lines as a result of hydrogen charging in austenite is clearly observable.

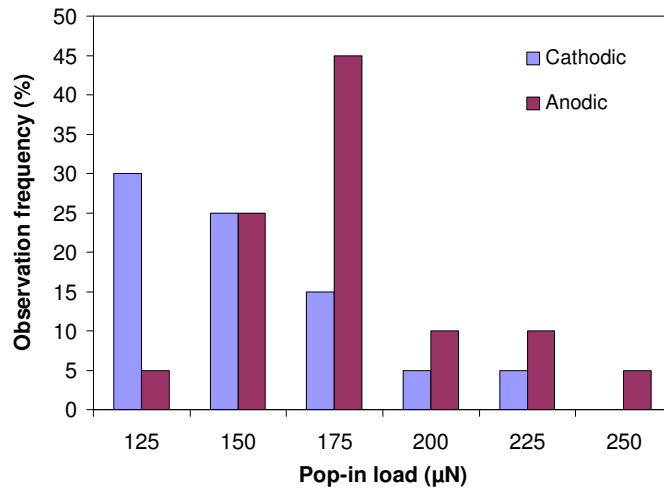


(a) As received

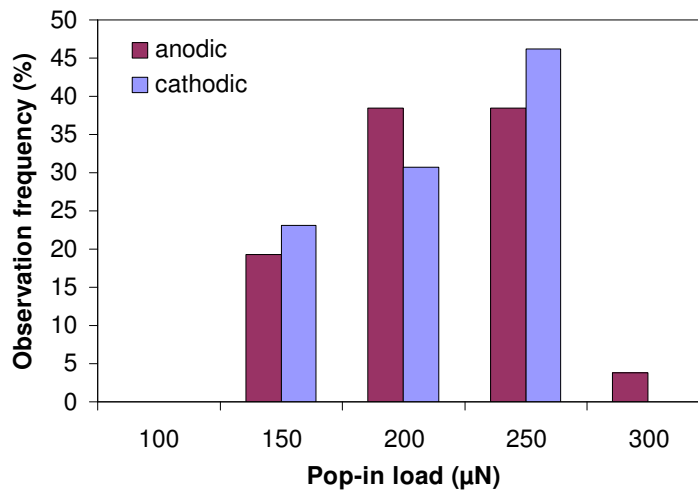


(b) Aged at 500 °C for 1 hour

Figure 5.67: Frequency of pop-in events under anodic and cathodic potential in ferrite and austenite phases of SDSS.



(a) Ferrite



(b) Austenite

Figure 5.68: Pop-in load distribution in austenite and ferrite phases of the as received SDSS sample for hydrogen charged (i.e. cathodic potential) and without hydrogen (i.e. anodic potential) conditions.

effect of hydrogen charging on pop-in load was inverse.

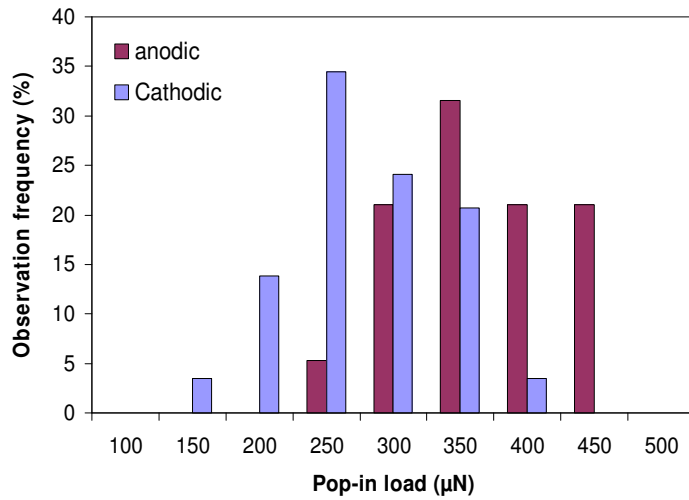
In order to reduce the dislocation density in the sample, it was heat treated at 500 °C in a vacuum better than 10^{-6} mbar for 1 h and then cooled in the furnace. The resulting pop-in event frequencies after the heat treatment are presented for both phases and for both anodic and cathodic potentials in figure 5.67b. The increase in the pop-in event frequencies for ferrite in comparison to the as received condition clearly shows that the dislocation density in this phase was reduced and the probability of probing a dislocation free region in the material was increased. However, an obvious change in pop-in events frequency was not observed for austenite. In the case of austenite phase in the aged sample, hydrogen charging again increased the dislocation density, which was observed in the form of the reduction in pop-in events (figure 5.67b) and was confirmed by observation of the slip lines formed during cathodic polarization. After the aging heat treatment the hydrogen effect on pop-in load distribution was similar to the ones observed before the heat treatment for the both phases. As can be seen in figure 5.69 the pop-in load distribution in ferrite was reduced due to the hydrogen charging (figure 5.69a) whereas for austenite increased (figure 5.69b).

Three different loads were used to perform the nanoindentations; 500 μ N, 1000 μ N, and 2000 μ N. In order to study the effect of strain rate on hardness, two different load functions were used for each of the mentioned peak loads:

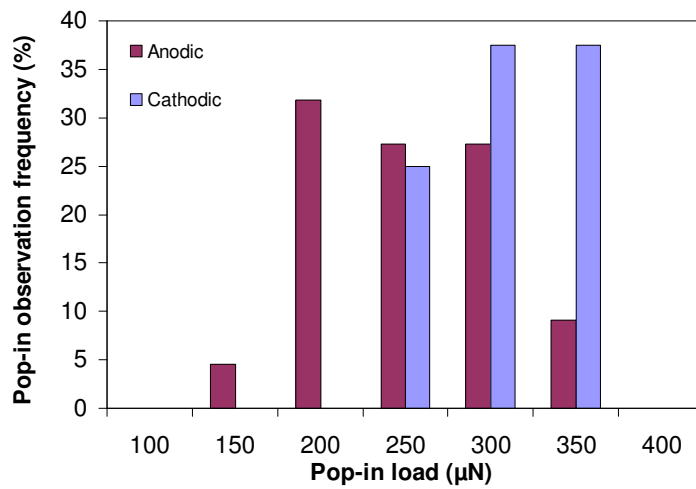
- a) Load functions with a constant loading rate of 100 μ N/s which are shown in figure 5.70.
- b) Load functions with a constant loading time of 2.5 seconds, which are shown in figure 5.71 ¹.

The nanoindentation experiments were performed on as received sample. The results for ferrite phase are summarized in figure 5.72. This figure clearly shows that no strain rate effect was observed for ferrite neither under anodic nor cathodic potentials. A clear effect of hydrogen on hardness of the ferrite was not observed. Similar curves for the austenite are presented in figure 5.73. A clear loading (strain) rate effect was observed in austenite phase after the hydrogen charging. In contrast to ferrite the hydrogen clearly increases hardness of the austenite.

¹Due to the complex geometry of the tip and the plastic zone during nanoindentation, there is no possibility to perform a quantitative analysis of the strain rate. However, the higher loading rate shown in figure 5.71 in comparison to figure 5.70 assures a higher strain rate.



(a) Ferrite



(b) Austenite

Figure 5.69: Pop-in load distribution in austenite and ferrite phases of the aged SDSS for hydrogen charged (i.e. cathodic potential) and without hydrogen (i.e. anodic potential) conditions.

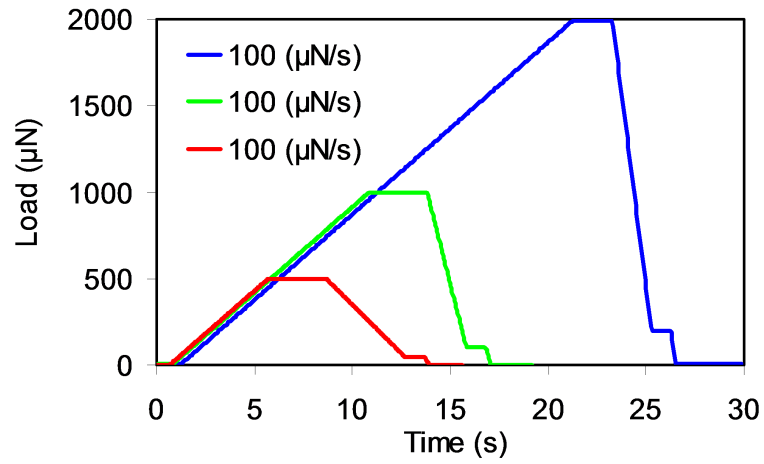


Figure 5.70: The load functions with constant loading rate of 100 $\mu\text{N/s}$ for each peak loads used to study the strain rate effect on hardness of the SDSS.

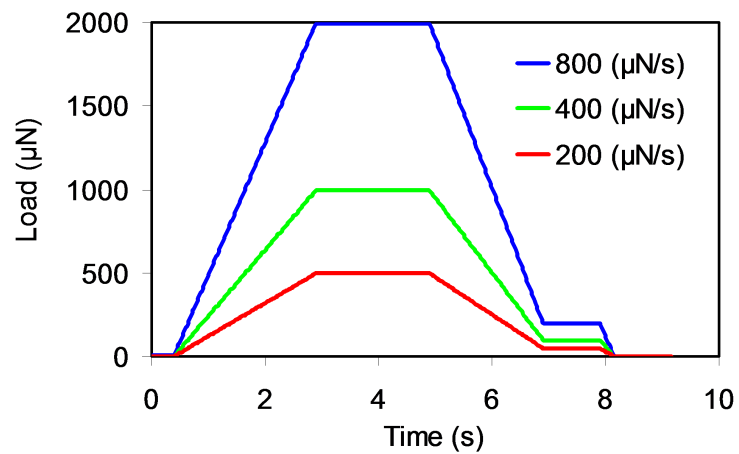
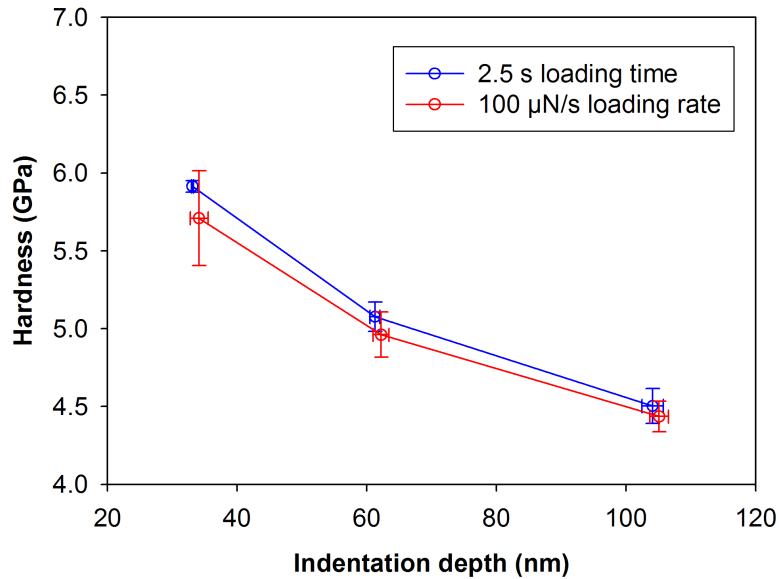
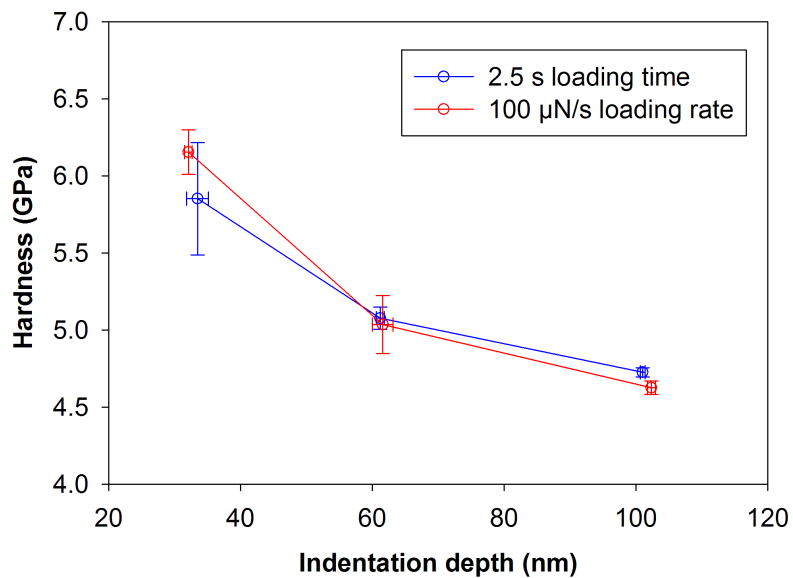


Figure 5.71: The load functions with constant loading time of 2.5 s for each peak loads used to study the strain rate effect on hardness of the SDSS.

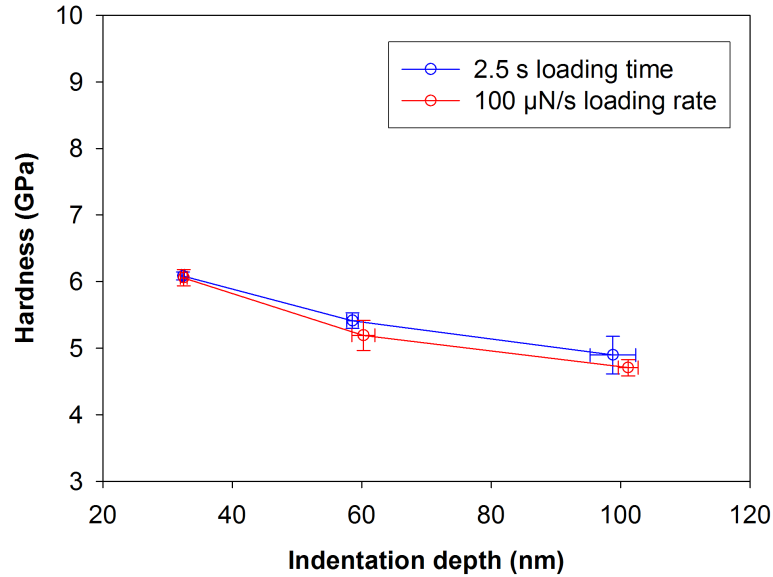


(a) As received sample under anodic potential

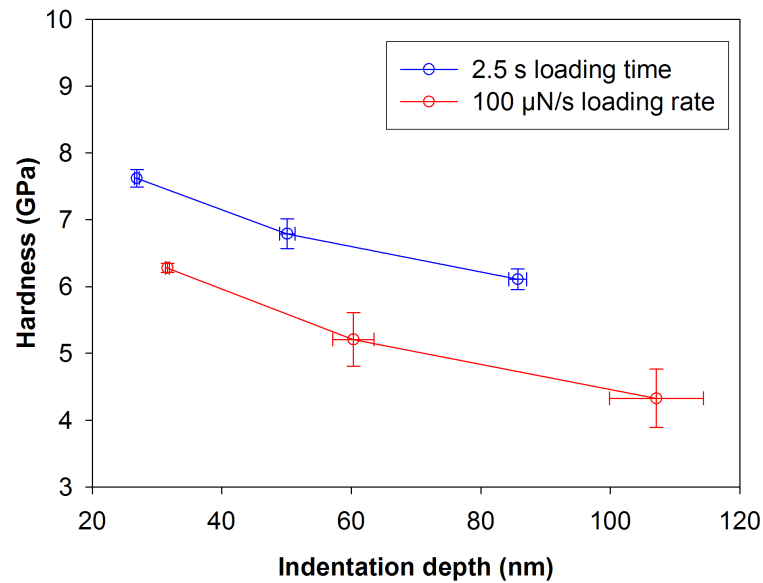


(b) As received sample under cathodic potential

Figure 5.72: The effect of loading rate and hydrogen charging on hardness of ferrite phase in as received SDSS at three different loads (i.e. 500 μN , 1000 μN , and 2000 μN) and two different loading rate. The blue points were measured with the load functions given in figure 5.71. The red points were measured with the load functions given in figure 5.70.



(a) As received sample under anodic potential



(b) As received sample under cathodic potential

Figure 5.73: The effect of loading rate and hydrogen charging on hardness of austenite phase in as received SDSS at three different loads (i.e. 500 μN , 1000 μN , and 2000 μN) and two different loading rate. The blue points were measured with the load functions given in figure 5.71. The red points were measured with the load functions given in figure 5.70.

5.7.3 Hydrogen effect on stainless steels¹

The austenitic stainless steels which contain less than about 18wt.%Ni, are known to transform to ϵ and α' martensites under the influence of strain or subzero cooling. There have been many studies on the effect of cold work on martensite transformation in stainless steel [260, 261, 262, 263, 264]. This transformation, however, can be triggered by hydrogen charging as well. The effect of hydrogen on the martensitic transformation in austenitic stainless steels has been demonstrated by a number of authors [263, 256, 265, 266, 267, 268]. X-ray diffraction (XRD) has shown that cathodic hydrogen charging can induce the formation of ϵ and α' martensites in the absence of strain or of subzero cooling. An expansion of the austenite lattice together with the formation of α' and ϵ phase was observed in cathodically charged metastable austenitic stainless steels at room temperature [1]. Cathodic charging produces the same martensitic phases at room temperature as those formed by transformation during low-temperature, and the lattice parameters of α' and ϵ phases formed by the different methods are very similar. There is not too much information available regarding the kinetic of this phase transformation.

This phase transformation elucidate the observation of slip lines on the surface of the austenite during hydrogen charging of SDSS (figure 5.66), as well as the increase in the hardness of austenitic stainless steel by cathodic polarization (figure 5.61). The phase transformation also results in plastic deformation which increases the dislocation density and consequently reduces the frequency of pop-in events, as shown in figure 5.67.

The reduction of pop-in load for ferrite after hydrogen charging is in agreement with the proposed model in 6.2. The increase in pop-in load for the hydrogen charged austenite in both austenitic stainless steel and SDSS, however, is probably due to the phase transformation happening during hydrogen charging².

The explanation of the loading (strain) rate effect on the hardness of the austenite in the SDSS requires detailed information from the underlying sub-microstructure of this phase³. Horvath et al. [269] conducted electron microscopy

¹The in situ electrochemical nanoindentation tests on SDSS were carried out in frame of a master thesis in cooperation with the Norwegian University of Science and Technology (NTNU *Norges teknisk-naturvitenskapelige universitet*). The primary result presented in the preceding sections are part of an ongoing project. Therefore the discussion will be provided here [259].

²Further studies with the help of analytical methods like XRD and phase analysis with high resolution OIM are planned in future experiments, in order to quantitatively resolve this phase transformation.

³By sub-microstructure the dislocation cell structure and precipitates distribution is meant

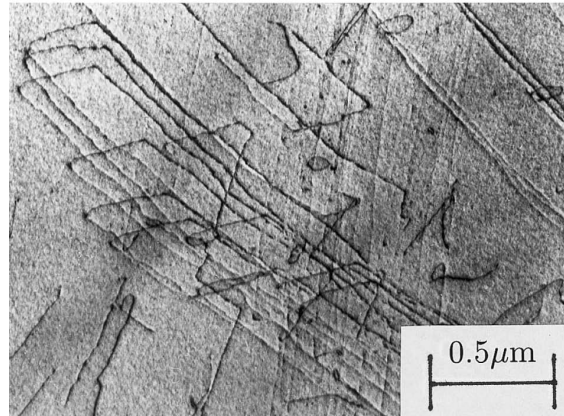


Figure 5.74: Electron micrograph of a precipitate free ferritic region belonging to a continuous ferritic grain cluster [269].

studies on microstructural changes taking place in ferrite and austenite phases of SDSS between room temperature and 500 °C. The sub-microstructure of a continuous volume of precipitate free ferrite in a solution annealed sample is presented in figure 5.74. The dislocation-rich regions in the continuous part of the austenitic phase is shown in figure 5.75. Definition of continuous or isolated grains is made upon the special topology of the SDSS microstructure. Figure 5.76 shows the typical microstructure of SDSS after electropolishing. Some of the isolated grains, which are surrounded by the grains of the other phase are marked in figure 5.76. All other non-isolated grains are considered as continuous. The dislocation density in the dislocation rich regions is reduced by recovery during aging heat treatment. In the austenite, the low stacking fault energy impedes the nonconservative dislocation motion. Therefore, the recovery rate is lower in austenite than in ferrite. Dislocation combination and annihilation are the recovery mechanisms in austenite leading to a uniform dislocation distribution without any sign of cell formation (figure 5.77). Because of the high dislocation mobility in the bcc ferrite, the dislocations can climb (and, therefore, cross slip) more easily, thus promoting recovery and resulting in a considerable reduction of the dislocation density and the formation of dislocation cells. Polygonization of dislocations leads to subgrain formation during aging. The interiors of the subgrains become almost free of dislocations, and the subgrain boundaries are straightened. Hence, the dislocation density of austenite and ferrite is further decreased after aging [269]. This results in a clear increase in pop-in event frequency for the ferrite phase in the aged sample, as shown in figure 5.67b. The other important factor defining the sub-microstructure of SDSS is the existing precipitates and their distribution in the alloy. The precip-

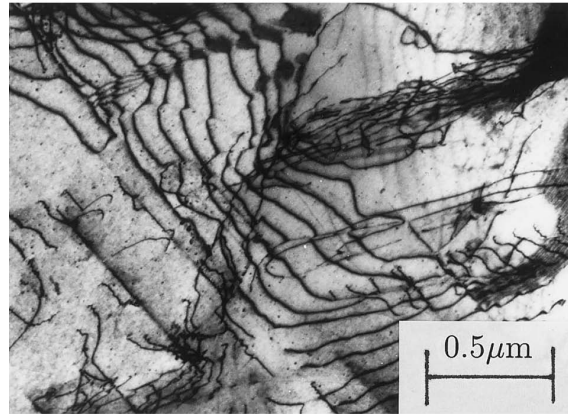


Figure 5.75: Electron micrograph of an austenitic region belonging to a continuous austenitic grain cluster [269].

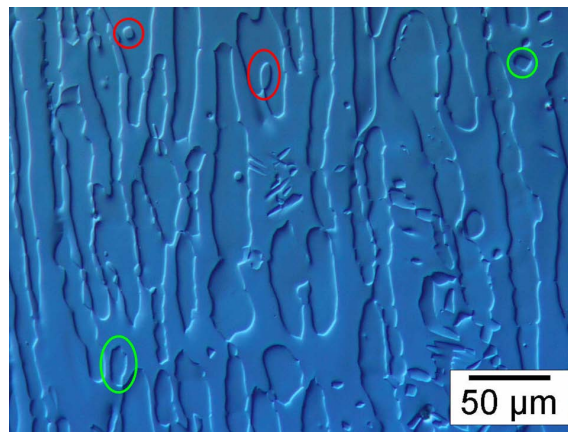


Figure 5.76: Micrograph of a typical SDSS sample microstructure. Austenite is the deeper electropolished phase. Isolated ferrite grains are marked with red colored lines and isolated austenites with green lines.

itation behavior in SDSS is very complicated since the higher level of alloying elements (Cr and Mo) accelerates the precipitation kinetics of harmful intermetallic phases [270]. However, only precipitation of Cr_2N and α' were possible in the range of temperature and time used for aging heat treatment in this study [269]. Since the activation energy for diffusion of interstitially dissolved nitrogen is very low, it can safely be assumed that the movement of nitrogen atoms easily takes place at the temperature of the aging treatment. The mobility of the dissolved nitrogen can lead to the formation of shortrange order regions in the vicinity of chrome and molybdenum atoms promoting nucleation and growth of precipitates. Due to the higher solubility limit for nitrogen in the austenite the precipitation of Cr_2N mainly happens in austenitic grains. It has been shown that small spherical particles of chromium nitride precipitates

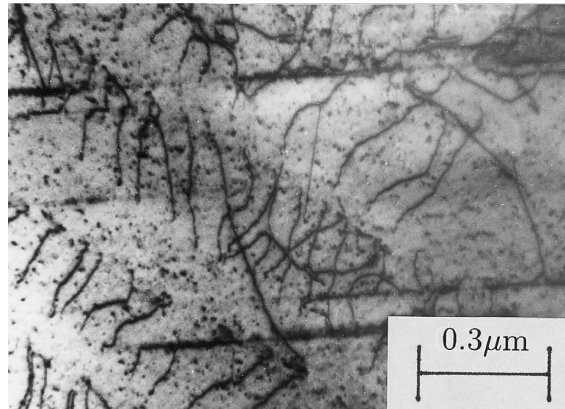


Figure 5.77: Electron micrograph of an austenitic region aged in 500 °C. The dislocation density is low and spherical Cr_2N particles are formed (black dots uniformly dispersed in the matrix are Cr_2N particles, compare with figure 5.75 where no precipitates are observable.). The dislocations interact with the particles [269].

and the dislocations interact with these particles as shown in figure 5.77. An increase in the coherent α' could be the reason for the change in the hardness of the ferrite after the heat treatment [269, 270]. To prove these assumptions further nanoindentation tests were performed in air on three different grains of each phases of as received and heat treated samples. In order to achieve reliable information from underlying sub-microstructure a matrix of 5×5 indents were performed with a distance of 3 μm from each other. Two different peak loads were used, 500 μN and 1000 μN . The matrix was repeated 3 times at the same grain for each peak load (i.e. 150 indents). This resulted in a total of 900 indents which are used to analyse the effect of heat treatment on the pop-in load and hardness. Figure 5.78 shows the effect of aging heat treatment on pop-in event frequency during nanoindentation of both phases. The aging treatment resulted in a clear increase in the pop-in events frequency (reduction of dislocation density) in ferrite, as predicted from above mentioned sub-microstructure evolution for ferrite. On the other hand, the pop-in events frequency during nanoindentation of austenite was reduced after the heat treatment. This is again in good agreement with the sub-microstructure evolution for austenite. Whereas the aging treatment may reduce the dislocation density in austenite, the formation of the uniformly distributed fine Cr_2N precipitates (figure 5.77) results in a non homogeneous dislocation nucleation at the interface of these precipitates during nanoindentation and thereby elimination of pop-in. The change in hardness, as shown in figure 5.79 provides further evidence for this theory. The increase in the hardness of austenite is in agreement with the formation of precipitates.

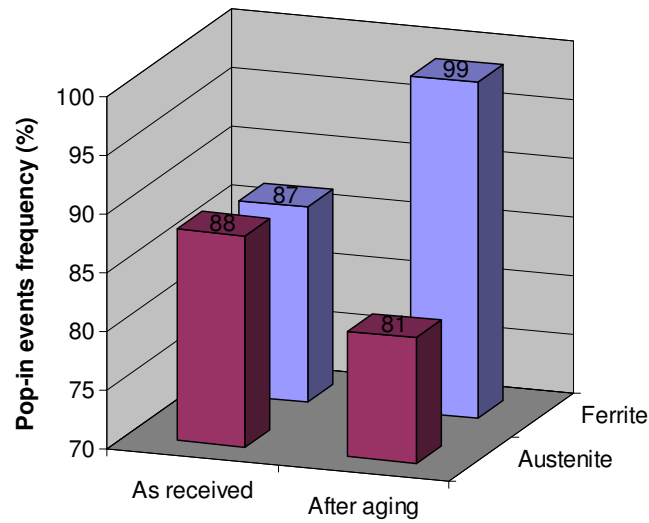


Figure 5.78: Effect of aging heat treatment on pop-in event frequency observed in SDSS

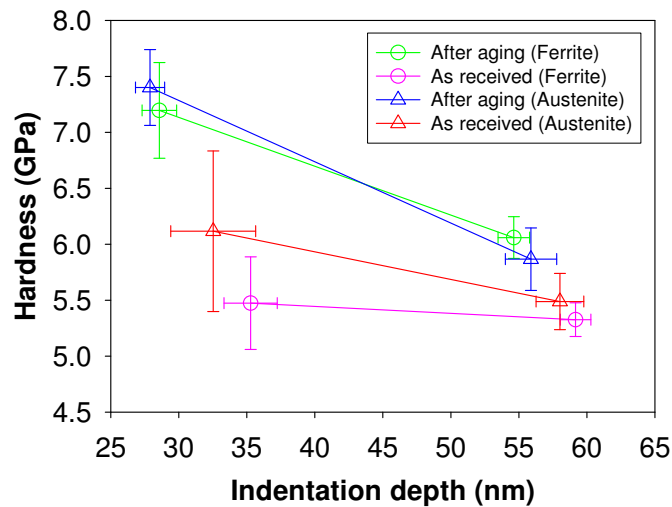


Figure 5.79: Effect of aging heat treatment on hardness of different phases in SDSS

The increase in the hardness of ferrite is also in agreement with the formation of coherent chromium rich α' regions in ferrite [271].

It is now possible, with the understanding of the underlying sub-microstructure in the samples before and after heat treatment, to explain the strain rate effect observed during hydrogen charging of as received austenite phase (figure 5.73). Figure 5.80 schematically shows the interaction of existing dislocations with

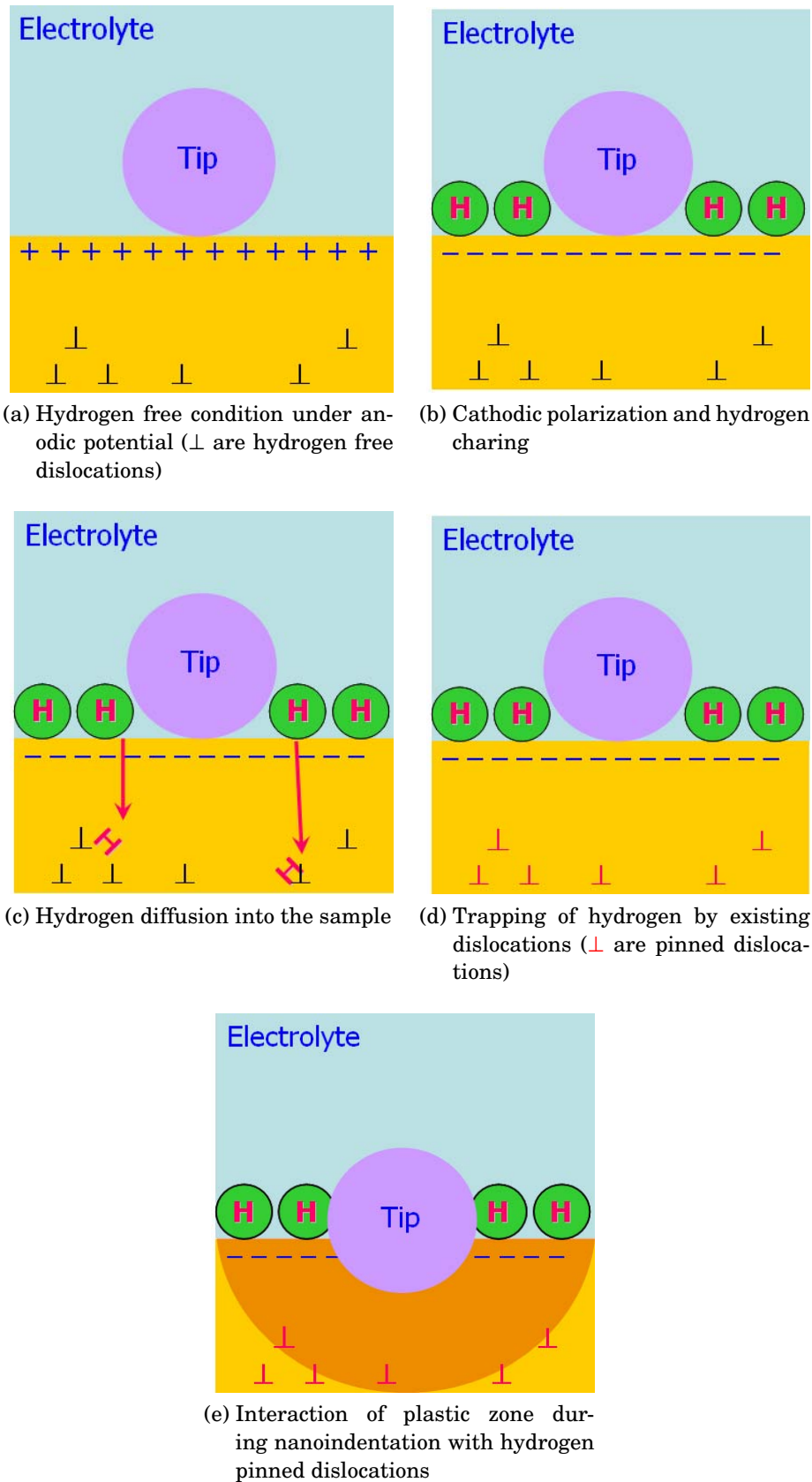


Figure 5.80: Schematic representation of existing dislocations in austenite phase of as received SDSS and their interaction with hydrogen and plastic zone during nanoindentation

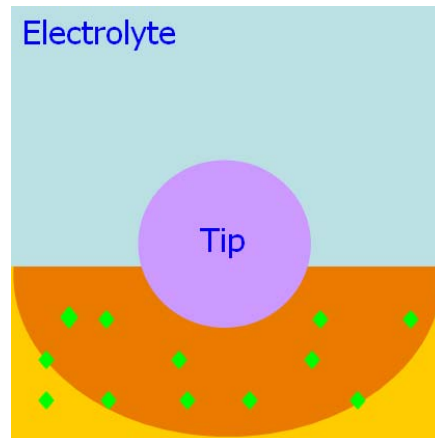


Figure 5.81: Schematic representation of plastic zone interaction with Cr_2N particles in the lattice (Green \blacklozenge are Cr_2N particles)

hydrogen. The cathodically charged hydrogen atoms (figure 5.80b) diffuse into the metal (figure 5.80c) and are trapped by existing dislocations in the sample (figure 5.80d). This results in pinning of dislocations. During indentation the plastic zone formed below the tip passes through these pinned dislocations. Dislocations within the plastic zone will be stopped until either the hydrogen atoms have sufficient time to feel the force of the dislocation and diffuse away from its preferred site, or the dislocation can overcome the dislocation-hydrogen pair for example by cross slipping. Both cases are thermally activated processes. However, the mobility of the hydrogen atom at room temperature in austenite is fast enough [272, 255], and the required thermal activation for removing hydrogen from pinned dislocations can be provided for austenite at room temperature. Therefore, room temperature strain rate sensitivity was observed in the hydrogen charged material. In the aged material, due to the formation of Cr_2N particles in the lattice (figure 5.77), even before the hydrogen charging, plastic zone was sensing the obstacles (i.e. Cr_2N particles) as shown schematically in figure 5.81. However, in this case the activation energy required for cross slipping or cutting the Cr_2N particles is higher than the energy required for activating the hydrogen pinned dislocations (i.e. depinning of the dislocations). Therefore, in order to see a rate effect either the temperature should be increased or a lower loading rate should be used¹.

The increase in hardness is related to the additional stress, $\Delta\tau$, required to force a dislocation line pass an array of rigid obstacles, described phenomeno-

¹Using lower loading (strain) rates during nanoindentation introduces additional errors due to the thermal drift.

logically by the familiar expression derived by Orowan

$$\Delta\tau = \left(\frac{\mu b}{\lambda} \right) \quad (5.7)$$

where λ is the mean distance between the obstacles, μ the shear modulus, and b is the Burgers vector. The equation (5.7) can be rewritten using the equation (3.40), as follow

$$\Delta H = 3\sqrt{3} \left(\frac{\mu b}{\lambda} \right) \quad (5.8)$$

where ΔH is the increase in the hardness resulting from the obstacles. If we consider that the pinned dislocations by hydrogen (figure 5.80c) in high strain rate acting as rigid obstacles then the mean distance between the obstacles is related to the pinned dislocation density according to

$$\lambda = \frac{1}{\sqrt{\rho_{pinned}}} \quad (5.9)$$

where ρ_{pinned} is the density of pinned dislocations which are contributed in increasing the hardness. Substituting λ in equation (5.8) results in

$$\Delta H = 3\sqrt{3}\mu b \sqrt{\rho_{pinned}} \quad (5.10)$$

As mentioned before the hardness can be related to the geometrically necessary dislocation density, ρ_G , and statistically stored dislocations, ρ_S , as given by equation (3.40). As a first approximation ρ_S can be assumed to be independent of strain (loading) rate. The ρ_G is a function of indentation depth according to equation (3.39). Therefore the observed increase in the hardness at higher loading rates for the same indentation depth, can be assumed to be due to the pinned dislocations. This means for a constant depth the difference of the observed hardness can be used to calculate the difference in pinned dislocation density, $\Delta\rho$, for two different loading rates according to equation (5.10). In order to do this, the results shown in figure 5.73b were fitted with Gao-Nix model described by equation (3.42). The resulted plot is shown in figure 5.82. Now fit curves can be used in order to find the hardness at the same depth for both loading rate. This is done for three different depths as shown in figure 5.82 with dashed green lines. The loading time to reach each indentation depth is depending on the used loading rate (figure 5.70 and figure 5.71). The difference between indentation times with the two loading rates in order to reach the same depth, Δt , can be estimated. Assuming the shear modulus of austenite in SDSS to be equal to 85 GPa [259] and Burgers vector equal to 0.28 nm, the difference in pinned

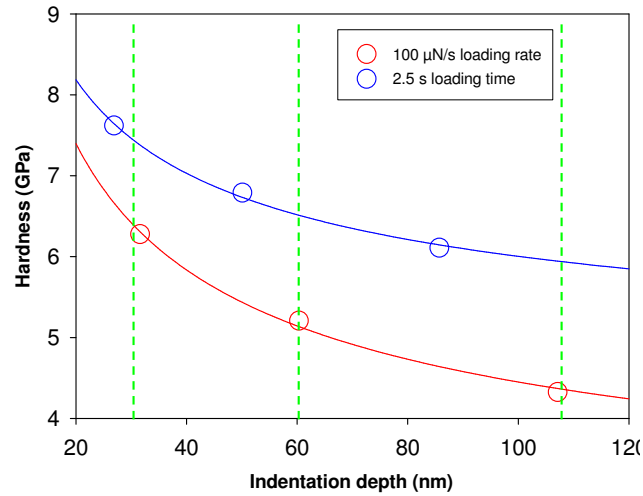


Figure 5.82: The effect of loading rate on hardness of austenite in as received SDSS. The data is fitted with Gao-Nix model

Table 5.10: Hardness of austenite at the same depth for different loading rate in hydrogen charged as received SDSS and calculated pinned dislocation density

Indentation depth (nm)	Hardness (GPa) (2.5 s loading time)	Hardness (GPa) (100 μ N/s loading rate)	$\Delta\rho$	Δt
30	7.8	6.8	6×10^7	2.5
60	6.5	5.1	1×10^8	7.5
110	5.9	4.3	2×10^8	17.5

dislocation density, ρ_{pinned} , can be calculated according to equation (5.10). This was calculated for the three given points in figure 5.82 (table 5.10). The results shown here are in good agreement with the proposed model for the observed strain rate sensitivity in austenite. By lowering the loading rate and increasing the time, the probability of de-pinning of the pinned dislocations is increasing as shown in figure 5.83.

In future by using a displacement controlled indentation test at different temperatures it is possible to gather quantitative information about the trapping energy of hydrogen into dislocations.

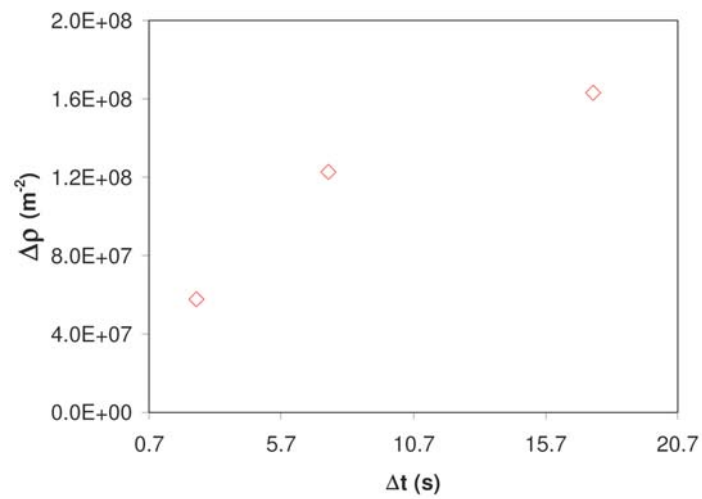


Figure 5.83: Difference in pinned dislocation density for different loading rates as function of time during nanoindentation of hydrogen charged austenite in as received SDSS sample.

CHAPTER 6

Discussion

There are no facts, only interpretations.

Morgenröte. Gedanken über die moralischen
FRIEDRICH NIETZSCHE

IN situ electrochemical nanoindentation experiments were performed in this study, in order to achieve a better understanding of hydrogen embrittlement. Different metals alloys and an intermetallic were studied by the developed technique. A clear effect of hydrogen on dislocation nucleation (pop-in) in all of the samples was observed. In this section a model based on linear elasticity for indentation induced homogeneous dislocation nucleation will be used to analyze the hydrogen induced change in the pop-in load.

6.1 Indentation induced homogeneous dislocation nucleation

One aspect of incipient plasticity that has not been elucidated in detail is the rate or time dependence of the pop-in phenomenon. For pure metals without significant surface films, where pop-in signals the nucleation of dislocations, one might expect a significant dependence on time and temperature since defect nucleation is thermally activated. The simple interpretation of pop-in proposed in literature (section 3.6.2.3) predicts a constant pop-in load during nanoindentation and does not consider the time dependence [163]. However, the observations suggest that even at subcritical loads, pop-in displacements can be triggered if sufficient time is allowed for a favorable thermal vibration to induce defect nucleation [273, 274, 275]. As an example figure 6.1 shows the effect

of loading time on pop-in and elastic events frequency during nanoindentation of (111) nickel single crystal. The increase in loading time resulted in higher frequency of pop-in events and reduced the elastic events. On the other hand decreasing the loading rate resulted in less pop-in events. It should be mentioned that in this experiments there is always either pop-in or complete elastic indentation (i.e. pop-in plus elastic events frequency is equal to 100%). Therefore no observation of pop-in means a fully elastic indent. The above observations sug-

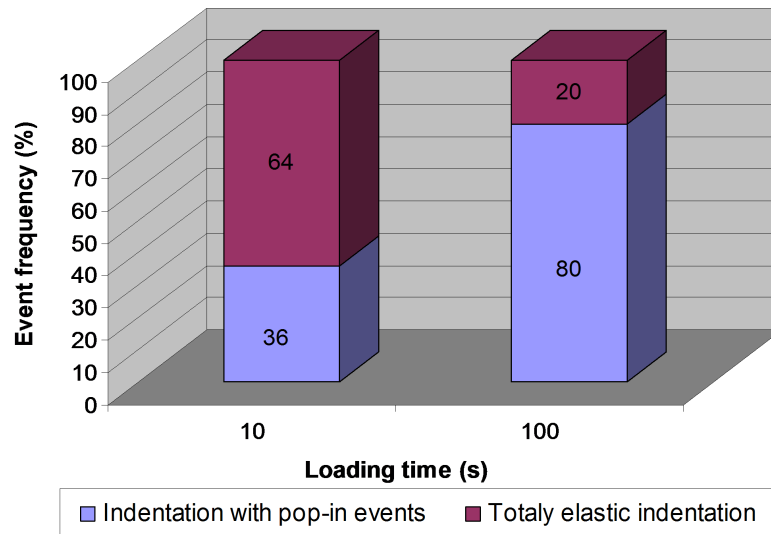


Figure 6.1: Effect of loading time on pop-in and elastic events frequency during nanoindentation on a (111) nickel single crystal.

gest an important contribution from thermal activation in incipient plasticity. For a given indenter tip, loading rate, and ambient condition, the first pop-in event does not always occur at the same applied load; there is a distribution of strengths required to initiate plastic flow beneath the indenter. This effect is illustrated for different metals in figure 6.2, where the load of the first pop-in is plotted on the ordinate axis, with the width of the pop-in event on the abscissa. Here the distribution of pop-in loads spreads quite significantly over about 100's of μN for a given material. At the same time, we observe that higher pop-in loads necessarily give rise to larger pop-in displacements; within the resolution of the instrument, the relationship between these variables seems linear in figure 6.2. This result is consistent with prior observations in a variety of metallic alloys [184, 276] and suggests that the strain accommodated by the displacement burst is a constant. In other words, the physical event(s) associated with the plastic accommodation burst are likely the same for every indentation, but

these events can occur at different levels of load or stress. This is shown schematically in figure 6.4. In a perfect displacement controlled nanoindenter unstable transition from elastic to plastic deformation would be followed by a reduction in load, as shown in figure 6.4a. Therefore, the pop-in load occurrence over a range of loads results in observation of different load drops according to the figure 6.4b. In the case of a load control system¹, however, unstable transition from elastic to plastic deformation will be followed by a pop-in (displacement jump) as shown in figure 6.4c. Consequently pop-in width will be defined through the difference of displacement of ideal elastic and plastic behavior at the pop-in load (figure 6.4d). In principle, there are a number of extrinsic effects that could produce the spread in pop-in loads described above, including, e.g., variations in specimen or surface quality. However, we also note a clear rate-dependence of the pop-in data presented in figure 6.1, where the shorter loading time corresponds to delay in pop-in and observation of fully elastic behavior. This result is in general agreement with the previous studies, which have reported time activated or rate dependent pop-in data for a number of crystalline materials [273, 274, 275]. As an example figure 6.5 shows a time activated pop-in observed during nanoindentation of FeAl intermetallic. Similar behavior for all other metals and alloys in this study were observed. There has not yet been any quantitative analysis of experimental data that supports this view. In what follows we consider the statistics of defect nucleation, and demonstrate that our experimental data can all be quantitatively rationalized on this basis.

For an indentation test, the applied shear stress that nucleates a dislocation can be assumed to be the maximum shear stress beneath the indenter at the onset of a pop-in. According to contact mechanics, the maximum shear stress is reached at a point approximately 0.48 times the contact radius (see 3.2) below the sample surface. The position, $h_{\tau_{max}}$, and value of the maximum shear stress, τ_{max} , are given by equation (3.14) and (3.15). This maximum shear stress is responsible for the homogeneous dislocation nucleation at $h_{\tau_{max}}$, as shown in figure 6.6. Classic dislocation nucleation theory, as summarized by Hirth and Lothe [26], suggests that the shear stress depends on the energy required to generate a dislocation loop. The free energy of a circular dislocation loop of radius r is given by

$$\Delta G = 2\pi r W + \pi r^2 \gamma - \pi r^2 b \tau \quad (6.1)$$

where W is the line energy of the dislocation loop, b is the Burgers vector², τ

¹To the knowledge of the author all commercially available nanoindentation systems are load controlled (see section 3.4).

²In the case of an fcc lattice b can be the Burgers vector for a partial dislocation

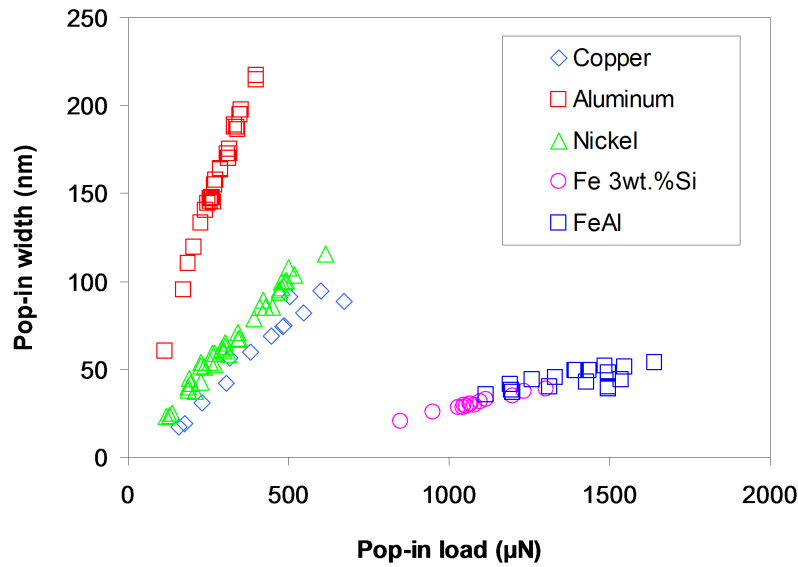


Figure 6.2: Relationship between the load of the first pop-in and the resulting displacement of the burst (pop-in width) for different materials.

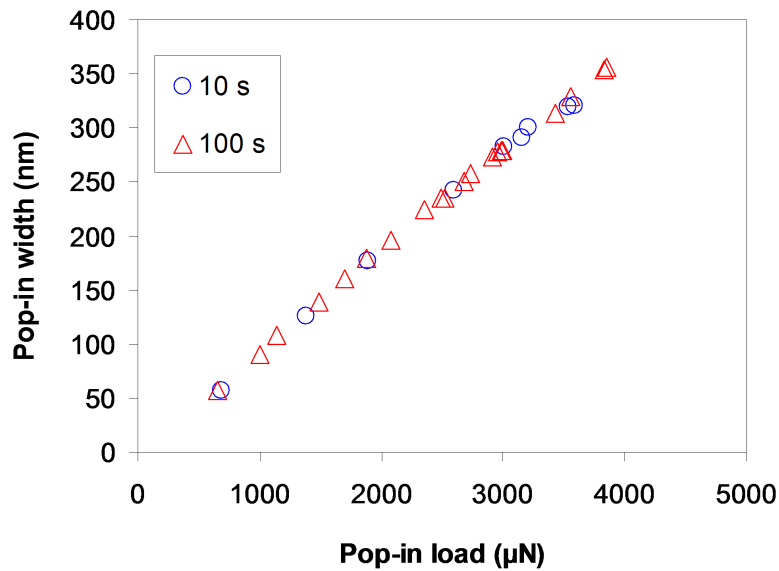


Figure 6.3: Relationship between the load of the first pop-in and the resulting displacement of the burst (pop-in width) for nanoindentation of nickel with two different loading times (from the same set of data given in figure 6.1). *These indentations were done by using a different tip from ones shown in figure 6.2 therefore the range of pop-in load is different*

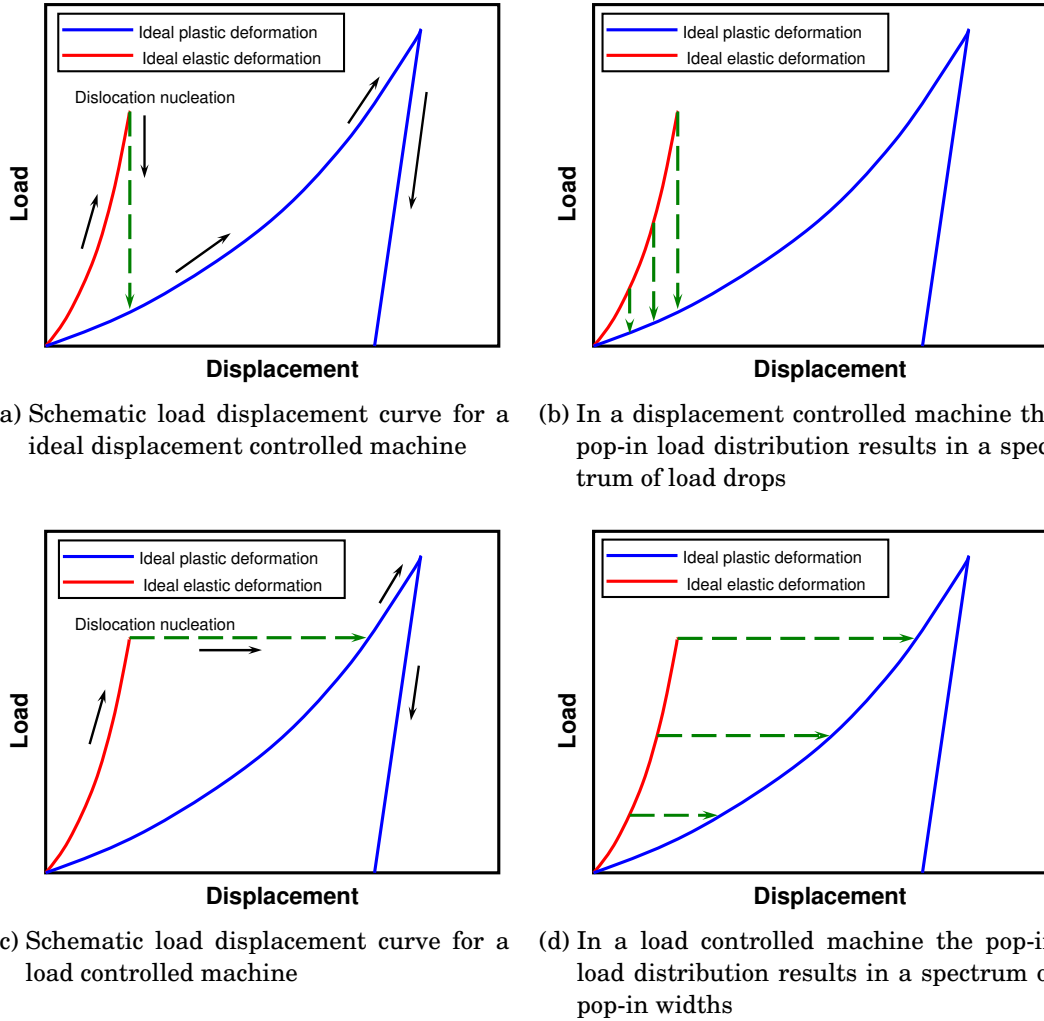


Figure 6.4: Schematic load displacement curve for a material which shows an unstable elastic to plastic transition by homogeneous dislocation nucleation.

is the external shear stress acting on the loop (i.e. Peach-Köhler force [277]), and γ is the SFE for fcc metals. The first term on the right-hand side of equation (6.1) describes the energy required to create a dislocation loop in a defect free lattice. The second term indicates the increase in energy due to the creation of a stacking fault. The sum is equal to the total increase in lattice energy due to the formation of a dislocation loop. The last term gives the work done by the applied stress τ as a result of the Burgers vector displacement and indicates the work done on the system to expand the dislocation. The line energy W for the loop, which results from the lattice strain in the vicinity of the dislocation for $r > \rho$, is given by [26]

$$W = \frac{2 - \nu}{1 - \nu} \frac{\mu b^2}{8\pi} \left(\ln \frac{4r}{\rho} - 2 \right) \quad (6.2)$$

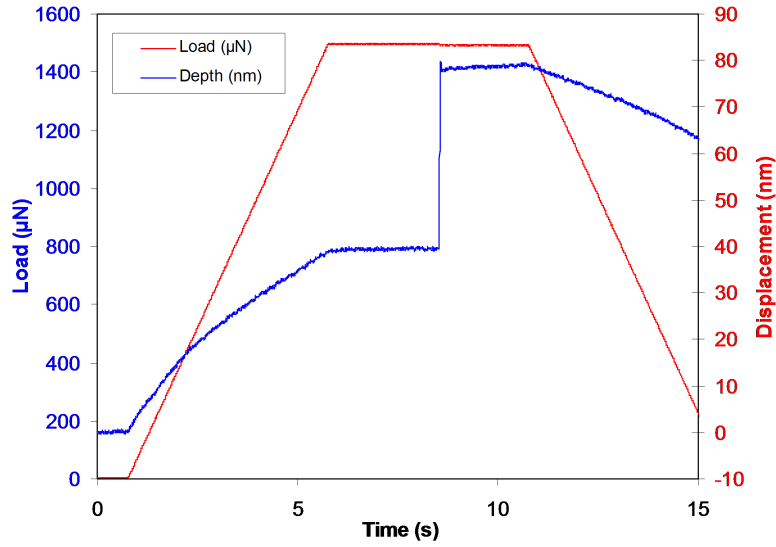


Figure 6.5: Time activated pop-in observed during nanoindentation of FeAl (100) single crystal. After a period of holding at a constant load a pop-in happens.

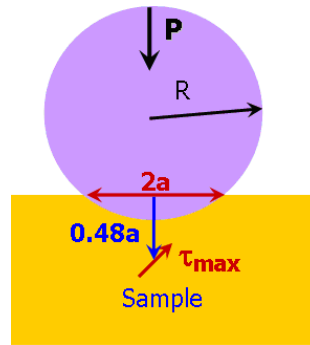


Figure 6.6: Position of the maximum shear stress responsible for the homogeneous dislocation nucleation beneath the tip at $h_{\tau_{max}}$ according to the Hertzain contact model

where μ is the shear modulus and ρ is the dislocation core radius. Using equation (6.2), the equation (6.1) can be rewritten as follow

$$\Delta G = \frac{2-\nu}{1-\nu} \frac{\mu b^2 r}{4} \left(\ln \frac{4r}{\rho} - 2 \right) + \pi r^2 \gamma - \pi r^2 b \tau \quad (6.3)$$

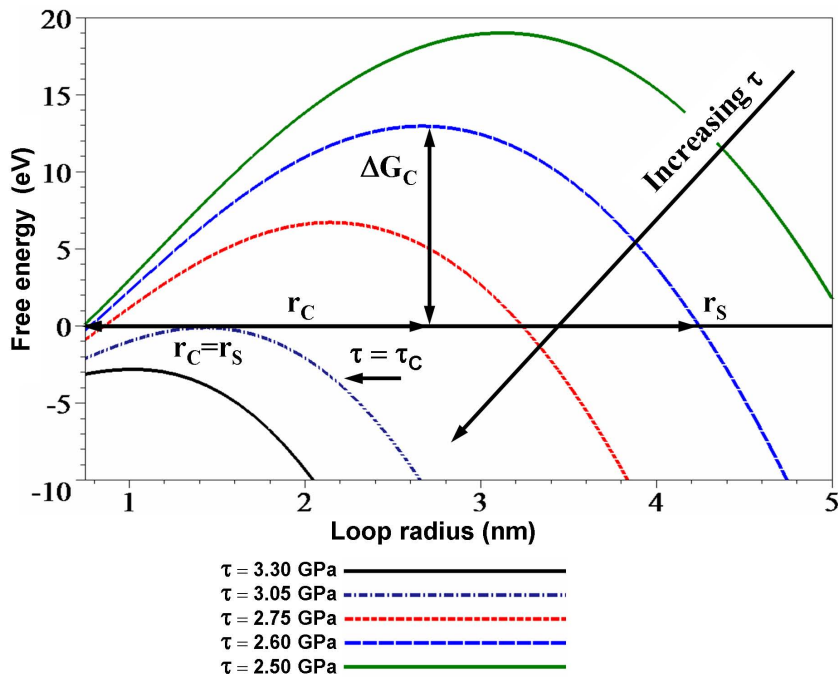
Figure 6.7 shows a plot of equation(6.3) calculated from the constants for nickel in table 6.1. From the thermodynamic point of view the primary condition for homogeneous dislocation nucleation is

$$\Delta G \leq 0$$

This happens as soon as the unstable loop radius reaches the minimum thermodynamically stable radius, r_s . Therefore, by setting the $\Delta G = 0$ a relation between the critical shear stress for dislocation nucleation and the stable dislocation loop radius, r_s can be defined (figure 6.7b).

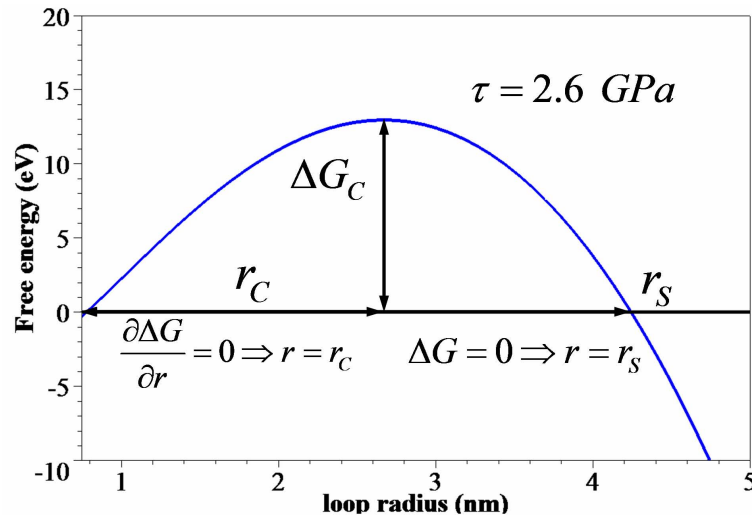
$$\tau = \frac{(2-\nu)Gb}{4\pi r_s(1-\nu)} \left(\ln \frac{4r_s}{\rho} - 2 \right) + \frac{\gamma}{b} \quad (6.4)$$

Figure 6.7 shows that the free energy for formation of a dislocation loop passes through a maximum which defines the activation energy for the process of homogeneous dislocation nucleation. For a given shear stress, at small radii, the total increase in the lattice energy as a result of the dislocation loop formation is larger than the external work done by the applied shear stress, and the total free energy is positive. This situation changes, however, as the radius grows in size, so that with larger radii, the free energy becomes negative. Therefore the free energy of formation has a critical maximum value ΔG_c at a loop size r_c

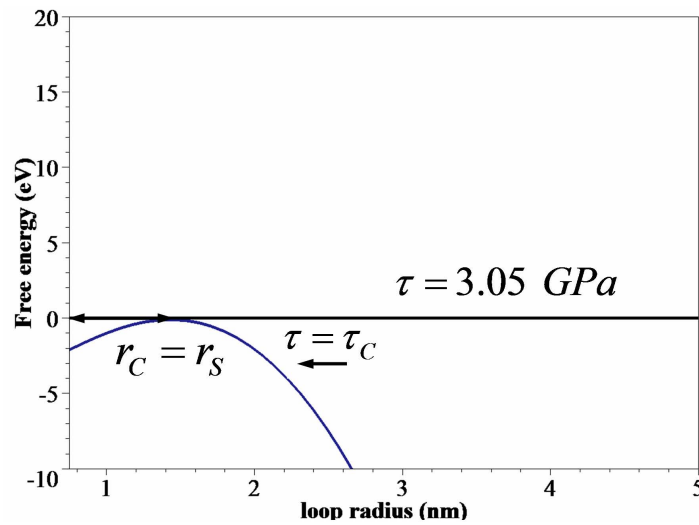


(a) Free energy curves for different shear stresses.

Figure 6.7: Change in free energy of homogeneous dislocation nucleation for nickel as a function of dislocation loop radius r for various applied shear stresses τ on the crystal lattice. The activation energy for dislocation nucleation ΔG_c , critical loop radius r_c , and minimum stable loop radius r_s are shown for different conditions (continued in next page).



(b) Free energy curve for $\tau = 2.6 \text{ GPa}$ with a positive activation energy for homogeneous dislocation nucleation.



(c) Free energy curve for $\tau = 3.05 \text{ GPa}$ with zero activation energy for homogeneous dislocation nucleation.

Figure 6.7: Change in free energy of homogeneous dislocation nucleation for nickel as a function of dislocation loop radius r for various applied shear stresses τ on the crystal lattice. The activation energy for dislocation nucleation ΔG_C , critical loop radius r_C , and minimum stable loop radius r_S are shown for different conditions (continued from previous page).

(figure 6.7b), which can be found by setting

$$\frac{\partial \Delta G}{\partial r} = 0$$

which results in

$$\frac{(2-\nu)\mu b^2}{4(1-\nu)} \left(\ln \frac{4r_c}{\rho} - 1 \right) - 2\pi r_c b \tau + 2\pi r_c \gamma = 0 \quad (6.5)$$

Solving the equation (6.5) for shear stress, τ , results in a relation between the critical loop radius, r_c and τ

$$\tau = \frac{(2-\nu)Gb}{8\pi r_c(1-\nu)} \left(\ln \frac{4r_c}{\rho} - 1 \right) + \frac{\gamma}{b} \quad (6.6)$$

This means that the growth of any nucleus with a radius smaller than r_c requires an activation energy to overcome the ΔG_c energy barrier for forming a stable dislocation loop ($r > r_s$), as shown in figure 6.7b. The available thermal energy at room temperature ($T = 298^\circ\text{C}$) is 0.026 eV. This situation can be expressed as

$$\Delta G(r_c) \leq 0.026 \text{ eV} \quad \text{or} \quad \sim \Delta G(r_c) \leq 0 \quad (6.7)$$

Therefore, where the free energy maximum, i.e. activation energy, is lower than 0.026 eV, spontaneous dislocation nucleation (i.e. pop-in) is possible. This is only the case if the applied shear stress is higher than the critical shear stress, τ_c (~ 3 GPa for nickel). In this case the critical loop radius, r_c , becomes equal to the minimum stable loop radius, r_s , as shown in figure 6.7c. The value of critical shear stress can be estimated by solving the equations (6.4) and (6.5) and setting $r_s = r_c$, as follows

$$\tau_c = \frac{2-\nu}{1-\nu} \left(\frac{\mu b}{\pi e^3 \rho} \right) - \left(\frac{\gamma}{b} \right) \quad (6.8)$$

Further, by using the equation (3.14), the shear stress may be related to the nanoindentation load and this makes it possible to define the lower threshold of the pop-in load as

$$P_{pop-in} = \left(\frac{\pi^3 R^2}{6E_r^2} \right) \left[3.22 \left[\frac{(2-\nu)}{(1-\nu)} \left(\frac{\mu b}{\pi e^3 \rho} \right) - \left(\frac{\gamma}{b} \right) \right] \right]^3 \quad (6.9)$$

This equation can predict the minimum observable pop-in load during a nanoindentation test.

At stresses higher than τ_c , the free energy curve is always negative (figure 6.7a). This is exactly what happens during a pop-in in nanoindentation.

Table 6.1: Physical constants used to reproduce the free energy plots of dislocation nucleation

Metal	E (GPa)	E_r (GPa)	μ (GPa)	ν	γ (J/m ²)	b (nm)	ρ (nm)	R (μ m)
Nickel	207	191	79	0.31	0.22	0.14	0.29	1
Copper	110	111	42	0.32	0.06	0.15	0.29	3
Aluminum (Partial)	62	67	23	0.35	0.11	0.17	0.33	3
Aluminum (Perfect)	62	67	23	0.35	0.11	0.29	0.29	3
Fe-3wt.%Si	222	202	85	0.32	–	0.25	0.17	2
FeAl	244	217	94	0.3	–	0.25	0.34	1.5

6.2 Hydrogen effect on dislocation nucleation

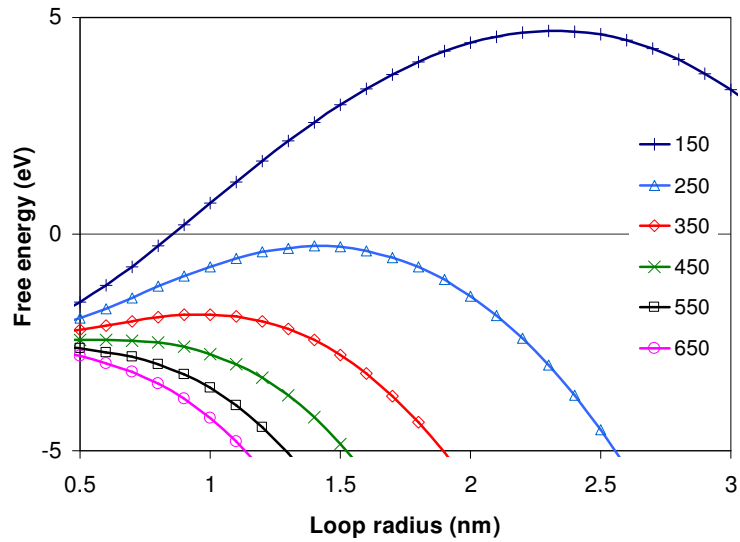
To check the validity and applicability of the proposed model the statistical pop-in results measured during nanoindentation of the different materials in this study were analyzed. In figure 6.8a, the free energy curves for all measured pop-in loads of copper (figure 6.8b) are plotted using the data in table 6.1. A very good agreement between the proposed homogeneous dislocation nucleation model and experimental results in copper was obtained at both cathodic and anodic potentials. This means that pop-ins were only observed for loads at which their free energy maximum was lower than the available thermal energy at room temperature. Similar curves for nickel are given in figure 6.9. Whereas a good agreement was found with the model for the pop-ins at anodic potential, the pop-ins at cathodic potentials seemed to overcome the existing energy barrier for dislocation nucleation at lower shear stresses (applied loads). Since the thermal energy available during nanoindentation at room temperature is very low (0.026 eV), the only possible external contribution to overcome the activation energy for dislocation nucleation is hydrogen, charged electrochemically into the metal. Hydrogen is therefore obviously reducing the activation energy required for dislocation nucleation in nickel. To include the effect of hydrogen in the proposed model (6.3) can be rewritten by introducing the effect of hydrogen as follows

$$\Delta G = \frac{2-\nu}{1-\nu} \frac{\mu_H b^2 r}{4} \left(\ln \frac{4r}{\rho_H} - 2 \right) + \pi r^2 \gamma_H - \pi r^2 b \tau \quad (6.10)$$

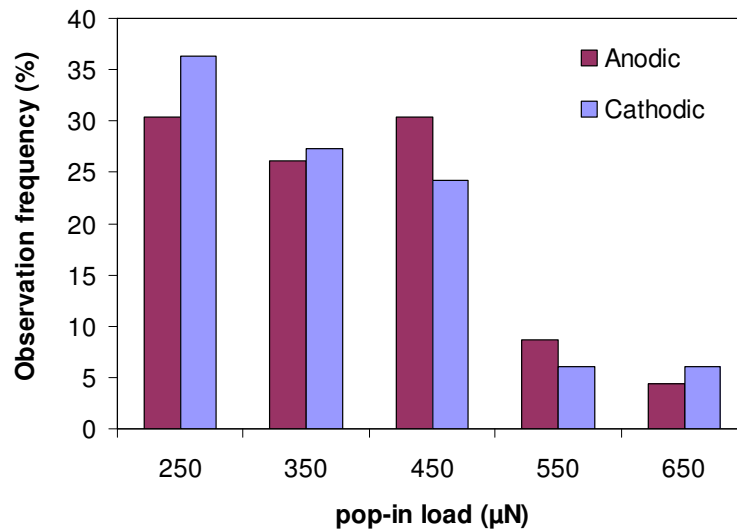
where μ_H is the altered modulus due to hydrogen, ρ_H is the hydrogen trapped dislocation core radius (see 2.3.3) and γ_H is the hydrogen affected stacking fault energy. The effects of hydrogen on the other parameters involved in equation (6.10) are either neglected or inapplicable. The experimental data can be used to calculate the effect of hydrogen on these constants. To do this, the rule of spontaneous homogenous dislocation nucleation shall be applied to equation(6.10), i.e. $\Delta G_C = 0$ and $\partial \Delta G / \partial r = 0$. This results in the following equations:

$$\tau_H = \frac{2-\nu}{1-\nu} \frac{\mu_H b}{4\pi r_C} \left(\ln \frac{4r_C}{\rho} - 2 \right) + \frac{\gamma_H}{b} \quad (6.11)$$

where τ_H is the shear stress required for the homogeneous dislocation nucleation in hydrogen charged nickel crystals. Using the most frequently observed pop-in load at a cathodic potential of 100 μN (figure 6.9b), the τ_H can be calculated by using equation (3.15), and can be inserted into equation (6.11). The

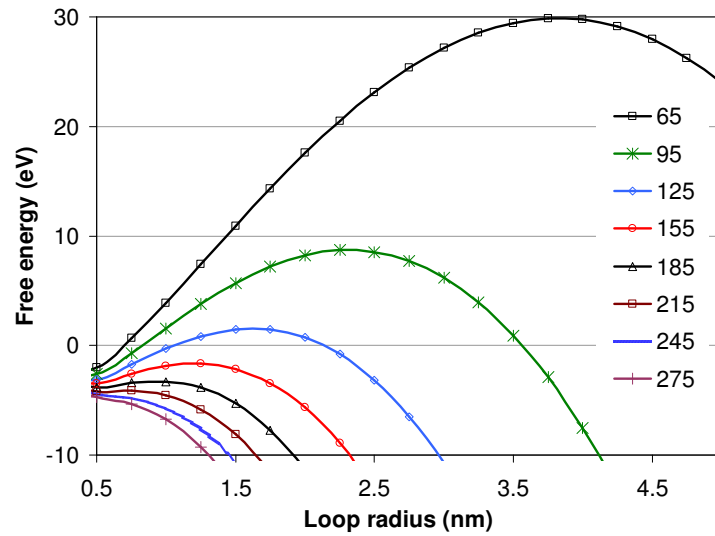


(a) Free energy of homogeneous dislocation nucleation as a function of the dislocation loop radius r in copper for different pop-in loads

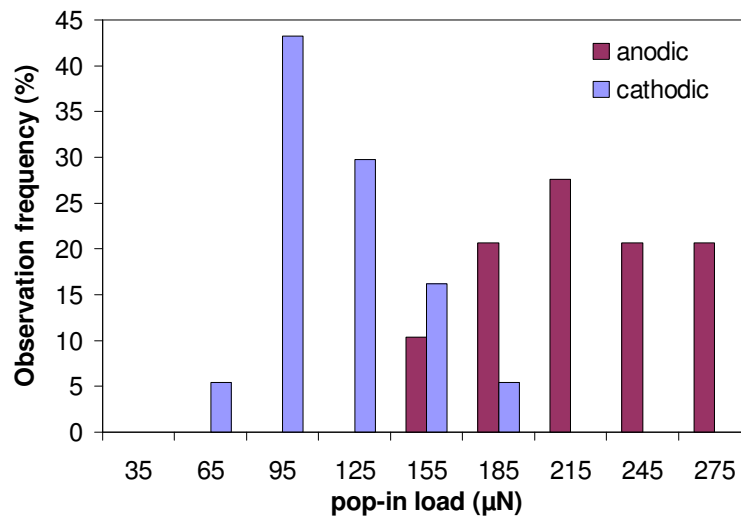


(b) Pop-in load distribution for copper under anodic and cathodic potentials

Figure 6.8: Change in free energy of homogeneous dislocation nucleation for copper as a function of the dislocation loop radius r for various experimentally observed pop-in loads in figure 6.8b



(a) Free energy of homogeneous dislocation nucleation as a function of the dislocation loop radius r in nickel for different pop-in loads

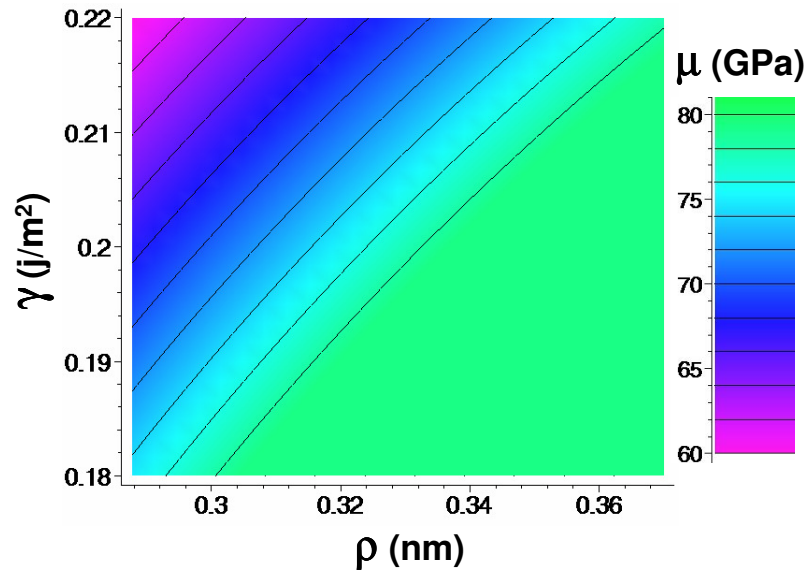


(b) Pop-in load distribution for nickel under anodic and cathodic potentials

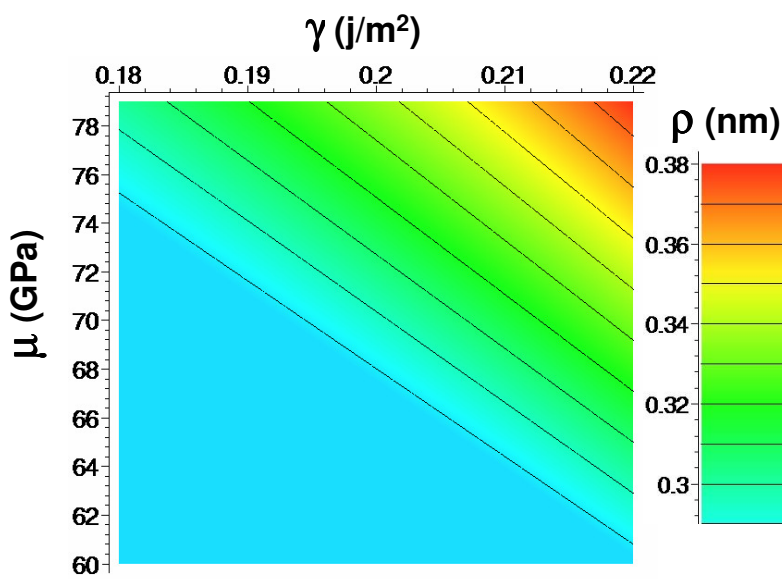
Figure 6.9: Change in free energy of homogeneous dislocation nucleation for nickel as a function of the dislocation loop radius r for various experimentally observed pop-in loads in figure 6.9b

resulting relation between the hydrogen affected parameters, μ_H , ρ_H , and γ_H is plotted in figure 6.10. The plot shows the values for shear modulus, dislocation core radius and stacking fault energy which fulfills equation (6.11) for the most frequently observed pop-ins load in the hydrogen charged nickel sample (100 μN).

A similar analysis has been done for dislocation nucleation in aluminum. However, the high ratio of stacking fault energy to shear modulus γ/μ makes the nucleation of partial dislocations in hydrogen free condition energetically unfavorable. This is shown in figure 6.11, where no free energy curves with activation energy lower than zero is observable. This shows that homogeneous dislocation nucleation in aluminum is in the form of a perfect dislocation nucleation. Therefore, the experimental results for aluminum were analyzed with a perfect dislocation nucleation model. The result is presented in figure 6.12. The effect of hydrogen on the dislocation core radius size and shear modulus was calculated by solving equation (6.11) and shown in figure 6.13. Simultaneous increase in core radius (hydrogen trapping in dislocation core) and reduction of the shear modulus of aluminum according to the graph in figure 6.13 can explain the reduction in pop-in load for the aluminum under cathodic potential (hydrogen charged aluminum). Similar analysis were performed for the hydrogen effect on pop-in load in Fe-3wt.%Si and FeAl samples. The resulting free energy curve together with the pop-in load distribution are given in figures 6.14 and 6.15. The effect of hydrogen on ρ and μ are calculated for Fe-3wt.%Si and FeAl and represented in figures 6.16 and 6.17 respectively. The hydrogen effect on each parameter, assuming that the other parameters are constant, is calculated and presented in table 6.2. The analysis of the experimental observations showed that hydrogen can affect the shear modulus, dislocation core radius, and in the case of partial dislocation nucleation in fcc metals, the SFE. In order to relate these effects to a mechanism of hydrogen embrittlement it shall be considered how each of these parameters may influence the mechanical behavior of the material.



(a) Iso-shear modulus contour lines



(b) Iso-dislocation core radius contour lines

Figure 6.10: Possible changes in shear modulus, dislocation core radius and SFE due to hydrogen for overcoming the homogeneous dislocation nucleation energy barrier in nickel (111) single crystal according to equation (6.11).

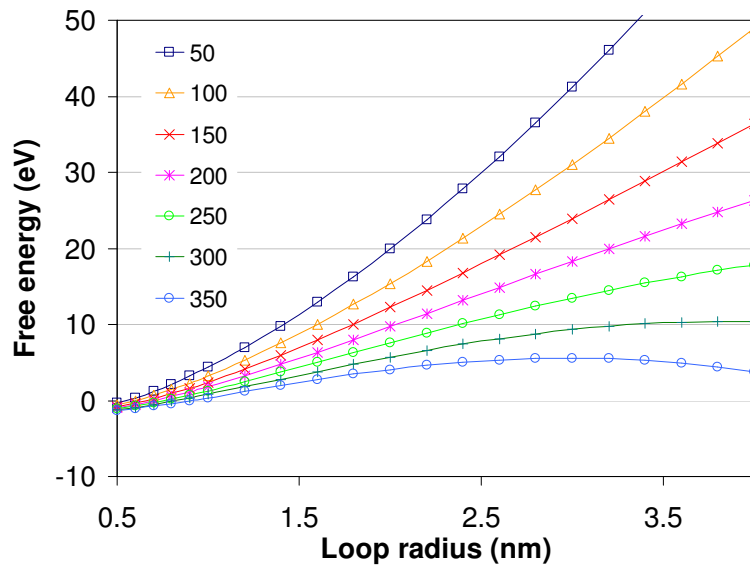
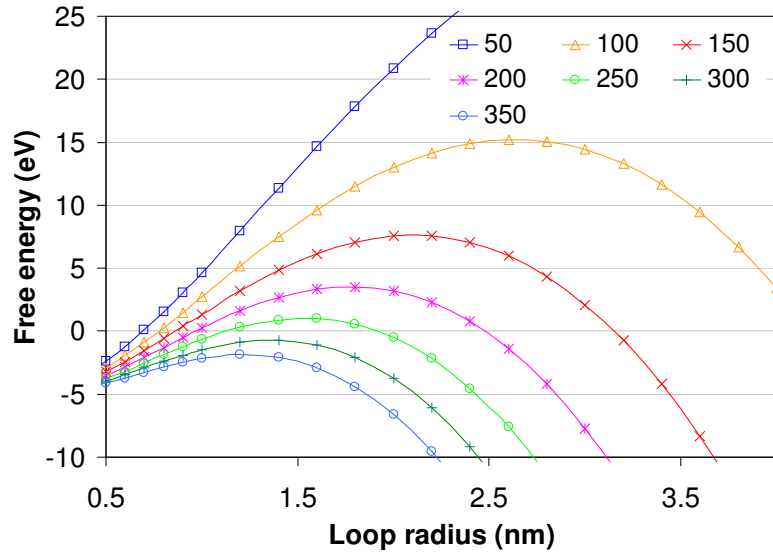
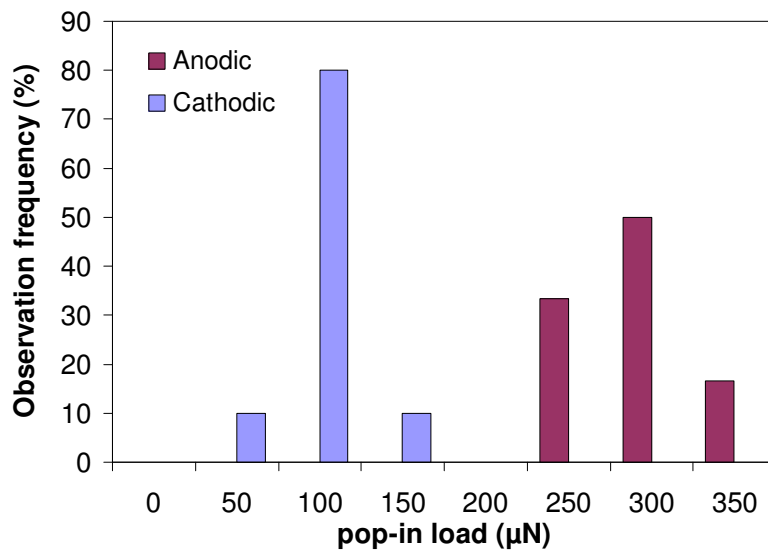


Figure 6.11: Change in free energy of homogeneous dislocation nucleation (partial dislocation) for aluminum as a function of the dislocation loop radius r for various experimentally observed pop-in loads in figure 6.12b



(a) Free energy of homogeneous dislocation nucleation as a function of the dislocation loop radius r in aluminum for different pop-in loads



(b) Pop-in load distribution for aluminum under anodic and cathodic potentials

Figure 6.12: Change in free energy of homogeneous dislocation nucleation (perfect dislocation) for aluminum as a function of the dislocation loop radius r for various experimentally observed pop-in loads in figure 6.12b

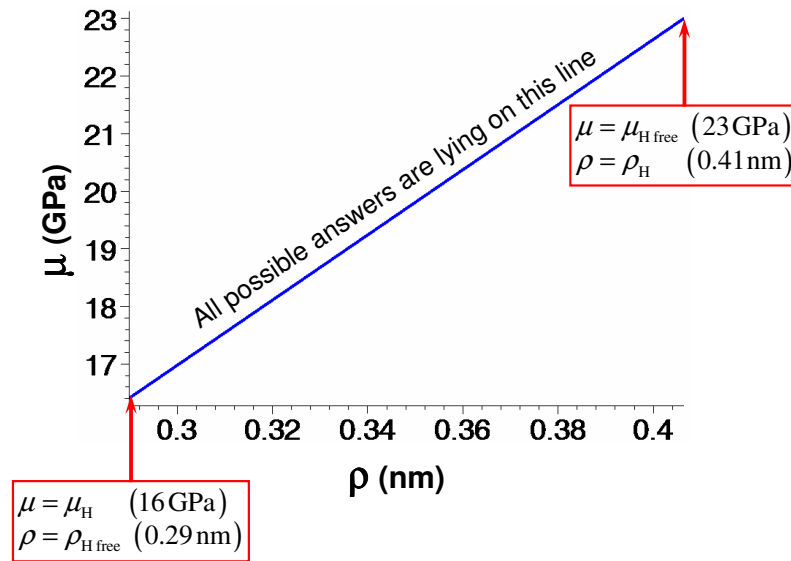
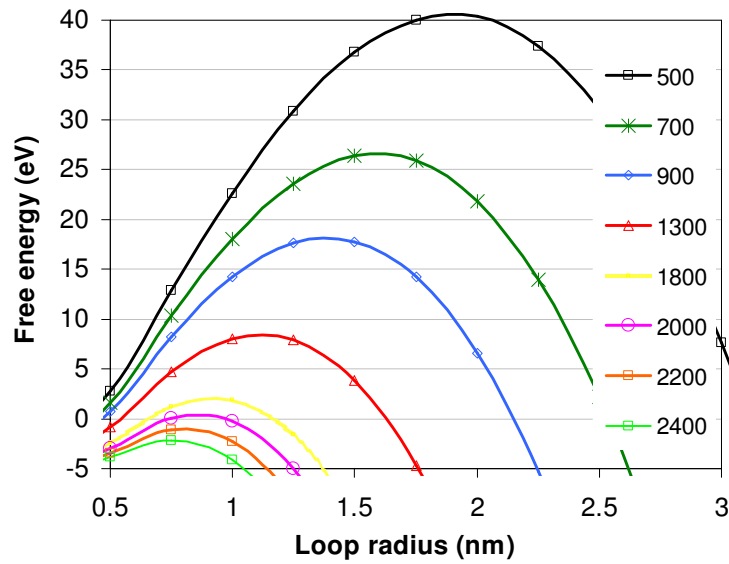


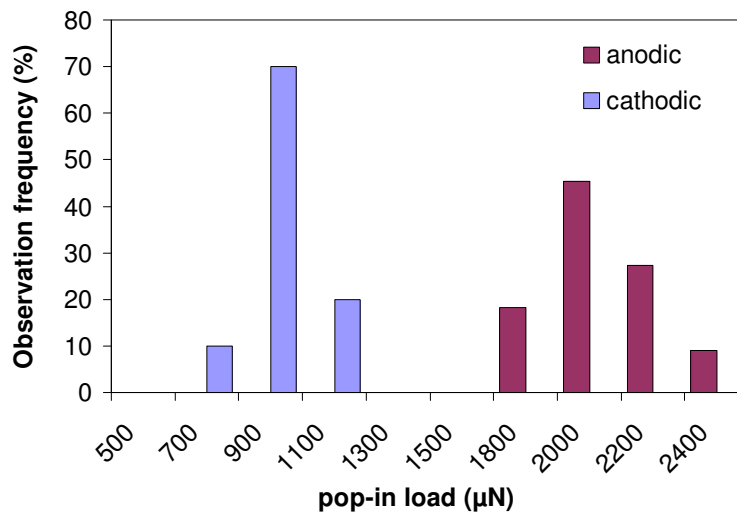
Figure 6.13: Possible changes in shear modulus and dislocation core radius due to hydrogen for overcoming the homogeneous dislocation nucleation (perfect dislocation) energy barrier in aluminum according to equation (6.11). All possible answers to equation (6.11) are lying on the line. Two extreme cases, where only μ or ρ is changing, are also shown.

Table 6.2: Hydrogen effect on shear modulus, dislocation core radius and SFE according to equation (6.11), when only one of these parameters were influenced by hydrogen

	Nickel	Aluminum (Partial)	Aluminum (Perfect)	Fe-3wt.%Si	FeAl
μ_H (GPa) ($\gamma_H = \gamma$ and $\rho_H = \rho$)	60	0.14	16.4	65	57
Reduction in μ (%)	24	99	29	23	39
γ_H (J/m ²) ($\mu_H = \mu$ and $\rho_H = \rho$)	0.168	0.033	n.a	n.a	n.a
Reduction in γ (%)	24	70	n.a	n.a	n.a
ρ_H (nm) ($\mu_H = \mu$ and $\gamma_H = \gamma$)	0.38	55	0.41	0.22	0.55
Increase in ρ (%)	31	16306	40	31	64

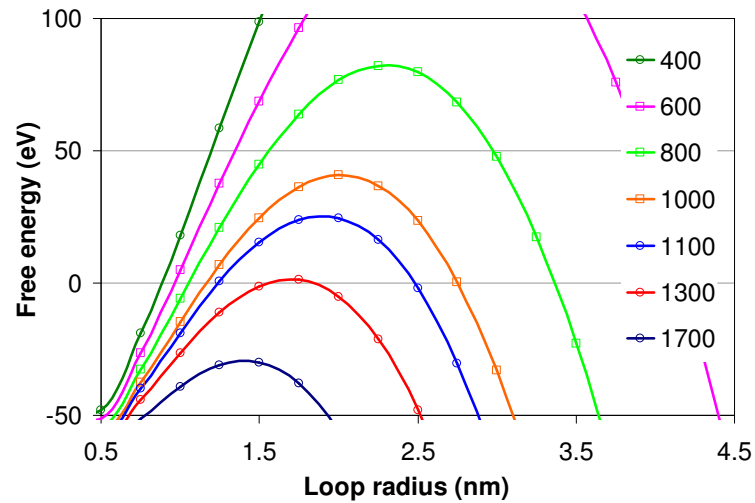


(a) Free energy of homogeneous dislocation nucleation as a function of the dislocation loop radius r in Fe-3wt.%Si for different pop-in loads

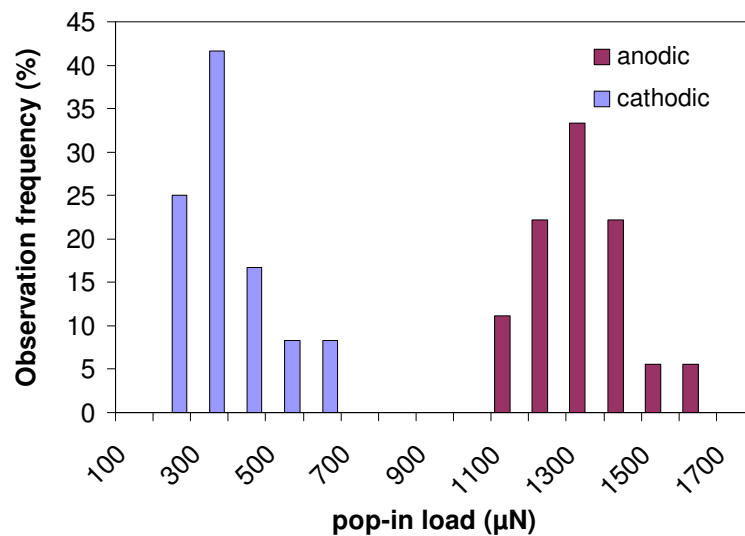


(b) Pop-in load distribution for Fe-3wt.%Si under anodic and cathodic potentials

Figure 6.14: Change in free energy of homogeneous dislocation nucleation (perfect dislocation) for Fe-3wt.%Si as a function of the dislocation loop radius r for various experimentally observed pop-in loads in figure 6.14b



(a) Free energy of homogeneous dislocation nucleation as a function of the dislocation loop radius r in FeAl for different pop-in loads



(b) Pop-in load distribution for FeAl under anodic and cathodic potentials

Figure 6.15: Change in free energy of homogeneous dislocation nucleation (perfect dislocation) for FeAl as a function of the dislocation loop radius r for various experimentally observed pop-in loads in figure 6.15b

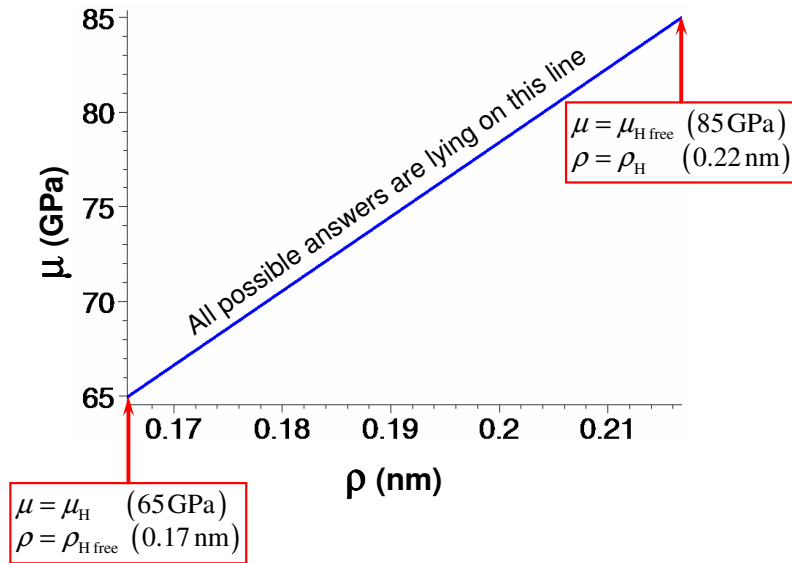


Figure 6.16: Possible changes in shear modulus and dislocation core radius due to hydrogen for overcoming the homogeneous dislocation nucleation energy barrier in Fe-3wt.%Si according to equation (6.11). All possible answers to equation (6.11) are lying on the line. Two extreme cases, where only μ or ρ is changing, are also shown.

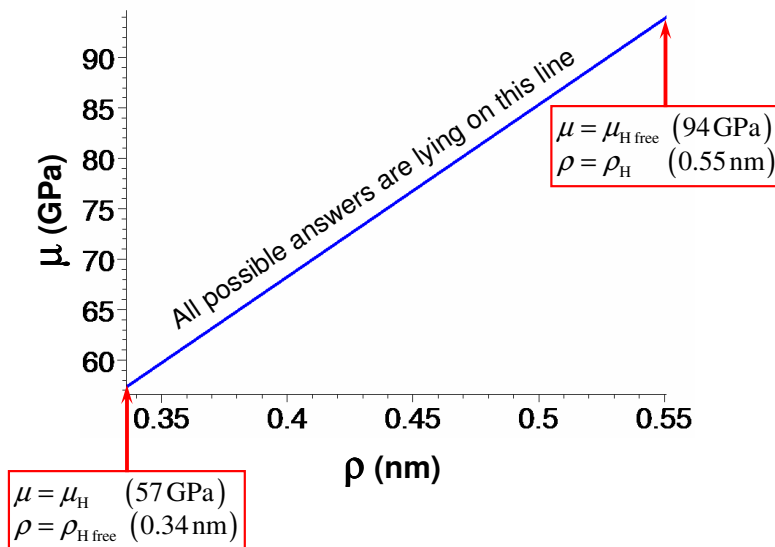


Figure 6.17: Possible changes in shear modulus and dislocation core radius due to hydrogen for overcoming the homogeneous dislocation nucleation energy barrier in FeAl according to equation (6.11). All possible answers to equation (6.11) are lying on the line. Two extreme cases, where only μ or ρ is changing, are also shown.

6.2.1 Shear modulus

The bulk modulus B is given by the second derivative of the crystal energy U_c with dilatation

$$B = - \left(\frac{d(V/V_0)}{dP} \right)^{-1} = V_{mole}^2 \frac{\delta^2 U_c}{\delta V^2} \quad (6.12)$$

In other words, the bulk modulus is a measure of the increase of the crystal energy with a change to the volume imposed by an external hydrostatic pressure, as given by the third term in the following equation:

$$U_c(V) = U_c(V_0) + \left(\frac{\delta U_c}{\delta V} \right)_{V_0} \cdot \delta V + \frac{1}{2} \left(\frac{\delta^2 U_c}{\delta V^2} \right)_{V_0} \cdot \delta V^2 + \dots \quad (6.13)$$

where V_0 is the molar volume at zero pressure and $U_c(V_0)$ is the crystal energy at equilibrium, i.e. $(\delta U_c / \delta V)_{V_0} = 0$. The increase of the crystal energy with increasing hydrostatic pressure is therefore given by the increase of the curvature of the potential surface in three dimensions. In a similar way, Young's modulus E can be approximated by the second derivative of the binding energy with bond distance and is related to the bulk and shear modulus by the equations

$$\mu = \frac{E}{2(1 + \nu)} \quad (6.14)$$

$$B = \frac{E}{3(1 - 2\nu)} \quad (6.15)$$

Rose et. al. [278, 279] have shown that metallic binding-energy distance curves can be approximately scaled into a single universal relation in each of the following cases:

1. Chemisorption on a metal surfaces [280]
2. Metallic and bimetallic adhesion [281]
3. The cohesion of bulk metals [278]

In each case, the energy relation can be expressed as

$$U_c(d) = \Delta U_c U_c^*(d^*) \quad (6.16)$$

Here $U_c(d)$ is the total energy as a function of the interatomic separation distance d , ΔU_c is the equilibrium binding energy, while $U_c^*(d^*)$ is an approximately universal function which describes the shape of the binding-energy curve

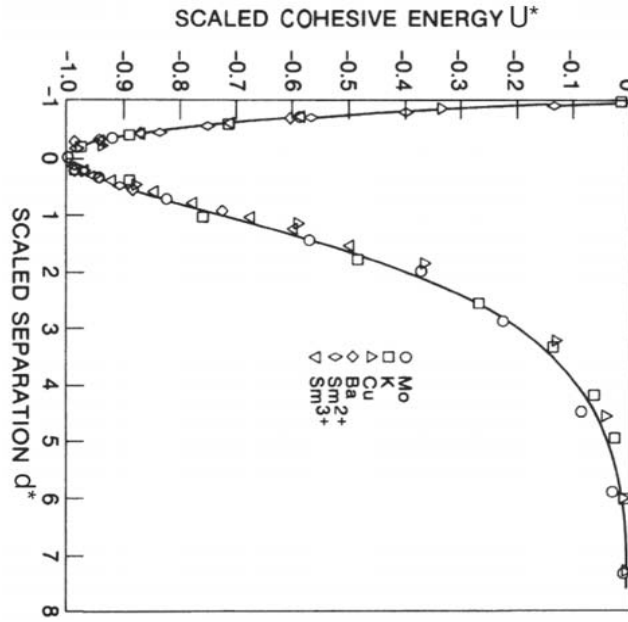


Figure 6.18: Bulk energies of various metals scaled using equation (6.16) and equation (6.17) [279].

for metals. The coordinate d^* is a scaled length defined by

$$d^* = \frac{(d - d_m)}{l} \quad (6.17)$$

Here d_m is the equilibrium separation and l is a scaling length which is to be determined. In each of the three systems were considered, it was found that l is reasonably well determined by the Thomas-Fermi screening length

$$l_{\text{TF}} = \frac{1}{3} \left(\frac{243\pi}{64} \right)^{1/6} n_{(d_m)}^{-1/6} \quad (6.18)$$

where $n_{(d_m)}$ is the electron density at the equilibrium position of the atom.

The total-energy-distance curve for a given physical situation is determined from the two scaling parameters ΔU_c and l once the general form of $U_c^*(d^*)$ is established. All currently available ab initio calculations for the cohesion and adhesion of metals, as well as the chemisorption of gas atoms on metal surfaces, are shown to be determined by this single relation. These findings suggest a commonality of metallic bonding. Figure 6.18 shows the bulk energies of various metals scaled using equation (6.16) and equation (6.17), which shows the universal nature of binding-energy-distance relations. From equations (6.16)–

(6.18),

$$\left[\frac{\partial^2 U_c(d)}{\partial d^2} \right]_{d=d_m} = \frac{\Delta U_c}{l^2} \left[\frac{\partial^2 U_c^*(d^*)}{\partial d^{*2}} \right]_{d^*=0} \quad (6.19)$$

The total cohesive-energy is a function of the separation between atoms for a uniformly dilated lattice. The separation between atoms can be characterized in terms of the Wigner-Seitz radius, r_{ws} as suggested by Rose et. al. [278]. The Wiener-Seitz radius is a parameter used to describe the density of a system. If the volume of a system V is equally divided amongst N particles then the volume for each particle is simply defined by

$$\frac{V}{N} = \frac{4}{3}\pi r_{ws}^3 \quad (6.20)$$

The bulk modulus at equilibrium given by equation(6.12) can be defined using Wigner-Seitz radius as follow

$$B = V^2 \frac{\partial^2 U_c(d)}{\partial V^2} = \frac{1}{12\pi r_{ws}} \frac{\partial^2 U_c(d)}{\partial r_{ws}^2} \quad (6.21)$$

Therefore for uniform dilation of a bulk metal, the equation(6.19) can be rewritten using equations (6.14), (6.15), and (6.21)

$$\frac{U_{Cohesive}}{l^2} \left[\frac{\partial^2 U_c^*(d^*)}{\partial d^{*2}} \right]_{d^*=0} = \mu \frac{8\pi(1+\nu)}{(1-2\nu)} r_{ws} \quad (6.22)$$

Because of the universality, the ratio of the second derivative in the large parentheses is independent of the metal considered.

This relation (equation (6.22)) has a simple physical meaning: the reduction in the shear modulus is equal to the reduction of the strength of the interatomic bonds, as assumed in the HEDE model.

6.2.2 Stacking fault energy

For the reduction in the surface energy by segregation of a solute on a surface Gibbs has derived the following isotherm

$$d\gamma = -\Gamma_A d\mu_A \quad (6.23)$$

$$\Gamma_A = \left. \frac{\partial \gamma}{\partial \mu_A} \right|_{n_B, T, \mathbf{a}} \quad (6.24)$$

where γ is the surface energy, μ_A is the chemical potential of solute atom A dissolved in a material of B atoms with a constant number n_B . The surface area \mathbf{a} is maintained constant, too, and Γ_A is the excess amount of A atoms in the neighborhood of the interface as compared with the bulk crystal and is defined by equation (6.24). Equation (6.23) predicts that the interface energy γ is reduced for a positive excess and an increasing chemical potential of A [282]. Although mainly used for surface adsorption, equation (6.23) has been applied successfully to grain and phase boundaries, and has been extended recently to other defects interacting with hydrogen [283]. Equation (6.23) predicts that the interface energy γ is reduced for a positive excess and an increasing chemical potential of A .

In our experiments it can be assumed, that the hydrogen concentration and its chemical potential in the point of dislocation nucleation (see figure 6.6) was constant. Therefore according to the Gibbs adsorption isotherm the reduction of SFE energy in hydrogen charged nickel can be only attributed to a positive excess of hydrogen on interface. This means segregation of hydrogen in to the stacking fault region. This is in good agreement with known tendency of hydrogen for segregation in to the internal boundaries as discussed in section 2.3.4.

This reduction of the stacking fault energy, however, alters the mechanical behavior by influencing the dissociation of partial dislocations. A perfect screw dislocation in an fcc crystal structure dissociates into two mixed partials separated by a stacking fault ribbon of w width. Only a perfect screw dislocation can cross slip. This mechanism is thermally activated and the cross slip probability depends on the work necessary for the recombination of the partials [284]. Each partial is submitted to two forces: the repulsion due to the other partial ($\propto 1/w$), and the attraction due to the stacking fault (constant and equal to γ , SFE). In the absence of external stress, the partials are in equilibrium at a distance at which the two forces balance each other. According to dislocation theory, the equilibrium separation of the partials dissociated from a mixed perfect dislocation that is inclined at an angle β to its Burgers vector, is given by [26]

$$w_e = \frac{\mu b^2}{8\pi\gamma} \frac{2-\nu}{1-\nu} \left(1 - \frac{2\nu \cos 2\beta}{2-\nu} \right) \quad (6.25)$$

According to equation (6.25), the reduction in stacking fault energy results in an increase in the separation of the partials. This means an increase in the activation energy required for cross-slip of the dislocations, which increases the tendency of the dislocations to stay on the same slip plane. This localizes slip and supports the HELP mechanism. This is in agreement with previously reported

observations of slip planarity in nickel both experimentally [80] and through simulations [56, 54, 51].

6.2.3 Dislocation core radius

The model presented in this work (equation (6.10)) is based on classical treatment of dislocations by elastic continuum theory. The dislocation core radius¹ was incorporated into this model by equation (6.2) which defines the dislocation line energy. According to this equation an increase in the dislocation core radius means reduction of dislocation line energy.

In a similar manner to reduction of the SFE by hydrogen, the Gibbs isotherm (equation (6.23)) can be used to explain the reduction of dislocation line energy. However, the excess Γ_A , as defined in the original work by Gibbs and given by equation (6.23), is sometimes difficult to determine since it requires a dividing interface to be placed in the right position. Wagner [283] proposed a new definition of the solute excess as

$$\Gamma_A = \left. \frac{\partial n_A}{\partial^{-1}} \right|_{n_B, T, V, \mu_A} \quad (6.26)$$

This definition provided the basis for a generalization of equation (6.23) including all kinds of defects, like dislocations and vacancies, besides surfaces and grain boundaries [282]. Applying this definition to dislocations yields the following excess definition

$$\Gamma_A^D = \left. \frac{\partial n_A}{\partial \ell} \right|_{n_B, T, V, \mu_A} \quad (6.27)$$

as a change of the number of A atoms by a change of the dislocation length ℓ at constant chemical potential of A and constant number of solvent B atoms. Thus

¹In the classical treatment of dislocations by elastic continuum theory there exists a singularity at the dislocation center. Therefore, a core region with radius ρ has to be excluded from the considerations in order to avoid a logarithmic divergence of the line energy W per unit length L

$$\frac{W}{L} = \frac{\mu b^2}{4\pi} \ln \frac{\mathcal{R}}{\rho} \quad (\text{screw dislocation})$$

$$\frac{W}{L} = \frac{\mu b^2}{4\pi(1-\nu)} \ln \frac{\mathcal{R}}{\rho} \quad (\text{edge dislocation})$$

where \mathcal{R} is the upper limit of integration and in the case of a crystal with many dislocations with both signs a reasonable approximation would be to take roughly half the average distance between the dislocations for \mathcal{R} .

the system is open regarding A but closed with respect to B . If different dislocation segments do not interact, n_A is a linear function of the total dislocation length ℓ .

Kirchheim[283] used this solute excess definition for dislocation, Γ^D , to derive the change in the Helmholtz free energy per unit length of dislocation by segregation of solute on dislocation as follow

$$\left. \frac{\partial \gamma_D}{\partial \mu_A} \right|_{n_B, T, V, \ell} = -\Gamma_A^D \quad (6.28)$$

According to equation (6.28) the line energy of a dislocation decreases with increasing solute chemical potential if the excess is positive, i.e. solute atoms segregate at the dislocation core¹.

Hence, the increase in the core radius is a direct evidence for decrease in dislocation line energy and hydrogen segregation on the dislocation line according to generalized Gibbs isotherm. This is in good agreement with the hydrogen trapping model described in 2.3.3, where trapping of hydrogen to dislocation core resulted in decrease of the energy state of the system.

The segregated hydrogen consequently influence the mechanical properties by pinning of dislocations and forming Cottrell atmosphere [285].

¹In section 2.3.3 it was shown that there is an affinity for hydrogen segregation in to the dislocation core

6.3 Time delay experiments

The time delay experiment was designed to test if the hydrogen below the tip is really responsible for the reduction of the pop-in load below the indenter tip and observation of hydrogen activated pop-in phenomenon. In the time delay experiments by holding the sample at two different loads the position of maximum shear stress is changed according to equation (6.29). Therefore, during hydrogen activated pop-in, the time to pop-in should be depending on the hold load, which defines the diffusion path, $l_{diffusion}$ for the hydrogen. The diffusion path is shown schematically in figure 6.19 and results in the following equation

$$l_{diffusion} = 1.22 \left(\frac{3PR}{4E_r} \right)^{\frac{1}{3}} \quad (6.29)$$

In figure 6.20 the time to pop-in (\approx diffusion time) versus the diffusion path

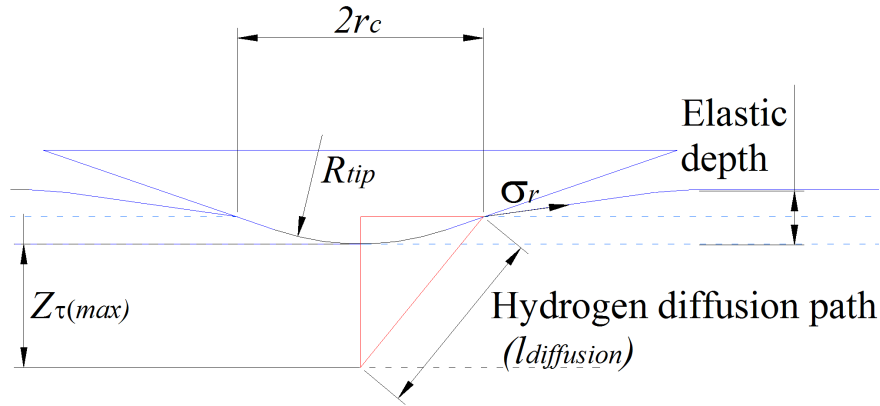


Figure 6.19: Schematic representation of the indentation geometry and hydrogen diffusion path in the experiments

is plotted for the time delay experiments with 130 μN and 175 μN holding load (figure 5.53). Based on a simple semi-infinite model the concentration of hydrogen at depth z and time t could be calculated by using the following equation

$$\frac{C(z,t) - C_S}{C_0 - C_S} = \text{erf} \left(\frac{z}{2\sqrt{Dt}} \right) \quad (6.30)$$

By setting the initial concentration of hydrogen, C_0 , to zero, the equation (6.30) will be reduced to

$$\frac{C(z,t)}{C_S} = \text{erfc} \left(\frac{z}{2\sqrt{Dt}} \right) \quad (6.31)$$

where C_S is the hydrogen surface concentration, $C(z,t)$ is the concentration at the depth of z and the time of t , and D is the diffusion coefficient for hydrogen

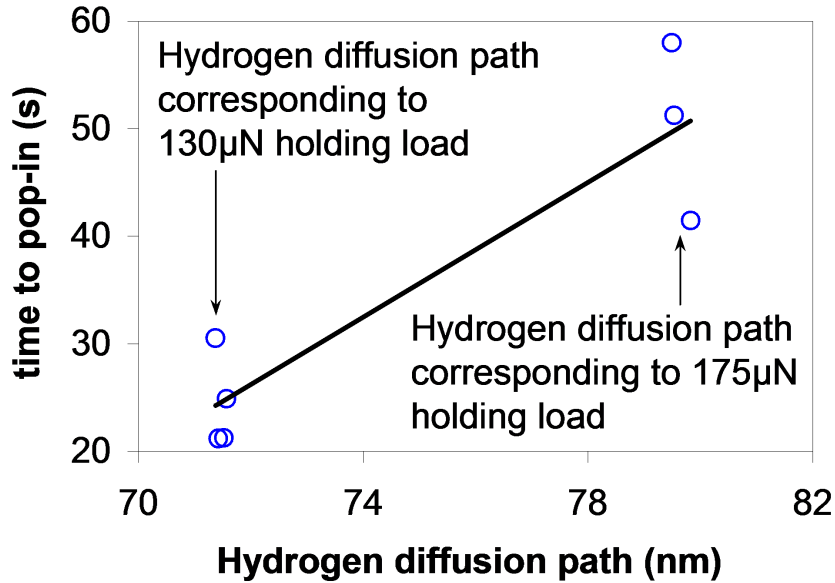


Figure 6.20: Change in observed time to pop-in with hydrogen diffusion path for the time delay experiments under cathodic potentials

in nickel. Taking a diffusion coefficient equal to $2 \times 10^{-10} \text{ cm}^2/\text{s}$, as reported by Doyle et al. [30] for single crystal nickel, and equating z to $l_{diffusion}$, we can express the hydrogen concentration at the point of maximum shear stress as a function of time. For the time delay experiments with the $130 \mu\text{N}$ hold load we used the average time to pop-in, i.e. 25 seconds, and measured the hydrogen concentration at $z_{\tau(max)}$. Assuming the same concentration is necessary to observe hydrogen activated pop-ins at $175 \mu\text{N}$ hold load, results in a diffusion time of 31 seconds. The experimentally observed higher time for diffusion (figure 6.20) could be due to the reduction of the hydrogen diffusion rate under the hydrostatic pressure state existing beneath the tip [1]. However, the measured delay time for the pop-ins at different loads agrees nearly quantitatively with the theoretical prediction for the diffusion time (figures 5.52d, 5.53d, and 6.20) and is opposite to the observations in inert environments [184, 276].

It should be emphasized that if the film properties change due to the applied cathodic potential, the pop-in should be observed instantaneously after onset of cathodic potential in figure 5.52 and 5.53. Since according to equation (3.11) the maximum tensile stress, $\sigma_{r(max)}$, which acts on the surface at the edge of the indenter tip (figures 3.8 and 6.21), i.e. in direct contact with electrolyte, is responsible for fracture of the surface film. Its value on the surface is given by

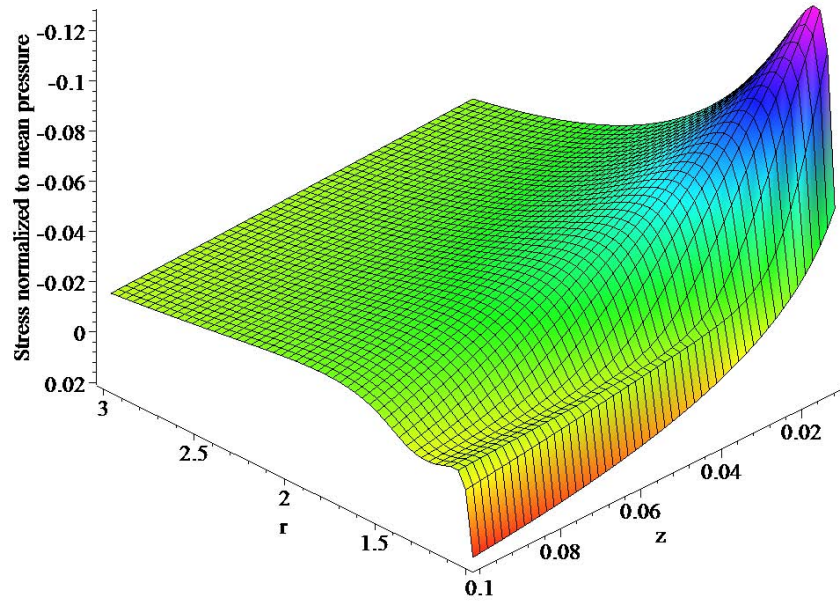


Figure 6.21: Graphical representation of the τ_{13} principle shear stress on the vicinity of the surface and edge of the tip, as a result of the elastic Hertzian contact between a flat surface and a spherical indent with a contact radius of $a = 1$ and $\nu = 0.3$ (z is the axis of symmetry). For $z = 0$, $\tau_{13} = \sigma_{r(max)}$

$$\sigma_{r(max)} = \frac{1}{3}(1 - 2\nu) \left(\frac{6E_r^2}{\pi^3 R^2} P \right)^{\frac{1}{3}} \quad (6.32)$$

Therefore, any change in the film due to hydrogen should be observed instantaneously but the opposite was observed experimentally.

CHAPTER 7

Conclusion and outlooks

Convictions are more dangerous enemies of truth than lies.

Menschliches, Allzumenschliches, Ein Buch für freie
Geister.
FRIEDRICH NIETZSCHE

7.1 Conclusion

A novel setup was developed for probing mechanical properties in situ and under controlled electrochemical conditions. The effect of hydrogen on mechanical properties of small volumes was studied by using the developed setup. In similar experiments carried out on different materials, different pop-in behaviors were observed. No hydrogen effect was observed for copper, which is in agreement with its non-sensitivity against hydrogen embrittlement. The phase transformation in austenite resulted in an increase of the pop-in load. The observed reduction in pop-in load during hydrogen charging of other samples, was related to the reduction of required activation energy for homogeneous nucleation of a circular dislocation loop below the tip. In a simple approach this can be considered as enhancement of dislocation activity due to hydrogen, or HELP. Further on, the classic dislocation theory was used to analyze the hydrogen effect on the observed reduction in activation energy. The hydrogen induced reduction of shear modulus, SFE, and dislocation core radius, reduces the required activation energy for homogeneous nucleation of dislocations.

The reduction of shear modulus, by considering the universality of the binding-energy distance curves in metals, can be directly related to a reduction of inter-

atomic bonds and cohesive energy. Consequently this was interpreted as an evidence for the HEDE model.

According to the Gibbs adsorption isotherm the reduction of SFE by hydrogen was explained by segregation of hydrogen into the stacking fault region. This lower SFE increases the equilibrium distance between the partials and consequently increases the activation energy for cross slipping. Therefore dislocations tend to stay on the same slip plane which results in slip planarity and slip localization. This was accounted as an evidence for the HELP mechanism.

On the basis of classical treatment of dislocations by elastic continuum theory, the reduction of the dislocation core radius is a direct measure of the reduction in dislocation line energy. However, in a similar manner to SFE, by using the generalized Gibbs isotherm the reduction of the dislocation line energy was related to the segregation of hydrogen on dislocation line.

Importantly it was shown that the main effect of hydrogen on mechanical behavior, is reduction of the activation energy for dislocation nucleation, which depending on experimental procedure used to observe the hydrogen effect, may be interpreted as HEDE or HELP.

Additionally it is shown that this technique can be used to study complex multi phase alloy systems like SDSS locally and in nano scale. The effect of hydrogen was independently examined on austenite and ferrite phases. The phase transformation of austenite was observed in situ during hydrogen charging. A rate dependent hardness was observed in hydrogen charged austenite and related to the pinning of dislocations by solute hydrogen. The analyzed rate dependency was in agreement with the proposed model.

7.2 Outlooks

The ability to perform local mechanical tests in nanoscale inside a solution, under electrochemical control, with in situ imaging possibility, makes the technique developed in this work a powerful tool to study environmental effects on mechanical properties locally. Additionally, surface films and their effect on mechanical properties, the so called *Rehbinder Effects*¹ [286] can be studied. Mechanical behavior of passive films and their effect on mechanical properties of metals is another interesting topic which can be studied with the aid of this method.

¹The reduction in the hardness and ductility of a material by a surface-active molecular film.

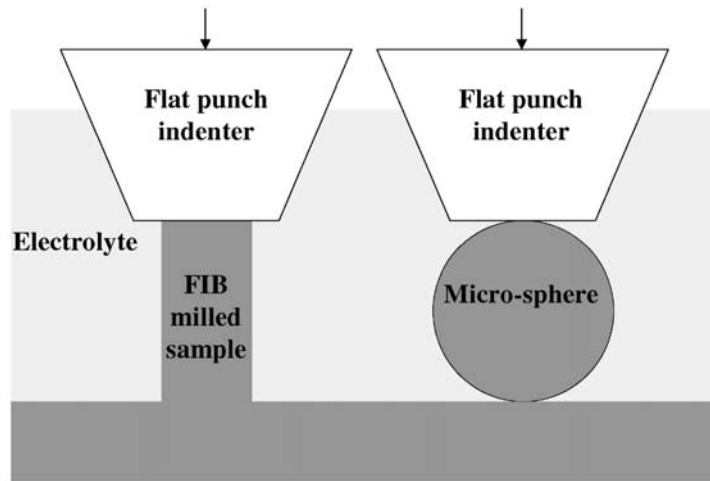


Figure 7.1: Schematic representation of in situ electrochemical micro-compression tests on micro pillars and micro spheres

This technique can be improved further by using the following possibilities both for further studies on hydrogen as well as other environmental effects and their interaction with mechanical properties.

7.2.1 Micro compression tests

Performing compression tests on micro-pillars and micro-spheres under a controlled electrochemical condition is one of the possibilities to utilize the technique further (figure 7.1). The well defined boundary conditions for hydrogen diffusion as well as perfectly defined stress and strain conditions make such tests a powerful technique for examination of hydrogen effect in micro scale. Figure 7.2 and figure 7.2 show some of the preliminary tests performed on micro-pillars in air [287].

7.2.2 Low temperature ECNI-AFM

Vehoff et al. [37] proposed a simple trapping model which assumes that a high density of deep traps is produced at the FPZ during crack growth. This model describes the pressure, temperature and frequency dependence of the crack growth rate. The model predicts two different behaviors for Fe-3wt.%Si and nickel, as shown in figure 7.4. In a similar manner the temperature effect, hydrogen overpotential (equivalent to hydrogen partial pressure) and time to observe the hydrogen activated pop-in in hold experiments can be used to revisit this model with the nanoindentation technique.

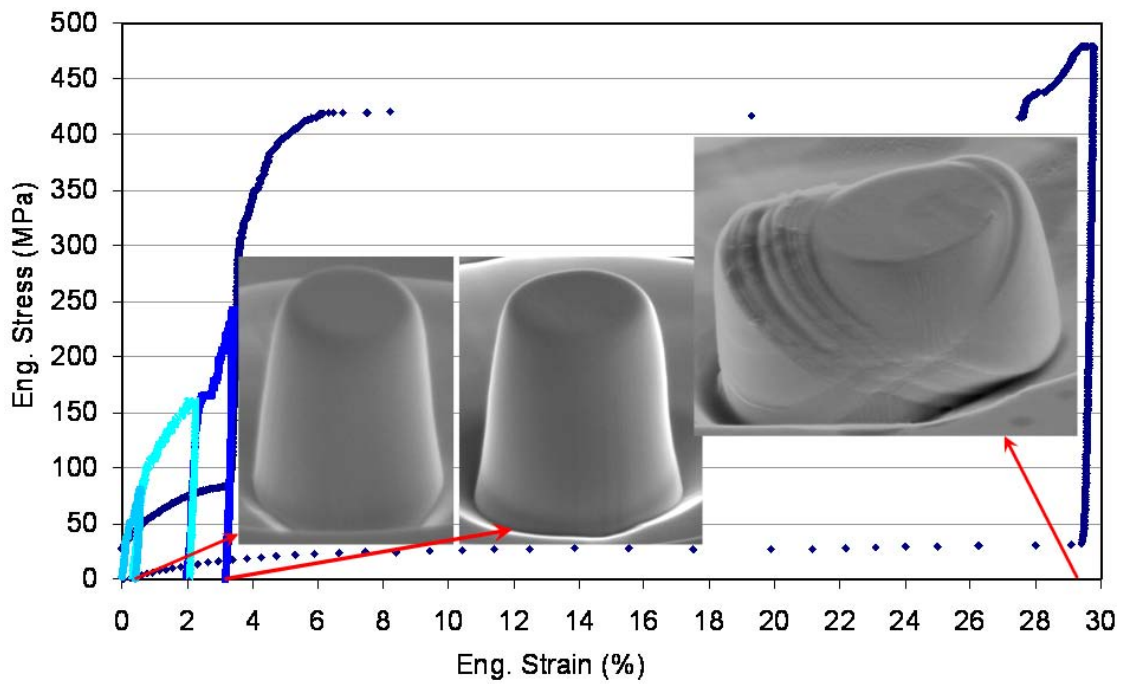


Figure 7.2: Micropillar test in air on single slip oriented single crystal nickel sample [287]

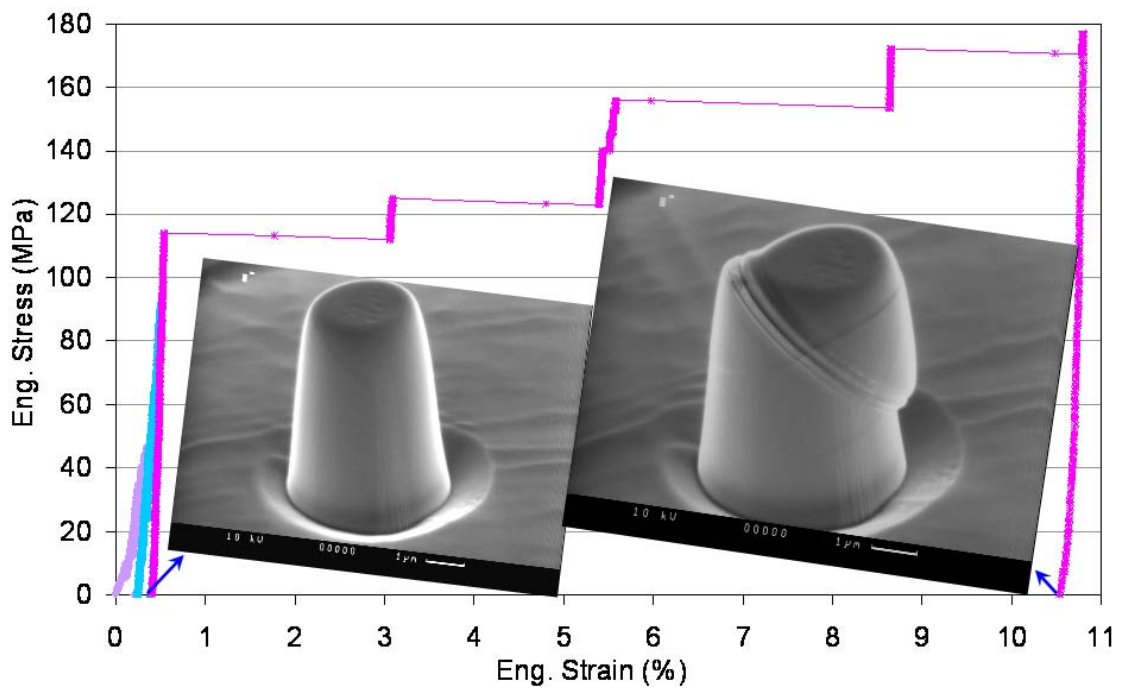
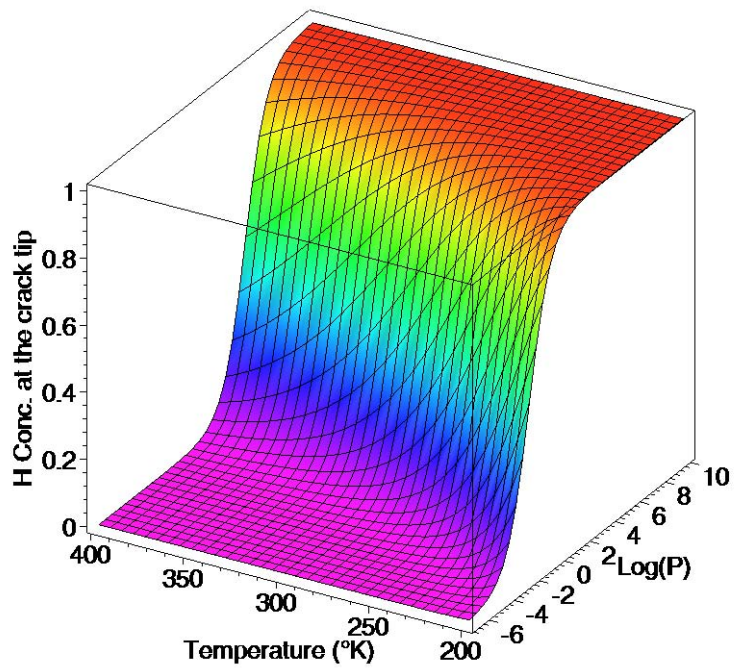
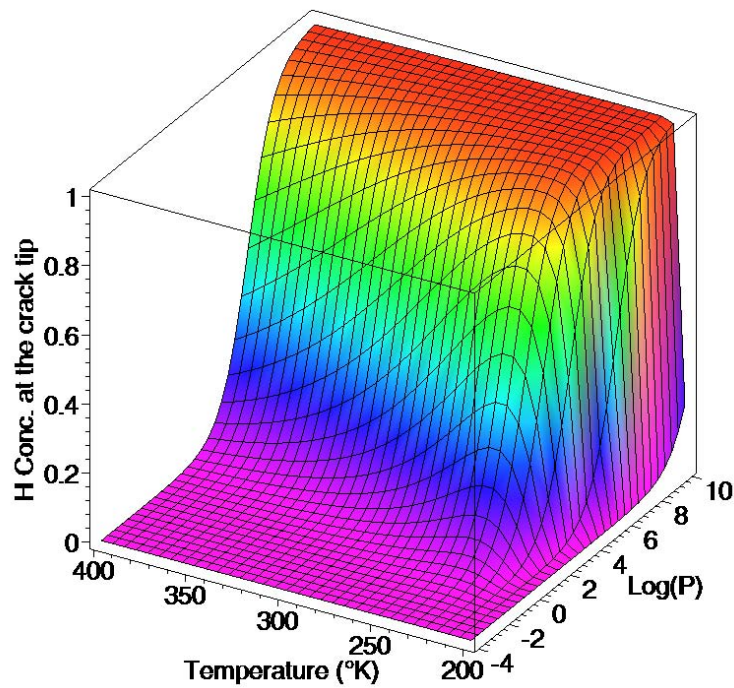


Figure 7.3: Micropillar test in air on double slip oriented single crystal nickel sample [287]



(a) Fe-3wt.%Si



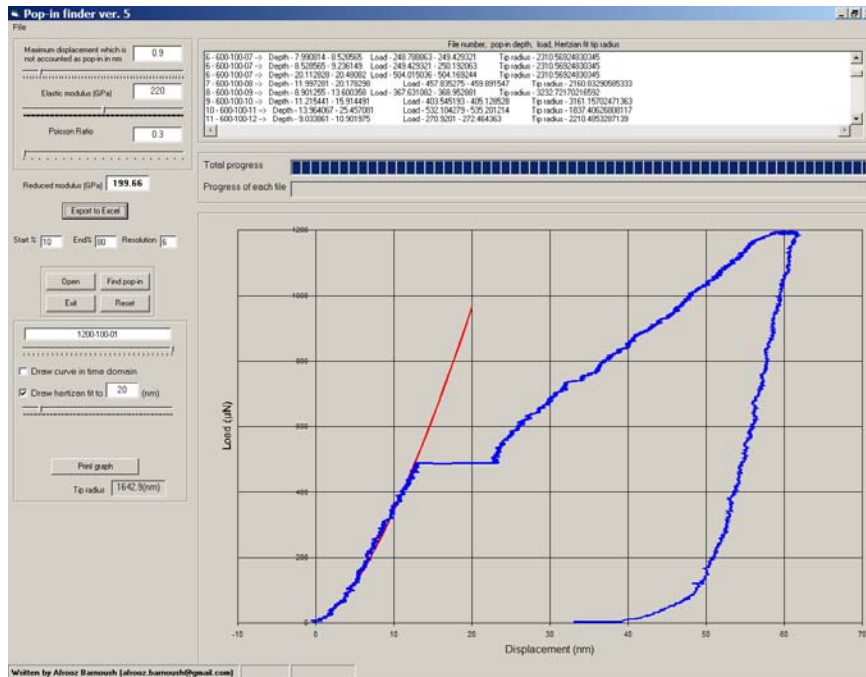
(b) Nickel

Figure 7.4: Trapping of hydrogen in FPZ as function of partial hydrogen pressure and temperature

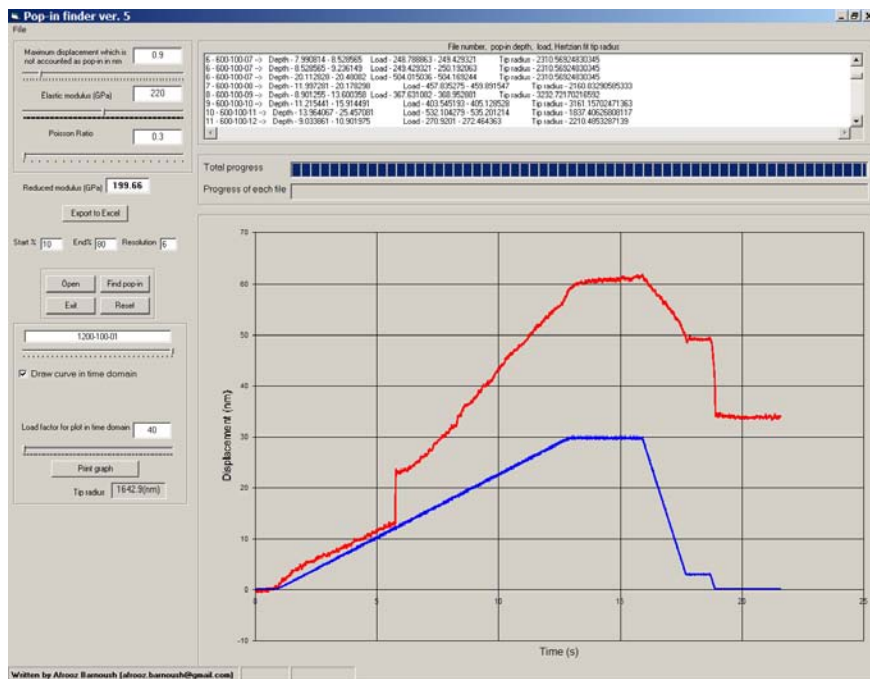
APPENDIX A

Pop-in finder program

In order to find the pop-in point in the nanoindentation data an special program was developed. The program analysis the imported tab delimited data from Hysitron software and finds the pop-in points within the data. The developed algorithm scans the data points in a range which is defined by user, and looks for the regions where according to a predefined value showing displacement at constant load which is the mathematical definition of the pop-in. Additional subroutines control the selected region to distinguish it from thermal drift or noise. Another subroutine uses the data of the first pop-in load to calculate the tip radius, maximum shear stress and the position of maximum shear stress by using the Hertzian contact model and material constants which are entered by user. The program provides graphical representation of the nanoindentation data in the form of load displacement and displacement time curves. The result of calculation, statistic of pop-ins and curves are saved as an Excel workbook. Figure [A.1](#) shows the graphical user interface of pop-in finder program.



(a) Load displacement presentation mode



(b) Displacement time presentation mode

Figure A.1: GUI of the pop-in finder program developed for automatic pop-in analysis of nanoindentation data, Load displacement presentation mode (a), and Displacement time presentation mode (b)

APPENDIX B

In situ ECNI-AFM operation

B.1 Overview

Essentially, the procedure for observing and nanoindenting samples in fluid is the same as that for NI-AFM in air; however, a special electrochemical cell (see section 4.3) is utilized to contain the electrolyte as shown schematically in figure 4.8. In addition, adjustments must be made for compensation of forces acting on the tip (see section 3.5.1). In order to perform an in situ electrochemical nanoindentation test, the following steps should be taken.

This appendix describes ECNI-AFM operation of the TriboScope[®] MultiMode[®] tandem system in fluid. Including mounting the electrochemical cell into the microscope, and then engaging the tip with the sample. This section assumes familiarity with NI-AFM operation of Triboscope[®] MultiMode[®] tandem system in air.



CAUTION! When nanoindenting samples in fluid, use extraordinary precautions against spillage. Fluids must NOT be spilled on or around the sample stage, electronic boxes, or other components containing electronic parts. Avoid spilling all corrosive fluids on exposed surfaces; otherwise, damage may result! In the case of a spill, immediately clean and dry all affected surfaces carefully.

B.2 Procedure

B.2.1 Starting the software

From the DOS prompt, change to the STM directory. Start the STM microscope's Z. EXE program in C:\STM by entering "Z". Set the microscope head configuration in the Command / Head list to STM. Set the scanner type by selecting "J" in the Command / Head / Select list. By hitting ESC key go to STM menu and there set the values as given in figure B.1.

B.2.2 Install the sample in the electrochemical cell

The electrochemical cell consists of a Teflon[®] assembly with a steel screw for fixing the sample as shown in figure The Teflon[®] part provides a deep pot for

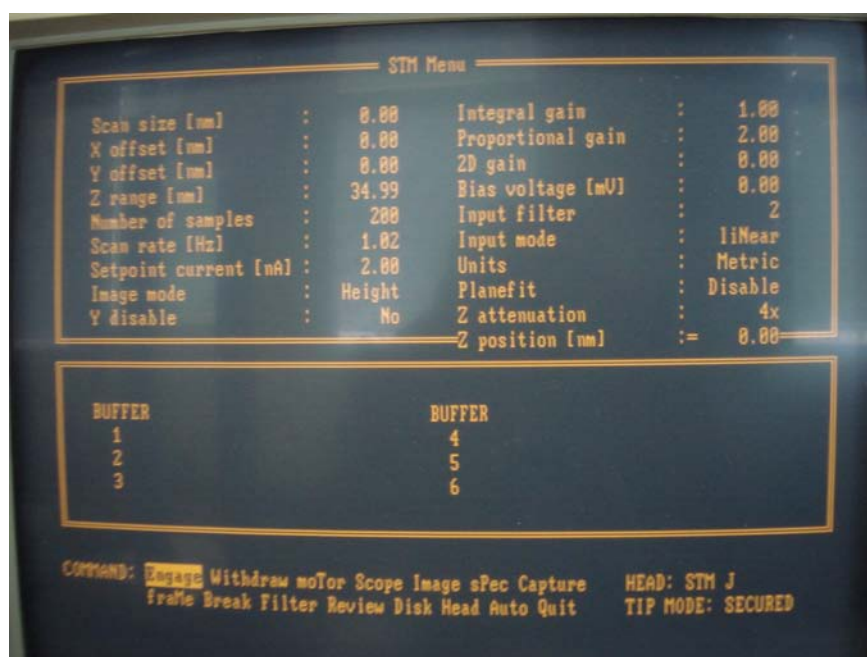


Figure B.1: Nanoscope screen with the appropriate values before engaging the tip



Figure B.2: Electrochemical cell and a typical sample to be fitted into it

holding the electrolyte on the top of the sample. The steel screw provides the pressure required for sealing the assembly as well as electrical connection to the sample for conducting the electrochemistry. Additionally its ferromagnetic property assures its magnetic attachments to the MultiMode[®] sample stage.

B.2.3 Install the electrochemical cell on the microscope stage

If the head is not already removed, do so now by unfastening the retaining springs (figure B.3) on either side. Gently lift the head off and set aside. This will expose the top of the scanner tube. Verify that the sample is installed firmly inside the electrochemical cell. Mount the electrochemical cell assembly containing the sample atop the scanner tube as shown in figure B.4. An internal magnet holds the steel screw of the electrochemical cell down. Be sure about



Figure B.3: Retaining springs



Figure B.4: Fixing the electrochemical cell on the microscope stage

its stability on the stage. Instability of the electrochemical cell on the stage is dangerous and results in the poor quality of the images and load displacement curves.

B.2.4 Install the nanoindentation head

With the sample in place, remount the nanoindentation head by gently lowering it over the electrochemical cell assembly on top of the scanner tube while checking for clearance as shown in figure B.5. The nanoindentation head must be raised adequately to clear the sample with the tip. If the head is positioned too low, toggle the tip Up switch (figure B.6) and use coarse adjustment screws (figure B.7) to raise the head adequately. Install the head carefully on the microscope, and be careful not to contact the sample with the tip. Secure both

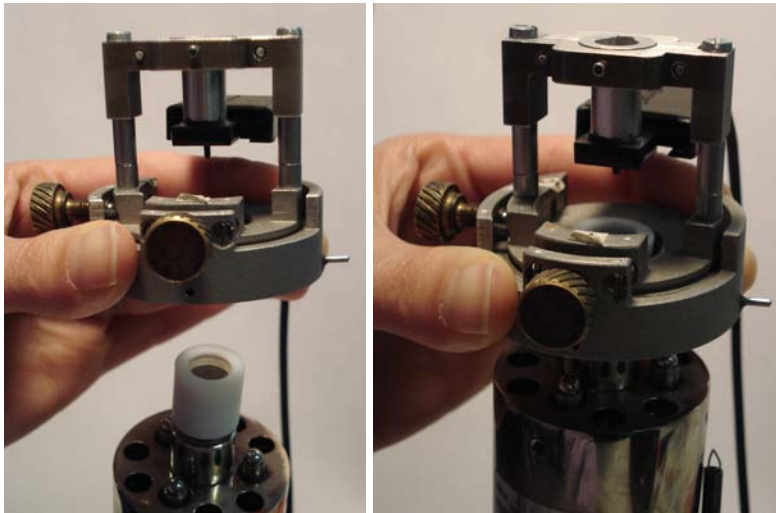


Figure B.5: Installation of the nanoindentation head on the microscope stage



Figure B.6: Tip up switch

retaining springs as shown in figure B.8.

B.2.5 Align the nanoindentation head on the microscope

Verify basic function of the motorized Z-axis by toggling the Up switch on the MultiMode[®] base (figure B.6). This activates the leadscrew at the rear of the unit to lift the head upward. The two forward screws will also have to be rotated to keep the head level while lifting. To verify rotation of the motorized screw, feel the flexible coupling on the base with your finger while the tip Up / Down switch is toggled.

Using the 25X magnifier to look from the side through the gap between the nanoindenter head and the microscope stage, focus on the tip. Use the coarse adjustment screws and motor Down switch (on the MultiMode[®] base) to adjust the tip's height just above the sample surface. The magnifier can be used to



Figure B.7: Coarse adjustment screws

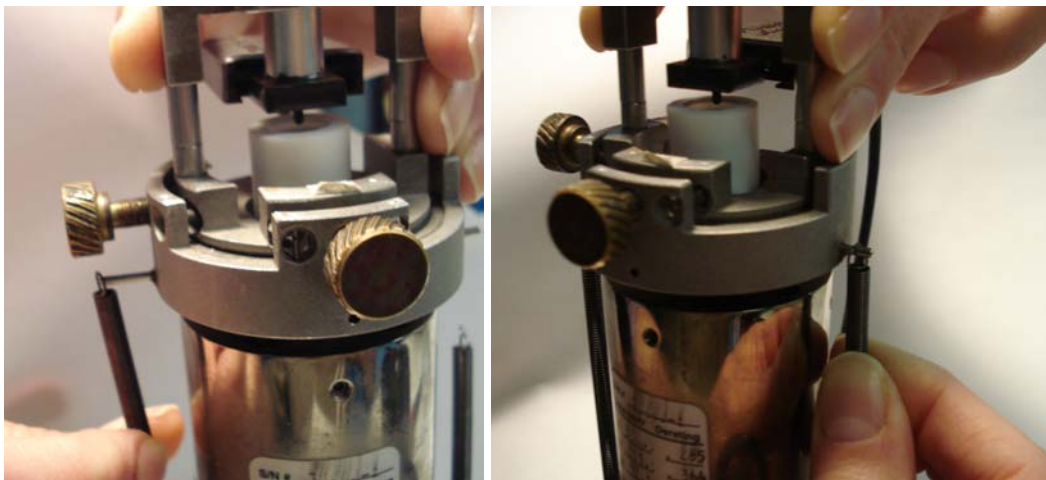


Figure B.8: Securing the retaining springs

monitor the tip while this is done. The tip should be positioned just high enough to reach the surface when engaged, but not so low as to risk crashing into it. Use the motorized screw to ensure the head is reasonably level.

B.2.6 Put the microscope inside the chamber

Carefully put the sample on the vibration isolation table and bring the protective atmosphere chamber slowly down as shown in figure B.9.

B.2.7 Engage the tip in air

Before engaging the tip zero-out the TriboScope[®] control unit (figure B.10).

Go to the command list (figure B.1) and select Engage. If for any reason the

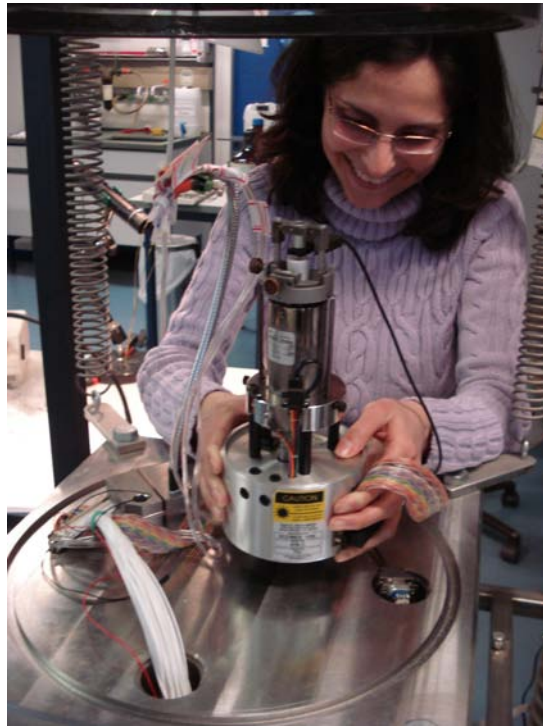


Figure B.9: Positioning Vibration isolation table



Figure B.10: The TriboScope[®] control unit

engage aborts because the SPM head is still too far away from the surface , select the *Withdraw* in menu and readjust the screws to start the tip closer to the sample surface by following the instruction in [B.2.5](#). Assuming the tip is better positioned after engaging again, an image should begin to appear on the image monitor.

B.2.8 Engage the tip in electrolyte

After engaging the tip successfully in air before addition of solution to the electrochemical cell the tip should be withdrawn. In command list by selecting *Withdraw* and hitting the enter key two times the tip will be above the surface in a distance about 4 μm . Now at this height it is safe to add the solution to the electrochemical cell very slowly from outside by injecting it through the microfill[®] pipet. Then zero-out the TriboScope[®] control unit. This may require longer time then zeroing out the controller in air since enough time should be given to equilibrate the forces acting on the tip (see section [3.5.1](#)). Then it is possible to engage the tip with the surface inside electrolyte. Sometimes it is helpfull to set the contact force to higher values then the usual value of 2 μN . This can be done by setting the *Setpoint* current in *STM* menu to higher values between 2 and 5 nA.



CAUTION! Do not use very high values of contact force, this may damage the surface as well as the tip.

PUBLICATIONS

In the frame of this PhD thesis a chapter in a book, several publications and conference papers were published. A Master thesis [259] in cooperation with the Norwegian University of Science and Technology (NTNU¹) conducted which was rewarded “A” grade.

Peer-reviewed publications

- [1] A. Barnoush, B. Yang, H. Vehoff: *Advances in Solid State Physics*, vol. 47 (Springer Berlin / Heidelberg 2008) Chap. Effect of hydrogen and grain boundaries on dislocation nucleation and multiplication examined with a NI-AFM, pp. 253–269
- [2] A. Barnoush, H. Vehoff: Electrochemical nanoindentation: A new approach to probe hydrogen/deformation interaction, *Scr. Mater.* **55**, 195–198 (2006)
- [3] A. Barnoush, H. Vehoff: In situ electrochemical nanoindentation of a nickel (111) single crystal: Hydrogen effect on pop-in behaviour, *Int. J. Mater. Res.* **97**, 1224–1229 (2006)
- [4] A. Barnoush, H. Vehoff: In situ electrochemical nanoindentation: A technique for local examination of hydrogen embrittlement, *Corros. Sci.* **50**, 259–267 (2008)
- [5] H. Vehoff, B. Yang, A. Barnoush, H. Natter, R. Hempelmann: Mechanical properties of nanomaterials examined with a NI-AFM, *International journal of research in physical chemistry and chemical physics (Zeitschrift für Physikalische Chemie)* **222**, 499–525 (2008)

¹Norges teknisk-naturvitenskapelige universitet

- [6] A. Barnoush, H. Vehoff: Hydrogen embrittlement of aluminum in aqueous environments examined by in situ electrochemical nanoindentation, *Scr. Mater.* **58**, 747–750 (2008)
- [7] H. Vehoff, B. Yang, A. Barnoush, H. Natter, R. Hempelmann: *Progress in Physical Chemistry*, vol. 2 (Oldenbourg Wissenschaftsverlag 2008) Chap. Mechanical properties of nanomaterials examined with a NI-AFM, pp. 275–301

Conference papers

- [1] A. Barnoush, H. Vehoff: Probing hydrogen embrittlement by in situ electrochemical nanoindentation, in *EuroCorr 2006* (Maastricht, Netherlands 2006)
- [2] A. Barnoush, H. Vehoff: Mechanism of hydrogen embrittlement in nickel, studied with in situ electrochemical nanoindentation, in *Corrosion2006–Research in progress* (San Diego, California, USA 2006)
- [3] A. Barnoush, H. Vehoff: In situ electrochemical nanoindentation: A novel technique to examine hydrogen embrittlement locally, in M. Anglada (Ed.): *Proceeding of the fourth meeting of the European school of materials science and engineering* (Barcelona, Spain. 2007)
- [4] A. Barnoush, H. Vehoff: The use of in situ electrochemical nanoindentation to study hydrogen embrittlement, in *EUROMAT 2007* (Nürnberg, Germany 2007)

REFERENCES

- [1] R. A. Oriani, J. P. Hirth, M. Smialowski (Eds.): *Hydrogen Degradation of Ferrous Alloys* (William Andrew Publishing/Noyes. 1985) (Cited on pages [1](#), [9](#), [28](#), [173](#) and [211](#).)
- [2] Y. Saito, R. Griese, J. Kessler, R. Kono, J. Fang: Hydrogen degradation of GaAs MMICs and hydrogen evolution in the hermetic package, in *Microwave and Millimeter-Wave Monolithic Circuits Symposium* (1995) pp. 119–122 (Cited on page [1](#).)
- [3] W. H. Johnson: On some remarkable change produced in iron and steel by the action of hydrogen and acids, *Proceedings of the Royal Society of London* **23**, 168–179 (1875) (Cited on pages [1](#) and [9](#).)
- [4] R. N. Iyer, H. W. Pickering: Mechanism and kinetics of electrochemical hydrogen entry and degradation of metallic systems, *Annual Review of Materials Science* **20**, 299–338 (1990) (Cited on pages [2](#) and [20](#).)
- [5] S. M. Myers, M. L. Baskes, H. K. Brinbaum, J. W. Corbett, G. G. Deleo, S. K. Estreicher, E. E. Haller, P. Jena, N. M. Johnson, R. Kirchheim, S. J. Pearton, M. J. Stavola: Hydrogen interactions with defects in crystalline solids, *Rev. Mod. Phys* **64**, 559 (1992) (Cited on pages [2](#), [9](#), [16](#), [17](#), [18](#) and [20](#).)
- [6] H. Vehoff: *Hydrogen in Metals III* (Springer Berlin / Heidelberg 1997) Chap. Hydrogen related material problem, pp. 215–274 (Cited on pages [2](#), [6](#), [20](#), [28](#) and [30](#).)
- [7] S. Lynch: Mechanisms of hydrogen assisted cracking - a review, in *International Conference on Hydrogen Effects on Materials Behavior and Corrosion Deformation Interactions* (Moran, WY; USA 2002) pp. 449–466 (Cited on pages [2](#), [20](#), [21](#) and [28](#).)

- [8] R. Gangloff: *Comprehensive Structural Integrity*, vol. Vol. 6 (Elsevier Science, New York, NY 2003) Chap. Hydrogen Assisted Cracking of High Strength Alloys, pp. 31–101 (Cited on pages 2, 20, 29 and 30.)
- [9] R. Gangloff: *Environment Induced Cracking of Metals* (Elsevier Science, Oxford, UK 2005) Chap. Critical Issues in Hydrogen Assisted Cracking of Structural Alloys (Cited on pages 2 and 20.)
- [10] A. Pundt, R. Kirchheim: Hydrogen in metals: Microstructural aspects, *Annu. Rev. Mater. Res.* **36**, 555–608 (2006) (Cited on pages 2, 15, 16, 19, 20, 21 and 64.)
- [11] G. Bergmann: *Untersuchungen zur Wasserstoffversprödung von NiAl, TiAl und CMSX-6*, Ph.D. thesis, Max-Planck-Institut für Eisenforschung (1995) (Cited on pages 6, 20, 22 and 23.)
- [12] R. A. Oriani, P. H. Josephic: Hydrogen-enhanced load relaxation in a deformed medium-carbon steel, *Acta Metall.* **27**, 997–1005 (1979) (Cited on pages 6, 20 and 28.)
- [13] W. Gerberich, R. Oriani: The necessity of both plasticity and brittleness in the fracture thresholds of iron, *Philosophical Magazine A* **63**, 363–376 (1991) (Cited on pages 7, 20 and 30.)
- [14] H. Vehoff, P. Neumann: Crack propagation and cleavage initiation in Fe-2.6%-Si single crystals under controlled plastic crack tip opening rate in various gaseous environments, *Acta Metall* **28**, 265 (1980) (Cited on pages 7, 20, 21, 22 and 126.)
- [15] T.-Y. Zhang, J. Hack: The equilibrium concentration of hydrogen atoms ahead of a mixed mode I-mode III crack tip in single crystal iron, *Metall. Mater. Trans. A* **30**, 155–159 (1999) (Cited on pages 7, 18 and 20.)
- [16] B. Bhatia, D. Sholl: Chemisorption and diffusion of hydrogen on surface and subsurface sites of flat and stepped nickel surfaces, *The Journal of Chemical Physics* **122**, 204707 (2005) (Cited on page 9.)
- [17] <http://www.uni-ulm.de/echem/> (Cited on pages 10 and 11.)
- [18] J. Bockris: Modern aspects of electrode kinetics, *Annu. Rev. Phys. Chem.* **5**, 477–500 (1954) (Cited on page 13.)

- [19] J. Bockris: Recent developments in the study of hydrogen overpotential., *Chemical Reviews* **43**, 525–577 (1943) (Cited on page 13.)
- [20] J. Bockris, E. Potter: The mechanism of hydrogen evolution at nickel cathodes in aqueous solutions, *The Journal of Chemical Physics* **20**, 614 (2004) (Cited on page 13.)
- [21] H. Flitt, J. Bockris: Hydrogen/metal interactions with special reference to electrochemical approaches, *Int. J. Hydrogen Energy* **6**, 119–138 (1981) (Cited on page 13.)
- [22] J. Bockris: *Modern Electrochemistry: an Introduction to an Interdisciplinary Area* (Plenum Press 2000) (Cited on page 13.)
- [23] J. Mao, R. McLellan: The thermodynamics of hydrogen-vacancy interactions in aluminum, *J. Phys. Chem. Solids* **63**, 2029–2036 (2002) (Cited on pages 15 and 16.)
- [24] Y. Tateyama, T. Ohno: Stability and clusterization of hydrogen-vacancy complexes in α -Fe: An ab initio study, *Physical Review B* **67**, 174105 (2003) (Cited on page 15.)
- [25] G. Lu, E. Kaxiras: Hydrogen embrittlement of aluminum: The crucial role of vacancies, *Phys. Rev. Lett.* **94**, 155501 (2005) (Cited on pages 15 and 16.)
- [26] J. P. Hirth, J. Lothe: *Theory of dislocations* (New York: Wiley 1981) (Cited on pages 17, 185, 187 and 207.)
- [27] R. Kirchheim, J. P. Hirth: Hydrogen adsorption at cracks in Fe, Nb and Pd, *Scripta Met.* **16**, 475–478 (1982) (Cited on page 17.)
- [28] J. Hirth, B. Carnahan: Hydrogen adsorption at dislocations and cracks in Fe, *Acta Metall.* **26**, 1795–1803 (1978) (Cited on page 18.)
- [29] R. Oriani: The diffusion and trapping of hydrogen in steel, *Acta Metall.* **18**, 147–157 (1970) (Cited on pages 18 and 28.)
- [30] D. Doyle, G. Palumbo, K. Aust, A. El-Sherik, U. Erb: The influence of intercrystalline defects on hydrogen activity and transport in nickel, *Acta Metall. Mater* **43**, 3027 (1995) (Cited on pages 20 and 211.)
- [31] D. Arantes, X. Huang, C. Marte, R. Kirchheim: Hydrogen diffusion and permeation in micro- and nanocrystalline nickel, *Acta Metall. Mater* **41**, 3215–3222 (1993) (Cited on page 20.)

- [32] K. Nibur, D. Bahr, B. Somerday: Hydrogen effects on dislocation activity in austenitic stainless steel, *Acta Mater.* **54**, 2677–2684 (2006) (Cited on pages [20](#), [21](#), [34](#), [80](#) and [152](#).)
- [33] X. Gao: Displacement burst and hydrogen effect during loading and holding in nanoindentation of an iron single crystal, *Scr. Mater.* **53**, 1315–1320 (2005) (Cited on pages [20](#), [21](#) and [34](#).)
- [34] V. Venegas, F. Caleyo, J. González, T. Baudin, J. Hallen, R. Penelle: EBSD study of hydrogen-induced cracking in API-5L-X46 pipeline steel, *Scr. Mater.* **52**, 147–152 (2005) (Cited on pages [20](#) and [21](#).)
- [35] S. A. Danilkin, M. Hölze, H. Fuess, H. Wipf, T. J. Udovic, J. J. Rush, V. E. Antonov, V. G. Gavriljukl: Crystal structure and lattice dynamics of hydrogen-loaded austenitic steel, *J. Phys. IV France* **112**, 407–410 (2003) (Cited on pages [20](#) and [21](#).)
- [36] H. Vehoff, W. Rothe: Gaseous hydrogen embrittlement in FeSi and Ni single crystals, *Acta Metall.* **31**, 1781 (1983) (Cited on pages [20](#), [21](#), [22](#), [29](#), [30](#) and [126](#).)
- [37] H. Vehoff, H. K. Klameth: Hydrogen embrittlement and trapping at crack tips in Ni single crystals., *Acta Metall.* **33**, 955–962 (1985) (Cited on pages [20](#), [21](#), [22](#), [29](#), [140](#) and [215](#).)
- [38] D. G. Ulmer, C. J. Alstetter: Hydrogen-induced strain localization and failure of austenitic stainless steels at high hydrogen concentrations, *Acta Metall. Mater* **39**, 1237 (1991) (Cited on pages [20](#), [21](#), [22](#) and [152](#).)
- [39] T. Matsumoto, J. Eastman, H. K. Birnbaum: Direct observations of enhanced dislocation mobility due to hydrogen, *Scripta metallurgica* **15**, 1033–1037 (1981) (Cited on pages [20](#), [21](#), [22](#), [25](#) and [31](#).)
- [40] I. M. Robertson, H. K. Birnbaum: HVEM study of hydrogen effects on the deformation and fracture of nickel., *Acta Metall.* **34**, 353–366 (1986) (Cited on pages [20](#), [22](#), [25](#), [31](#) and [140](#).)
- [41] H. K. Birnbaum, P. Sofronis: Hydrogen-enhanced localized plasticity-a mechanism for hydrogen-related fracture, *Materials Science and Engineering A* **A176**, 191–202 (1994) (Cited on pages [20](#), [21](#), [22](#), [25](#) and [31](#).)

- [42] I. M. Robertson, D. Teter: Controlled environment transmission electron microscopy, *J. Microsc. Res. Tech.* **42**, 260 (1998) (Cited on pages [20](#), [22](#), [25](#), [28](#) and [31](#).)
- [43] P. J. Ferreira, I. M. Robertson, H. K. Birnbaum: Hydrogen effects on the interaction between dislocations, *Acta Mater.* **46**, 1749–1757 (1998) (Cited on pages [20](#), [21](#), [22](#), [25](#), [26](#), [27](#) and [31](#).)
- [44] P. J. Ferreira, I. M. Robertson, H. K. Birnbaum: Hydrogen effects on the character of dislocations in high-purity aluminum, *Acta Mat.* **47**, 2991 (1999) (Cited on pages [20](#), [22](#), [25](#), [26](#) and [31](#).)
- [45] I. M. Robertson: The effect of hydrogen on dislocation dynamics, *Engineering Fracture Mechanics* **68**, 671–692 (2001) (Cited on pages [20](#), [21](#), [22](#), [31](#) and [32](#).)
- [46] D. F. Teter, I. M. Robertson, H. K. Birnbaum: The effects of hydrogen on the deformation and fracture of β -titanium, *Acta Mater.* **49**, 4313–4323 (2001) (Cited on pages [20](#), [21](#), [22](#), [25](#), [28](#) and [31](#).)
- [47] Y. R. Sucre, A. Iost, J. B. Vogt, D. Najjar, Y. I. Chumlyakov: Mechanical properties of austenitic stainless steel single crystals: influence of nitrogen and hydrogen content, *Metall. Mater. Trans. A* **31A**, 153–161 (2000) (Cited on pages [20](#), [21](#) and [152](#).)
- [48] W. T. Shmayda, Y. Cao, J. A. Szpunar: Effects of textures on hydrogen diffusion in nickel, *LLE Review (Publication of Laboratory for Laser Energetics (LLE) of the University of Rochester)* **91**, 125–129 (2002) (Cited on pages [20](#) and [21](#).)
- [49] D. Paraventi, T. Angeliu, G. Was: Effect of hydrogen on creep in high-purity Ni-16Cr-9Fe alloys at 360°C, *Corrosion* **58**, 675–686 (2002) (Cited on pages [20](#) and [21](#).)
- [50] P. Combette, J. Perez, P. Gobin: Influence of hydrogen on the internal friction of nickel, *Brit. J. Appl. Phys.* **1**, 1075–1078 (1968) (Cited on pages [20](#) and [21](#).)
- [51] J. Chateau, D. Delafosse, T. Magnin: Numerical simulations of hydrogen-dislocation interactions in fcc stainless steels. part I: hydrogen-dislocation interactions in bulk crystals, *Acta Mater.* **50**, 1507–1522 (2002) (Cited on pages [20](#), [21](#) and [208](#).)

- [52] A. Kimura, H. Izumi, H. Saitoh, T. Misawa: Modeling hydrogen transport causing environmental embrittlement in Co_3Ti alloys, *Intermetallics* **3**, 115–123 (1995) (Cited on pages [20](#), [21](#) and [22](#).)
- [53] M. Wen, S. Fukuyama, K. Yokogawa: Atomistic simulations of effect of hydrogen on kink-pair energetics of screw dislocations in bcc iron, *Acta Mater.* **51**, 1767–1773 (2003) (Cited on pages [20](#) and [21](#).)
- [54] M. Wen, S. Fukuyama, K. Yokogawa: Hydrogen-affected cross-slip process in fcc nickel, *Physical Review B* **69**, 174108 (2004) (Cited on pages [20](#), [21](#) and [208](#).)
- [55] M. Wen, X.-J. Xu, Y. Omura, S. Fukuyama, K. Yokogawa: Modeling of hydrogen embrittlement in single crystal Ni, *Computational Materials Science* **30**, 202–211 (2004) (Cited on pages [20](#) and [21](#).)
- [56] M. Wen, S. Fukuyama, K. Yokogawa: Atomistic simulations of hydrogen effect on dissociation of screw dislocations in nickel, *Scr. Mater.* **52**, 959–962 (2005) (Cited on pages [20](#), [21](#) and [208](#).)
- [57] G. Lu, Q. Zhang, N. Kioussis, E. Kaxiras: Hydrogen-enhanced local plasticity in aluminum: An ab initio study, *Physical review letter* **87**, 095501 (2001) (Cited on pages [20](#) and [21](#).)
- [58] D. Delafosse, T. Magnin: Hydrogen induced plasticity in stress corrosion cracking of engineering systems, *Engineering Fracture Mechanics* **68**, 693–729 (2001) (Cited on pages [20](#) and [21](#).)
- [59] A. Bussiba, H. Alush, Y. Katz: Corrosion/deformation interactions in uranium/water systems, *Materials science research international* **3**, 244–251 (1997) (Cited on pages [20](#) and [21](#).)
- [60] P. Sofronis, H. K. Birnbaum: Mechanics of the hydrogen-dislocation-impurity interactions-i. increasing shear modulus, *Journal of the Mechanics and Physics of Solids* **43**, 49–90 (1995) (Cited on pages [20](#) and [21](#).)
- [61] Y. Liang, P. Sofronis, N. Aravas: On the effect of hydrogen on plastic instabilities in metals, *Acta Mater.* **51**, 2717–2730 (2003) (Cited on pages [20](#) and [21](#).)

- [62] S. Serebrinsky, E. Carter, M. Ortiz: A quantum-mechanically informed continuum model of hydrogen embrittlement, *Journal of the Mechanics and Physics of Solids* **52**, 2403–2430 (2004) (Cited on pages [20](#) and [21](#).)
- [63] M. Menard, J. Olive, A. Brass, I. Aubert: Effects of hydrogen charging on surface slip band morphology of a type 316 L stainless steel, in *Long Term Prediction & Modelling of Corrosion (EUROCORR 2004)* (EUROCORR 2004, Nice France 2004) (Cited on pages [20](#) and [21](#).)
- [64] D. Jiang, E. A. Carter: First principles assessment of ideal fracture energies of materials with mobile impurities: implications for hydrogen embrittlement of metals, *Acta Mater.* **52**, 4801–4807 (2004) (Cited on pages [20](#) and [21](#).)
- [65] D. E. Jiang, E. A. Carter: Diffusion of interstitial hydrogen into and through bcc Fe from first principles, *Physical review B* **70**, 064102 (2004) (Cited on pages [20](#) and [21](#).)
- [66] J.-S. Wang: The thermodynamics aspects of hydrogen induced embrittlement, *Engineering Fracture Mechanics* **68**, 647–669 (2001) (Cited on pages [20](#) and [21](#).)
- [67] C. Zmudzinski, G. Pressouyre, L. Bretin: Optimization of steels likely to be subjected to hydrogen action, Commission of the European Communities, *Synopsis of Results of the First Programme on the Production and Utilization of Hydrogen*, pp. 525–547 (1982) (Cited on pages [20](#) and [22](#).)
- [68] H. Matsui, H. Kimura, S. Moriya: The effect of hydrogen on the mechanical properties of high-purity iron. I.—softening and hardening of high-purity iron by hydrogen charging during tensile deformation, *Mater. Sci. Eng.* **40**, 207–216 (1979) (Cited on pages [21](#), [22](#), [23](#) and [24](#).)
- [69] S. Moriya, H. Matsui, H. Kimura: The effect of hydrogen on the mechanical properties of high-purity iron. II.—effect of quenched-in hydrogen below room temperature, *Mater. Sci. Eng.* **40**, 217–225 (1979) (Cited on pages [21](#), [22](#) and [23](#).)
- [70] H. Matsui, H. Kimura, A. Kimura: The effect of hydrogen on the mechanical properties of high-purity iron. III.—the dependence of softening on specimen size and charging current density, *Mater. Sci. Eng.* **40**, 227–234 (1979) (Cited on pages [21](#), [22](#) and [23](#).)

- [71] A. Kimura, H. Kimura: Hydrogen embrittlement in high purity iron single crystals, *Materials Science and Engineering* **77**, 75–83 (1986) (Cited on pages [21](#) and [22](#).)
- [72] S. X. Xie, J. P. Hirth: The effect of hydrogen on reversible and irreversible softening of spheroidized steel, *Materials Science and Engineering* **60**, 207–212 (1983) (Cited on pages [21](#) and [22](#).)
- [73] H. Kimura, H. Matsui: Mechanism of hydrogen-induced softening and hardening in iron, *Scripta Metallurgica* **21**, 319–324 (1987) (Cited on pages [21](#), [22](#) and [31](#).)
- [74] A. Kimura, H. K. Birnbaum: Plastic softening by hydrogen plasma charging in pure iron, *Scripta Metallurgica* **21**, 53–57 (1987) (Cited on pages [21](#) and [22](#).)
- [75] T.-Y. Zhang, W.-Y. Chu, C.-M. Hsiao: Mechanism of hydrogen induced softening, *Scripta Metallurgica*, Volume 20, Issue 2, February 1986, Pages 225-230 **20**, 225–230 (1986) (Cited on pages [21](#) and [22](#).)
- [76] S. L. Kampe, D. A. Koss: The effect of stress state on the hydrogen embrittlement of nickel, *Acta Metall.* **34**, 55–61 (1986) (Cited on pages [21](#) and [22](#).)
- [77] W. Zheng, D. Hardie: The effect of hydrogen on the fracture of a commercial duplex stainless steel, *Corros. Sci.* **32**, 23–36 (1991) (Cited on pages [21](#) and [22](#).)
- [78] F. Iacoviello, M. Habashi, M. Cavallini: Hydrogen embrittlement in the duplex stainless steel Z2CND2205 hydrogen-charged at 200°C, *Materials Science and Engineering A* **224**, 116–124 (1997) (Cited on pages [21](#) and [22](#).)
- [79] F. Zucchi, V. Grassi, C. Monticelli, G. Trabanelli: Hydrogen embrittlement of duplex stainless steel under cathodic protection in acidic artificial sea water in the presence of sulphide ions, *Corros. Sci.* **48**, 522–530 (2006) (Cited on pages [21](#) and [22](#).)
- [80] W. McInteer, A. W. Thompson, I. M. Bernstein: The effect of hydrogen on the slip character of nickel, *Acta Metall.* **28**, 887 (1980) (Cited on pages [22](#), [31](#), [140](#) and [208](#).)

- [81] A. Zielinski: Hydrogen-assisted degradation of some non-ferrous metals and alloys, *Journal of Materials Processing Technology* **109**, 206–214 (2001) (Cited on page 22.)
- [82] J. Eastman, F. Heubaum, T. Matsumoto, H. K. Birnbaum: The effect of hydrogen on the solid solution strengthening and softening of nickel, *Acta Metall.* **30**, 1579–1586 (1982) (Cited on page 22.)
- [83] E. Sirois, H. Birnbaum: Effects of hydrogen and carbon on thermally activated deformation in nickel, *Acta Metall. Mater.* **40**, 1377–1385 (1992) (Cited on pages 22, 31 and 140.)
- [84] D. Abraham, C. Altstetter: Hydrogen-enhanced localization of plasticity in an austenitic stainless steel, *Metall. Trans. A* **26** (1995) (Cited on pages 22, 31 and 152.)
- [85] L. Marton: Electron microscopy of biological objects, *Physical Review* **46**, 527–528 (1934) (Cited on page 25.)
- [86] M. Whelan: Dislocation interactions in face-centred cubic metals, with particular reference to stainless steel, *Proceedings of the Royal Society of London. Series A, Mathematical and Physical Sciences* **249**, 114–137 (1959) (Cited on page 25.)
- [87] G. M. Bond, I. M. Robertson, H. K. Birnbaum: On the determination of the hydrogen fugacity in an environmental cell tem facility., *Scripta metallurgica* **20**, 653–658 (1986) (Cited on page 25.)
- [88] T. Tabata, H. K. Birnbaum: Direct observations of hydrogen enhanced crack propagation in iron, *Scripta Metallurgica* **18**, 231–236 (1984) (Cited on page 25.)
- [89] G. Bond, I. Robertson, H. Birnbaum: The influence of hydrogen on deformation and fracture processes in high-strength aluminum alloys, *Acta Metall.* **35**, 2289–2296 (1987) (Cited on page 25.)
- [90] P. Rozenak, I. Robertson, H. Birnbaum: HVEM studies of the effects of hydrogen on the deformation and fracture of AISI type 316 austenitic stainless steel., *Acta Metall. Mater.* **38**, 2031–2040 (1990) (Cited on pages 25 and 152.)

- [91] D. Shih, I. Robertson, H. Birnbaum: Hydrogen embrittlement of alpha titanium- in situ tem studies, *Acta Metall.* **36**, 111–124 (1988) (Cited on pages 25 and 26.)
- [92] T. Tabata, H. Birnbaum: Direct observations of the effect of hydrogen on the behavior of dislocations in iron, *Scr. Metall.* **17**, 947–950 (1983) (Cited on page 25.)
- [93] G. Bond, I. Robertson, H. Birnbaum: On the mechanisms of hydrogen embrittlement of Ni₃Al alloys, *Acta Metall.* **37**, 1407–1413 (1989) (Cited on page 25.)
- [94] A. Troiano: The role of hydrogen and other interstitials in the mechanical behavior of metals, *Trans. ASM* **52**, 54–80 (1960) (Cited on page 28.)
- [95] J. Hirth: Effects of hydrogen on the properties of iron and steel, *Metall. Trans. A* **11A**, 861–890 (1980) (Cited on page 28.)
- [96] B. Makenas, H. Birnbaum: Phase changes in the niobium–hydrogen system. I.–accommodation effects during hydride precipitation, *Acta Metall.* **28**, 979–988 (1980) (Cited on page 28.)
- [97] J. Morlet, H. Johnson, A. Troiano: A new concept of hydrogen embrittlement in steel, *Journal of the Iron and Steel Institute* **189**, 37–44 (1958) (Cited on page 28.)
- [98] M. Whiteman, A. Troiano: Hydrogen embrittlement of austenitic stainless steel, *Corrosion* **21**, 53–56 (1965) (Cited on pages 28 and 152.)
- [99] H. A. Wriedt, R. A. Oriani: Effect of tensile and compressive elastic stress on equilibrium hydrogen solubility in a solid, *Acta Metall.* **18**, 753–760 (1970) (Cited on page 28.)
- [100] R. Oriani: A mechanistic theory of hydrogen embrittlement of steels, *Ber. Bunsenges. Phys. Chem* **76**, 848–857 (1972) (Cited on pages 28 and 29.)
- [101] R. Oriani, P. Josephic: Equilibrium aspects of hydrogen-induced cracking of steels, *Acta Metall.* **22**, 1065–1074 (1974) (Cited on page 28.)
- [102] J. Li, R. Oriani, L. Darken: The thermodynamics of stressed solids, *Zeitschrift fur Physikalische Chemie Neue Folge* **49**, 271–290 (1966) (Cited on page 28.)

- [103] G. Pressouyre: Trap theory of hydrogen embrittlement, *Acta Metall.* **28**, 895–911 (1980) (Cited on page 28.)
- [104] C. J. McMahon: Hydrogen-induced intergranular fracture of steels, *Engineering Fracture Mechanics* **68**, 773–788 (2001) (Cited on page 28.)
- [105] R. Oriani: Hydrogen effects in high-strength steels, First International Conference on Environment-induced Cracking of Metals, NACE-10. NACE, Houston, TX pp. 439–447 (1990) (Cited on page 29.)
- [106] R. Oriani: Hydrogen—the versatile embrittler, *Corrosion* **43**, 390–397 (1987) (Cited on pages 29 and 30.)
- [107] M. Daw, M. Baskes: Embedded-atom method: Derivation and application to impurities, surfaces, and other defects in metals, *Physical Review B* **29**, 6443–6453 (1984) (Cited on page 31.)
- [108] M. Daw, M. Baskes: Semiempirical, quantum mechanical calculation of hydrogen embrittlement in metals, *Phys. Rev. Lett.* **50**, 1285–1288 (1983) (Cited on page 31.)
- [109] M. Daw, M. Baskes: Application of embedded atom method to hydrogen embrittlement, *Chemistry and Physics of Fracture* pp. 196–218 (1987) (Cited on page 31.)
- [110] P. Ferreira, I. Robertson, H. Birnbaum: Influence of hydrogen on the stacking fault energy of an austenitic stainless steel, *Materials Science Forum* **207**, 93–96 (1995) (Cited on page 31.)
- [111] X. Tang, A. W. Thompson: Hydrogen effects on slip character and ductility in Ni-Co alloys, *Materials Science and Engineering, A* **186**, 113–119 (1994) (Cited on page 31.)
- [112] C. Beachem: New model for hydrogen-assisted cracking—hydrogen embrittlement—, *Metall. Trans.* **3**, 437–451 (1972) (Cited on page 31.)
- [113] L. A. Bottomley, J. E. Coury, P. N. First: Scanning probe microscopy, *Anal. Chem.* **68**, 185R–230R (1996) (Cited on pages 33 and 64.)
- [114] B. Bhushan, A. V. Kulkarni, W. Bonin, J. T. Wyrobek: Nanoindentation and picondentation measurements using a capacitive transducer system in atomic force microscopy, *Philosophical Magazine A: Physics of Condensed Matter, Structure, Defects and Mechanical Properties* **74**, 1117–1128 (1996) (Cited on page 33.)

- [115] M. Oden, H. Ljungcrantz, L. Hultman: Characterization of the induced plastic zone in a single crystal TiN(001) film by nanoindentation and transmission electron microscopy, *J. Mater. Res.* **12**, 2134–2142 (1997) (Cited on page 33.)
- [116] T. A. Michalske, J. E. Houston: Dislocation nucleation at nano-scale mechanical contacts, *Acta Mater.* **46**, 391 (1998) (Cited on pages 33, 80 and 81.)
- [117] J. D. Kiely, J. E. Houston: Nanomechanical properties of Au (111), (001), and (110) surfaces, *Phys. Rev. B* **57**, 12588 (1998) (Cited on pages 33 and 80.)
- [118] H. Bei, E. P. George, J. L. Hay, G. M. Pharr: Influence of indenter tip geometry on elastic deformation during nanoindentation, *Phys. Rev. Lett.* **95**, 1–4 (2005) (Cited on page 33.)
- [119] M. Göken, M. Kempf, M. Bordenet, H. Vehoff: Nanomechanical characterizations of metals and thin films, *Surf. Interface Anal.* **27**, 302–306 (1999) (Cited on pages 33 and 80.)
- [120] K. Durst, M. Göken, H. Vehoff: Finite element study for nanoindentation measurements on two-phase materials, *J. Mater. Res.* **19**, 85–93 (2004) (Cited on pages 33 and 71.)
- [121] M. Henning, H. Vehoff: Local mechanical behavior and slip band formation within grains of thin sheets, *Acta Mater.* **53**, 1285–1292 (2005) (Cited on page 33.)
- [122] M. T. Welsch, M. Henning, M. Marx, H. Vehoff: Measuring the plastic zone size by orientation gradient mapping (OGM) and electron channeling contrast imaging (ECCI), *Advanced Engineering Materials* **9**, 31–37 (2007) (Cited on page 33.)
- [123] M. Kempf, M. Göken, H. Vehoff: Nanohardness measurements for studying local mechanical properties of metals, *Applied Physics A Materials Science & Processing* **66**, S843–S846 (1998) (Cited on page 34.)
- [124] B. Yang, H. Vehoff: The effect of grain size on the mechanical properties of nanonickel examined by nanoindentation, *Zeitschrift fuer Metallkunde/Materials Research and Advanced Techniques* **95**, 499–504 (2004) (Cited on pages 34 and 80.)

- [125] B. Yang, H. Vehoff: Grain size effects on the mechanical properties of nanonickel examined by nanoindentation, *Materials Science and Engineering A* **400-401**, 467–470 (2005) (Cited on pages [34](#) and [80](#).)
- [126] D. Bahr, K. Nibur: Probing hydrogen-deformation interactions using nanoindentation., *International Conference on Hydrogen Effects on Materials Behavior and Corrosion Deformation Interactions* pp. 165–172 (2002) (Cited on page [34](#).)
- [127] D. Bahr, K. Nibur, K. Morasch, D. Field: Hydrogen and deformation: Nano- and microindentation studies, *JOM* **55**, 47–50 (2003) (Cited on page [34](#).)
- [128] D. Tabor: *The Hardness of Metals* (Oxford University Press 1951) (Cited on pages [35](#) and [39](#).)
- [129] V. Lysaght: *Indentation Hardness Testing* (New York, NY: Reinhold Publishing Corp. 1949) (Cited on page [35](#).)
- [130] E. Schweitzer, K. Durst, D. Amberger, M. Göken: The mechanical properties in the vicinity of grain boundaries in ultrafine-grained and polycrystalline materials studied by nanoindentations, *Materials Research Society Symposium - Proceedings* **819**, 79–84 (2004) (Cited on page [35](#).)
- [131] Y. Shibutani, A. Koyama: Surface roughness effects on the displacement bursts observed in nanoindentation, *J. Mater. Res.* **19**, 183–188 (2004) (Cited on pages [35](#) and [80](#).)
- [132] Y. Shibutani, T. Tsuru, A. Koyama: Nanoplastic deformation of nanoindentation: Crystallographic dependence of displacement bursts, *Acta Mater.* **55**, 1813–1822 (2007) (Cited on pages [35](#) and [80](#).)
- [133] G. Pharr, W. Oliver: Nanoindentation of silver-relations between hardness and dislocation structure, *J. Mat. Res.* **4**, 94–101 (1989) (Cited on page [36](#).)
- [134] B. Yang, H. Vehoff: Dependence of nanohardness upon indentation size and grain size – A local examination of the interaction between dislocations and grain boundaries, *Acta Mater.* **55**, 849–856 (2007) (Cited on pages [36](#), [74](#) and [80](#).)
- [135] K. Johnson: *Contact mechanics* (Cambridge university press 2003) (Cited on pages [37](#), [39](#), [51](#), [52](#) and [70](#).)

- [136] H. Hertz: Über die berührung fester elastischer körper, *J. Reine Angew. Math.* **92**, 156–171 (1881) (Cited on pages 37 and 77.)
- [137] v. M. T. Huber: Zur theorie der berührung fester elastischer körper, *Ann. Physik* **14**, 153–163 (1904) (Cited on page 39.)
- [138] A. Fischer Cripps: *Nanoindentation*, First ed., Mechanical Engineering Series (New York, NY: Springer-Verlag 2002) (Cited on pages 48, 51, 52 and 76.)
- [139] L. Howes: Elastic recovery at hardness indentations, *J. Mat. Sci.* **16**, 2745–2752 (1981) (Cited on page 51.)
- [140] *Triboscope Nanomechanical Test System User's Manual*, Minneapolis, MN. (1996) (Cited on pages 54 and 56.)
- [141] R. Sonnenfeld, P. Hansma: Atomic-resolution microscopy in water, *Science* **232**, 211 (1986) (Cited on page 64.)
- [142] R. Sonnenfeld, B. Schardt: Tunneling microscopy in an electrochemical cell: Images of ag plating, *Appl. Phys. Lett.* **49**, 1172 (1986) (Cited on page 64.)
- [143] G. Binnig, H. Rohrer, C. Gerber, E. Weibel: Vacuum tunneling, *Physica B & C* **109–110**, 2075–2077 (1982) (Cited on page 64.)
- [144] B. Drake, C. B. Prater, A. L. Weisenhorn, S. A. Gould, T. R. Albrecht, C. F. Quate, D. S. Cannell, H. G. Hansma, P. K. Hansma: Imaging crystals, polymers, and processes in water with the atomic force microscope., *Science* **243**, 1586–1589 (1989) (Cited on page 64.)
- [145] S. Manne, P. K. Hansma, J. Massie, V. B. Elings, A. A. Gewirth: Atomic-resolution electrochemistry with the atomic force microscope: Copper deposition on gold, *Science* **251**, 183–186 (1991) (Cited on page 64.)
- [146] G. Binnig, C. Gerber, E. Stoll, T. R. Albrecht, C. F. Quate: Atomic resolution with atomic force microscope, *Europhys. Lett.* **3**, 1281–1286 (1987) (Cited on page 64.)
- [147] W. Polewska, M. R. Vogt, O. M. Magnussen, R. J. Behm: In situ STM study of Cu(111) surface structure and corrosion in pure and Benzotriazole-containing sulfuric acid solution, *J. Phys. Chem. B* **103**, 10440–10451 (1999) (Cited on pages 64 and 107.)

- [148] J. Scherer, B. M. Ocko, O. M. Magnussen: Structure, dissolution, and passivation of Ni(111) electrodes in sulfuric acid solution: an in situ stm, x-ray scattering, and electrochemical study, *Electrochim. Acta* **41**, 1169–1191 (2003) (Cited on pages [64](#) and [140](#).)
- [149] W. A. Bonin: Us patent no. 5553486 assigned to hysitron inc. "apparatus for microindentation hardness testing and surface imaging incorporating a multi-plate capacitor system", United States Patent (1994) (Cited on page [64](#).)
- [150] N. Yu, W. A. Bonin, A. A. Polycarpou: High-resolution capacitive load-displacement transducer and its application in nanoindentation and adhesion force measurements, *Rev. Sci. Instrum.* **76**, 1–8 (2005) (Cited on page [64](#).)
- [151] M. Seo, M. Chiba, K. Suzuki: In-situ nanoindentation of a single crystal iron(100) surface passivated in pH 8. 4 boric-borate solution, *Critical Factors in Localized Corrosion III: A Symposium in Honor of the 70 th Birthday of Jerome Kruger* pp. 1–10 (1998) (Cited on page [64](#).)
- [152] M. Chiba, M. Seo: Mechanoelectrochemical properties of passive iron surfaces evaluated by an in situ nanoscratching test, *J. Electrochem. Soc.* **150**, B525 (2003) (Cited on page [64](#).)
- [153] M. Seo, M. Chiba, K. Suzuki: Nano-mechano-electrochemistry of the iron (100) surface in solution, *J. Electroanal. Chem.* **473**, 49–53 (1999) (Cited on page [64](#).)
- [154] M. Chiba, M. Seo: Effects of dichromate treatment on mechanical properties of passivated single crystal iron (100) and (110) surfaces, *Corros. Sci.* **44**, 2379–2391 (2002) (Cited on page [64](#).)
- [155] M. Seo, M. Chiba: Nano-mechano-electrochemistry of passive film surfaces, *Electrochim. Acta* **47**, 319–325 (2001) (Cited on page [64](#).)
- [156] M. Seo, Y. Kurata: Nano-mechano-electrochemical properties of passive titanium surfaces evaluated by in-situ nano-indentation and nano-scratching, *Electrochim. Acta* **48**, 3221–3228 (2003) (Cited on page [64](#).)
- [157] M. Seo, Y. Kurata, M. Chiba: Frictional coefficients of the passive titanium surfaces evaluated with in-situ and ex-situ nano-scratching tests, *Journal of Corrosion Science & Engineering* **6** (2003) (Cited on page [64](#).)

- [158] M. Seo, D. Kawamata: Nano-scratching in solution to the single-crystal Ta (100) subjected to anodic oxidation, *J. Phys. D: Appl. Phys.* **39**, 3150–3156 (2006) (Cited on page 64.)
- [159] I. R. Kramer, L. J. Demer: Effects of environment on mechanical properties of metals, *Progress in Materials Science* **9**, 133–199 (1961) (Cited on page 64.)
- [160] S. Venkataraman, D. Kohlstedt, W. Gerberich: Continuous microindentation of passivating surfaces, *J. Mater. Res* **8**, 685–688 (1993) (Cited on pages 64 and 80.)
- [161] A. B. Mann, J. B. Pethica: Nanoindentation studies in a liquid environment, *Langmuir* **12**, 4583–4586 (1996) (Cited on page 64.)
- [162] J. Kiely, D. A. Bonnell: Quantification of topographic structure by scanning probe microscopy, *J. Vac. Sci. Technol. B* **15**, 1483–1493 (1997) (Cited on page 71.)
- [163] K. Durst, B. Backes, O. Franke, M. Göken: Indentation size effect in metallic materials: Modeling strength from pop-in to macroscopic hardness using geometrically necessary dislocations, *Acta Mater.* **54**, 2547–2555 (2006) (Cited on pages 72, 74, 80 and 183.)
- [164] W. Nix, H. Gao: Indentation size effect in crystalline materials: a law for strain gradient plasticity, *Journal of the Mechanics and Physics of Solids* **46**, 411 (1998) (Cited on page 72.)
- [165] K. Durst, B. Backes, M. Göken: Indentation size effect in metallic materials: Correcting for the size of the plastic zone, *Scr. Mater.* **52**, 1093–1097 (2005) (Cited on page 74.)
- [166] Z. Zhang, H. Kristiansen, J. Liu: A method for determining elastic properties of micron-sized polymer particles by using flat punch test, *Computational Materials Science* **39**, 305–314 (2007) (Cited on page 74.)
- [167] M. D. Uchic, D. M. Dimiduk: A methodology to investigate size scale effects in crystalline plasticity using uniaxial compression testing, *Materials Science and Engineering A* **400-401**, 268–278 (2005) (Cited on page 74.)

- [168] C. Volkert, E. Lilleodden: Size effects in the deformation of sub-micron Au columns, *Philosophical Magazine* **86** (33-35 SPEC. ISSUE), pp. 5567-5579 **86**, 5567–5579 (2006) (Cited on page [74](#).)
- [169] H. Guo, B. Lu, J. Luo: Response of surface mechanical properties to electrochemical dissolution determined by in situ nanoindentation technique, *Electrochem. Commun.* **8**, 1092–1098 (2006) (Cited on page [74](#).)
- [170] W. Oliver, G. Pharr: Improved technique for determining hardness and elastic modulus using load and displacement sensing indentation experiments, *J. Mater. Res.* **7**, 1564–1583 (1992) (Cited on pages [75](#) and [93](#).)
- [171] A. Bolshakov, G. Pharr: Influence of pileup on the measurement of mechanical properties by load and depth sensing indentation techniques, *J. Materials Research* **13**, 1049–1058 (1998) (Cited on page [76](#).)
- [172] A. Gouldstone, H.-J. Koh, K.-Y. Zeng, A. E. Giannakopoulos, S. Suresh: Discrete and continuous deformation during nanoindentation of thin films, *Acta Mater.* **48**, 2277–2295 (2000) (Cited on page [76](#).)
- [173] H. Leipner, D. Lorenz, A. Zeckzer, H. Leia, P. Grau: Nanoindentation pop-in effect in semiconductors, *Physica B* **308-310**, 446–449 (2001) (Cited on pages [77](#) and [80](#).)
- [174] J. il Jang, M. Lance, S. Wen, T. Y. Tsui, G. Pharr: Indentation-induced phase transformations in silicon: influences of load, rate and indenter angle on the transformation behavior, *Acta Mater.* **53**, 1759–1770 (2005) (Cited on page [77](#).)
- [175] Y. Gogotsi, A. Kailer, K. Nickel: Phase transformations in materials studied by micro-Raman spectroscopy of indentations, *Mater. Res. Innovations* **1**, 3–9 (1997) (Cited on page [77](#).)
- [176] B. Wolf, A. Richter: The concept of differential hardness in depth sensing indentation, *New Journal of Physics* **5**, 15.1–15.17 (2003) (Cited on page [77](#).)
- [177] Y. Gogotsi, V. Domnich, S. Dub, A. Kailer, K. Nickel: Cyclic nanoindentation and Raman microspectroscopy study of phase transformations in semiconductors, *J. Mater. Res* **15**, 872 (2000) (Cited on page [77](#).)

- [178] D. Chrobak, A. Chrobak, R. Nowak: Nanoindentation of GaAs (001) surface. a molecular dynamics study, *Solid state Phenomena* **130**, 213–217 (2007) (Cited on page 77.)
- [179] A. Kailer: Phase transformations of silicon caused by contact loading, *J. Appl. Phys.* **81**, 3057 (1997) (Cited on page 77.)
- [180] V. Domnich: Effect of phase transformations on the shape of the unloading curve in the nanoindentation of silicon, *Appl. Phys. Lett.* **76**, 2214 (2000) (Cited on pages 77 and 79.)
- [181] C. P. Frick, T. W. Lang, K. Spark, K. Gall: Stress-induced martensitic transformations and shape memory at nanometer scales, *Acta Mater.* **54**, 2223–2234 (2006) (Cited on page 77.)
- [182] N. Gane, F. P. Bowden: Microdeformation of solids, *J. Appl. Phys.* **39**, 1432–1435 (1968) (Cited on page 77.)
- [183] J. B. Pethica, D. Tabor: Contact of characterised metal surfaces at very low loads: deformation and adhesion, *Surf. Sci.* **89**, 182–190 (1979) (Cited on page 79.)
- [184] D. F. Bahr, D. E. Kramer, W. W. Gerberich: Non-linear deformation mechanisms during nanoindentation, *Acta Mater.* **46**, 3605–3617 (1998) (Cited on pages 80, 81, 184 and 211.)
- [185] W. W. Gerberich, J. C. Nelson, E. T. Lilleodden, P. Anderson, J. T. Wyrobek: Indentation induced dislocation nucleation: The initial yield point, *Acta Mater.* **44**, 3585–3598 (1996) (Cited on pages 80 and 81.)
- [186] S. G. Corcoran, R. J. Colton, E. T. Lilleodden, W. W. Gerberich: Anomalous plastic deformation at surfaces: Nanoindentation of gold single crystals, *Physical review B* **55**, R16057 (1997) (Cited on pages 80 and 81.)
- [187] J. K. Mason, A. C. Lund, C. A. Schuh: Determining the activation energy and volume for the onset of plasticity during nanoindentation, *Phys. Rev. B* **73**, 1–14 (2006) (Cited on page 80.)
- [188] A. Lund: Incipient plasticity during nanoindentation at elevated temperatures, *Appl. Phys. Lett.* **85**, 1362 (2004) (Cited on page 80.)
- [189] D. Rodriguez-Marek, M. Pang, D. Bahr: Mechanical measurements of passive film fracture on an austenitic stainless steel, *Metall. Mater. Trans. A* **34**, 1291–1296 (2003) (Cited on page 80.)

- [190] Y. Yao, X. Cao, L. Qiao, W. Chu: Yield point phenomena during nanoindentation, *Tribology Trans.* **47**, 239–247 (2004) (Cited on page 80.)
- [191] B. Yang, H. Vehoff, R. Hempelmann: The deformation behaviour of electrodeposited nanocrystalline ni in an atomic force microscope with a newly developed in situ bending machine, *Int. J. Mater. Res.* **97**, 1220–1223 (2006) (Cited on page 80.)
- [192] A. Ngan, L. Zuo, P. Wo: Probabilistic nature of the nucleation of dislocations in an applied stress field, *Scr. Mater.* **54**, 589–593 (2006) (Cited on page 80.)
- [193] M. Göken, M. Kempf: Pop-ins in nanoindentations- the initial yield point, *Zeitschrift für Metallkunde* **92**, 1061–1067 (2001) (Cited on page 80.)
- [194] Y. Gaillard, C. Tromas, J. Woïrgard: Pop-in phenomenon in MgO and LiF: observation of dislocation structures, *Philos. Mag. Lett.* **83**, 553–561 (2003) (Cited on page 80.)
- [195] D. Bahr, J. Nelson, N. Tymiak, W. Gerberich: The mechanical behavior of a passivating surface under potentiostatic control, *J. Mater. Res.* **12**, 3345–3353 (1997) (Cited on page 80.)
- [196] W. Gerberich, S. Venkataraman, H. Huang, S. Harvey, D. Kohlstedt: The injection of plasticity by millinewton contacts, *Acta Metall. Mater.* **43**, 1569–1576 (1995) (Cited on page 80.)
- [197] W. Zielinski, H. Huang, S. Venkataraman, W. Gerberich: Dislocation distribution under a microindentation into an iron-silicon single crystal, *Philosophical magazine. A. Physics of condensed matter. Structure, defects and mechanical properties* **72**, 1221–1237 (1995) (Cited on page 81.)
- [198] A. Minor, S. Asif, Z. Shan, E. Stach, E. Cyrankowski, T. Wyrobek, O. Warren: A new view of the onset of plasticity during the nanoindentation of aluminium, *Nat. Mater.* **5**, 697–702 (2006) (Cited on page 81.)
- [199] A. Minor, E. Lilleodden, E. Stach: Direct observations of incipient plasticity during nanoindentation of Al., *J. Mater. Res.* **19**, 176–182 (2004) (Cited on page 81.)
- [200] A. Minor, E. Lilleodden, E. Stach, J. J.W. Morris: In-situ transmission electron microscopy study of the nanoindentation behavior of Al, *J. Electron. Mater.* **31**, 958–964 (2002) (Cited on pages 81 and 82.)

- [201] K. Van Vliet, J. Li, T. Zhu, S. Yip, S. Suresh: Quantifying the early stages of plasticity through nanoscale experiments and simulations, *Physical Review B* **67**, 104105 (2003) (Cited on page 81.)
- [202] J. Li, K. Van Vliet, T. Zhu, S. Yip, S. Suresh: Atomistic mechanisms governing elastic limit and incipient plasticity in crystals, *Nature* **418**, 307–310 (2002) (Cited on pages 81 and 83.)
- [203] T. Zhua, J. Lib, K. J. Vlietc, S. Ogataf, S. Yipb, S. Suresha: Predictive modeling of nanoindentation-induced homogeneous dislocation nucleation in copper, *Journal of the Mechanics and Physics of Solids* **52**, 691 (2004) (Cited on page 81.)
- [204] D. Lorenz, A. Zeckzer, U. Hilpert, P. Grau, H. Johansen, H. S. Leipner: Pop-in effect as homogeneous nucleation of dislocations during nanoindentation, *Phys. Rev. B* **67**, 172101 (2003) (Cited on page 81.)
- [205] G. E. Dieter: *Mechanical metallurgy* (McGraw-Hill Book Company 2001) (Cited on page 81.)
- [206] N. H. MacMillan: The theoretical strength of solids, *J. Mater. Sci.* **7**, 239–254 (1972) (Cited on pages 82 and 83.)
- [207] F. C. Roesler: Brittle fractures near equilibrium, *Proc. Phys. Soc. B* **69**, 981–992 (1956) (Cited on page 85.)
- [208] B. Lawn, R. Wilshaw: Indentation fracture: principles and applications, *J. Mater. Sci.* **10**, 1049–1081 (1975) (Cited on page 85.)
- [209] Y. G. Wang, L. J. Qiao, K. W. Gao, Y. J. Su, W. Y. Chu, Z. L. Wang: Measurement of the fracture toughness and critical stress for cracking in SnO₂ nanobelts using nanoindentation, *Acta Metall. Sinica* **40**, 594–598 (2004) (Cited on page 86.)
- [210] A. A. Volinsky, J. B. Vella, W. W. Gerberich: Fracture toughness, adhesion and mechanical properties of low-K dielectric thin films measured by nanoindentation, *Thin Solid Films* **429**, 201–210 (2003) (Cited on page 86.)
- [211] T. W. Scharf, H. Deng, J. A. Barnard: Mechanical and fracture toughness studies of amorphous SiC-N hard coatings using nanoindentation, *Journal of Vacuum Science & Technology a-Vacuum Surfaces and Films* **15**, 963–967 (1997) (Cited on page 86.)

- [212] J. N. Ding, Y. G. Meng, S. Z. Wen: Mechanical properties and fracture toughness of multilayer hard coatings using nanoindentation, *Thin Solid Films* **371**, 178–182 (2000) (Cited on page 86.)
- [213] H. Gengnagel, W. Schwab: Light figures, their formation and application for determining the orientation of crystals, *Zeitschrift fur Metallkunde* **57**, 281–287 (1966) (Cited on page 87.)
- [214] P. Dettner: *Electrolytic and Chemical Polishing of Metals* (Ordentlich 1988) (Cited on page 90.)
- [215] W. Oliver, G. Pharr: Measurement of hardness and elastic modulus by instrumented indentation: Advances in understanding and refinements to methodology, *J. Mater. Res.* **19**, 3–20 (2004) (Cited on page 93.)
- [216] A. Kimura, H. Birnbaum: The effects of cathodically charged hydrogen on the flow stress of nickel and nickel–carbon alloys, *Acta Metall.* **35**, 1077–1088 (1987) (Cited on pages 103 and 140.)
- [217] N. Ansari, R. Balasubramaniam: Determination of hydrogen diffusivity in nickel by subsurface microhardness profiling, *Materials Science & Engineering A* **293**, 292–295 (2000) (Cited on page 103.)
- [218] W. M. Robertson: Hydrogen permeation, diffusion and solution in nickel, *Zeitschrift fur Metallkunde* **64**, 436–443 (1973) (Cited on page 104.)
- [219] E. Casas: *Untersuchung des Einflusses der Ex-Situ Wasserstoffbeladung auf die mechanischen Eigenschaften von Nickel*, Internship report, Saarland university (September 2006–Februar 2007) (Cited on page 106.)
- [220] T. Ishikawa, R. McLellan: The diffusivity of hydrogen in copper at low temperatures, *J. Phys. Chem. Solids* **46**, 445–447 (1985) (Cited on page 107.)
- [221] D. DeWulf, A. Bard: Electrochemical determination of hydrogen transport through copper, *J. Electrochem. Soc.* **132**, 2965 (1985) (Cited on pages 107 and 108.)
- [222] M. Lohrengel, H. Speckmann, J. Schultze, H. Strenblow: Growth, corrosion and capacity of copper oxide films investigated by pulse techniques, *Electrochim. Acta* **32**, 733–42 (1987) (Cited on page 107.)

- [223] H. Strehblow, B. Titze: The investigation of the passive behavior of copper in weakly acid and alkaline solutions and the examination of the passive film by ESCA and ISS, *Electrochim. Acta* **25**, 839–850 (1980) (Cited on page [107](#).)
- [224] R. Babić, M. Metikoš-Huković, A. Jukić: A study of copper passivity by electrochemical impedance spectroscopy, *J. Electrochem. Soc.* **148**, B146 (2001) (Cited on page [107](#).)
- [225] D. Tromans, R. Sun: Anodic behavior of copper in weakly alkaline solutions, *J. Electrochem. Soc.* **139**, 1945 (1992) (Cited on page [107](#).)
- [226] F. Brizuela, R. Procaccini, S. Ceré, M. Vázquez: Anodically grown films on copper and copper–nickel alloys in slightly alkaline solutions, *J. Appl. Electrochem.* **36**, 583–590 (2006) (Cited on page [107](#).)
- [227] V. Brusic, M. Frisch, B. Eldridge, F. Novak, F. Kaufman, B. Rush, G. Frankel: Copper corrosion with and without inhibitors, *J. Electrochem. Soc.* **138**, 2253–2259 (1991) (Cited on page [107](#).)
- [228] A. Hassel, M. Lohrengel: Initial stages of cathodic breakdown of thin anodic aluminium oxide films, *Electrochim. Acta* **40**, 433–437 (1995) (Cited on page [111](#).)
- [229] H. Takahashi, K. Kasahara, K. Fujiwara, M. Seo: The cathodic polarization of aluminum covered with anodic oxide films in a neutral borate solution. i. the mechanism of rectification, *Corros. Sci.* **36**, 677–688 (1994) (Cited on page [111](#).)
- [230] C. Lin, M. Porter, K. Hebert: Surface films produced by cathodic polarization of aluminum, *J. Electrochem. Soc.* **141**, 96 (1994) (Cited on page [111](#).)
- [231] H. Kaesche: Investigation of uniform dissolution and pitting of aluminium electrodes, *Werkst Korros* **14**, 557 (1963) (Cited on page [111](#).)
- [232] J. Kunze: Untersuchungen zur elektrochemischen polarisation von aluminium in gepufferter natriumchloridlösung, *Corros. Sci.* **7**, 273–287 (1967) (Cited on page [111](#).)
- [233] K. Nisancioglu, H. Holtan: Cathodic polarization of commercially pure aluminium, *Corros. Sci.* **19**, 537–552 (1979) (Cited on page [111](#).)

- [234] A. Kolics, A. Besing, P. Baradlai, R. Haasch, A. Wieckowski: Effect of pH on thickness and ion content of the oxide film on aluminum in NaCl media, *J. Electrochem. Soc.* **148**, B251 (2001) (Cited on page 111.)
- [235] W. Stumm: *Chemistry of the solid-water interface* (Wiley New York 1992) (Cited on page 111.)
- [236] E. McCafferty: Lewis acid/Lewis base effects in corrosion and polymer adhesion at aluminum surfaces, *J. Electrochem. Soc.* **150**, B342 (2003) (Cited on page 112.)
- [237] E. McCafferty, J. P. Wightman: Determination of the concentration of surface hydroxyl groups on metal oxide films by a quantitative XPS method, *Surf. Interface Anal.* **26**, 549–564 (1998) (Cited on page 112.)
- [238] E. McCafferty, J. Wightman: Determination of the surface isoelectric point of oxide films on metals by contact angle titration, *J. Colloid Interface Sci.* **194**, 344–355 (1997) (Cited on page 112.)
- [239] M. Doerner, W. Nix: A method for interpreting the data from depth-sensing indentation, *J. Mater. Res.* **1** (1986) (Cited on page 112.)
- [240] B. MacDougall, J. Bardwell: Passivation of iron in sulfate, perchlorate, and borate solutions: Role of borate in the passivation process, *J. Electrochem. Soc.* **135**, 2437 (1988) (Cited on pages 127 and 140.)
- [241] M. Büchler, P. Schmuki, H. Böhm: Iron passivity in borate buffer, *J. Electrochem. Soc.* **145**, 609 (2005) (Cited on page 128.)
- [242] M. Yamaguchi, H. Nishihara, K. Aramaki: The inhibition of passive film breakdown on iron in a borate buffer solution containing chloride ions by organic anion inhibitors, *Corros. Sci.* **36**, 241–258 (1994) (Cited on page 128.)
- [243] R. Balasubramaniam: Hydrogen in iron aluminides, *J. Alloys Compd.* **330-332**, 506–510 (2002) (Cited on pages 133 and 134.)
- [244] N. Stoloff, C. Liu: Environmental embrittlement of iron aluminides, *Intermetallics* **2**, 75–87 (1994) (Cited on page 134.)
- [245] G. Chen, C. Liu: Moisture induced environmental embrittlement of intermetallics, *Int. Mater. Rev.* **46**, 253–270 (2001) (Cited on page 134.)

- [246] C. T. Liu, E. P. George: Environmental embrittlement in boron-free and boron-doped FeAl (40 at. % Al), *Metall. Trans. A* **24**, 1285–1290 (1990) (Cited on page 134.)
- [247] J. W. Cohron, Y. Lin, R. H. Zee, E. P. George: Room-temperature mechanical behavior of FeAl: effects of stoichiometry, environment, and boron addition, *Acta Mater.* **46**, 6245–6256 (1998) (Cited on page 134.)
- [248] N. De Cristofaro, S. Frangini, A. Mignone: Passivity and passivity breakdown on a β -FeAl intermetallic compound in sulphate and chloride containing solutions, *Corros. Sci.* **38**, 307–315 (1996) (Cited on page 134.)
- [249] S. Frangini, R. Giorgi, J. Lascovich, A. Mignone: XPS study of passive films formed on an iron - aluminium intermetallic compound in acid solution, *Surf. Interface Anal.* **21**, 435–441 (1994) (Cited on pages 134 and 135.)
- [250] B. MacDougall, M. Cohen: Anodic oxidation of nickel in neutral sulfate solution, *J. Electrochem. Soc.* **121**, 1152 (1974) (Cited on page 140.)
- [251] B. MacDougall, M. Cohen: Anodic oxide films on nickel in acid solutions, *J. Electrochem. Soc.* **123**, 191 (1976) (Cited on pages 140 and 141.)
- [252] B. MacDougall, M. Cohen: Mechanism of the anodic oxidation of nickel, *J. Electrochem. Soc.* **123**, 1783 (1976) (Cited on page 140.)
- [253] R. Newman: Beyond the kitchen sink, *Nature* **415**, 743–4 (2002) (Cited on page 151.)
- [254] W. Godoi, N. Kuromoto, A. Guimarães, C. Lepienski: Effect of the hydrogen outgassing time on the hardness of austenitic stainless steels welds, *Materials Science & Engineering A* **354**, 251–256 (2003) (Cited on page 152.)
- [255] V. N. Shivanyuk, J. Foct, V. G. Gavriljuk: Hydrogen-enhanced microplasticity of austenitic steels studied by means of internal friction, *Materials Science and Engineering A* **300**, 284–290 (2001) (Cited on pages 152 and 179.)
- [256] A. Pontini, J. Hermida: X-ray diffraction measurement of the stacking fault energy reduction induced by hydrogen in an AISI 304 steel, *Scr. Mater.* **37**, 1831–1837 (1997) (Cited on pages 152 and 173.)

- [257] A. Glowacka, W. A. Swiatnicki, E. Jezierska: Hydrogen-induced defects in austenite and ferrite of a duplex steel, *Journal of Microscopy* **223**, 282–284 (2006) (Cited on page [152](#).)
- [258] M. Henning: *Size Effects on Mechanical Properties*, Ph.D. thesis, Saarland university (2007) (Cited on pages [152](#) and [153](#).)
- [259] M. Øverland: *Hydrogen Induced Cracking in Super duplex Stainless Steels: Determination of Local Material Properties*, Master's thesis, NTNU (2007) (Cited on pages [160](#), [173](#), [180](#) and [227](#).)
- [260] J. Breedis: Influence of dislocation substructure on the martensitic transformation in stainless steel, *Acta Metall.* **13**, 239–250 (1965) (Cited on page [173](#).)
- [261] J. Breedis, W. Robertson: The martensitic transformation in single crystals of iron-chromium-nickel alloys, *Acta Metall* **10**, 1077–1088 (1962) (Cited on page [173](#).)
- [262] J. Breedis, W. Robertson: Martensitic transformation and plastic deformation in iron alloy single crystals, *Acta Metall.* **11**, 547–559 (1962) (Cited on page [173](#).)
- [263] V. Gavriljuk, A. Tarasenko, A. Tereshchenko, K. Ullakko: Phase transformations and relaxation phenomena caused by hydrogen in stable austenitic stainless steels, *Acta Metall. Mater.* **43**, 559–568 (1995) (Cited on page [173](#).)
- [264] J. Patel, M. Cohen: Criterion for the action of applied stress in the martensitic transformation, *Acta Metall* **1**, 531–538 (1953) (Cited on page [173](#).)
- [265] P. Rozenak, R. Bergman: X-ray phase analysis of martensitic transformations in austenitic stainless steels electrochemically charged with hydrogen, *Materials Science & Engineering A* **437**, 366–378 (2006) (Cited on page [173](#).)
- [266] M. Usui, S. Asano: On the phase transformation of type 304 stainless steel caused by cathodic hydrogen charging, *Scripta Metallurgica et Materialia(UK)* **31**, 445–448 (1994) (Cited on page [173](#).)

- [267] J. Vogt: Hydrogen-induced phase transformation in a high nitrogen austenitic stainless steel, *Corros. Sci.* **41**, 519–528 (1998) (Cited on page 173.)
- [268] Q. Yang, J. Luo: Martensite transformation and surface cracking of hydrogen charged and outgassed type 304 stainless steel, *Materials Science & Engineering A* **288**, 75–83 (2000) (Cited on page 173.)
- [269] W. Horvath, W. Prantl, H. Stroisznigg, E. Werner: Microhardness and microstructure of austenite and ferrite in nitrogen alloyed duplex steels between 20 and 500°C, *Materials Science and Engineering: A* **256**, 227–236 (1998) (Cited on pages 173, 174, 175 and 176.)
- [270] T. Otárola, S. Hollner, B. Bonnefois, M. Anglada, L. Coudreuse, A. Mateo: Embrittlement of a superduplex stainless steel in the range of 550–700°C, *Engineering Failure Analysis* **12**, 930–941 (2005) (Cited on pages 175 and 176.)
- [271] K. Weng, H. Chen, J. Yang: The low-temperature aging embrittlement in a 2205 duplex stainless steel, *Materials Science & Engineering A* **379**, 119–132 (2004) (Cited on page 177.)
- [272] V. Olden, C. Thaulow, R. Johnsen, E. Østby: Cohesive zone modeling of hydrogen-induced stress cracking in 25% cr duplex stainless steel, *Scr. Mater.* **57**, 615–618 (2007) (Cited on page 179.)
- [273] W. Wang, C. Jiang, K. Lu: Deformation behavior of Ni₃Al single crystals during nanoindentation, *Acta Mater.* **51**, 6169–6180 (2003) (Cited on pages 183 and 185.)
- [274] C. Schuh, A. C. Lund: Application of nucleation theory to the rate dependence of incipient plasticity during nanoindentation, *J. Mater. Res.* **19**, 2152–2158 (2004) (Cited on pages 183 and 185.)
- [275] Y. Chin, A. Ngan: Time-dependent characteristics of incipient plasticity in nanoindentation of a Ni₃Al single crystal, *Acta Mater.* **50**, 1599–1611 (2002) (Cited on pages 183 and 185.)
- [276] Y. L. Chiu, A. H. W. Ngan: A tem investigation on indentation plastic zones in Ni₃Al(Cr,B) single crystals, *Acta Mater.* **50**, 2677–2691 (2002) (Cited on pages 184 and 211.)

- [277] M. Peach, J. Koehler: The forces exerted on dislocations and the stress fields produced by them, *Physical Review* **80**, 436–439 (1950) (Cited on page 187.)
- [278] J. Rose, J. Smith, J. Ferrante: Universal features of bonding in metals, *Physical Review B* **28**, 1835–1845 (1983) (Cited on pages 204 and 206.)
- [279] J. Rose, J. Smith, F. Guinea, J. Ferrante: Universal features of the equation of state of metals, *Physical Review B* **29**, 2963–2969 (1984) (Cited on pages 204 and 205.)
- [280] J. Smith, J. Ferrante, J. Rose: Universal binding-energy relation in chemisorption, *Physical Review B* **25**, 1419–1422 (1982) (Cited on page 204.)
- [281] J. Smith, J. Ferrante, J. Rose: Diatomic molecules and metallic adhesion, cohesion, and chemisorption: A single binding-energy relation, *Physical Review B* **25**, 1419–1422 (1982) (Cited on page 204.)
- [282] R. Kirchheim: Reducing grain boundary, dislocation line and vacancy formation energies by solute segregation: Ii. experimental evidence and consequences, *Acta Mater.* **55**, 5139–5148 (2007) (Cited on pages 207 and 208.)
- [283] R. Kirchheim: Reducing grain boundary, dislocation line and vacancy formation energies by solute segregation. i. theoretical background, *Acta Mater.* **55**, 5129–5138 (2007) (Cited on pages 207, 208 and 209.)
- [284] J. Bonneville, B. Escaig: Cross-slipping process and the stress-orientation dependence in pure copper, *Acta Metall.* **27**, 1477–1486 (1979) (Cited on page 207.)
- [285] R. Reed-Hill, R. Abbaschian: *Physical metallurgy principles* (PWS Publishing Company, Boston 1994) (Cited on page 209.)
- [286] E. Shchukin: Physicochemical mechanics in the works of PA Rehbinder and his scientific school, *Colloid Journal* **61**, 545–552 (1999) (Cited on page 214.)
- [287] N. Kheradmand: *Micro-pillars compression test*, Master's thesis, Saarland university (2007) (Cited on pages 215 and 216.)

INDEX

- E_r , 32
- ν , 32
- γ_{LG} , 57
- γ_{SG} , 57
- γ_{SL} , 57
- $h_{Vickers}$, 88

- ab initio, 182
- AFM, 56

- Backscatter electron, 99
- borate buffer solution, 119
- Bulk modulus, 181
- Buoyant force, 58

- conical indenter, 119
- contact angle, 57

- Damage parameter, 6
- ductile to brittle transition, 5

- EBSD, 75
- EC-AFM, 56
- EC-STM, 56
- ECCI, 28
- EDM, 75, 98
- EDX, 136
- Electrical discharge machining, 75
- Electron backscatter diffraction, 75
- Electron channeling contrast imaging, 28
- energy dispersive x-ray analysis, 136

- fcc, 166, 175, 184

- FPZ, 24, 27
- fracture process zone, 7

- Gibbs adsorption isotherm, 183
- Gibbs isotherm, 189
- GND, 62

- HAR, 11
- HEAC, 24, 25
- HEDE, 24, 27, 183, 188
- Helmholtz free energy, 185
- HELP, 24, 26, 27, 188
- HER, 9, 11
- hydrogen activated pop-in, 186
- Hydrogen enhanced decohesion, 24
- Hydrogen enhanced localized plasticity, 24
- Hydrogen evolution reaction, 9, 11

- IEP, 97, 98, 106
- IHAC, 24, 25
- interfacial tension, 57
- ISE, 62
- isoelectric point, 97

- Meniscus force, 57
- microhardness, 86

- OCP, 97, 98, 106
- OGM, 28
- open circuit potential, 97
- orientation gradient mapping, 28

- Poisson's ratio, 32, 34

Rate-determining step, [11](#)
RDS, [11](#)
reduced modulus, [32](#)

SEM, [28](#), [43](#), [56](#), [75](#)
SFE, [27](#), [166](#), [171](#), [175](#), [183](#), [184](#), [188](#)
SPM, [28](#), [43](#), [56](#), [62](#)
stacking fault energy, [27](#)
STM, [28](#), [56](#)

TEM, [21](#), [23](#), [27](#), [56](#)
Thomas-Fermi screening, [182](#)

Vickers indent, [86](#)

wetting angle, [57](#)

X-ray photoelectron spectroscopy, [93](#)
XPS, [93](#), [119](#)
XRD, [153](#), [154](#)

Young's modulus, [181](#)